University of Alberta

A Study of Six-Axis MEMS Sensors for Load Detection in Biomedical Applications

by

David Craig Benfield

A thesis submitted to the Faculty of Graduate Studies and Research
in partial fulfillment of the requirements for the degree of

Doctor of Philosophy

Department of Mechanical Engineering

Spring, 2012
Edmonton, Alberta

Dedication

To the former and future members of the U of A Ski Team.

Abstract

Quantification of the loads applied in biomedical applications has the potential to increase patient safety during surgical procedures and to improve the knowledge of the mechanical behavior of biological tissues. To capture the complexity of loads in biological systems, the acquisition of 3D forces and moments at multiple locations represents an optimal solution. In order to be implemented successfully, a sensor platform with these capabilities should be compact, biocompatible, and minimally invasive. A solution for a specific application in scoliosis correction surgery has been examined in detail. This solution consists of multiple piezoresistive microelectromechanical systems sensors deployed onto existing surgical equipment in a form that allows them to transmit six-axis load information wirelessly. This research has been divided into five main phases: the design and numerical simulation of interfacial piezoresistive sensor pads, microfabrication and device design refinement, characterization of the sensor pads to determine parametric effects on device sensitivity, packaging of sensor pads to integrate wireless and power components and to install them on the surgical equipment, and finally the calibration of the packaged six-axis sensor array. The sensor array developed was determined to be capable of detecting 3D forces and moments with high sensitivity over a limited range, with appropriate power consumption for the scoliosis surgery application.

Acknowledgement

I would like to thank my supervisors, Dr. Walied Moussa and Dr. Edmond Lou, for their support and advice throughout this research project. I would also like to acknowledge my fellow graduate students in our MEMS design group. In particular, I would like to thank Jonathan Lueke for his assistance with the flip-chip and wire bonding systems and Hossam Gharib for his advice on piezoresistive simulation and microfabrication. Daniel Zbinden also deserves credit for his M.Sc. work in Electrical Engineering developing the wireless and power modules used for this sensor array. The technical and administrative staff at the University have also been very helpful throughout my degree, and I will specifically mention Andrew Campbell, Rick Conrad, Gail Dowler, Bernie Faulkner, and Roger Marchand from the Mechanical Engineering department, as well as Stephanie Bozic, Scott Munro, and Les Schowalter from the NanoFab. Summer students Jordan Larson and Kevin Peterson also must be acknowledged for their work in commissioning the diffusion doping furnace and six-axis load application device, respectively. I would also like to thank NSERC, Alberta Innovates Technology Futures (Alberta Ingenuity Fund), and the University of Alberta for the financial support of this research.

Table of Contents

List of Tables

List of Figures

List of Symbols, Abbreviations, and Nomenclature

Abbreviation	Definition
ACA	anisotropic conductive adhesive
ACF	anisotropic conductive film
AIS	adolescent idiopathic scoliosis
AR	aspect ratio, D/Ød, l/w
ARDE	aspect ratio dependent etching
[$\boldsymbol{B}$], [$\boldsymbol{C}$], [$\boldsymbol{D}$]	calibration matrices
b	contact width
BOE	buffered oxide etching
$\boldsymbol{c}$	anisotropic second-order stiffness tensor
C_S	surface concentration
$C(x,t)$	concentration profile
CD	Cotrel-Dubousset
coined bump	flattened stud bump
cryo-etch	cryogenic DRIE
COD	center of detection
D	membrane flexural rigidity, diffusion coefficient
D_0	diffusion coefficient at infinite temperature
DAQ	data acquisition system
DRIE	deep reactive ion etching
DLP	digital light processing
DUV	deep ultraviolet
Δ	delta (change)
δ	Kronecker delta
[$\boldsymbol{E}$], [$\boldsymbol{S}$]	sensitivity matrices
$\boldsymbol{E}$	electric field vector
E	Young's modulus
E_a	activation energy
$erfc(x)$	error function

$exp(x)$	exponential function
F	force
$\{\boldsymbol{F}\}$	3D force vector
$f_i(\boldsymbol{Vn})$	sensor array calibration function
f	frequency, sliding frictional coefficient
FEA	finite element analysis
FFT	fast Fourier transform
FPCB	flexible printed circuit board
$[\boldsymbol{G}]$, $[\boldsymbol{P}]$, $[\boldsymbol{Q}]$	six-axis calibration matrices
g-f	grams force
$g_i(\boldsymbol{V})$	sensor pad calibration function
HF	hydrofluoric acid
HMDS	hexamethyldisilazane (adhesion promoter)
H_2O_2	hydrogen peroxide
H_2SO_4	sulphuric acid
$\boldsymbol{I}$	identity tensor
ICPRIE	inductively coupled plasma reactive ion etch
in vivo	within the living
in utero	in the womb
$\boldsymbol{J}$	current density vector
k	Boltzmann's constant
$[\boldsymbol{k}]$	calibration matrix
KOH	potassium hydroxide
$\{\boldsymbol{L}\}$	six-axis load vector at the load cell
l	length
l_1	direction cosine
LPCVD	low pressure chemical vapor deposition
l/w	aspect ratio
M	moment
m_1	direction cosine
MEMS	microelectromechanical systems

mesa	a raised structure or block
N_S	normal sensitivity
n_1	direction cosine
n-type	semiconductor with excess negative charge carriers
NINT	National Institute for Nanotechnology
ν	Poisson's ratio
$p(x,y)$	membrane loading function
p-type	semiconductor with excess positive charge carriers
PCB	printed circuit board
pedicle	portion of vertebrae
$\boldsymbol{\pi}$	fourth-order piezoresistivity tensor
$\boldsymbol{\rho}$	second-order resistivity tensor
ρ_0	isotropic scalar unstressed resistivity
$\bar{\rho}$	average resistivity
$Q(t)$	total number of dopant atoms
q	magnitude of applied distributed load
R^2	coefficient of determination
R	resistance
R_S	sheet resistance
R_X, R_Y	shear sensitivity ratio
RIE	reactive ion etching
$\{\boldsymbol{S}\}$	six-axis load vector at the sensor array
SALAD	six-axis load application device
SEM	scanning electron microscope
SiO_2	silicon dioxide
sq	square
stud bump	single ball bond
$\boldsymbol{\sigma}$	second-order stress tensor
T	temperature
t	time
TSV	through-silicon via

UV	ultraviolet
V	voltage
$\{\boldsymbol{V}\}$	4-term voltage vector
$\{\boldsymbol{Vn}\}$	16-term voltage vector
w	width
w	perpendicular membrane deflection
X_S	X-axis shear sensitivity
X-ducer	Motorola branded four-terminal gauge
Y_S	Y-axis shear sensitivity
Ω/sq	ohms per square (non-SI unit for sheet resistance)

Chapter 1: Introduction

A methodology to detect forces and moments applied in biomedical applications is described. Specifically conceived for an application in scoliosis correction surgery, a sensor array concept using several interfacial force detection components to resolve six-axis loading is introduced. Background information on the scoliosis deformity, the surgical correction procedure, and the expected loads is provided. An overview of the sensing system is presented, with a focus on the challenges encountered during development, deployment, and characterization. Finally, an outline of the remainder of this thesis is provided.

1.1 - Thesis Objectives

The quantification of applied biomedical loads has the potential to optimize orthopaedic surgical procedures. This quantification can provide feedback to surgeons that can complement their physical dexterity and also may be used to enhance knowledge of the mechanical behavior of biological tissues. The primary objective of this research was the design, fabrication, and calibration of a sensor array capable of detecting three-dimensional (3D) forces and moments in biomedical applications in orthopaedics. This sensor array was specifically designed for an application in scoliosis correction surgery. The detection of the applied forces and moments in this application presented several significant challenges for a sensor array, including size constraints, relatively large force and moment ranges, and the need for non-invasive deployment.

Previous work performed as part of my Master's research [1, 2] used numerical and analytical techniques to develop a sensing methodology capable of detecting six-axis loads. This sensing methodology utilized microelectromechanical systems (MEMS) sensor pads to retrofit the existing scoliosis instrumentation. The research presented in this thesis is an investigation into the feasibility of this sensing methodology. This investigation has included research on several aspects of the MEMS sensor pads, including piezoresistive sensing elements, through-silicon vias, aspect ratio dependent etching, microfabrication precision and tolerances, characterization, and various solutions

for attachment to circuit boards and external components. The requirement that the sensor pads be retrofit onto existing surgical equipment led to research in deployment and packaging, including the study of flip-chip and wire bonding techniques, specific characterization of isotropic and anisotropic conductive adhesives, interfacing the sensor pads with a wireless data transmission system, and reviewing methods to maintain biocompatibility requirements. The calibration of such a sensor array created additional challenges. These challenges included determination of sensitivity, verification of multi-axis detection capabilities, and the study of sensor performance as wireless, power, and packaging components were integrated.

1.2 - Motivation

Investigation of a load detection system used to measure six-axis loads during scoliosis correction surgery was the main objective of this research. Surgeons expressed a desire to fully quantify the 3D forces and moments applied at each location along the spine where the spinal fusion hardware interfaces with biological tissues. The quantification of these loads is particularly important to the success of the surgery, as the loads significantly contribute to accidental vertebral breakage, the development of pseudoarthroses, spinal screw pull-out or failure, and the quality of correction that may be achieved [3, 4]. Accurate quantification of the applied loads in spinal surgery also has potential to enhance knowledge of the spine's mechanical behaviour, improving presurgical planning models and the overall success rates of the procedures [5-8]. To achieve this objective, a sensing system capable of being installed at several locations along the spine and detecting six-axis loads has been developed.

1.2.1 - In Vivo Load Measurement in Biomedical Applications

Mechanical loads applied in biomedical applications are defined as the forces and moments that are caused by the interaction of the medical instrumentation with biological tissues. These loads may be directly applied by the surgeons, such as during the correction of a separated shoulder. In addition, these loads may be

induced after a medical procedure by the implanted instrumentation, such as in the corrective operation of dental braces. Other such orthopaedic and biomedical applications in which applied loads are important include surgical implant installation, joint replacement surgery, spinal fusion surgery, orthopaedic bracing, and many others.

Biomechanical load information collected *in vivo* often does not include the full 3D force and moment information [7-13]. This lack of information creates significant challenges in terms of fully characterizing biomedical loads applied. Additional challenges encountered during detection of these loads are caused by the statically indeterminate load situations produced between the medical implants and biological tissues [5, 7, 8, 14]. The tactile nature of orthopaedic surgery often leads to situations where loads are applied with several different surgical tools (including the surgeons' hands) simultaneously, creating unique and statically indeterminate systems. If the loads are not detected at each interface between the biological and implanted components in the system, inaccuracies in the detected loads may result. Patient-to-patient variation creates additional challenges to accurate load detection, such as wide ranges in biological material properties, unique structural arrangements, and varied surgical objectives [9, 15-17].

The accurate measurement of biomechanical loads is important for several reasons. Forces and moments applied by surgeons are not typically quantified during surgical procedures, meaning that the surgeon's tactile skill, or "surgical feel", is relied upon to apply the loads correctly. This method of load application may lack accuracy and repeatability when compared to loads applied using a quantifying method or system, and also makes it difficult to instruct other surgeons on proper technique. Improper load application during surgical procedures can lead to complications such as suboptimal corrections, bone fractures, equipment failure, pseudoarthroses, ligament and joint damage, and other complications [6, 18]. Measurement of loads applied by implanted instrumentation post-surgery is also important, for reasons such as the active

monitoring of healing, determining patient compliance with bracing and activity regimens, optimizing corrective loads, and detecting hardware failure [8, 19].

The quantification of biomechanical loads offers advantages in a wide array of applications. This diversity requires that specific implementation strategies be developed to create sensing systems tailored to the individual application. As stated above, force and moment measurement systems may have uses in surgical tools, medical implants, orthotic braces, and prosthetics.

Common to all of these applications are the following basic requirements: biocompatibility, sterilizability, and minimally treatment disruptive use.

Biocompatibility implies that the sensing system will have an acceptably low level of toxic or harmful effects on the patient's tissues. This definition includes the integrity of the device: non-toxic substances that could be dislodged from the device where they would contaminate or damage the biological zone also must be eliminated. In certain cases, it may be acceptable to use materials in the sensing system that are not specifically biocompatible provided that they are sufficiently encapsulated in a biocompatible material and will not come into contact with biological tissues. The performance requirements for biocompatible materials may vary depending on the application of the sensing system designed; a material to be used in a surgical tool such as a clamp or grasper will have a different set of biocompatible material requirements when compared to a sensing element that will be permanently implanted. Depending on the application, biocompatibility may also include sterilizability.

Sterilizability is defined as the ability to remove all microorganisms and biological contaminants from the sensing system. For typical surgical tools and implants, usually composed of surgical-grade stainless-steel, this process consists of autoclaving, which is a sterilization method using high-pressure, superheated steam. Since most sensing devices contain electronics that would be damaged by the autoclaving process, ethylene oxide, irradiation, dry heat, or other methods of sterilization may be employed. These methods also have potential to damage equipment, so the sensing system must be adequately durable to survive the specific sterilization regime chosen. Further details on sterilization are provided

in Section 5.5.2. It is also important to note that once an instrument enters the sterile field, it will not be possible for the engineer to physically touch the sensing system before the procedure. This implies that equipment will need to be stored in a standby mode between sterilization and use. Taking the sensing system out of the standby mode before performing the procedure must be a task that the surgeon or nurse can perform quickly and easily, to avoid altering standard surgical protocols.

Minimally treatment disruptive use of a sensing system mandates that the surgical protocols must not be altered in a way that puts a patient at risk. Any advantages which may be gained through the collection of biomechanical load data are negated if the collection of said data poses additional hazards to the patient. Ideally, the employed method of sensor implementation for force and moment collection should allow surgical implants and tools to be used in the same way as their non-instrumented counterparts. This condition poses additional design considerations on the sensor system to ensure full and seamless integration into the existing hardware. These considerations may include size constraints, strength and durability requirements, and other design parameters related to package integration.

1.2.2 - Description of Scoliosis

Scoliosis is a condition characterized by abnormal lateral curvature of the spine and vertebral rotation [3, 4]. This condition is the most common spinal deformity, causing three-dimensional anatomical anomalies that may include changes to the rib cage structure, pelvic tilt, and uneven hips or shoulders [3, 4]. Symptoms of scoliosis may also include difficulty with extended periods of sitting or standing, back pain and fatigue, aesthetic asymmetries such as a “rib hump”, and associated psychological or emotional stress [3, 4, 20, 21]. In more severe cases, arthritis, nerve damage, paralysis, respiratory distress, cardiopulmonary symptoms, and other serious complications may result [20, 21].

There are three main types of scoliosis: Congenital, neuromuscular, and idiopathic. Congenital scoliosis is usually caused by skeletal deformation

occurring *in utero*, and neuromuscular scoliosis is caused by neurological abnormality, especially those related to conditions such as cerebral palsy, muscular dystrophy, spina bifida, or paralysis. In contrast, idiopathic scoliosis occurs for no known reason, and presents mainly in adolescent females [3, 4]. This type, known as adolescent idiopathic scoliosis, or AIS, is the most common variety [4]. Approximately 2-3% of children have AIS and 10% of this group requires some form of treatment. Treatment will generally consist of observation, bracing, and in severe cases, surgery [3, 4].

1.2.3 - Surgical Treatment

The corrective procedure for cases of scoliosis which require surgery is spinal fusion. This procedure was greatly improved through the development of the Harrington Rod instrumentation [22] which utilized internal fixation to correct the lateral component of the curvature, stabilizing the spine with a system of rods and hooks until fusion occurred. Further development of internal fixation methods using hooks, screws, rods, and cables was performed by Dwyer, Zielke and Pellin, Herndon, and others [23-27]. More recently, fixation methods using pedicle screws have become more commonplace. These methods have been reported as being safer and feasible for younger patients [16]. One such method is described using the Cotrel-Dubousset (CD) instrumentation [28].

Spinal fusion using CD instrumentation utilizes hooks and pedicle screws which are inserted into the vertebrae of the spine. Further research has demonstrated that using pedicle screws in place of the hooks for three-dimensional corrections produces better results [29-31]. This may be attributed to the thoracic pedicle screws having greater pullout strength than hooks [32] and superior load-sharing properties in fracture constructs when applied in greater numbers [7]. Surgeons pre-bend steel or titanium rods into the desired final shape for the spine. The rods are then inserted into U-shaped notches located in the head of each screw. During the insertion process, forces and moments are applied by the surgeons to deflect the spine into the shape defined by the rods. The revised spinal curvature is then maintained by locking the rods into place

using retaining bolts which thread into the screw heads. Figure 1.1 shows a radiograph of a scoliotic spine after a surgical fusion procedure performed using the CD instrumentation set. The patients requiring surgery typically suffer from scoliotic curves which are severe, and require large 3D forces and moments to correct and hold them in the modified position. Figure 1.2 shows pre-operative and post-operative radiographs of a scoliotic spine and indicates the forces and moments applied to the spine to perform the correction. Quantification of these forces and moments is fundamentally important to the success of the procedure: Excessive loads may cause surgical equipment failure, pseudoarthroses, and patient discomfort while inadequate loads may produce a sub-optimal correction, leading to a loss of patient mobility and increased patient recovery times [6, 18].

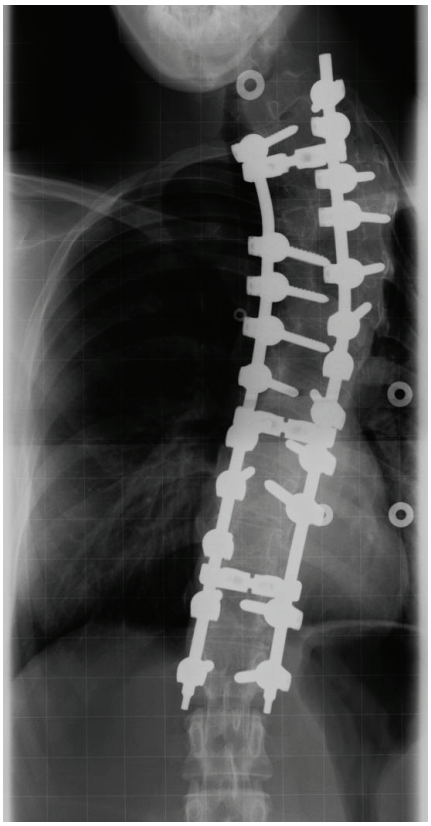

Figure 1.1. A post-operative radiograph of a scoliotic spine corrected using the CD instrumentation set. Two rods have been installed on either side of the vertebral column, each are fixed in place with multiple pedicle screws. (Image used with permission of the Glenrose Rehabilitation Hospital.)

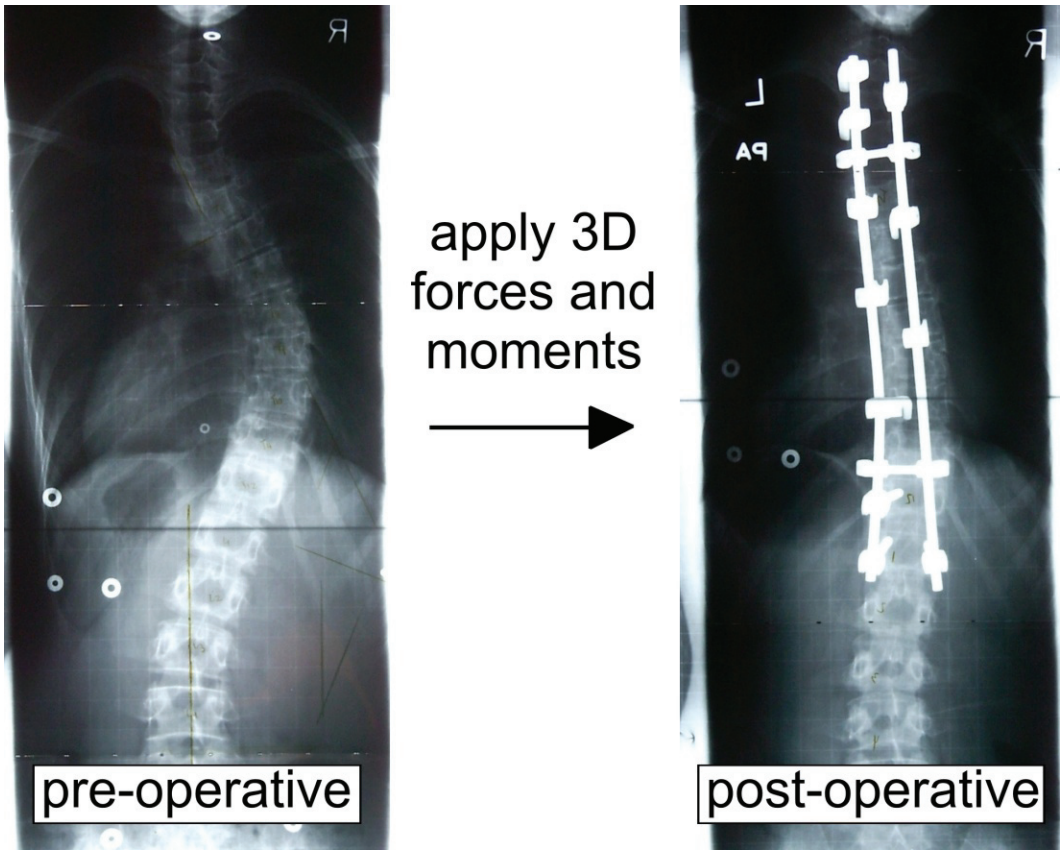

Figure 1.2. Pre-operative and post-operative radiographs of a scoliotic spine. Force and moment application during correction using the CD instrumentation is indicated. (Images used with permission of the Glenrose Rehabilitation Hospital.)

1.2.4 - Force and Moment Ranges

The use of the CD instrumentation for scoliosis correction surgery applies loads to the spine both during and after the corrective procedure. Previous experimental work determining the loads applied in scoliosis correction surgery has included several different methods of load detection, and is discussed in further detail in Section 2.2. These include detection systems integrated into the pedicle screws as well as those in other locations [5, 8-14, 19, 23, 33-38]. Numerical studies of the spine have also been used to estimate loads applied during spinal fusion procedures [39, 40]. Numerical methods provide more intra-operative load data than those obtained in experimental collection experiments. However, since these

numerical studies are approximating complex biomedical load scenarios, their outcomes must be rigorously verified experimentally.

Upon assimilation of the experimental and numerical data referenced above, 3D load ranges have been developed for a sensing system located at the rod-screw interface of the CD set. The sensor array should be able to measure forces of up to ±1000N and moments of up to ±4N-m. For optimal characterization of the loads applied to the patient's spine, measurement of the six-axis loads applied should be performed at every screw installed during the surgical procedure.

1.3 - Proposed Approach

The sensor array, which was simulated in previous work [1, 2], has been developed and examined for its ability to detect the six-axis loads applied to the spine during scoliosis correction surgery. This development has included design, analytical modelling, numerical simulation, manufacturing, characterization, packaging, and calibration of the sensor array. To ensure that use of the sensor array was minimally treatment disruptive, a design augmenting the existing pedicle screws used with the CD instrumentation set was developed. An augmented design minimized potential negative effects to the surgical protocols and eliminated concerns associated with redesigning the pedicle screws and CD instrumentation. Considering this design constraint, it was determined that the sensor array solution should detect forces and moments at the interfaces between the rods and screws. To accomplish this, the developed sensor array used sensing elements located within the U-shaped notches located in the heads of the pedicle screws. In order to physically fit the sensing elements within the notches of the pedicle screws, MEMS components were selected.

1.3.1 - Sensor Array Concept

The sensor array consists of a set of MEMS sensors, wireless module, power module, and package, all of which are integrated onto a pedicle screw. The MEMS sensors consist of four deformable silicon membranes, each utilizing a set

of four piezoresistive sensing elements. Each set of piezoresistors on a membrane is referred to as a sensor pad, and is sensitive to shear and normal force loads (three-axis). The four sensor pads are placed at different locations within the U-shaped notch of the pedicle screw and are operated in parallel to detect the six-axis loads applied.

Power and wireless modules are attached externally to the pedicle screws and allow the sensor array to operate as a self-contained unit. This is particularly important to allow the sensing system to operate without interfering with surgical protocols. Packaging the sensors, wireless components, and power module for component interconnection and biocompatibility is another challenge. A flexible printed circuit board (FPCB) has been designed and wrapped around the head of the screw, allowing the components to be distributed on different surfaces. The sensing, wireless, and power components are mounted onto the FPCB using an anisotropic adhesive or using wire bonded gold stud bumps and a non-conductive adhesive underfill. Through-silicon vias (TSVs) are used on the sensing components to reduce their footprints on the FPCB within the U-shaped notches. Component alignment onto the FPCB pads is achieved using a flip-chip system, which is capable of applying force, heat, and ultrasonic power to aide in connection and curing of adhesives. The sensor array mounted to the head of the pedicle screw is shown schematically in Figure 1.3.

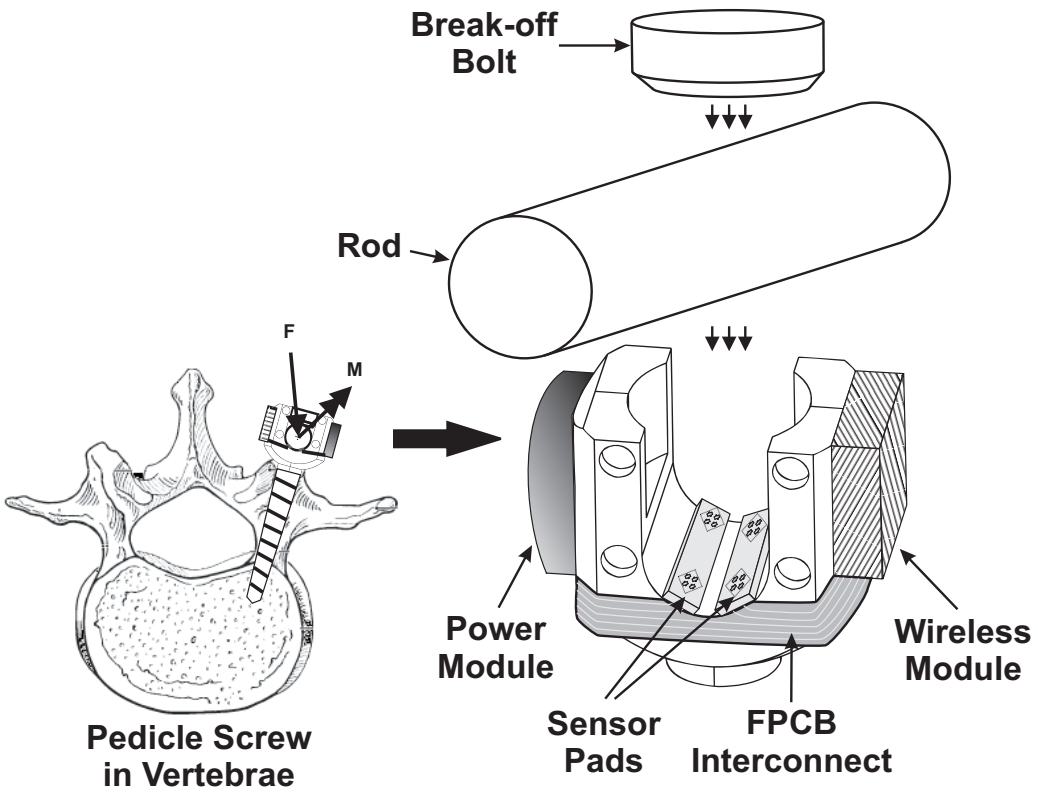

Figure 1.3. A schematic of the proposed sensor array mounted to the head of a pedicle screw for use in scoliosis correction surgery.

1.3.2 - Sensor Array Calibration

Two phases of calibration of the sensor array have been performed. The first calibration phase consisted of an unpackaged characterization of the individual sensor pads. This allowed the shear and normal force sensitivity of the sensor pads to be determined, and acted as a final verification of performance for the manufactured devices. This method of characterization also eliminated any discrepancy in performance or issues with alignment that may occur due to the packaging of the devices. Details of this characterization are provided in previous work [1, 2, 41], as well as in Section 4.3, and consisted of the application of normal, shear, and combined loading to the sensor pads. This analysis allowed parametric adjustment of sensor pad features while monitoring output sensitivity.

The second phase of device calibration for the sensor array was performed on a custom-built load application frame, known as the Six-Axis Load

Application Device, or SALAD. The SALAD consisted of a five-axis actuation stage with a commercially available six-axis load cell rigidly attached. The actuation stage was modular, consisting of three linear and two rotary actuators mounted in a stack and connected to the base of the frame. A fixed stage was also mounted to the frame and positioned above the movable stage and load cell. Manual, individual adjustment of the stage actuators allowed known loads to be applied to the instrumented pedicle screw, which was held between the upper stage and commercial load cell / lower stage. Further details on the SALAD are provided in Section 6.2. Outputs from the six-axis commercial load cell and the instrumented scoliosis screw were then analyzed to determine calibration equations.

Raw data produced using the SALAD calibration system consisted of 32 output voltages (16 differential channels) from the piezoresistors on the instrumented pedicle screw and 12 output voltages (6 differential channels) from the commercial load cell. These outputs were collected using a single, high speed data acquisition system (DAQ) to simplify further calculation. Calibration equations, which may be linear or non-linear, were then determined by comparing the outputs from the commercial load cell and the sensor array. The difference in the physical location of the actual detection points between the two load cells was also considered when performing calibration. The design of the SALAD allowed the input loads to be applied individually or in combination, so that nonlinearity and crosstalk between load channels could be detected.

1.3.3 - Surgical Operation Specifications

During scoliosis correction surgery, the surgeon will install the instrumented pedicle screws in the same manner as with a standard screw. The rod will be placed in the U-shaped notch of the screw and preloaded with a retaining bolt. After preloading, the sensor array will be capable of detecting 3D forces and moments applied to the spine by the rod through the pedicle screws.
These screws will record and display data via the wireless system during the correction phase of the surgery. If necessary, the instrumented screws may then

be removed and replaced with non-instrumented screws for permanent installation.

In order to detect the 3D loads applied, the rods must be aligned so they may affect the deformable silicon diaphragms of the sensor pads. Deflection of a diaphragm causes a stress distribution to be produced, affecting the four piezoresistors. The outputs from the four piezoresistors have been shown to be proportionally related to the three-axis (normal and shear) forces applied to each sensor pad. The normal and shear loads from each of the four sensor pads are then combined to produce the 3D forces and moments experienced by the pedicle screw. The piezoresistors produce a total of 16 differential output voltages on each screw. This data is multiplexed and transmitted to a data acquisition system using the wireless transmitter, where it can be converted to force and moment information using a calibration equation determined experimentally.

This sensor array is capable of detecting six-axis loads and has been specifically designed for use in scoliosis correction surgery. If applied in a surgical setting, the real-time data produced could be used as an overload detection warning system and as a method to ensure that loads are distributed appropriately among the vertebrae. In addition, the loads collected during the procedure will assist in the development of numerical models of the spine's mechanical behavior, allowing for the development of advanced pre-surgical planning techniques and improving surgical outcomes. Future uses for this type of sensor array and calibration system include various other applications where 3D forces and moments can be collected. These uses may include biomedical applications such as prostheses, joint replacement implants, orthopaedics, and dental braces. The array described has shown to have high sensitivity, adjustable load ranges, and may be packaged to be biocompatible and sterilizable. These features make it versatile and desirable for biomedical use. Sensor arrays using this sensing regime also have potential for applications in non-biomedical force-detection.

1.4 - Thesis Organization

This thesis is divided into seven chapters. Chapters one and seven comprise the introduction and conclusions respectively. Chapter two presents the relevant literature, chapter three focuses on production of the piezoresistive sensing components, chapter four details a sensitivity analysis of the piezoresistive sensing components, chapter five describes packaging and deployment techniques, and chapter six gives a description of device calibration. Further detail on the contents of chapters two through six is provided below.

Chapter two will discuss the relevant literature, beginning with biomedical sensing. Sensing using MEMS devices will then be introduced. The theoretical background on piezoresistance and membrane deflection will be detailed, followed by a presentation of pressure sensing and interfacial sensing devices which utilize a piezoresistor-on-membrane sensing scheme. Background information relevant to the microfabrication, packaging, and electrical interconnection of the presented MEMS sensor array is also described.

Chapter three provides a detailed description of the design and microfabrication of the piezoresistive sensing components. This includes analytical and numerical studies of piezoresistor-on-membrane devices. The microfabrication process flow is presented in detail, including explanations of specific process steps. In-depth details are also provided on the commissioning of a diffusion furnace for piezoresistive doping, determining the tolerance limits of microfabrication processes, and performing high aspect ratio silicon etching.

A parametric analysis is described in chapter four which focuses on the shear and normal sensitivity of the sensor pads. Geometric and material properties of the piezoresistive devices were varied as three-axis sensitivity was monitored. Numerical and experimental techniques were used to perform this parametric analysis. This chapter describes specific sensitivity trends resulting from varying the parameters, and the sensor pad parameters which have the greatest effect on shear and normal sensitivity are isolated.

Chapter five explains the packaging techniques used to deploy the piezoresistive devices on the scoliosis pedicle screws. The techniques described

include FPCB design and production, as well as the flip-chip and wire bonding technologies used to attach the MEMS devices to these FPCBs. Adhesive selection methodology and usage for the isotropic conductive adhesives, anisotropic conductive adhesives, and sealants are also explained. Incorporation of these techniques with the TSVs produced in microfabrication is also covered.

Calibration of the packaged sensor array is the topic of chapter six. The design and construction of the custom calibration frame is described. This includes incorporation of the DAQ and collection of differential voltage outputs. Calibration equations are described, including the derivation of cross-sensitivity terms. Sensitivity, load capacity, linearity, and other artifacts of calibration are determined.

Chapter 2: Literature Review

Relevant literature is discussed. Load measurement techniques for biomedical applications are introduced, followed by specific information on detection in scoliosis correction surgery. Sensing applications using MEMS devices are then discussed. The piezoresistive sensing regime is explained and examples of piezoresistor-on-membrane devices, including pressure sensors and interfacial devices, are provided. Specific background information regarding the microfabrication of such sensing systems is also detailed. Finally, information on deployment and packaging using flip-chip, wire bonding, and FPCBs is introduced.

2.1 - Introduction

The analytical background and literature precedent relating to the development of the scoliosis sensor array have been reviewed. Preliminary review of sensor technology has indicated that the design introduced in Section 1.3 is within the realm of existing MEMS sensor capabilities, however, a design with the specific parameters required for this application has not been reported previously. As this sensor array utilizes a piezoresistor-on-membrane layout, analytical background of piezoresistance and membrane deformation has been presented. This background was essential for the accurate numerical and experimental characterization of the sensor pad components (as presented in Sections 3.3, 4.2, and 4.3). Implementation of the sensor array onto existing surgical instrumentation has also led to significant research contributions in packaging and deployment (as presented in Section 5), so fundamental background material in this area has also been presented.

2.2 - Load Measurement in Biomedical Applications

Due to the wide variety of applications in which quantification of biomedical forces and moments are of interest, many different load detection systems exist. Instrumented medical implants for the hip, knee, femur, spine, and shoulder have previously been developed [5, 8, 34]. A common implementation methodology

utilizes one or more strain gauges to instrument medical implants, adding the capability to detect loading. This method is versatile as it allows the sensing system to produce outputs in the form of voltages, which may be displayed, stored, and manipulated electronically. The load detection capability may be in one or more directions, with the capability to detect three-dimensional (3D) forces and moments (so called six-axis detection capability) occurring in devices developed more recently [42-46]. In addition, load detection systems for use at biomedical interfaces have been developed. The applications for such systems include prosthetics, bedsore detection systems, and insole load mapping technology [43, 47-49]. The quantification of interface load data is important as it provides localized information on how surface pressure and shear loads are distributed over an application site.

A situation where biomedical load information is limited occurs during scoliosis correction surgery. Measurement of these in-vivo forces in the operating room is not a novel idea. However, most of the work was done many years ago, measuring only the compression or distraction forces applied during the Harrington rod procedure [10, 18, 23, 33, 35, 36]. Recent studies were more focused on the vertebral body forces and loads [8, 14]. Rohlmann *et al*. developed a telemetrised instrumentation to study the loading on internal spinal fixation devices and his group also measured the forces on the instrumented rod [19]. Further research by Lou *et al.* and Duke measured 2D loading using an instrumented rod rotator system and an instrumented hook/screw system, respectively [9, 11]. The data presented in literature is incomplete as it does not include load detection at all of the locations along the spine where the implants and biological components interface. In addition, these systems do not have the capability to fully capture 3D forces and moments applied during the corrective procedure.

2.3 - Microelectromechanical Systems Sensing

Microelectromechanical systems, or MEMS, refers to a technological subset of devices characterized by their small size and components which undergo

electrical and mechanical interactions. These devices include sensors and actuators with characteristic dimensions smaller than one millimeter, utilizing operative regimes which include thermal, fluidic, magnetic, resonant, optical, piezoelectric, capacitive, or piezoresistive systems. The small size of MEMS devices often enables them to take advantage of dominant physics principles that are altered when compared to macro-scale devices. Some examples of successful MEMS devices include ink-jet printer heads, micro-mirror arrays for DLP projectors, and automotive airbag accelerometers [50, 51].

The MEMS industry commonly makes use of bulk microfabrication techniques originally developed for the microelectronics industry. This allows MEMS devices to be produced in large volumes at a low per-unit cost. These bulk microfabrication techniques also define the materials that may be used for production, which typically include silicon, polymers, and metals. The use of lithographic techniques on flat, single-crystal silicon substrates is a common method of fabrication, allowing for accurate in-plane patterns to be copied onto the substrates, enabling production of 3D devices through repetitive steps of patterning, physical and chemical deposition, oxide formation, extrusion, and etching.

The compact size and high functionality of MEMS sensors make them well suited for detection in applications where space is limited or conventional sensing techniques are overly expensive or cumbersome. Three-axis accelerometers for cellular phones, pressure sensors for medical applications, and gyroscopes for automotive stability control systems are examples of MEMS devices that may be produced using single-crystal silicon and operate using a piezoresistive sensing regime. The load cell for use in the scoliosis surgery application presented in this document is also an example of such a device. The piezoresistive regime was chosen for this application because of its linearity, the relative ease of sensitivity adjustment by varying the concentration of dopants, and the excellent properties of silicon as a mechanical material [52-54]. This MEMS sensing scheme allowed six-axis sensors to be developed that can be made compact enough to be integrated into the existing pedicle screws.

2.4 - Piezoresistive Theory

Piezoresistance is defined as a change in resistivity corresponding to stress. Although some amount of piezoresistance is present in many materials, the semiconductors silicon and germanium were first noted as having significant piezoresistive coefficients by Smith [54]. Research into the use of semiconductors as transducers followed this discovery, with substantial research being contributed by Pfann, Mason, Herring, and others [52, 55-57]. The use of silicon as the material of choice in the semiconductor industry has caused more recent work on piezoresistance to be focused on silicon [58-66].

Silicon is a Group IV element (this grouping refers to its four valence electrons, and is typical nomenclature in the field of semiconductor physics) and crystallizes into a diamond cubic structure [67]. As is characteristic of semiconductors, the resistivity of silicon may be controlled by varying the temperature, changing the concentration of impurities, or by irradiating with light or high-energy electrons. Adding impurities to silicon in the form of Group III or Group V elements create p-type and n-type semiconductors, respectively [67]. The terms p-type and n-type refer to the positive and negative polarities of the charge carriers which are transported. In the production of piezoresistors, phosphorus, a Group V element, may be introduced to the crystal lattice of silicon to provide an extra conduction electron, thus creating n-type silicon. Conversely, boron, a Group III element, may be introduced to the crystal lattice of silicon to create a lack of a conduction electron (also known as positive hole), creating p-type silicon. This lightly doped silicon is referred to as an extrinsic semiconductor, while pure silicon is referred to as an intrinsic semiconductor [67].

The change in resistance for doped silicon under stress is substantially greater than the effect due to the geometric change of the material [68]. This geometric effect is the dominant cause of resistance change in a stretched metallic wire, for example. The explanation for the piezoresistance phenomenon causing the additional resistance change in silicon is that the applied stress (and resultant

strain on the crystal lattice) changes the mobility of the charge carriers [54]. This effect is dependent on the orientation of the applied stress and current flow relative to the crystal orientation of silicon, indicating that piezoresistance in single crystal silicon is orthotropic [54]. Figure 2.1 illustrates the crystal structure of single crystal silicon [67].

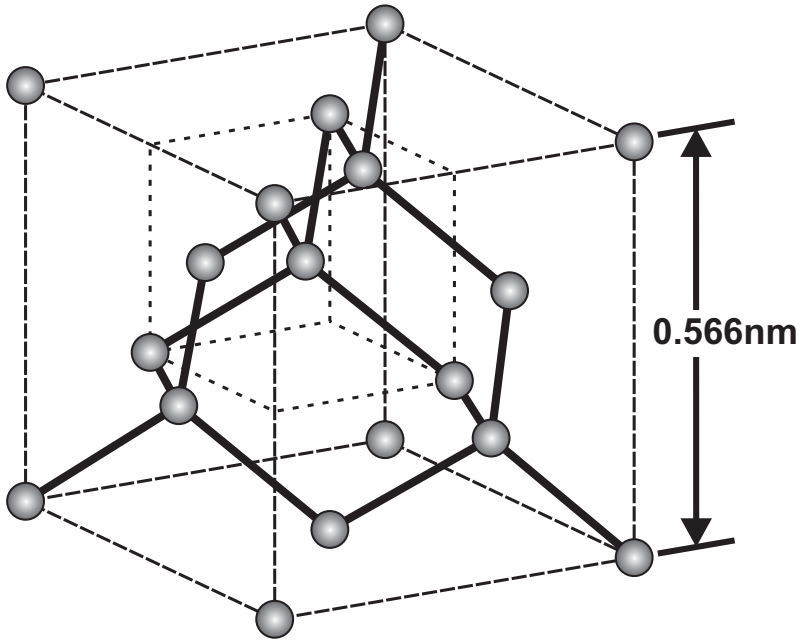

Figure 2.1. Diamond cubic crystal structure of single crystal silicon (modified from [67]). Orthotropic physical properties are the result of symmetry in the crystal lattice.

The fundamental equations of piezoresistance are shown in tensor form below. Beginning with Ohm's law:

$$\boldsymbol{E} = \boldsymbol{\rho J} \tag{2.1}$$

$\boldsymbol{E}$ is the electric field vector, $\boldsymbol{J}$ is the current density vector, and $\boldsymbol{\rho}$ is the second-order resistivity tensor defined by:

$$\boldsymbol{\rho} = \rho_0(\boldsymbol{I} + \boldsymbol{\pi\sigma}) \tag{2.2}$$

ρ_0 is the isotropic (scalar) resistivity of the unstressed crystal, $\boldsymbol{I}$ is the identity tensor, $\boldsymbol{\pi}$ is the fourth-order piezoresistivity tensor, and $\boldsymbol{\sigma}$ is the second-order stress tensor. Components of Equation (2.2) are defined as follows:

$$\rho_{TU} = \rho_0 \delta_{TU} + \rho_0 \pi_{TUVW} \sigma_{VW} \tag{2.3}$$

The subscripts *T*,*U*,*V*, and *W* indicate that Einstein summation convention (of Euclidean space) applies to the terms of Equation (2.3), and δ is the Kronecker delta. As $\boldsymbol{\rho}$ and $\boldsymbol{\sigma}$ each have six independent components, Equation (2.2) also may be described in the matrix notation [69] as follows:

$$\begin{pmatrix} \rho_1 \\ \rho_2 \\ \rho_3 \\ \rho_4 \\ \rho_5 \\ \rho_6 \end{pmatrix} = \begin{pmatrix} \rho_0 \\ \rho_0 \\ \rho_0 \\ 0 \\ 0 \\ 0 \end{pmatrix} + \rho_0 \begin{pmatrix} \pi_{11} & \pi_{12} & \pi_{13} & \pi_{14} & \pi_{15} & \pi_{16} \\ \pi_{21} & \pi_{22} & \pi_{23} & \pi_{24} & \pi_{25} & \pi_{26} \\ \pi_{31} & \pi_{32} & \pi_{33} & \pi_{34} & \pi_{35} & \pi_{36} \\ \pi_{41} & \pi_{42} & \pi_{43} & \pi_{44} & \pi_{45} & \pi_{46} \\ \pi_{51} & \pi_{52} & \pi_{53} & \pi_{54} & \pi_{55} & \pi_{56} \\ \pi_{61} & \pi_{62} & \pi_{63} & \pi_{64} & \pi_{65} & \pi_{66} \end{pmatrix} \begin{pmatrix} \sigma_1 \\ \sigma_2 \\ \sigma_3 \\ \sigma_4 \\ \sigma_5 \\ \sigma_6 \end{pmatrix} \tag{2.4}$$

The diamond cubic crystal structure of silicon allows symmetric operations to be performed which simplify $\boldsymbol{\pi}$ [68]. When aligned with a crystallographic coordinate system, the piezoresistive tensor (in matrix notation) may be expressed in terms of three independent components, as shown in Equation (2.5) [68].

$$\begin{pmatrix} \pi_{11} & \pi_{12} & \pi_{12} & 0 & 0 & 0 \\ \pi_{12} & \pi_{11} & \pi_{12} & 0 & 0 & 0 \\ \pi_{12} & \pi_{12} & \pi_{11} & 0 & 0 & 0 \\ 0 & 0 & 0 & \pi_{44} & 0 & 0 \\ 0 & 0 & 0 & 0 & \pi_{44} & 0 \\ 0 & 0 & 0 & 0 & 0 & \pi_{44} \end{pmatrix} \tag{2.5}$$

To express the components of the vectors and tensors shown above in terms of a non-crystallographic coordinate system, rotational tensors (or matrices) may be employed [68, 69].

The piezoresistive properties may be defined for silicon by π_{11}, π_{12}, π_{44}, and ρ_0. Table 2.1 specifies these coefficients for lightly-doped p-type and n-type silicon. In addition to the impurity type used, impurity concentration and temperature have significant effects on the piezoresistive and resistivity coefficients. Resistivity tends to decrease as impurity concentration increases and as temperature increases beyond about 200K [52, 55, 62, 70]. Piezoresistance is shown to decrease as temperature increases and when the impurity concentration increases beyond about 10^{17}atoms/cm^3 [63, 71-73]. It is also worth noting that at higher impurity concentrations, the temperature dependence of the piezoresistance

is reduced. These factors are some of several to consider when designing piezoresistors for use as sensors.

Table 2.1. Unstressed resistivity and piezoresistive coefficient values for lightly-doped silicon (values from [54, 68]).

Silicon Doping	ρ_0 (Ω-cm)	π_{11} (10^{-11}/Pa)	π_{12} (10^{-11}/Pa)	π_{44} (10^{-11}/Pa)
n-type	11.7	-102.2	53.4	-13.6
p-type	7.8	6.5	-1.1	138.6

2.5 - Piezoresistive Sensing Elements

When designing piezoresistive sensors, several factors are important to consider. As stated in Section 2.4, piezoresistance in single crystal silicon is orthotropic. This indicates that piezoresistors will behave differently depending on their orientation relative to the underlying crystal structure of the silicon. Kanda has produced charts which demonstrate the variation of piezoresistive coefficients depending on orientation [74]. These charts indicate that an orientation change of only 45° will reduce the piezoresistive component of device sensitivity from the maximum to minimum value. For example, for p-type silicon on a (1 0 0) plane, applied uniaxial stress will cause the greatest change in resistance in a piezoresistor when applied along a [1 1 0] direction, taking advantage of the large π_{44} component.

Unstressed resistance is another key factor to consider when designing piezoresistors. Ohm's law specifies that resistance and input voltage determine the power consumption of a resistor; these parameters also affect sensitivity, noise, and dynamic range in sensing applications [75, 76]. Low resistance sensors are also more prone to resistive heating, which can affect the device sensitivity and physical integrity of piezoresistive devices and packages. The impurity type, impurity concentration, impurity depth profile, resistor geometry, as well as any contact resistance between the piezoresistor and the measuring device, determines the resistance of a silicon piezoresistor. The impurity concentration and depth profile are controlled by the doping procedure selected, which will be discussed further in the Section 3.4.5. The piezoresistor surface geometry remains as the

major influence on resistance, which allows the definition of sheet resistance (R_S) shown in Equation (2.6).

Assuming a resistor with average resistivity ($\bar{\rho}$) in the shape of a rectangular prism with length, width, and depth dimensions given by l, w, and d, respectively:

$$R_S = \frac{\bar{\rho}}{d}, R = R_S \frac{l}{w} \tag{2.6}$$

This equation implies resistance (R) is proportional to sheet resistance and aspect ratio (l/w). Sheet resistance is expressed in (non-SI) units of ohms per square (Ω/sq), producing resistance in ohms (Ω) when multiplied by aspect ratio [77]. A higher aspect ratio may be used to reduce power consumption, however, the overall physical resistor size also must be considered in the design. One strategy to increase the aspect ratio (and thereby resistance) of a piezoresistor is to use a folded design. This style of resistor structure allows for a high aspect ratio resistor to be placed in a small area. Resistors which require more area on a device can cause detection to take place out of the highest stress zone, reducing sensitivity. This is especially important in membrane and cantilever devices, where maximum stresses will occur in relatively small areas. Reducing the size of a piezoresistor while increasing the aspect ratio also necessitates that manufacturing tolerances will become more critical. In addition, reducing piezoresistor cross-sectional areas reduces the maximum current that can flow through a device, which may manifest as problems with resistive heating and failure at the contacts.

The electrical resistance of the contacts attached to the piezoresistor may have a substantial effect on the performance of a resistor. The additional resistance occurs due to non-ohmic contact between the silicon and metal. Non-ohmic contact refers to any non-linear or asymmetric relationship between applied voltage and current draw. This is a diodic effect, referred to as a Schottky Barrier. A graph of a non-ohmic contact that was produced using a piezoresistor is shown in Figure 2.2. The contact resistance may be reduced in piezoresistors by using p-type dopants, increasing the doping concentration (to levels greater than

5×10^{19}atoms/cm^3 for n-type silicon and greater than 10^{16}atoms/cm^3 for p-type silicon), annealing after creating the silicon-metal junction, or by adding an intermediary material to the contact [78-80].

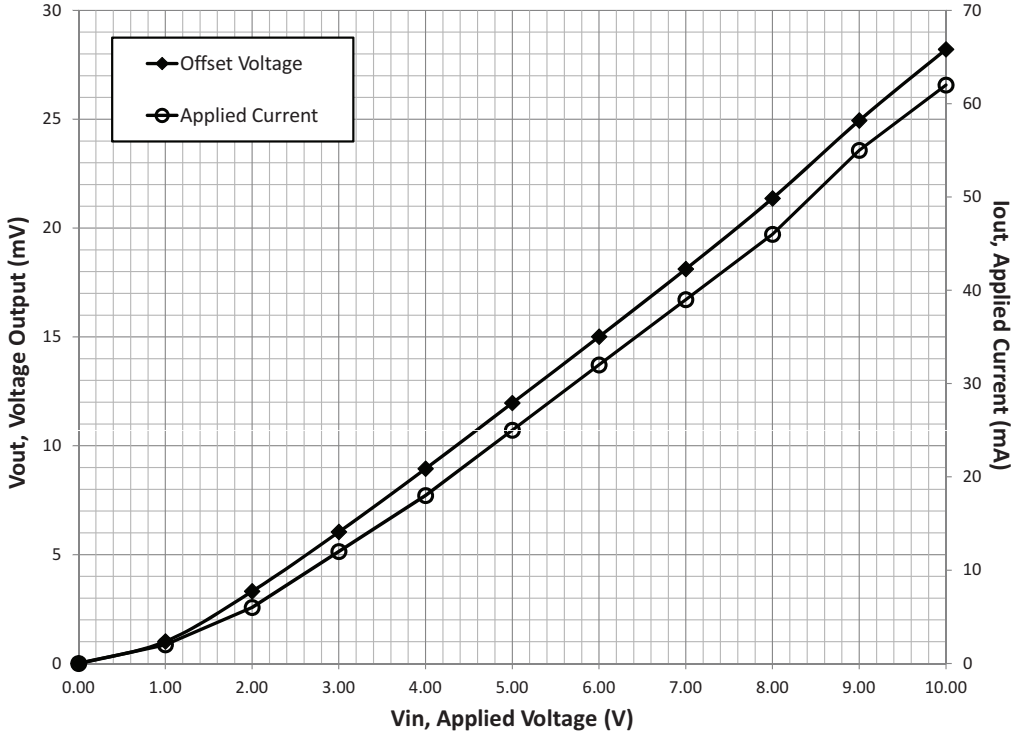

Figure 2.2. Nonlinear offset voltage produced and input current drawn as supply voltage is varied on a piezoresistor.

Noise is another important factor to consider in the design of piezoresistors. Within the sensors themselves, shot noise, thermal (Johnson-Nyquist) noise, and pink (1/*f* or Hooge) noise are the most significant [75, 76]. Shot noise is caused by random fluctuations of charge carriers in semiconductor junctions [75, 76]. Thermal noise is caused by energy dissipation through the vibration of charge carriers in a resistor [75, 76]. Pink noise has empirically been shown to be inversely proportional to the number of charge carriers in a resistor, and may occur due to charges becoming trapped during current flow [75, 76, 81]. Shot and thermal noise have flat spectral power densities, while pink noise is inversely proportional to frequency.

Piezoresistors will typically have their noise spectrum dominated by pink noise sources as they are more often operated at low frequencies. This favors a high impurity concentration or a physically large resistor to increase the number of charge carriers and decrease the pink noise. Vandamme *et al.* also found that annealing could reduce pink noise by improving the quality of the crystal lattice [82]. An increased bias voltage was also reported to be beneficial for reducing thermal noise, provided the resistive heating was controlled [76].

2.5.1 - Rectangular Piezoresistors and the Wheatstone Bridge

Integrating the piezoresistors into a sensing system usually requires a method of converting the resistance change due to applied stress into a voltage output. Commonly, this is performed using a Wheatstone bridge circuit. A Wheatstone bridge is an arrangement of four resistors in which their electrical imbalance may be measured as an output voltage. Figure 2.3 shows a schematic of a Wheatstone bridge circuit. One sensing resistor and three balance resistors are required for a Wheatstone bridge circuit to operate, although additional sensing resistors may replace the balance resistors for added sensitivity. When more than two sensing resistors are used, the additional resistors must vary their resistance in the opposite direction as the others to achieve a net positive effect on sensitivity. The chief advantage of a Wheatstone bridge circuit with two or four active resistors is temperature compensation: When the resistance of the sensing resistor is changed due to a temperature variation, an equivalent change is produced in the other resistor on that half of the bridge. These two changes in resistance will have cancelling effects on the voltage output. Figure 2.4 shows a membrane sensor with a Wheatstone bridge integrated into the top surface. This bridge circuit uses two sensing piezoresistors and two balance piezoresistors for temperature compensation. The balance resistors are not referred to as active because their orientations do not subject them to significant longitudinal stresses.

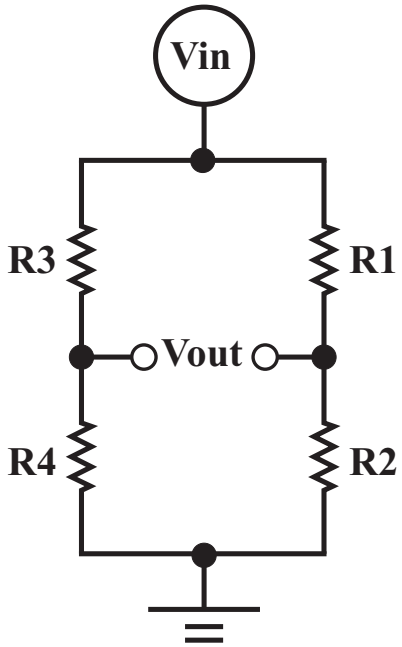

Figure 2.3. The Wheatstone bridge circuit.

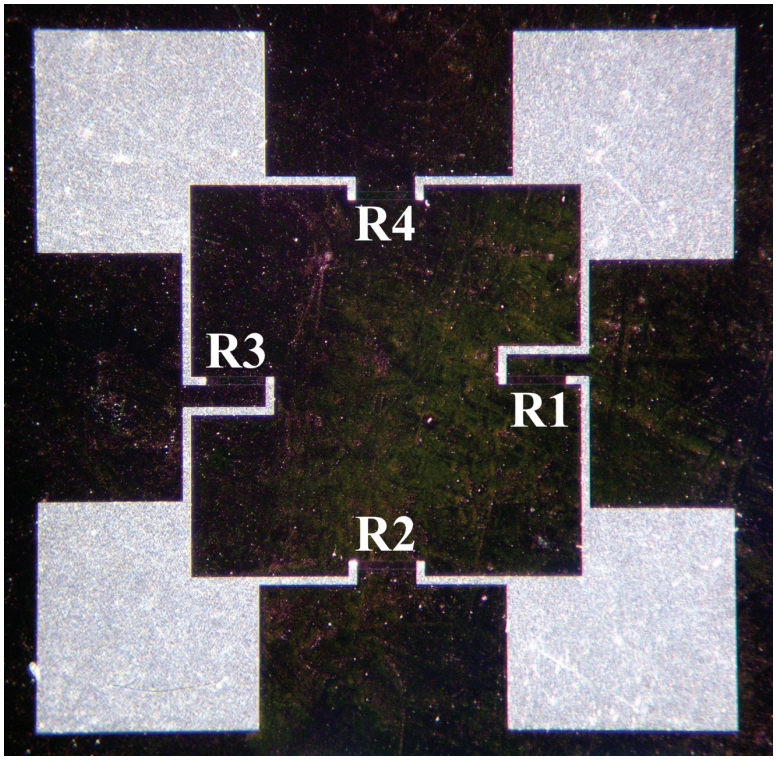

Figure 2.4. A membrane sensor with labelled rectangular piezoresistors forming a Wheatstone bridge circuit. R1 and R3 are sensing piezoresistors, R2 and R4 are balance piezoresistors.

Analytically, a rectangular piezoresistor operates as follows: Beginning with the 3D form of Ohm's law shown in Equation (2.1) and rotating the components of the terms from the crystallographic coordinate system to an arbitrary "primed" coordinate system defined by the orientation of the resistor relative to the crystal lattice produces:

$$E'_T = \rho'_{TU} J'_U \tag{2.7}$$

Assuming that the current is flowing only along the long axis of the prismatic, rectangular resistor (this resistor has dimensions $l \times w \times d$ which are respectively aligned with the 1, 2, and 3 axes of the primed coordinate system), the relations defined in Equation (2.8) may be produced. (Further details of this analysis may be found in Bao [68].)

$$\begin{aligned} E'_1 &= \rho'_{11} J'_1 \\ E'_2 &= \rho'_{12} J'_1 \end{aligned} \tag{2.8}$$

The relations $E'_1 = V_{in}/l$ and $I'_1 = J'_1 wd$ may be used with the above to produce:

$$R = \frac{l\rho'_{11}}{wd} \tag{2.9}$$

For the resistance of the unstressed piezoresistor (R_0), Equation (2.6) may be used, replacing the $\bar{\rho}$ term with unstressed resistivity ρ_0. Assuming small deflections permits the dimensions of the resistor to cancel out.

$$\frac{\Delta R}{R_0} = \frac{R - R_0}{R_0} = \frac{\rho'_{11} - \rho_0}{\rho_0} \tag{2.10}$$

Comparing Equation (2.10) with Equation (2.3) allows the following relationship to be produced:

$$\frac{\rho'_{11} - \rho_0}{\rho_0} = \pi'_{11VW} \sigma'_{VW} \tag{2.11}$$

Equation (2.11) is equivalent to the following in the matrix notation:

$$\frac{\rho'_1 - \rho_0}{\rho_0} = \pi'_{11}\sigma'_1 + \pi'_{12}\sigma'_2 + \pi'_{13}\sigma'_3 + \pi'_{14}\sigma'_4 + \pi'_{15}\sigma'_5 + \pi'_{16}\sigma'_6 \tag{2.12}$$

Assuming that the stress is applied uniaxially along the long axis of the resistor, only the $\pi'_{11}\sigma'_1$ term remains on the right hand side of Equation (2.12).

Coordinate transformation of the π'_{11} term back to the crystallographic orientation allows the following equation to be developed:

$$\frac{\Delta R}{R_0} = (\pi_{11} + 2(\pi_{44} + \pi_{12} - \pi_{11})(l_1^2 m_1^2 + l_1^2 n_1^2 + m_1^2 n_1^2))\sigma'_1 \qquad (2.13)$$

The l_1, m_1, and n_1 terms are direction cosines between the crystallographic and primed coordinate systems. For the case of a 45° rotation about the 3 axis, Equation (2.13) reduces to:

$$\frac{\Delta R}{R_0} = \left(\frac{\pi_{11}+\pi_{12} + \pi_{44}}{2}\right)\sigma'_1 \qquad (2.14)$$

In p-type silicon, this rotational transformation allows the high value of the π_{44} coefficient to be dominant, thus confirming that piezoresistors on a (1 0 0) plane should be oriented in a [1 1 0] direction (which is equivalent to this rotation) for maximum sensitivity.

2.5.2 - Four-Terminal Gauges

An alternative to the Wheatstone bridge configuration for obtaining voltage outputs from piezoresistors is the four-terminal gauge. Functionally, a four-terminal gauge operates using a quasi-Hall effect, where stress and electric current in a piezoresistor creates an electric field transverse to this current [63, 65, 66]. In actual operation, a four-terminal gauge works in a similar way to a full Wheatstone bridge circuit: An input voltage is applied across two terminals and an output voltage is collected from two different terminals. The construction of a four-terminal gauge, however, differs substantially from that of the Wheatstone bridge. A four-terminal gauge consists of a single resistor with, as the name implies, four electrical terminals. The resistor is often shaped like an "X", with one arm of the "X" for each terminal. This led Motorola to dub the four-terminal gauges incorporated into their pressure sensors "X-ducers" [83]. Figure 2.5 shows a four-terminal gauge schematically and Figure 2.6 shows a photomicrograph of a four-terminal gauge on a silicon membrane.

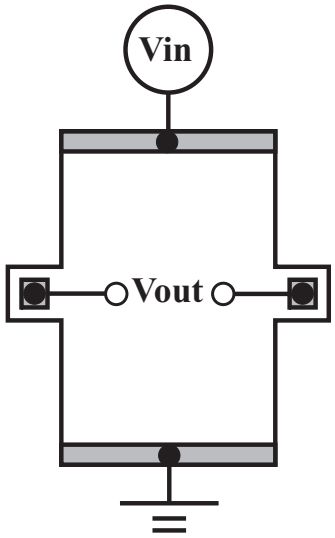

Figure 2.5. A schematic of a four-terminal gauge.

Figure 2.6. A membrane sensor utilizing a four-terminal gauge.

The analytical treatment for a piezoresistive four-terminal gauge begins in much the same way as the rectangular piezoresistor described in Section 2.5.1. Since the source voltage is again applied along the long axis of the (generally

rectangular) piezoresistor, Equation (2.8) may be used. Equating the J'_1 terms produces the following:

$$E'_2 = E'_1 \frac{\rho'_{12}}{\rho'_{11}} \tag{2.15}$$

The input and output voltages are given by:

$$\begin{aligned} V_{in} &= \int_0^l E'_1 \, dx' = E'_1 l \\ V_{out} &= \int_0^w E'_2 \, dy' = E'_2 w \end{aligned} \tag{2.16}$$

Combining Equations (2.15) and (2.16) and solving for V_{out}, the equation derived in [65] may be reproduced.

$$V_{out} = \frac{\rho'_{12}}{\rho'_{11}} \frac{w}{l} V_{in} \tag{2.17}$$

The solution of Equation (2.17) requires that ρ'_{11} and ρ'_{12} be determined. Converting again to matrix notation and applying Equation (2.4) gives the following:

$$\frac{\rho'_{12}}{\rho'_{11}} = \frac{(\pi'_{61}\sigma'_1 + \pi'_{62}\sigma'_2 + \pi'_{63}\sigma'_3 + \pi'_{64}\sigma'_4 + \pi'_{65}\sigma'_5 + \pi'_{66}\sigma'_6)}{(1 + \pi'_{11}\sigma'_1 + \pi'_{12}\sigma'_2 + \pi'_{13}\sigma'_3 + \pi'_{14}\sigma'_4 + \pi'_{15}\sigma'_5 + \pi'_{16}\sigma'_6)} \tag{2.18}$$

The terms in the denominator due to the ρ'_{11} term may then be removed as they are much smaller than unity. Applying a uniaxial stress along the long axis of the resistor as in the case of the rectangular two-terminal resistor leaves:

$$V_{out} = \pi'_{61}\sigma'_1 \frac{w}{l} V_{in} \tag{2.19}$$

Equation (2.19) converts to the following in the crystallographic coordinate system:

$$V_{out} = (\pi_{11} - \pi_{12} - \pi_{44})(l_1^3 l_2 + m_1^3 m_2 + n_1^3 n_2)\sigma'_1 \frac{w}{l} V_{in} \tag{2.20}$$

However, Equation (2.20) reduces to zero when the direction cosines for a 45° rotation are input. This indicates that a four-terminal gauge will have zero sensitivity when oriented in the same direction as the two-terminal resistor at maximum sensitivity. Aligning the crystallographic coordinate system with the primed coordinate system (0° rotation) similarly produces zero sensitivity, so

rotation of the applied uniaxial stress is considered. Independent rotation of the stress and piezoresistivity terms in Equation (2.18) allow the maximum sensitivity for a four-terminal gauge to be achieved on a (1 0 0) plane when the applied stress is oriented in a [1 1 0] direction and the long axis of the gauge is oriented in the [1 0 0] direction. The sensitivity in this situation for a p-type device is approximated by the following relationship:

$$V_{out} = \frac{\pi_{44}}{2}\sigma_1 \frac{w}{l} V_{in} \tag{2.21}$$

Additional calculation details involving this analytical solution may be found in literature [68]. The aspect ratio (l/w) of the four-terminal gauge has also been shown to affect device sensitivity. Equation (2.21) indicates that a higher aspect ratio will produce a lower voltage output. However, since a lower aspect ratio device is shown to have lower resistance and higher power consumption by Equation (2.6) a compromise must be made. The discussion by Bao *et al.* discusses geometric correction factors for Equation (2.21), determining that an aspect ratio of approximately two is a good compromise between sensitivity and power consumption [66]. This theoretical analysis of a four-terminal gauge has been used to verify the numerical simulation parameters presented in Section 3.3.4.

A four-terminal gauge provides temperature compensation with a compact device footprint, allowing larger electrical contacts and, in some cases, fewer electrical traces than with a Wheatstone bridge circuit [63, 84]. Gridchin *et al.* compared the four-terminal gauge and Wheatstone bridge. Their analysis determined that the theoretical maximum sensitivity of a four-terminal gauge is 75% of a full Wheatstone bridge. This sensitivity proportion may be higher if any of the resistors in the Wheatstone bridge are subjected to lower stress, thereby giving the four-terminal sensor comparable sensitivity [84]. For these reasons, four-terminal gauges have been selected for use as transducers in this application.

2.6 - Membrane Theory

The stresses that the piezoresistors in the scoliosis sensor array must detect are produced by the deflection of a membrane. Membranes are commonly used in

pressure sensors where an applied pressure differential causes the deformation and stress. Concentrating this pressure (or distributed load) at the center of a membrane (as a point load) approximately doubles the stress response and output produced by a piezoresistor [85]. In both cases, the maximum stresses will be produced along the edges of the membrane. Specifically in the cases of rectangular (or square) membranes, the maximum stresses will be produced at the midpoints of the longer edges [85]. The stress distributions in a membrane also may be shown to vary depending on the load application location. This property may be extended to include the creation of a unique stress distribution corresponding to the direction and magnitude of an angled load. By using piezoresistors to measure the stresses near the midpoint of each edge on a square membrane, three-axis components of an angled load may be resolved [51, 86, 87].

2.6.1 - Membrane Deflection

Analytically determining the stresses in a built-in square membrane (all sides fully-fixed) is a complicated exercise when considering an angled load that is not necessarily centred. In the simplified case of a thin membrane composed of isotropic material and subjected to a normal, distributed load (pressure), the analysis outlined by Timoshenko [85] begins with the equation for small deflections with dominant bending effects:

$$\nabla^4 w = \frac{p(x,y)}{D} \tag{2.22}$$

w is the deflection perpendicular to the membrane, $p(x,y)$ is the loading function, and D is the membrane's flexural rigidity, defined:

$$D = \frac{Eh^3}{12(1-\nu^2)} \tag{2.23}$$

E is Young's modulus, ν is Poisson's Ratio, and h is the thickness of the membrane. If the edge length of the membrane is defined as a, q is the magnitude of the applied distributed load, and $\alpha_m = m\pi/2$, w may be defined as follows:

$$w = \frac{4qa^4}{\pi^5 D} \sum_{m=1,3,5,\ldots}^{\infty} \frac{(-1)^{\frac{m-1}{2}}}{m^5} cos \frac{m\pi x}{a} \left(1 - \frac{\alpha_m \tanh \alpha_m + 2}{2 \cosh \alpha_m} \cosh \frac{m\pi y}{a} + \frac{1}{2 \cosh \alpha_m} \frac{m\pi y}{a} \sinh \frac{m\pi y}{a}\right) \tag{2.24}$$

The coordinate system used in Equation (2.24) is defined with the origin at the centre of the membrane with the *x* and *y* axes running parallel with the edges. This coordinate system is defined in Figure 2.7.

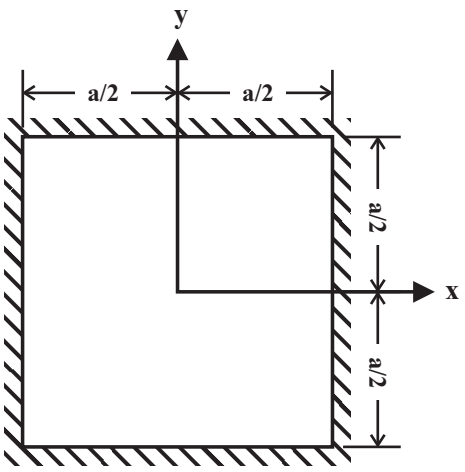

Figure 2.7. The membrane coordinate system and edge lengths.

The built-in (fully-fixed) boundary condition implies that all four edges do not rotate and are subjected to the same bending moments. This leads to the edge constraints defined by Equation (2.25).

$$\left(\frac{\partial w}{\partial y}\right)_{y=a/2} + \left(\frac{\partial w_1}{\partial y} + \frac{\partial w_2}{\partial y}\right)_{y=a/2} = 0$$
$$\left(\frac{\partial w}{\partial x}\right)_{x=a/2} + \left(\frac{\partial w_1}{\partial x} + \frac{\partial w_2}{\partial x}\right)_{x=a/2} = 0 \tag{2.25}$$

The w_1 and w_2 terms represent membrane deflection due to moments at the edges. These constraints can then be modified into Equation (2.26).

$$\frac{C_i}{i}\left(\tanh\alpha_i + \frac{\alpha_i}{\cosh^2\alpha_i}\right) + \frac{8i}{\pi}\sum_{m=1,3,5,\ldots}^{\infty}\frac{C_m}{m^3}\frac{1}{\left(1+\frac{i^2}{m^2}\right)^2} = \frac{4qa^2}{\pi^3}\frac{1}{i^4}\left(\frac{\alpha_i}{\cosh^2\alpha_i} - \tanh\alpha_i\right) \tag{2.26}$$

The C_i and C_m terms are series constants and $\alpha_i = i\pi/2$ $(i = 1,3,5,\ldots)$. This can be used to create a system of linear equations which were solved in the literature [85]. These results produced the following equations:

$$w_{(x=0,y=0)} = 0.00126qa^4/D$$
$$M_{xx_{(x=a/2,y=0)}} = M_{yy_{(x=0,y=a/2)}} = -0.0513qa^2 \tag{2.27}$$
$$M_{xx_{(x=0,y=0)}} = M_{yy_{(x=0,y=0)}} = 0.0231qa^2$$

Analytical results for the stress distributions in anisotropic membranes, which may not satisfy the thin membrane assumption and are subjected to angled, non-centred loads, are beyond the scope of this thesis to calculate. However, the analytical equations for this simplified situation have been used to determine appropriate numerical parameters for more complicated membrane analyses, as presented in Section 3.3.3. It should also be noted that these stress distributions are further complicated by contact stress effects on the surfaces of the membranes due to the load application method, which further justifies the numerical analysis performed.

2.6.2 - Contact Stress Effects

A point load can be applied analytically with ease as a mathematical construct. In experimental situations however, a point load is inevitably distributed over an area corresponding to localized deflections of the load applicator and target. Numerical analysis can simulate either of the above situations, although the distributed model will produce results which correspond more accurately to reality; forces applied on an infinitesimal area generate extremely high local stresses that are unrealistic. The contact loads applied by the rods to the deformable membranes in the scoliosis surgery application may be idealized as

angled point or line loads. However, the localized stress distributions are better represented analytically using Hertzian and Smith-Liu techniques [88, 89].

The Hertzian and Smith-Liu analyses can predict contact stresses between elastic cylinders laying parallel to each other. Assuming the contact area is shaped like a long, narrow rectangle, the load *(F)* is evenly distributed along the length *(l)* of this rectangle, and that the load is elliptically distributed along the width *(2b)*, the half-width is defined as follows:

$$b = \sqrt{\frac{2F}{\pi l}\Delta},\ \Delta = \frac{\frac{1-\nu_1^2}{E_1} + \frac{1-\nu_2^2}{E_2}}{\frac{1}{d_1} + \frac{1}{d_2}} \tag{2.28}$$

The Young's modulus, Poisson's ratio, and diameter of each cylinder are given by E, ν, and d, respectively. These parameters, as well as the coordinate system used, are shown in Figure 2.8. It should also be noted that this analysis is valid in the case when one of the cylinders has an infinite or negative diameter value.

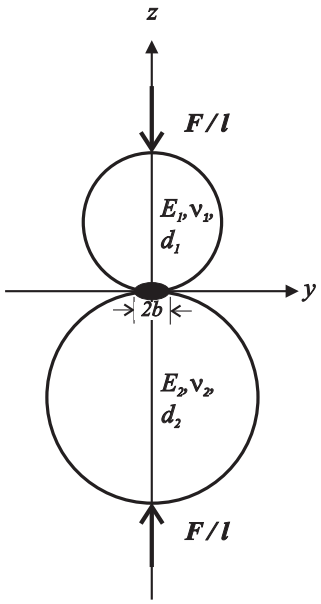

Figure 2.8. The coordinate system used for the Smith-Liu contact analysis.

The Smith-Liu equations are capable of including shear stresses due to friction (the sliding frictional coefficient is given by f) and are written as follows:

$$\sigma_{xx} = -\frac{b}{\pi\Delta}\left\{z\left(\frac{b^2+2z^2+2x^2}{b}\phi - \frac{2\pi}{b} - 3x\psi\right) + f\left[(2x^2-2b^2-3z^2)\psi + \frac{2\pi x}{b} + 2(b^2-x^2 - z^2)\frac{x}{b}\phi\right]\right\} \quad (2.29)$$

$$\sigma_{yy} = -\frac{2\nu b}{\pi\Delta}\left\{z\left(\frac{b^2+z^2+x^2}{b}\phi - \frac{\pi}{b} - 2x\psi\right) + f\left[(x^2-b^2-z^2)\psi + \frac{\pi x}{b} + (b^2-x^2-z^2)\frac{x}{b}\phi\right]\right\} \quad (2.30)$$

$$\sigma_{zz} = -\frac{b}{\pi\Delta}[z(b\phi - x\psi) + fz^2\psi] \quad (2.31)$$

$$\sigma_{zx} = -\frac{b}{\pi\Delta}\left\{z^2\psi + f\left[(2x^2+b^2+2z^2)\frac{z}{b}\phi - \frac{2\pi z}{b} - 3xz\psi\right]\right\} \quad (2.32)$$

where,

$$\phi = \frac{\pi(M+N)}{MN\sqrt{2MN+2x^2+2z^2-2xb^2}}$$

$$\psi = \frac{\pi(M-N)}{MN\sqrt{2MN+2x^2+2z^2-2xb^2}}$$

$$M = \sqrt{(b+x)^2+z^2}, N = \sqrt{(b-x)^2+z^2}$$

As in the case of membrane deflection analysis, the influence of contact loads create stress distributions on the membranes which are best predicted using numerical methods, specifically FEA. Section 3.3.2 describes how appropriate FEA parameters were determined for membranes undergoing contact using the above analytical method. Furthermore, Section 4 contains numerical and experimental output describing how changes to the stress distributions on membranes incorporating piezoresistors affect their ability to resolve the direction and magnitude of an applied angled load.

2.7 - Pressure Sensors

Sensors utilizing membrane and piezoresistor sensing schemes are commonly used to detect pressure differentials. This type of MEMS device will often use piezoresistors in Wheatstone bridge configurations or four-terminal gauges as

detection mechanisms. Typically, the piezoresistors are placed near membrane edges to capture the largest stresses during deformation. In operation, a pressure differential between the two sides of the membrane causes it to deform. This sensing mode can also be used to detect absolute pressure if an evacuated cavity is created and sealed around one side of the membrane. The pressure differential leads to deflection of the membrane and creation of a stress distribution on the membrane surface. The stress distribution is detected by the piezoresistors as a resistance change, which is usually measured as change in voltage created with the detection circuitry.

Several examples of MEMS pressure sensors using a piezoresistive scheme are described in literature [86, 90-93]. This application represents one of the first MEMS devices with a high adoption rate, with usage increasing since this concept was first described in 1962 by Tufte [94]. Advantages such as highly linear sensing, low unit cost, the ease with which bulk microfabrication can increase production volume, and compact size have contributed to the success of this type of device. Pressure ranges commonly detected with MEMS sensors vary from below 1kPa to greater than 100MPa [95].

2.8 - Interfacial Devices

The concept of piezoresistors on a membrane surface has also been extended to multi-axis sensing. These membrane devices have been used to measure interfacial or tactile loads by taking advantage of non-uniform stress distributions on the membrane surface when subjected to a combination of shear and normal loading. The non-uniformity of these stress distributions can be increased by adding features such as mesas, or raised sections, to the surface of the membrane where the loads are applied. Mesas allow increased sensitivity to shear loads by transmitting a lateral force to the membrane as a bending moment, amplifying the stress in certain areas. In some devices, removing material from the membrane surface has also been performed to increase the sensitivity. In most cases, interfacial devices operate using multiple piezoresistors in parallel. These piezoresistors are distributed over the membrane surface to detect the non-

uniform stress distribution. Post-processing of the piezoresistor outputs is then performed to convert the resistance or voltage measurements back into three-axis force data.

Membrane devices for measuring tactile and interfacial forces have been described in literature, with applications in robotics, force feedback apparatus, surgical equipment, and controller systems [42-48, 96-98]. The loads detected with these devices are usually small, with three-axis load ranges commonly less than 10N. The sensitivity of MEMS tactile devices can be high, and depending on the application, higher sensitivity may be desired in either normal or shear directions. MEMS devices give the designer greater control of the sensitivity and load range of sensors due to the high performance and versatility of the materials and sensing techniques used. This concept is further explored in Section 4.

2.9 - Deployment and Packaging

The success of tactile and other types of MEMS devices utilizing membranes depends greatly upon the deployment solution applied. The sensing elements of the MEMS device must be exposed to the environmental inputs, yet still be adequately protected from damage caused by other aspects of the environment. For example, in a pressure sensing application, the package must allow one side of the membrane to be exposed to a pressurized working fluid, but be able to shield the piezoresistors and electrical components from shorting or corrosion. A successful deployment for a MEMS sensor should have the following properties: compactness, to take advantage of the small size of the MEMS sensor; durability, which is imperative for continued safe use of a device; and non-interference, to avoid having an adverse effect on the sensitivity or other performance parameters of the device.

Deployment in a surgical application raises additional requirements associated with the packaging of MEMS devices. Biocompatibility is a specific concern, implying that high durability packaging will be required and that material selection is of utmost importance. Biocompatible packages must also prevent any components from being freed from the package under any

circumstance where they could become lodged in a patient. Surgical sensors need to be sterilizable, which is a requirement that, depending on the type of sterilization used, may require the device to be hermetically sealed and resilient to elevated temperatures [99]. It is also advantageous for MEMS sensors used in surgical applications to be packaged in a low profile way to allow them to be seamlessly integrated into existing surgical instrumentation. This allows their implementation without affecting existing surgical protocols, which is important for collecting load information without extending surgeries and putting patients at increased risk.

Several technologies can be applied for packaging MEMS sensors which are used in surgical and biomedical applications: through-silicon vias, flexible printed circuit boards, wire bonding, and flip-chip alignment and adhesion.

2.9.1 - Through-Silicon Vias

Through-silicon vias (TSVs) are conductive paths running vertically through a silicon wafer, serving as electrical connections between the top and bottom surfaces. The integration of TSVs into MEMS sensors offers several advantages: vertical chip stacking which allows a reduction of device footprint size; increased interconnect density; the possibility of placing connectors directly under the sensing elements; simplified options for protecting the electrical connections; and high compatibility with flip-chip packaging options. A TSV typically consists of a through hole in the wafer, an insulation layer preventing conduction into the bulk substrate, metallization to produce contact pads, a seed layer, and a conducting fill. Figure 2.9 shows a cross section of a typical TSV.

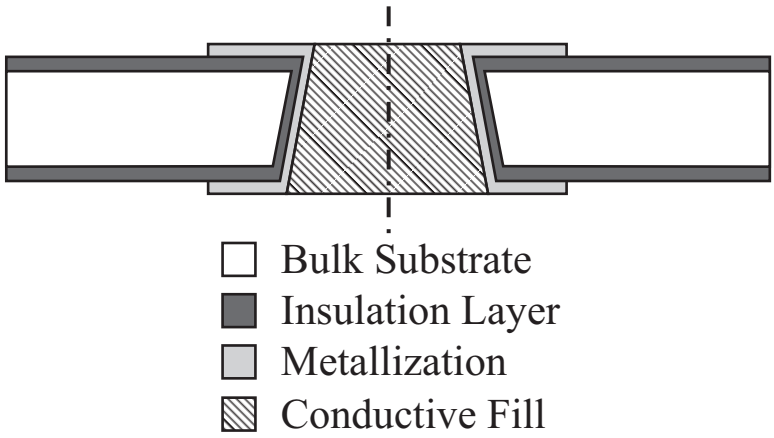

Figure 2.9. Schematic illustration of a through-silicon via.

Several designs for TSVs may be found in literature [100-114]. Typically, conducting fill materials used are electroplated copper, and polysilicon deposited using low pressure chemical vapor deposition (LPCVD). Silicon oxide, parylene, and silicon nitride are common insulation layer materials. Since copper may not adhere well to the insulating layer, a seed layer commonly consisting of titanium, tantalum, and copper is applied prior to electroplating. After the conductive fill is electroplated or deposited, any excess seed or fill materials may be removed by polishing the substrate.

Regardless of the composition of the TSV fill material, through-holes must be etched into the wafer to produce space for the conductive path. To produce high aspect ratio holes, this step is usually done using an inductively coupled plasma reactive ion etch (ICPRIE) or cryo-etch process. These processes are discussed in more detail in Section 3.4. For both etch types, aspect ratio dependent etching (ARDE) is a factor which must be considered. Essentially, ARDE is a phenomenon where etch rate is reduced as the aspect ratio (depth/diameter) is increased. This is due to several factors, including ion shadowing, differential charging, neutral shadowing, and Knudsen transport of neutrals [115, 116]. Functionally, ARDE implies that etching must be timed for the smallest holes on the wafer being processed and that a physical limit exists in terms of TSV diameter. Ideally, a TSV hole should be completely through the wafer and have smooth sidewalls that are vertical or have a consistent taper. Etch

rates, ARDE, undercut, hole tapering, bowing, and black silicon (silicon grass) production are factors relevant to TSV production and are discussed in literature [116-120].

Electroplating and LPCVD are commonly used to fill the TSV hole as sputtering may not be able to produce an adequate conductive surface on near vertical sidewalls in a high aspect ratio hole. Techniques such as collimated sputtering and pressure control have been shown to be useful in achieving uniformly coated sputtered surfaces and enhanced sidewall coverage [121-123]. In the simplified case of low aspect ratio holes, particularly those with a high degree of taper, it may be possible to produce TSVs using a sputtered conductor only, without requiring a deposited or electroplated fill. The high taper could be produced using a plasma etch with a modified oxygen flow rate or a potassium hydroxide (KOH) etch process.

2.9.2 - Flexible Printed Circuit Boards

Printed circuit boards (PCBs) are used in many applications in the electronic device industry. Essentially, a PCB must provide electrical interconnection traces and structural support for electronic components used in a device or circuit. In their simplest form, a PCB consists of a conductive layer (usually copper) bonded to an insulating material (usually woven glass and epoxy). This copper layer can then be patterned using silk screening, photolithography, mechanical milling, or other methods to produce the desired pattern of contact pads and electrical traces. More complicated circuit boards utilizing multiple conductive and insulating layers, drilled and filled via holes, and insulating coatings are also produced.

Flexible printed circuit boards are differentiated from conventional PCBs by virtue of their flexible core which is commonly made from polyimide. The FPCB technology offers advantages when producing low volume packages; wiring harnesses interconnecting separate components and conventional PCBs may be replaced by a single, compact FPCB. In addition, FPCBs are often much thinner than conventional PCBs, with achievable thicknesses below 100µm. They also offer additional packaging options in terms of 3D component placement, as

FPCBs can be flexed, twisted, and folded into a variety of shapes. Packages containing moving components or those that are subjected to excessive vibrations also benefit from the application of FPCBs [124-127].

2.9.3 - Wire Bonding

Wire bonding is a packaging technique utilizing heat and ultrasonic power to adhere fine wires (25μm) to contact pads for electrical connection purposes. Most wire bonders are either wedge-wedge or ball-stitch bonders. A wedge-wedge bonder operates by feeding gold or aluminum wire through an angled hole in the tool tip. The bond is made by compressing wire between the tip and the pad while applying heat and ultrasonic power to locally weld the wire to the pad. This type of bonder only allows bonding in one direction. A ball-stitch bonder uses a hollow ceramic capillary tool that the wire is fed through axially. An electrical arc is used to melt a short length of wire into a ball on the tip of the tool. The ball is then bonded to the electrical pad using a similar method as with the wedge-wedge tool, and the second (stitch) bond may then be placed in any direction from the first bond. Gold wire must be used for ball-stitch bonding as the ball forming current required is excessively high for aluminum. A schematic of a ball-stitch bond is shown in Figure 2.10.

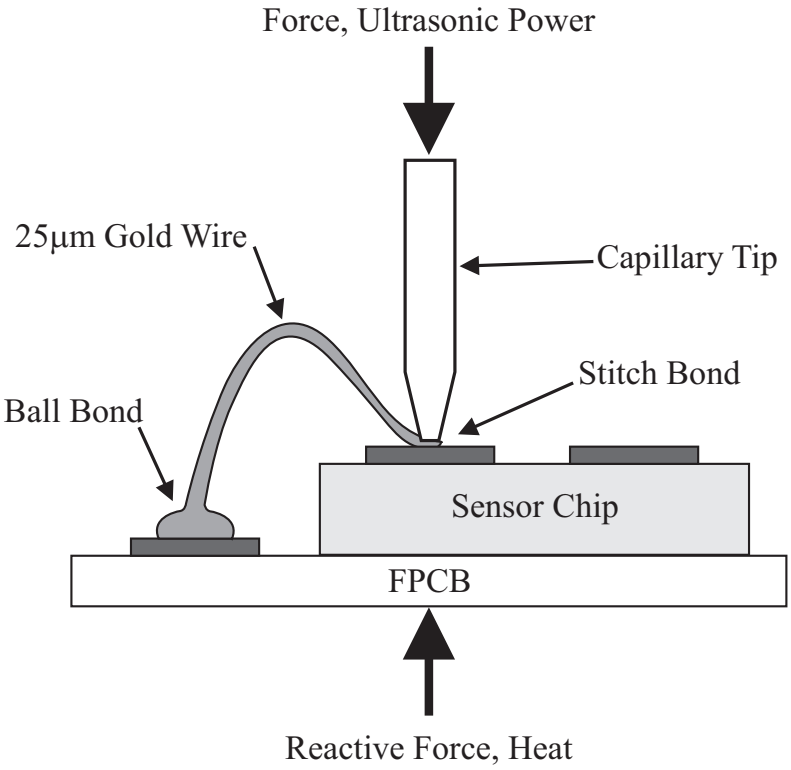

Figure 2.10. A ball-stitch wire bond.

Of particular importance to MEMS packaging techniques which utilize TSVs and flip-chip is the production of stud bumps. Stud bumps are ball bonds that are immediately terminated without creating a wedge bond and electrical connection. Instead, the stud bump is coined by compressing it using the wire bonder and a solid tool. This allows an amount of gold to be placed on an electrical contact pad and raised above the pad surface. The gold stud bump then can provide electrical conductivity for a flip-chip connection, and be bonded using a non-conductive adhesive.

2.9.4 - Flip-Chip

A flip-chip system refers to a packaging tool which allows one chip (or PCB, FPCB, die, or device) to be vertically aligned, stacked, and adhered to another. Central to a flip-chip system is a movable placement head and optical prism alignment system. This allows vertical alignment and stacking by letting the user see the top of a die and the bottom of a chip overlaid, allowing the contact pads on

each be aligned and then brought into contact. Secondary to the alignment system is one or more adhesion modules. These adhesion modules can consist of force, heat, or ultrasonic power applicators, and are operated after the chip is brought into contact with the die to bond them. For example, a flip-chip system may use heat and compression (a thermocompression bond) to reflow solder between contact pads on a chip and a die. A schematic of a flip-chip bond is shown in Figure 2.11.

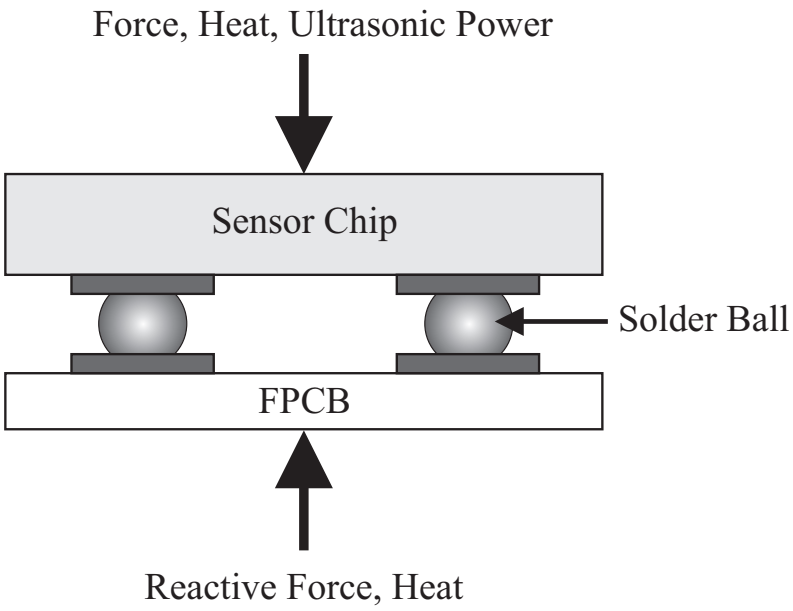

Figure 2.11. A schematic of a flip-chip bond. Heat, force, and ultrasonic power are being used to melt solder balls which have been placed on the contact pads of an FPCB.

The vertical stacking that a flip-chip system allows is beneficial for packaging in biomedical MEMS sensor applications for several reasons: the reduction of component and package footprint size, enhanced durability by removing the need for fine wires, better protection of electrical contacts by allowing them to be sealed between a chip and FPCB, and simplified assembly of fine-pitch connectors. A wide variety of adhesion techniques are possible with a flip-chip packaging system, including the use of adhesive underfill with conductive wire bonded stud bumps.

2.10 - Conclusions

A review of the literature relevant to the main topics of this thesis has been presented. This has included a review of work performed to detect loads in biomedical applications, with specific focus on those used in scoliosis correction surgery. This review has determined that a piezoresistive MEMS solution will provide appropriate capabilities for the detection of six-axis loads in the scoliosis surgery application. In addition, background material relevant to the numerical and experimental characterization of piezoresistor-on-membrane devices has been presented. Since research contributions were also made in the microfabrication, packaging, and deployment of MEMS sensors, background material in these areas was also discussed.

Chapter 3: Sensor Design and Microfabrication

Detailed methodology for the development cycle of a piezoresistive MEMS sensor is described. This cycle begins with the analytical and numerical analyses of piezoresistors. The incorporation of piezoresistors into a single crystal silicon membrane is then detailed. A mature microfabrication process flow used to manufacture prototype sensors is then provided, and specific details on the relevant processes to produce devices which are ready for characterization are presented. Challenges encountered during this development cycle are described, and solutions to these challenges are explored. These challenges included manufacturing limitations based on alignment and fabrication precision, the commissioning of a piezoresistive doping furnace, and high aspect ratio silicon etching.

3.1 - Introduction

The detection of 3D force and moment loads applied during scoliosis correction surgery represents a unique sensing scenario. These six-axis loads are relatively large compared to the pedicle screws through which they are applied, and must be detected without negatively interfering with surgical protocols or patient safety. Sensors used for this application must also be biocompatible, avoid compromising the structural integrity of the pedicle screws, and be compatible with a compact wireless system and power module. Previous work performed on this project by our research group [1, 2, 128], as introduced in Section 1.3, has determined that a sensor array utilizing four piezoresistive MEMS sensors will be capable of meeting these requirements.

Each of the piezoresistive MEMS sensors incorporated into this sensor array was required to be sensitive to three-axis (shear and normal force) loads. Analytical and numerical investigation into the design of this piezoresistive MEMS sensor, referred to individually as a “sensor pad”, determined that implementing multiple piezoresistive sensing elements (four-terminal gauges, as described in Section 2.5.2) onto a deformable silicon membrane could achieve three-axis sensitivity. Further study into the feasibility of this design has been

performed. This study incorporated an iterative development cycle including analytical design, numerical simulation, microfabrication, and characterization. At all phases of this design cycle, consideration of constraints placed on the sensor pads has been performed. These constraints included those placed on the sensor pad by the scoliosis surgery application, as well as those existing due to material and microfabrication limitations.

3.2 - Sensor Pad Design

Several potential designs of piezoresistive MEMS sensors were evaluated during the development of the three-axis sensor pads. Designs utilizing stress concentrating features (such as holes) for sensitivity enhancement were excluded due to the imparted strength reduction. Extended features such as cantilevered and narrow fixed-fixed beams were also avoided to prevent reductions in strength and stiffness. A membrane design was eventually chosen as that layout has been proven in the pressure sensor industry and was specifically known to be compatible with piezoresistive sensing elements.

Four-terminal piezoresistive sensors were chosen for the sensor pad for several reasons: they are linear in their response to applied stress, they are temperature compensating, their sensitivity is adjustable with a simple change of the impurity concentration, their footprint on the silicon wafer is simple and compact, and they do not require the use of a Wheatstone bridge circuit to produce voltage outputs [63, 66, 68]. The sensitivity of four-terminal gauges is also comparable to a Wheatstone bridge piezoresistor configuration, as was discussed in Section 2.5.2 [84].

Several piezoresistive MEMS devices found in literature were shown to be sensitive to three-axis loading, and could be manufactured using conventional microfabrication techniques [42-46, 48, 49, 96-98, 129-132]. However, the load ranges of these devices were generally lower than those required for the scoliosis surgery application. This is due to the fact that the bulk of research into three-axis devices centres on tactile sensing applications.

To operate in the scoliosis surgery application, this three-axis sensor pad must be capable of detecting shear and normal forces with comparable sensitivities. In certain cases of operation where a lack of friction exists between the membrane surface and force application mechanism, a mesa, or raised feature, could be added to the centre of the membrane at the force application site. Several other devices described in literature have used mesas to increase their shear sensitivities [44, 46, 133]. Although the specific usage of a mesa varies depending on the application, the typical mode of operation is to use the mesa's height to convert a shear load into a bending moment that has a greater effect on the stress distribution on the membrane surface.

The power consumption of the piezoresistive sensor pads is another factor taken into consideration with their design. The pads will be used with a compact wireless system that has been developed by a collaborating team in the biomedical industry, and lowered power consumption is desirable for integration with that system. As described in Section 2.5.2, the power consumption of a four-terminal gauge depends only on the length to width ratio and the sheet resistivity. A 2:1 length to width ratio provides a four-terminal gauge with a good combination of high sensitivity and low power consumption [66]. However, the power consumption of a 2:1 aspect ratio device will still be substantially higher than a serpentine resistor operated within a Wheatstone bridge. To compensate for this issue, a lower dopant concentration may be used, as discussed in Sections 2.4 and 2.5. It should also be noted that ohmic electrical connections may be made between metal contact features and piezoresistors more easily with the p-type piezoresistors doped with boron used for this research.

The new sensor pad design uses square membranes with edge lengths of 750µm and an average thickness of 100µm. These dimensions were chosen to achieve adequate strength for the scoliosis surgery application. The four-terminal piezoresistive gauges were placed near the centre of each of the membrane edges in order to detect stresses in a location near where the maximums occur. The piezoresistors are 100µm × 50µm in size with a doping concentration of approximately 4×10^{19}atoms/cm^3. The doping was performed with boron to

produce p-type resistors with a resistance of 100Ω/sq. A mesa with a height of approximately 300μm and diameter of approximately 500μm was added to the membrane surface to ensure adequate shear sensitivity was provided for this application. Figure 3.1 illustrates the design of the sensor pad. These parameters have largely been developed using FEA to produce a sensor array capable of resolving forces of up to ±1000N and moments of up to ±4N-m in 3D during surgery, which are the load ranges introduced in Section 1.2.4.

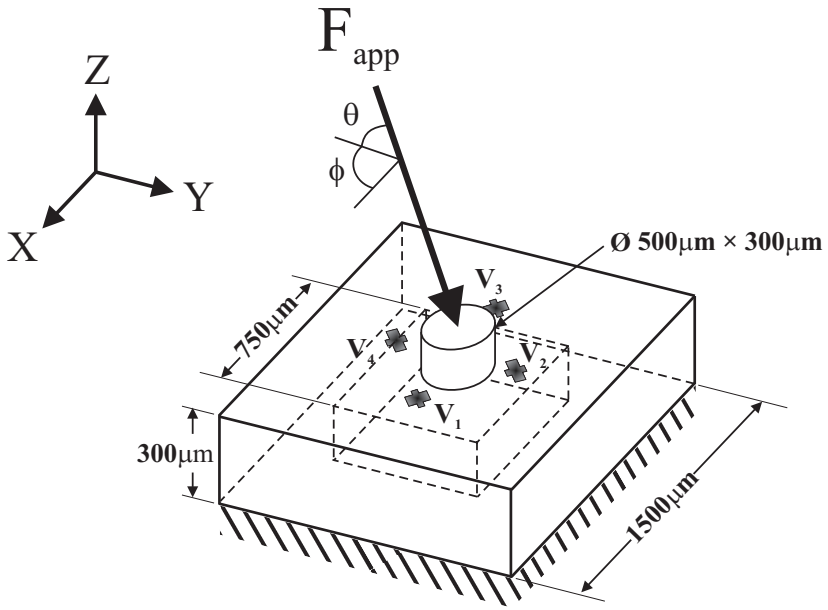

Figure 3.1. The sensor pad design with a mesa attached.

3.3 - Numerical Simulation

Finite element analysis has been implemented to determine appropriate initial parameters for the sensor pads as applied to the pedicle screws used in scoliosis correction surgery. These analyses included models representing the screw and rod construct, either whole or in part, as well as simulations individually incorporating the constituent contact, membrane deflection, and piezoresistive regimes. These component models were used to determine FEA parameters for the full model by comparing numerical outputs with results from analytical problems with known solutions. Theoretical bases for the three regimes have been presented in Sections 2.5 and 2.6.

3.3.1 - Preliminary Numerical Analyses

The initial analyses performed using FEA evaluated how the 3D loads applied by the surgeons using the corrective rod were transmitted into the U-shaped notch of a pedicle screw. The analyses were performed using commercial FEA software (ANSYS Inc. ANSYS® Multiphysics™). This preliminary modelling did not include electrical element (piezoresistor) simulation, and represented structural features with 3D 10-node tetrahedral solid elements. The steel components, namely the rod and pedicle screw components of the Cotrel-Dubousset instrumentation set, were modelled as an isotropic material with E=207GPa and ν=0.3. Silicon was modelled as an orthotropic material with stiffness tensor coefficients c_{11}=165.7GPa, c_{12}=63.9GPa, c_{44}=79.6GPa. Symmetry was utilized in these analyses to allow the models developed to solve with reduced computational time.

The surgical protocols involving load application were used to develop the loads and boundary conditions used in the preliminary FEA. This load application process begins with the surgeon placing the rod into the U-notch and securing it with a break-off bolt. This process preloads the construct and allows forces and moments applied to the rod in a non-normal direction to be transmitted into the screw (and spine). In the numerical model, this preload force was applied as a normal load pressing the rod into the U-notch. Additional six-axis loads corresponding to those expected during surgery were then applied to the numerical model.

The design for the sensor array to detect these six-axis loads was developed using this preliminary numerical model; details of this simulation and design development have been published previously [1, 2]. Essentially, four sensor pads, each sensitive to three-axis force loads, were determined to be appropriate for detection of six-axis loads transmitted from the rod to the U-notch of the pedicle screw head. The preliminary numerical analysis showed that four sensor pads, placed in the U-notch of the pedicle screw so that they contacted the rod, produced unique contact load distribution patterns corresponding to the six-

axis loads applied to the rod. Further refinement of the sensor array design distributed the four sensor pads onto two sensor strips, each composed of single crystal silicon, laying parallel to the rod in the U-notch. The sensor strips spanned the entire width of the U-notch, and were positioned on both sides of the hook to contact the rod at an angle of approximately 30º. Figure 3.2 shows a schematic of a screw head with sensor strips installed; contact load distributions (D_1 and D_2) are shown in response to 3D forces and moments applied. In order to further define the design of the sensor pads, two lines of symmetry were utilized in certain numerical models, as shown in Figure 3.3.

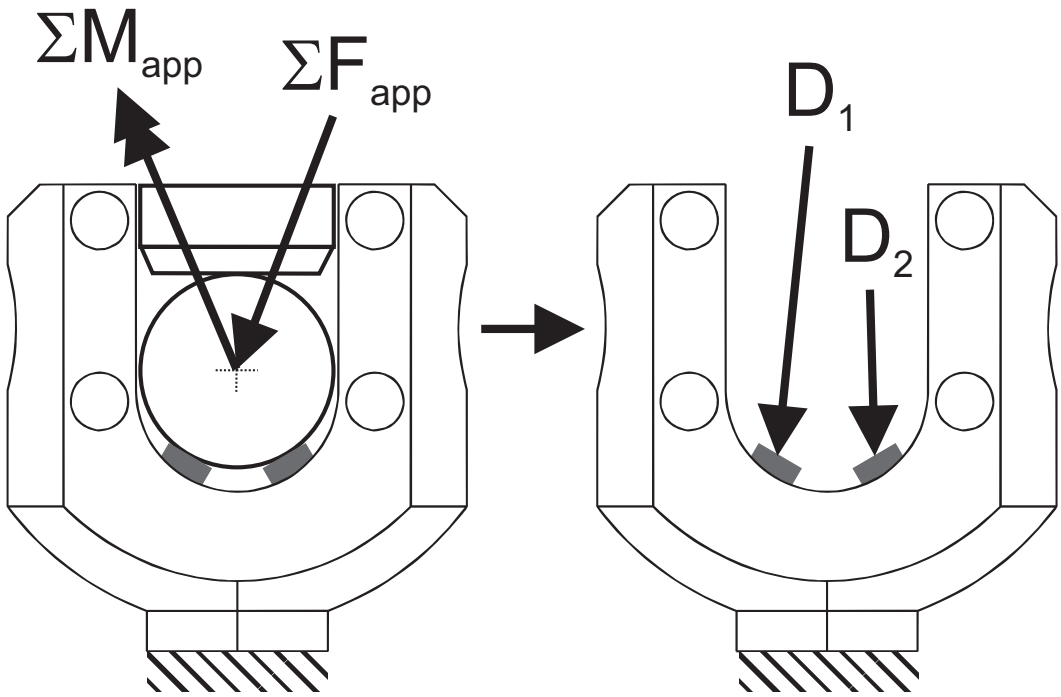

Figure 3.2. Conversion of 3D forces and moments applied to the instrumented screw head into reaction force distributions on the sensor strips.

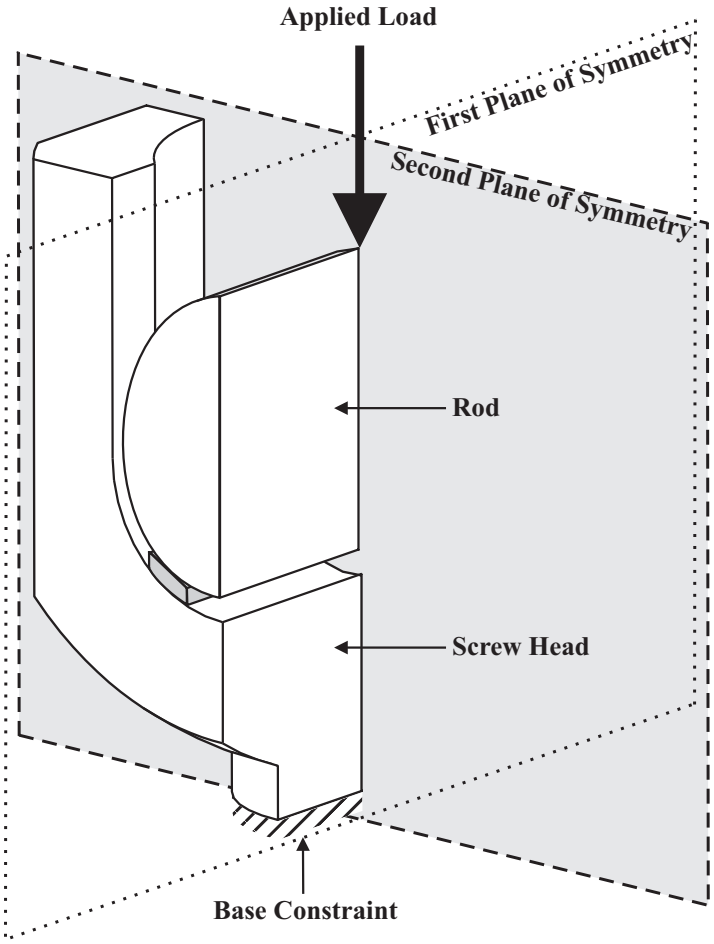

Figure 3.3. A quarter model of the screw head used for numerical analysis.

3.3.2 - Contact Analysis Parameters

In order to specifically define initial sensor pad parameters, the numerical quarter-screw sensor model needed to be evaluated using appropriate FEA parameters. This included accurate determination of contact loads produced between the sensor pads and rod. A comparison between numerical results and analytical solutions for contact problems with known solutions was used to obtain these parameters. This involved generating the von Mises stress distribution and contact width for a contact problem between a steel cylinder and silicon strip using FEA and analytical equations from Section 2.6.2. A correlation of numerical and analytical results (within 3%) was obtained using contact and target elements on the surfaces of the 3D structural elements when the mesh size was reduced to less than half of the analytically calculated contact width (below

200μm for this device). This analysis is described in detail in previous research [1, 2]. Accurate calculation of contact loads with FEA allowed further sensor pad design and analysis to be simplified by allowing the contact loads to be converted to reaction loads that may be directly applied to the sensor pad surface. This simplification also allowed the sensor pads to be evaluated separately from the rod and screws.

3.3.3 - Membrane Analysis Parameters

Deflection of the silicon membranes due to the applied contact loads from the rod was an important parameter to model in the FEA of the sensor pads. In order to accurately simulate membrane deflection, appropriate structural elements must be used in the numerical study. To determine the membrane parameters, a 1mm square membrane of varying thickness was evaluated with analytical and numerical methods. The membrane in the study was subjected to a pressure load of 100kPa and the maximum deformation was calculated. Isotropic material properties of E=120GPa and ν=0.28 were used to simplify the analytical method illustrated in Section 2.6.1 [134]. This study, which is detailed further in previous research [1, 2], determined that an element edge length less than 25μm produced a good correlation in deflection and stress-strain distribution between numerical and analytical calculations. This study also determined that a membrane with a thickness greater than 5% of its edge length (i.e. 50μm for the 1mm membrane) is not appropriate for evaluation with the analytical method described. This is due to thin diaphragm assumptions made in the derivation of the analytical equations breaking down [85, 88].

3.3.4 - Piezoresistive Analysis Parameters

Special considerations were taken when modelling piezoresistive components using FEA in both pad models and the rod and pedicle screw simulations. Piezoresistors were meshed with elements corresponding to the structural elements used, with additional degrees of freedom for the electrical parameters. The p-type piezoresistive and resistivity properties were defined as in Table 2.1

for lightly doped silicon (π_{11}=6.5×10^{-11}/Pa, π_{12}=-1.1×10^{-11}/Pa, π_{44}=138.1×10^{-11}/Pa, and ρ=7.8Ω−cm). These parameters were used for the initial FEA, and could later be modified to reflect different doping concentrations.

The FEA parameters necessary to accurately model the four-terminal gauges were determined using a simplified 3D model of a 100µm × 50µm piezoresistor. This model allowed an output voltage to be generated as a uniaxial load was applied to a four-terminal gauge. The four-terminal gauge could be rotated and the FEA mesh size could be adjusted to evaluate the effects on the output. This study confirmed that a p-type device on the (1 0 0) plane will have maximum sensitivity when the applied stress is aligned with the <1 1 0> direction and the long axis of the four-terminal gauge is at a 45° angle to this load (i.e. in the <1 0 0> direction). This model also determined that a mesh size below 10µm will produce acceptably low errors in output voltages, and is described in further detail in previous work [1, 2].

3.3.5 - Parametric Pad Modelling

With appropriate FEA parameters developed for the major regimes in the simulation, a numerical model of the sensor pad could be developed. This model allowed the performance of the sensor pads to be evaluated as geometric and electrical parameters were varied. This was an important step in the numerical modelling, as it allowed variations due to manufacturing, packaging, and characterization to be quantified for their effects on potential device performance. The numerical model generated simulated voltage outputs for each of the four-terminal gauges on the pad which could then be correlated with variations in loading as well as applied parametric changes. The parametric model used was similar to the sensor pad schematic shown in Figure 3.1, however, several parameters were varied (within ranges defined by microfabrication capabilities), as indicated in the cross-section shown in Figure 3.4.

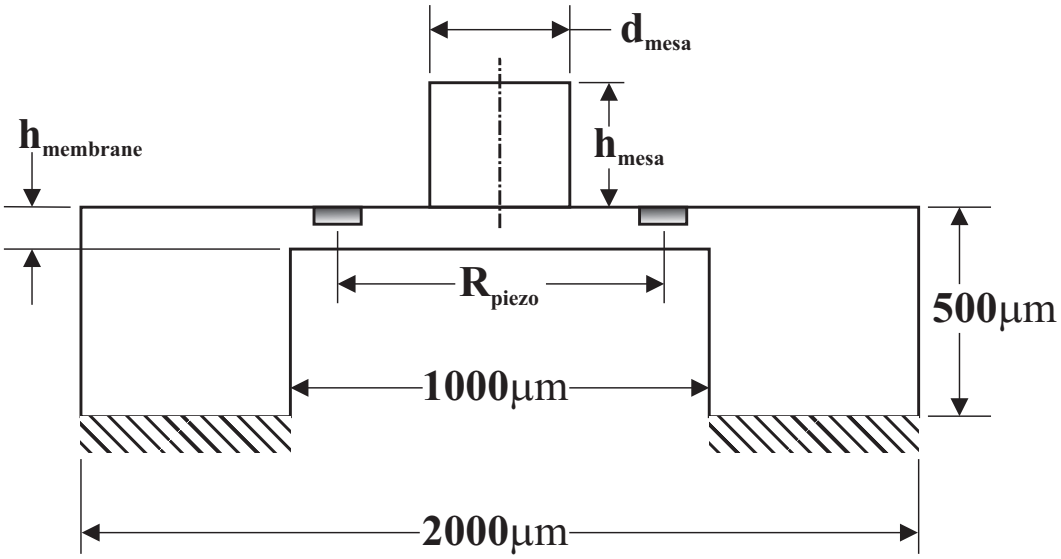

Figure 3.4. Cross-sectional view of the parametric sensor pad model.

The loads and boundary conditions applied to the parametric pad model can either be representative of the contact loads applied by the rod or a general combination of normal and shear forces. In all models examined, the base of the sensor pad was fully constrained (mechanically) and input potential differences were applied across the long axes of the four-terminal gauges. In addition to the magnitude and direction of applied loads, parameters such as location of the piezoresistors on the membrane surface, the size and location of the applied load distributions, and membrane edge lengths and thicknesses were found to have a substantial effect on the stress-strain distribution in the membrane surfaces of the sensor pads. Determination of equations to convert the four voltage outputs from the four-terminal gauges back into shear and normal force information, as well as further details on the effects of parametric changes and sensor pad performance, are described in Section 4.

3.4 - Microfabrication of Prototype Devices

Microfabrication is necessary for verification of FEA simulations and the production of prototype devices. A process flow has been developed for the sensor pads that will allow them to be manufactured according to specifications determined using FEA, and subsequently integrated into packaging and mounted

on the pedicle screw. An overview of the manufacturing scheme is presented first, with specific details of the individual processes provided afterward. Extended details on technical issues which occurred during the development of various phases of this process are presented separately in Sections 3.5 and 3.7.

Two separate techniques were used to verify that the process steps were performed successfully and that the overall process flow was appropriate for manufacturing the sensor pads. First, when possible during microfabrication, characterization of individual process step results was performed. This included techniques such as optical inspection, profilometry, ellipsometry, and spectral reflectance measurement. Second, specialized devices were fabricated as part of the sensor pad manufacturing procedure which allowed specific aspects of performance to be determined. These devices included Greek and Kelvin crosses to determine sheet and contact resistances [52, 58, 59], silicon pressure sensors with known performance characteristics (similar to those produced in Chang [90], and individual four-terminal gauges with varying orientations and sizes.

The manufacturing scheme used to manufacture the prototype devices is presented. Several manufacturing runs were performed during the development of the sensor pads, incorporating various design features. The main manufacturing steps for the final design are shown schematically in Figure 3.5 with relevant steps numbered. The sensor pads were produced using 100mm double-sided polished silicon substrates that were initially 300µm thick. These substrates, or wafers, were cleaned and a thermal oxide layer was grown on the surfaces, as shown in step 1 in Figure 3.5. Step 2 used a photolithography process to pattern the silicon dioxide (SiO_2). This involved applying a layer of photoresist, exposing portions of it through a photomask using UV light, and developing to remove the exposed portions. Step 3 involved the completion of the photolithography process by etching through the exposed SiO_2 using a buffered oxide etch (BOE) and a reactive ion etching (RIE) process. The photomask pattern transferred to the developed photoresist defined alignment marks and the location of the TSV holes. The remainder of the photoresist was then removed. A cryo-etch process was then performed to etch through-holes in

the wafer (step 4). A new SiO_2 layer was then grown on the wafer to be used for a diffusion mask. A second photolithography step was performed to etch the SiO_2 and define the location of the piezoresistors. Step 5 shows the thermal diffusion process used to dope the wafer with boron. Following this, the diffusion mask was removed, and a thermal drive-in and oxide growth process was performed, as shown in step 6. A third lithography step was then performed to open electrical contacts to the piezoresistors in the SiO_2 (step 7). Step 8 included sputtering aluminium on both sides of the wafer and two lithography steps to pattern electrical contact pads on the front and back surfaces. A sixth lithography step was performed on the backside of the wafer to pattern the SiO_2 for etching (step 9). In step 10, a deep reactive ion etching (DRIE) process was performed on the backside of the wafer to create the membranes. The wafers were annealed, diced to separate the individual pads, and mesas were adhered to the top surfaces of the membranes (step 11). Finally, the TSVs were filled with isotropic conductive adhesive (step 12) to begin to prepare the prototypes for packaging and characterization.

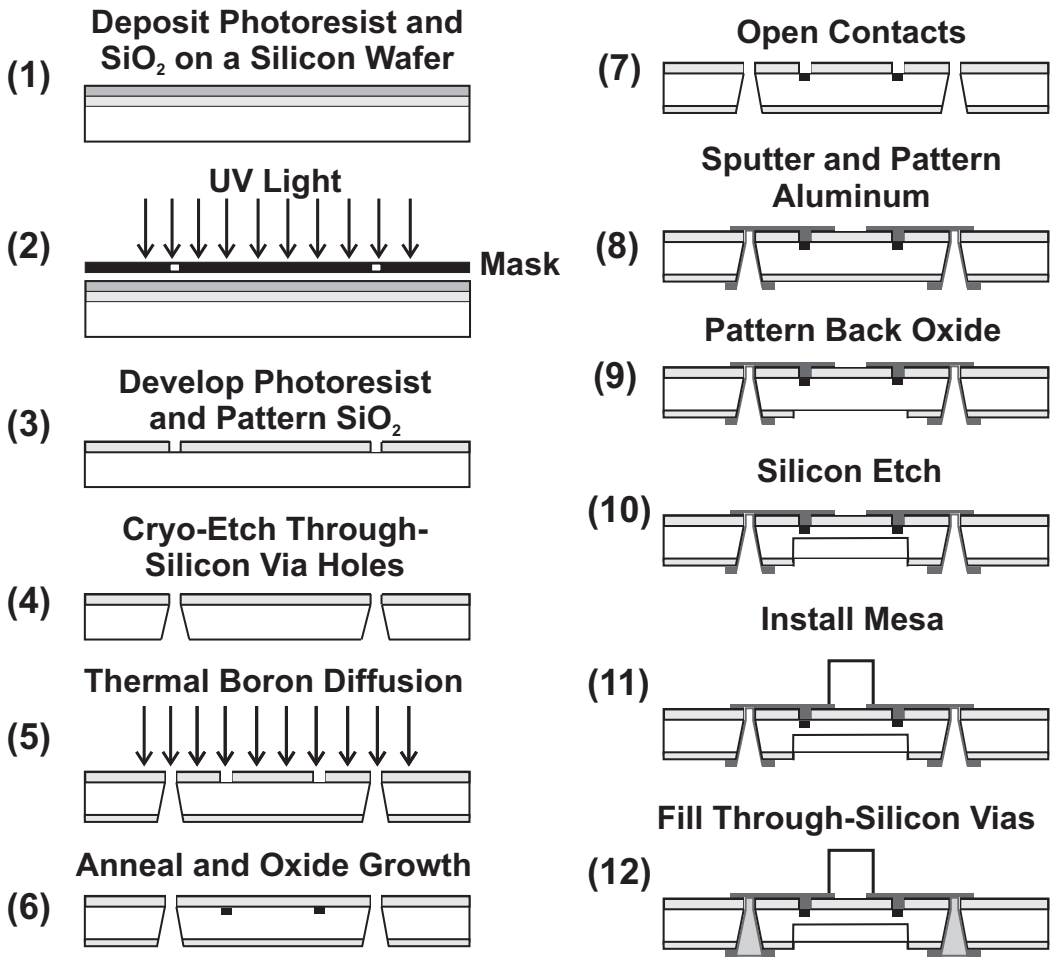

Figure 3.5. An overview of the manufacturing process flow for the prototype sensor pads. Descriptions of the steps are found in Section 3.4.

The set of six photomasks used in this process defined piezoresistor, membrane, and electrical contact geometries. Changes to these geometries required the generation of a different set of photomasks. The process flow used did, however, allow several adjustments which would affect the performance of the sensor pads without requiring a completely different mask set. Specific parameters which could be varied during manufacturing included piezoresistor doping concentration, membrane thickness, and mesa height. Altering the thermal boron diffusion time, temperature, or source material would change the piezoresistive and resistivity coefficients of the piezoresistors. Adjusting the backside etch depth by varying the DRIE program and duration could change the membrane

thicknesses. Mesa height and composition could be adjusted by adhering different materials to the top surface of the membrane. These alternative mesa materials could include a thick photoresist such as SU-8 (patterned using an additional photolithography step) which could be applied with different thicknesses.

3.4.1 - Silicon Substrate Selection and Surface Preparation

Several types of single-crystal silicon substrates, or wafers, are available. This variety includes different sizes, with diameters ranging from 25mm – 300mm, and thicknesses, with common values being lower than 1mm. Extremely thin substrates, with thicknesses of less than 100μm, are typically bonded or otherwise attached to a thicker "handle wafer" to reduce the fragility in handling. These substrates are referred to as silicon on insulator (SOI) wafers, as the process and handle wafers are separated by a silicon dioxide layer. Wafers are sliced and polished to have their plane surfaces corresponding to a crystal plane in the underlying silicon. The (1 0 0) and (1 1 1) plane orientations are the most common, although other varieties of wafers are produced to utilize the orthotropic electrical and mechanical properties. This crystal plane orientation, as well as the background dopant type, may be indicated by one or more flats ground into the edges of the wafer. The large flat on most wafers also indicates the <1 1 0> direction. Figure 3.6 shows an n-type (1 0 0) wafer with the large flat shown oriented toward the bottom of the image. As indicated in Section 2.4, the electrical and mechanical properties vary in single-crystal silicon according to orthotropic stress-strain and resistivity equations. Additionally, the silicon planes may be etched at different rates using an anisotropic process such as KOH. For a (1 0 0) wafer, this etch will produce hole sidewalls with a 54.7º angle from the horizontal as the (1 0 0) plane etches much faster than the (1 1 1) plane.

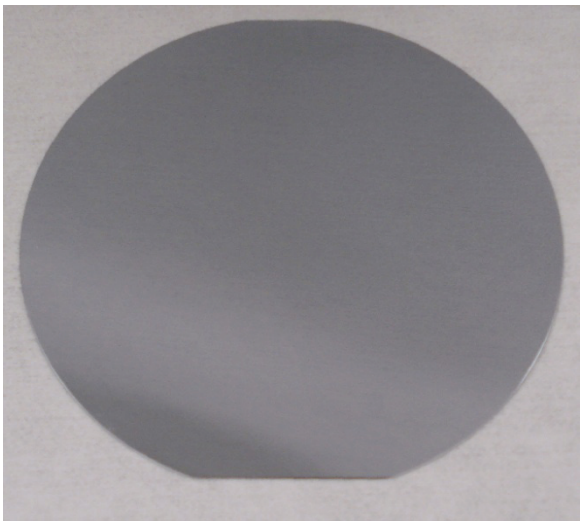

Figure 3.6. A 100mm single crystal silicon substrate. The large flat at the bottom indicates the <1 1 0> direction and the small flat at the top indicates n-type doping and (1 0 0) crystal plane orientation.

The concentration of impurities is another significant variable for substrate selection. This is known as the background doping and may be altered in terms of impurity type and concentration. Typically, wafers will not be composed of pure silicon and are lightly doped with either boron or phosphorus, producing a resistivity of 1-10Ω-cm. This resistivity corresponds to a doping of 1×10^{15} - 1×10^{16}atoms/cm^3 for p-type silicon doped with boron and 5×10^{14} - 4×10^{15}atoms/cm^3 for n-type silicon doped with phosphorus. When fabricating piezoresistors, selecting a background doping with the opposite polarity of the desired piezoresistor allows the junction isolation phenomenon to prevent current flow from the piezoresistor into the bulk of the substrate.

Silicon substrates may be purchased with one or both surfaces precisely ground, however, it still may be necessary to clean them prior to processing. A mixture of one part 30% hydrogen peroxide (H_2O_2) is added to two or three parts 96% sulphuric acid (H_2SO_4) to create a cleaning agent known as piranha. Piranha activates to remove organic material in an exothermic reaction that may reach 120ºC. The acidity of piranha may also react with metal or plastic, so care should be taken when selecting containers and when cleaning substrates that have already

had processing performed. Other less aggressive methods exist to clean substrates that have metal on their surfaces. These methods include the use of oxygen plasma to ash photoresist and other contaminants. Alternatively, acetone or other less aggressive solvents may be used to clean substrates, a process that can be aided using an ultrasonic bath.

3.4.2 - Silicon Dioxide Production and Etching

The use of silicon dioxide layers is important for the piezoresistor manufacturing process. This material may function as an electrical insulator, an etch stop, or a hard mask for specific processing steps such as doping. Although SiO_2 can be deposited using methods such as chemical vapor deposition, the most common method of SiO_2 production is the exposure of a silicon wafer to oxygen in an elevated temperature environment. These oxygen molecules can be obtained from H_2O in a wet or steam oxidation or from O_2 in a dry oxidation. The wet oxidation environment will grow SiO_2 at a faster rate but (generally) with less uniformity and lowered quality. Higher temperatures also increase the rate of oxide production. The temperature range for oxide growth is typically 800-1200°C, which limits the materials that may be present on the wafer during the oxide production process. Since the silicon in the SiO_2 comes from the wafer itself, surface depletion should be considered during oxide growth. The silicon surface depletion rate is 44% of SiO_2 growth rate. Specific equations for estimating SiO_2 growth rates may be found in literature [51, 135].

Silicon oxide may be etched and patterned using several methods. A buffered oxide etch (BOE) process uses a mixture of hydrofluoric acid (HF) and surfactant to etch SiO_2 isotropically at approximately 55nm/min. The BOE process may be masked with several common photoresists and materials, although the isotropic nature limits the minimum feature sizes attainable. This etch can also be used on an unmasked wafer to remove native oxide layers which form in air and may be only a few nanometers in thickness. Alternatively, a reactive ion etch (RIE) can be performed to etch SiO_2 anisotropically. This equipment uses CF_4 gas to etch the oxide in a vacuum chamber. An electric field propels the

ionized gas (plasma) toward the wafer, where it reacts to directionally etch the exposed SiO_2. Similar masking protocols can be used during RIE as with BOE, although photoresist layers exposed to plasma in an etch process become substantially more difficult to remove from the wafer.

3.4.3 - Photolithography

Photolithography is the primary method for pattern application to silicon substrates. This process uses UV light to selectively expose a 2D pattern onto a layer of photoresist, which is a light sensitive media that has been applied to the wafer. Depending upon the type of photoresist, the exposed or unexposed portion is removed during the developing step in this process. The patterned photoresist remaining on the wafer after developing may then be used as a mask during subsequent etches or other process steps. After the desired processing is completed, the remaining photoresist will typically be removed prior to the next manufacturing step.

Selective exposure is provided using a 1:1 scale chrome-on-glass photomask. Photomasks are produced using a high-resolution laser mask writer, which allows a chrome layer to be patterned through exposure of a photoresist layer, development, and chrome etching. The mask writer uses a precision motor to control the exposing laser according to a pattern defined by a data file. Minimum feature size on the chrome is approximately 0.6μm using a mask writer [135, 136]. This feature size is limited by the wavelength of light used to expose the photoresist; consequently, ultraviolet (UV) or deep ultraviolet (DUV) light is used. Using 1:1 photomasks and UV exposure wavelengths, minimum feature sizes of 1.0μm may be routinely produced for MEMS devices. However, immersion lithography and other advanced techniques have enabled features below 22nm to be produced [137].

Several types of photoresist are available for use during photolithography. These light-sensitive chemicals are designed to adhere to a wafer and protect it during subsequent processing. Photoresist is most commonly applied using spin-on methods, although spray-on or electrophoretic methods are also available.

Spin-on application achieves a uniform photoresist thickness which is dependent on the photoresist viscosity as well as specific spin speed and time variables used. The thickness of a photoresist layer is important for two main reasons: proper photolithographic exposure energy is dependent upon this thickness, and the process step that the photoresist is masking will also require a specific thickness due to the consumption rate of photoresist during that process. In general, finer features require thinner layers of photoresist and deep etches require thicker layers. Typical thicknesses of photoresist vary from approximately 1-15μm, although thicknesses of up to 2mm are possible.

Adhesion promoters such as hexamethyldisilazane (HMDS) may be applied to (non-metallic) substrates to aide in photoresist application. Moreover, photoresist films must be baked after the spin-on application process to harden them and remove solvent. This baking process also removes the water from the photoresist, so rehydration is necessary before exposure to ensure proper development. Ambient humidity (ideally around 40-50%) is adequate for rehydration; longer rehydration times are required for thicker layers of photoresist.

Exposure energy and development time for photoresist are dependent on the thickness and type of photoresist applied. Exposure energy, when specifically defined as the amount of light energy the unmasked photoresist is subject to, will depend on the light source being used and the exposure time. Inadequate exposure will manifest with photoresist not being evenly removed from the wafer after development. Excess exposure can lead to pattern degradation, particularly around square corners and smaller features. Development, which typically involves submerging the exposed substrate in a solvent, is similarly sensitive to the solvent concentration and submersion time. Excessive solvent concentration or development time will cause issues similar to those created by over-exposure, and inadequate solvent concentration or development time will cause issues similar to under-exposure. Exposure and development are very sensitive to equipment and chemical selection, so photomask specific calibration of photolithographic processes needs to be performed to achieve acceptable results.

3.4.4 - Silicon Etching

Etching the base silicon is the fundamental process used to create the TSV holes and to thin the substrate for membrane production in this process flow. As the thickness of the substrate is often several orders of magnitude thicker than typical oxide or metal layers used in MEMS fabrication, special consideration is given to silicon etching techniques. Several methods exist to etch silicon, including RIE, the Bosch process, cryogenic etching, and KOH etching. Of these methods, the RIE will etch thick layers isotropically, the KOH will etch anisotropically according to the crystal planes of the silicon, and the Bosch and cryogenic etch processes will etch anisotropically according to the orientation of the wafer in the etch chamber. The ability of the Bosch and cryogenic etch processes to etch deep holes with near-vertical sidewalls has made them the primary processes used for silicon etching in this microfabrication.

Both Bosch and cryogenic etching are DRIE processes which can produce high aspect ratio holes in silicon. Defined here as the hole depth over diameter (D/Ød), aspect ratio is an important consideration in silicon etching. Essentially, the ions in the charged plasmas used in DRIE processes will collide with more free atoms on their way to the bottom of a high aspect ratio hole, thereby reducing the etch rate. This phenomenon is known as aspect ratio dependent etching (ARDE) and is described in more detail (with references) in Section 2.9.1. Figure 3.7 (with general trend information obtained from Yeom *et al.* [116]) shows etch rates in terms of aspect ratio for DRIE. The functional consequences of ARDE are that holes on a wafer with varying diameters will not etch to equivalent depths in the same amount of time, and it also places an overall limit on the dimensions of holes that can be produced in silicon.

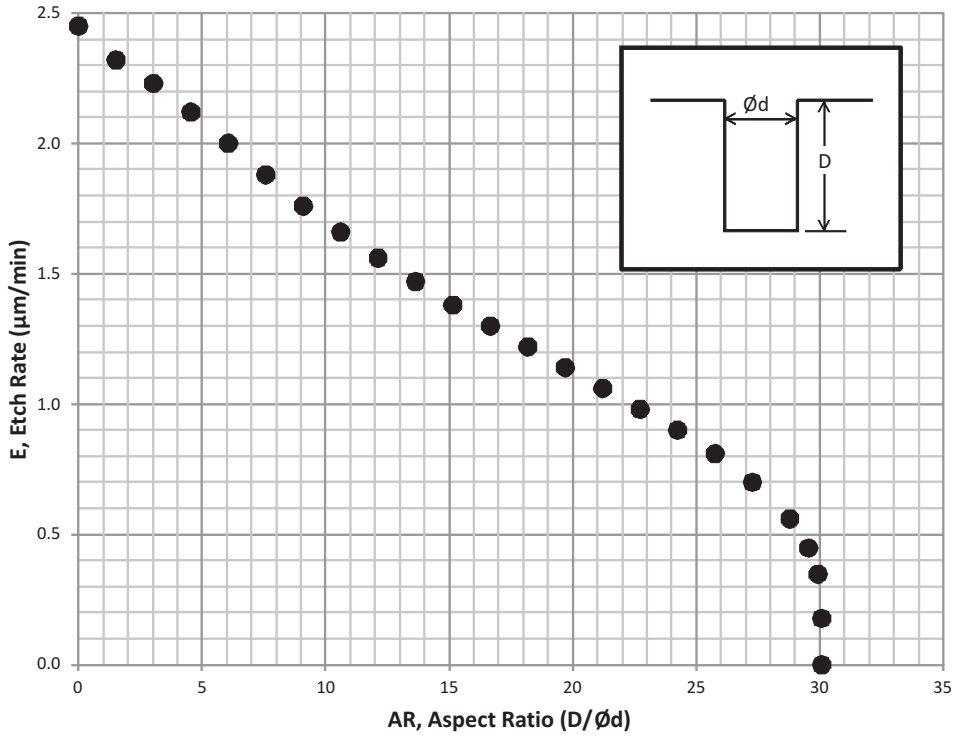

Figure 3.7. Etch rate in silicon as a function of aspect ratio. General trend model obtained from Yeom *et al.* [116].

The Bosch process is similar to the RIE process described in Section 3.4.2, except that it alternates etch and passivation cycles to achieve a deep etch with a high aspect ratio. The etch cycles use an SF_6 and O_2 gas source to create a plasma which directionally etches the silicon. The anisotropy of the etch cycle is somewhat limited, and is thus alternated with a passivation cycle every few seconds or approximately 1-2µm of etching. The passivation cycles use C_4F_8 to create a chemically inert, Teflon-like coating on the surfaces of the holes being produced. This coating acts to protect the sidewalls of the holes being etched while still allowing the holes to be made deeper by being permeable to the ions bombarding the bottom of the holes. The cyclic nature of the Bosch etch process leads to rough "scalloped" hole sidewalls, as shown in a scanning electron microscope (SEM) image in Figure 3.8. Photoresists, oxides, or metals may be used as masks for the Bosch process.

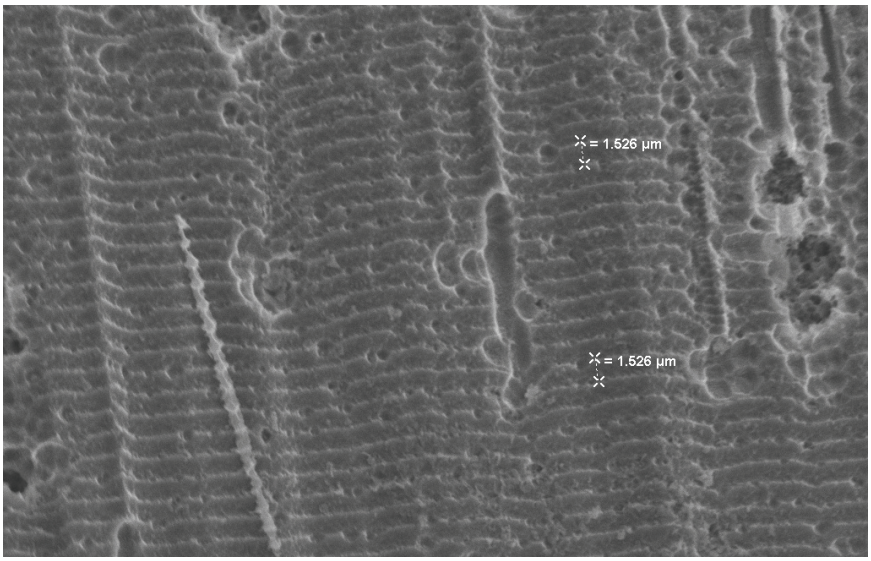

Figure 3.8. An SEM micrograph depicting a "scalloped" sidewall profile of a hole created using the Bosch process. Each etching cycle has been shown to remove approximately 1.5µm of silicon.

Cryogenic etching (cryo-etch) allows the creation of anisotropic holes by keeping the wafer at a very low temperature to retard isotropic chemical etching while allowing directional ion bombardment. Specifically, the low temperature enables passivation through the formation of SiO_XF_Y on hole sidewalls [119, 138]. Temperatures of -110ºC are typically necessary for this process, and are achieved by back-cooling the wafer chuck with liquid nitrogen. Plasma consisting of SF_6 and O_2 is used in this process, and by varying the gas ratios the sidewall angle of the holes may be fine-tuned. Cryo-etch is not a cyclic process, so holes produced will have smoother sidewalls than those made using the Bosch process. An SEM micrograph of a hole created using the cryo-etch process is shown in Figure 3.9. Due to the low temperatures, photoresist masks may crack during etching, so a hard mask made of metal or oxide should be used. Selectivity can be extremely high with cryo-etching, potentially exceeding a 1000:1 $Si:SiO_2$ removal ratio, depending on the exposed silicon percentage.

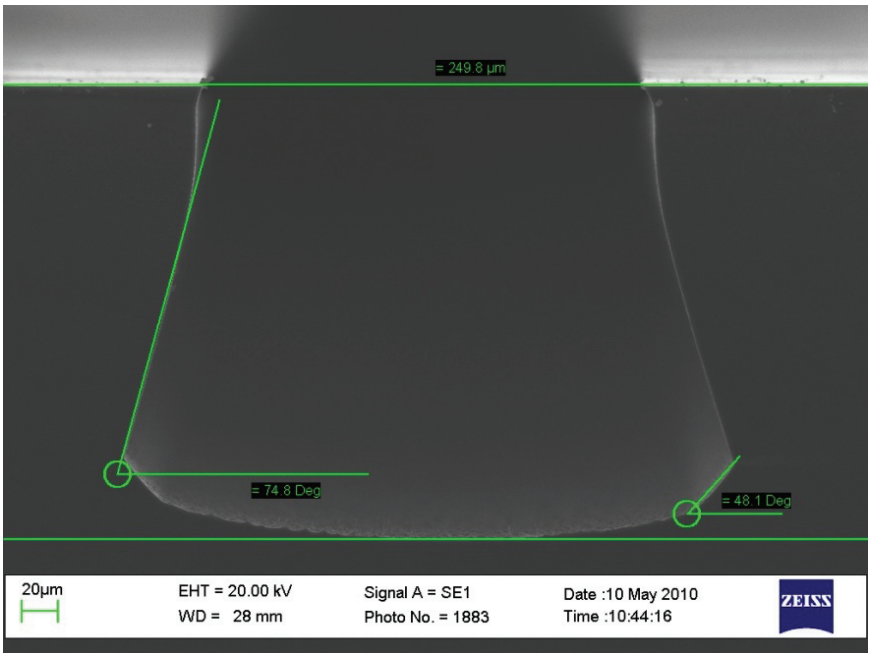

Figure 3.9. Smooth sidewalls created using the cryogenic etch process. (SEM micrograph courtesy of Scott Munro, U of A NanoFab.)

Silicon etching with DRIE involves adjustment of several parameters including etch power, gas flow rate, temperature, exposed silicon ratio, and etch and cycle times. These process parameters must be fine tuned for each microfabrication run to ensure that the desired end-product etching is achieved. Common issues with DRIE include varying hole sidewall angles and quality, black silicon or silicon grass formation, non-uniformity of hole depths, wafer breakage, isotropic etching, unpredictable etching speed, and so on. Parametric variation to DRIE processes and the resultant effect on etch quality is discussed further in literature [118-120, 138].

3.4.5 - Silicon Doping

The background doping of silicon wafers consists of impurities (usually boron or phosphorus) within the crystal lattice. However, due to their uniform and low concentration, these impurities are not often usable for piezoresistive sensor applications. To produce functional sensors, it becomes necessary to introduce relatively high dopant concentrations to specified areas of the wafer. Typically,

the areas doped for these sensor components will be composed of impurities with opposing polarities to the background doping. This facilitates junction isolation, thereby preventing current leakage from the doped areas into the bulk silicon wafer.

The most common doping processes are diffusion and ion implantation. Diffusion utilizes a solid, liquid, or gaseous source to introduce a very high concentration of impurities to the surface of the wafer. High temperatures (800-1200ºC) [135, 139] are then used to allow the impurities to diffuse into the bulk of the wafer. Ion implantation uses an electric field to accelerate the impurity atoms and bombard them into the wafer. High energies (10-5000keV) are required to implant the dopant ions, and a high temperature anneal is required post-implantation to repair the crystal structure damage created by the implantation process [51, 135]. The equipment required for ion implantation is considerably more complex and expensive than for diffusion. For this reason, diffusion was chosen as the primary method of doping for this research.

The diffusion method used during the manufacturing process for the scoliosis sensor array made use of solid boron sources (Techneglas BoronPlus GS-126). To use these sources, the silicon substrates are first masked using a patterned SiO_2 layer. The slower diffusion rate of boron in SiO_2 ($6.2\times10^{-19}cm^2/s$ at 1000°C [140]) compared to silicon ($2.2\times10^{-14}cm^2/s$ at 1000°C [135, 141]) allows a 1200nm thick mask layer to be sufficient. The solid sources are then brought up to a holding temperature of 700ºC in a doping furnace tube to ensure any moisture present has been removed. The furnace is purged with a dry nitrogen flow during the process to prevent oxide growth on the wafers during the diffusion. After a 20-30 minute hold, the substrates are placed next to the sources (within 1.5-2.5mm) and are slowly reinserted into the furnace. The furnace is then ramped up to the doping temperature of 900-950ºC at a rate of 7K/min. A controlled ramp rate and slow insertion into the furnace are necessary to avoid any thermal cracking or warping of the wafers. The substrates and sources are then held at the doping temperature for 60 minutes, achieving a surface sheet resistivity of approximately 50Ω/sq after this pre-deposition step. The furnace is

then ramped down to 700ºC and the wafers are slowly pulled from the furnace. Following the diffusion, the masking SiO_2 layer is removed. Finally, a high temperature (1000ºC) anneal and thermal oxide growth is performed for four and two hours, respectively, to drive-in the boron atoms deeper into the wafer and produce surface insulation (400-600nm) for the piezoresistors.

The high temperatures used during the diffusion process described above produce a depth concentration profile for dopant atoms that may be theoretically modelled using Gaussian and Error Function equations [52, 135]. The sources evolve B_2O_3 when they are at the doping temperature, producing a high concentration of boron atoms near the surface of the wafer, known as a boron glass layer. This phase is known as constant-source diffusion, and produces a depth profile which may be modelled using an Error Function, as shown in Equation (3.1).

$$C(x,t) = C_S erfc\left(\frac{x}{2\sqrt{Dt}}\right) \tag{3.1}$$

The x term represents the depth below the surface, and t is the time. The C_s term represents the surface concentration, which is a function of the dopant source and is limited by the dopant solubility (which is also a function of temperature). Values for dopant solubility of boron in silicon are given by Vick and Whittle [142]. D is the diffusion coefficient defined by:

$$D = D_0 exp\left(\frac{-E_a}{kT}\right) \tag{3.2}$$

The D_0 term represents the diffusion coefficient at infinite temperature, E_a is the activation energy, k is the Boltzmann constant (8.617×10^{-5}eV/K), and T is the temperature (in Kelvin). For boron in silicon, D_0 is defined as 0.76cm^2/s and E_a is defined as 3.46eV [143]. Alternatively, values for D are plotted against temperature in literature [135, 142].

After pre-deposition has been modelled using Equation (3.1), the total number of dopant atoms introduced to the doped area can be calculated using Equation (3.3).

$$Q(t) = \int_0^\infty C(x,t)\,dx = \frac{2}{\sqrt{\pi}} C_S\sqrt{Dt} \tag{3.3}$$

The thermal annealing process constitutes the drive-in, or limited source, diffusion phase. This phase allows the atoms to move deeper into the wafer with the boron sources removed. This phase produces a depth profile which may be modelled using a Gaussian distribution, as shown in Equation (3.4).

$$C(x,t) = \frac{Q(t)}{\sqrt{\pi D t}} exp\left(-\frac{x^2}{4Dt}\right) \tag{3.4}$$

The oxide growth step following the thermal annealing will consume the top layer of doped silicon. The silicon consumption rate is 44% of the total oxide growth rate, as described in Section 3.4.2. Figure 3.10 shows the boron concentration depth profile simulated with these equations for the fabrication parameters given above.

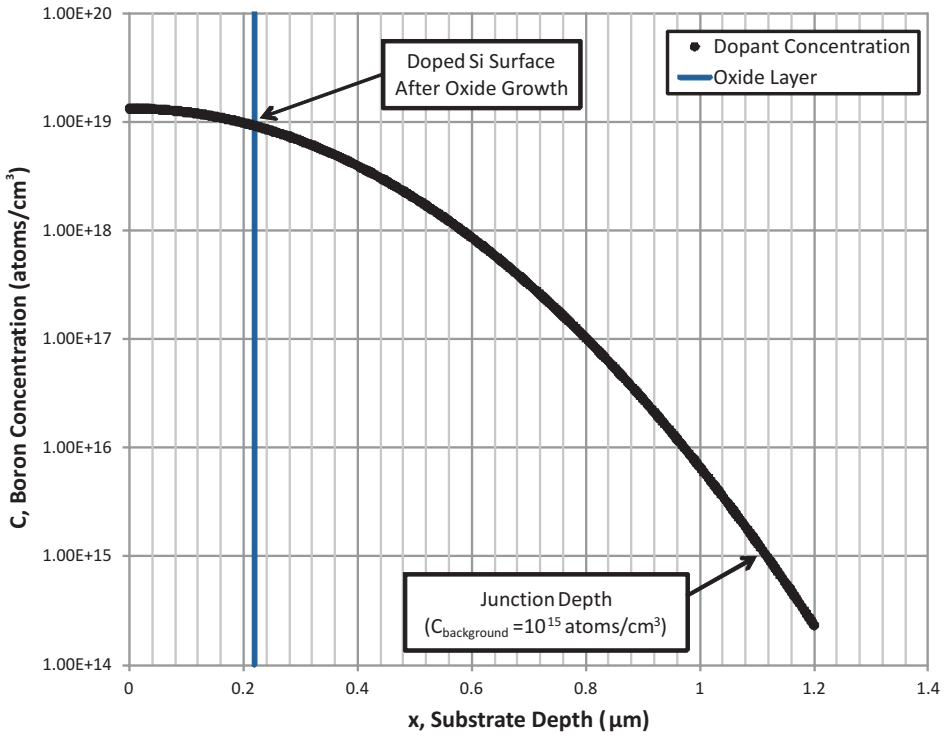

Figure 3.10. Modelled boron concentration depth profile. Surface concentration after doping, annealing, and oxide growth is approximately 9.3×10^{19}atoms/cm^3.

3.4.6 - Sputtering and Metal Etching

Sputtering is a technique used for coating thin layers of material (typically metals) onto a substrate. A low-pressure chamber, similar to those used in plasma etching, is utilized to reduce the amount of free atoms present. An electric field is used to create plasma, which then bombards a target (the sputtering material supply) with ions (typically argon). Atoms freed from the target then can travel and bond with the substrate surface. Generally this process is used to create layers which are less than 1000nm thick. Sputtering may be used to create uniform or compound material coatings, with parameters such as vacuum pressure, source quality, plasma energy, and collimation [121-123] being important for the quality of the sputtered material. The metal deposited in this process was aluminum, which has excellent adhesion and conductive properties when used with silicon wafers. To improve the contact between the piezoresistors and the sputtered aluminum, care needed to be taken to remove all native oxide from the contact points.

Etching of aluminum and other metal layers is fundamentally similar to oxide etching with BOE, as described in Section 3.4.2. An isotropic wet etch consisting of acids and other chemicals is generally used for metal etching. Depending upon chemical composition and concentration, controlled etching of thin layers can be performed. The etchant for aluminum consists of a mixture of phosphoric acid, nitric acid, acetic acid, and water, which etches at a rate of up to 660nm/min [144]. Photoresists are common mask materials for metal etching.

In order to achieve improved (ohmic) conductivity between the sputtered and patterned aluminum and the piezoresistors, a short anneal may be performed. This is particularly important for piezoresistors with lower dopant concentrations. This anneal is performed for approximately 20 minutes at 450ºC, and allows silicon to diffuse into the aluminum to lower the resistance across the contact [79, 135]. This resistance may also be improved prior to piezoresistor use by applying a (relatively) high current across the silicon-metal interface. In addition to creating heat localized at the high resistance interface, the current breaks the Schottky barrier to create an ohmic contact, thus providing a path for electron

flow. In practice, the Schottky barrier could be broken by increasing the potential difference across the silicon-metal interface until measured current flow increased, and linear behavior was observed.

3.4.7 - Physical Processing

Dicing and other physical manufacturing processes needed to be performed after microfabrication was completed to prepare the devices for packaging. Although wafers may be scored and broken along their crystal planes, dicing is a more accurate method of dividing up individual devices. Dicing is performed using a very fine saw (approximately 55μm wide) which cuts the wafers under a jet of water. The saw is optically aligned to visible features on the wafer surface. The wafer is held under the saw using an adhesive tape, which prevents the saw blade or the water jet from flinging cut sections of wafer off of the chuck. Proper use of the adhesive tape prevents components from being lost or broken, so special care needs to be taken, especially when dicing smaller sections of wafers.

Another physical manufacturing process that needed to be performed prior to packaging was the application of mesas on top of the membranes. Various adhesives were tested for their ability to bond to the silicon and provide a raised load application area. Viscous adhesives such as epoxies were able to create a raised bump that could be used for load application after hardening, although thin adhesives, such as cyanoacrylates, were superior if bonding a separate material for use as a mesa. A microscope and adhesive dispensing system were used to ensure consistency in mesa application. An alternative technique for mesa creation that was examined was the use of a thick photoresist such as SU-8, although this method would need to be performed prior to dicing the wafer.

3.5 - Mask Misalignment

In order to fabricate more complex MEMS structures such as piezoresistors, photolithography with multiple masks must be performed. To align the subsequent masks with features already created on a substrate, alignment marks are used. Typically, the alignment marks consist of a 2D shape, such as a cross,

on the first layer and a negative version of the same shape on the subsequent layers. The negative shape is expanded slightly to facilitate slight misalignments on the order of 1-2µm. For noninverted photomasks (where the features drawn with the CAD software correspond to the glass regions of the mask) that are almost completely covered with chrome, windows should be placed around the alignment marks. These windows allow the user to perform gross orientation of the mask to the substrate more quickly. Figure 3.11 shows an alignment mark used for this process. The darker cross has been etched into the wafer and the four, lighter-coloured squares serve as the negative cross on the photomask. The arms of the cross on the wafer are 10µm narrower than the spacing between the squares, allowing for visual inspection of the 5µm gaps for precise alignment on the order of 1-2µm. Several sets of alignment marks are placed on each photomask to achieve rotational alignment. Figure 3.12 shows the positioning of these alignment mark sets relative to a substrate.

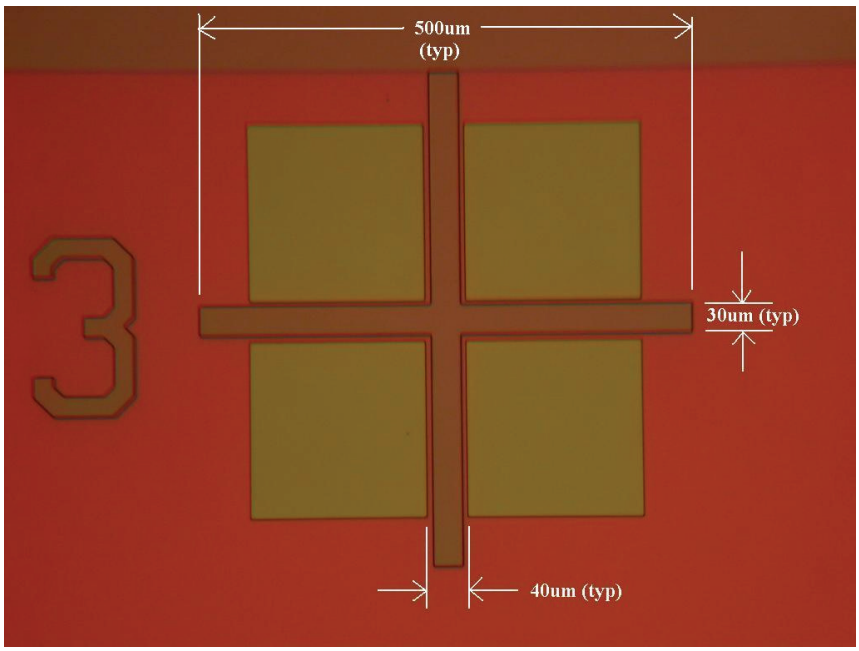

Figure 3.11. Alignment marks used in the microfabrication process. The darker cross feature is etched into the wafer, and the lighter square features are present on the photomask.

Figure 3.12. Alignment marks on a substrate. The coordinate system was arbitrarily chosen with the left central alignment mark set as the origin. Coordinate values are in microns.

A technical issue was found with the mask set in which the first set of alignment marks was aligned normally, but the additional sets could not be aligned. The left central alignment mark was aligned properly and assigned the (0.00, 0.00) coordinate. The right central alignment mark was then aligned, but it was only possible to do so in the Y direction. This alignment mark was thus positioned at (63380.30, 0.00). The positional distortions of the six alignment marks are shown in Figure 3.13, and are tabulated in Table 3.1.

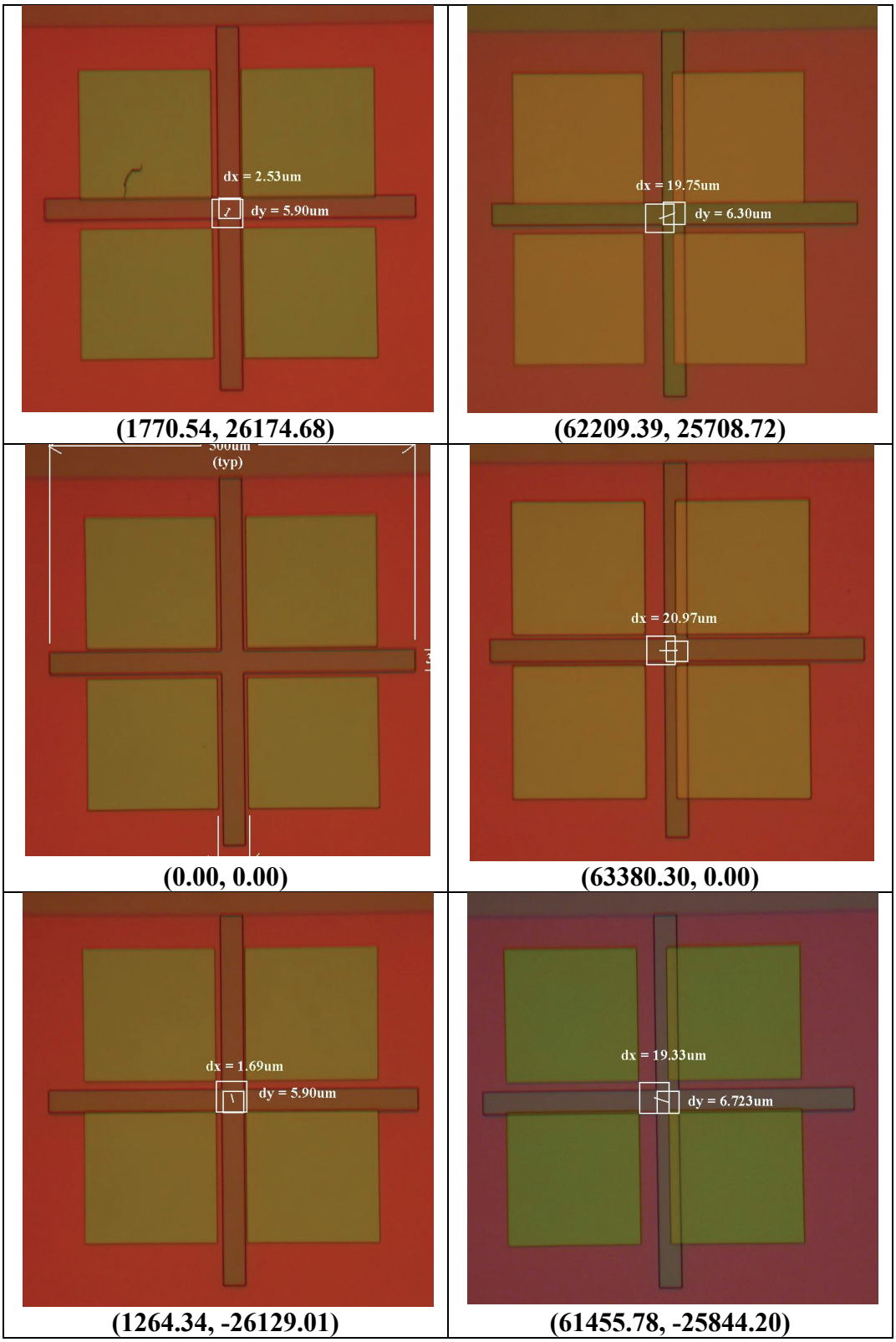

Figure 3.13. Alignment mark distortions with their relative coordinates displayed.

Table 3.1. Measured distortion values in the six alignment mark sets.

Location	*X-Y Coordinates (μm)*	*dX (μm)*	*dX/X (%)*	*dY (μm)*	*dY/Y (%)*
Top Left	(1770.54, 26174.68)	-2.53	-0.1429*	-5.90	-0.02254
Mid Left	(0.00, 0.00)	0	0*	0	0*
Low Left	(1264.34, -126129.01)	-1.69	-0.1337*	5.90	-0.02258
Top Right	62209.39, 25708.72)	-19.75	-0.03175	-6.30	-0.02451
Mid Right	(63380.30, 0.00)	-20.97	-0.03309	0	0*
Low Right	(61455.78, -25844.20)	-19.33	-0.03145	6.72	-0.02600
Average	--	--	-0.03210	--	-0.02391

* Values omitted from the average due to the small coordinate dimension.

The above data was collected by optical inspection of the mask and substrate features. The data indicated that alignment was not possible using this mask set due to a contraction factor of 0.03210% in the X direction and 0.02391% in the Y direction. Although the size difference between the two masks was small, it still prevented layer alignment with greater than 10μm accuracy for all devices on the substrate. This error was discovered to be due to a problem with the photomask writer, and required that the photomasks be reprinted and all processing restarted.

3.6 - Diffusion Furnace Development

During the development cycle of the piezoresistive sensors, the diffusion furnace at the NanoFab facility was decommissioned. The costs and impracticality of doping small-batches of prototype devices off-site was determined to be excessive, so a replacement diffusion furnace needed to be acquired. A smaller tube-style furnace (Carbolite GHA 12/450) was purchased for use with a 155mm ID quartz tube. This furnace is shown in Figure 3.14. The boron sources mentioned in Section 3.4.5 were also acquired and a process was developed to dope silicon wafers for the creation of piezoresistors. Preparation of both the diffusion furnace and the boron sources was required prior to production doping.

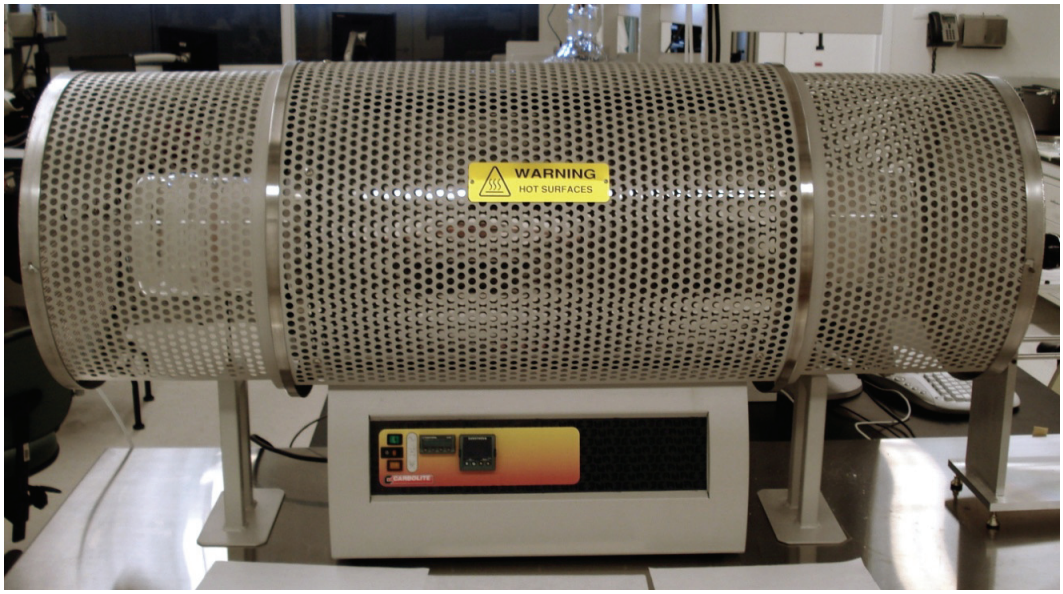

Figure 3.14. The Carbolite diffusion furnace.

3.6.1 - Diffusion Furnace Preparation

Appropriate control of temperature was the first aspect of the diffusion furnace which was examined during commissioning. Insulating plugs and quartz caps were obtained for the ends of the furnace tube to prevent heat loss and to control gas flow. However, it was desirable to use the furnace without the exhaust-side insulation plug to facilitate a simpler and safer hot-loading protocol. As described in Section 3.4.5, the boron sources needed to be heated up to a holding temperature of 700ºC, at which point the wafers could be inserted. Removing the exhaust-side insulation plug for this procedure was hazardous as its extreme heat, cylindrical profile, and brittle, particulating nature made it very difficult to handle. Unfortunately, tests performed without the exhaust-side insulation plug demonstrated that maximum temperatures of only 850ºC could be achieved with a N_2 flow rate of 22L/min. This temperature, as well as the heating rate as the furnace approached it, was not adequate for the doping process. Further usage of the furnace necessarily required both insulation plugs to be installed, and extreme caution needed to be used when manipulating the exhaust-side insulation plug. Figure 3.15 shows a heating profile of the furnace with both of the insulation plugs installed, illustrating the maximum heating and cooling rates for the system.

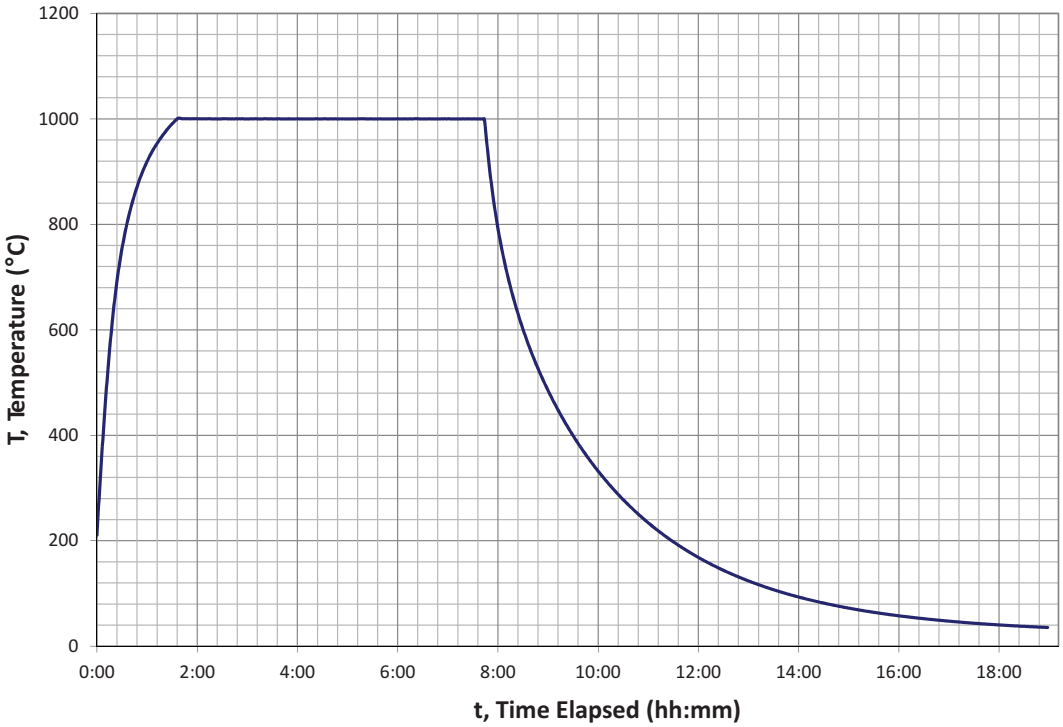

Figure 3.15. Heating profile for the doping furnace with both insulation plugs installed under 15L/min of N_2.

Controlling the water and oxygen levels in the diffusion furnace was also necessary during boron doping. Both O_2 and H_2O had potential to cause oxide growth on the wafers during the high temperature diffusion process, which would compromise the doping rate. To prevent oxide growth, the furnace tube was purged with dry nitrogen throughout the doping procedure. Dry nitrogen (with less than 10ppm H_2O) was required at a flow rate high enough to prevent moist air backflow from the exhaust port. To examine the O_2 and H_2O levels in the furnace tube, bare silicon wafers were loaded and held at 1000ºC for 8 hours. If the oxide growth was less than 10nm on the wafers following this process, the nitrogen water content and flow rate were deemed acceptable for thermal diffusion [139].

The standard procedure to measure oxide film thickness was using a spectral reflectance system (Filmetrics FILMeasure). This type of measurement system detects light reflected off of a film in a perpendicular direction, emitting a range of wavelengths in order to detect film thickness and refractive index. This

system was able to detect film thicknesses from 30nm-50µm with an accuracy of ±1nm at 500nm of SiO_2. Since oxide growth rate is thickness dependent, this system was not capable of accurately measuring thin layers (less than 10nm) of oxide growth on bare silicon wafers. However, due to the speed of measurement with this system, it was used to make initial measurements of oxide film thicknesses to determine if a film thicker than 30nm had been produced.

For thin films that could not be measured with the spectral reflectance system, a spectral ellipsometry system (VASE) was used. This technique uses low incidence angle reflectance and analysis of polarization to evaluate films ranging from 0.1nm-10µm with ±0.1nm accuracy. Ellipsometry is substantially more time consuming than spectral reflectance, due to the separate light source and detector that must be precisely aligned before a measurement can be taken. Measurements at different incidence angles also need to be taken during ellipsometry, further adding to the required measurement time.

Several silicon substrates were prepared for a tube furnace trial by removing their native oxide layers using a BOE dip followed by a short RIE. The RIE was done to remove any oxide growth which may have occurred during the rinse cycle performed after the BOE step. The ellipsometer was used to confirm that these oxide removal steps were successful. The furnace was loaded with the bare silicon substrates and the nitrogen flow was started. The substrates were held at 1000ºC for 8 hours, after which they were re-measured for oxide growth, first with the spectral reflectance system and then with the spectral ellipsometry system if SiO_2 layers were suspected of being thinner than 30nm.

An initial experiment was performed with the nitrogen flow set to zero. The spectral reflectance measurement indicated that oxide films between 168nm and 182nm were produced. A subsequent experiment utilized National Institute for Nanotechnology (NINT) building nitrogen at a flow rate of 6L/min. This produced oxide films between 40nm and 48nm, which were still unacceptably thick. On further investigation, an issue was uncovered with the NINT building nitrogen supply lines: They had been flushed with water during pressure testing, and had been producing unacceptably wet nitrogen ever since. Until this issue

was resolved, further processing was performed using bottled nitrogen that was specified to contain less than 5ppm H_2O. Further measurement of oxide growth rates in the diffusion furnace were able to confirm oxide growth of less than 10nm (measured with the ellipsometer) at nitrogen flow rates of 10L/min and 15L/min.

3.6.2 - Diffusion Source Preparation

After determining appropriate parameters for temperature and gas flow controls on the diffusion furnace, the boron sources were prepared. This preparation consisted of holding the sources at deposition temperature (900-950ºC) for 18 hours in an environment of 75% dry nitrogen and 25% oxygen. This aging procedure was used to remove all moisture from the sources and achieve a more constant B_2O_3 evolution rate [139]. Increased oxygen flow could also have been used for source aging to ensure no organic material remained on the source. This process was performed over two days with the N_2 and O_2 gas supply set to 10L/min. It is worth noting that on the preparation of the first source, a T-sized gas cylinder was exhausted after 14 hours of aging. Nitrogen was used during the remaining four hours of source preparation.

The prepared sources needed to be stored in an environment free from moisture and other contaminants. The manufacturer specified that storage conditions for the sources are ideally in the furnace at 600ºC under dry nitrogen flow [139]. Due to the costs of nitrogen and electricity to store the sources in this manner, it was decided to store the sources in a sealed storage box which was constantly purged with dry nitrogen. It was determined that this alternative storage method would create an acceptably small reduction in doping uniformity and source longevity. To compensate for this storage method, additional source temperature stabilization at 700ºC for at least 15 minutes would be performed after storage to remove any moisture or contaminants that may have been collected.

3.6.3 - Diffusion Process Verification

Diffusion doping was attempted with unmasked silicon substrates prior to a piezoresistor production run. The substrates were prime n-type (100) wafers to match those used during the device fabrication process. Prime wafers were also used to avoid introducing any impurities into the boron sources, quartz furnace tube, or quartz carrier boats. To prepare the wafers for diffusion process verification, they were cleaned in 3:1 piranha for two hours and native oxide was removed using a 10-minute BOE dip followed by a 60-second RIE. The prepared boron diffusion sources were loaded into the tube furnace and a diffusion process was performed. The first step involved stabilizing the furnace at 700ºC with 15L/min of N_2 flow. A chart showing the remainder of the diffusion temperature profile is shown in Figure 3.16.

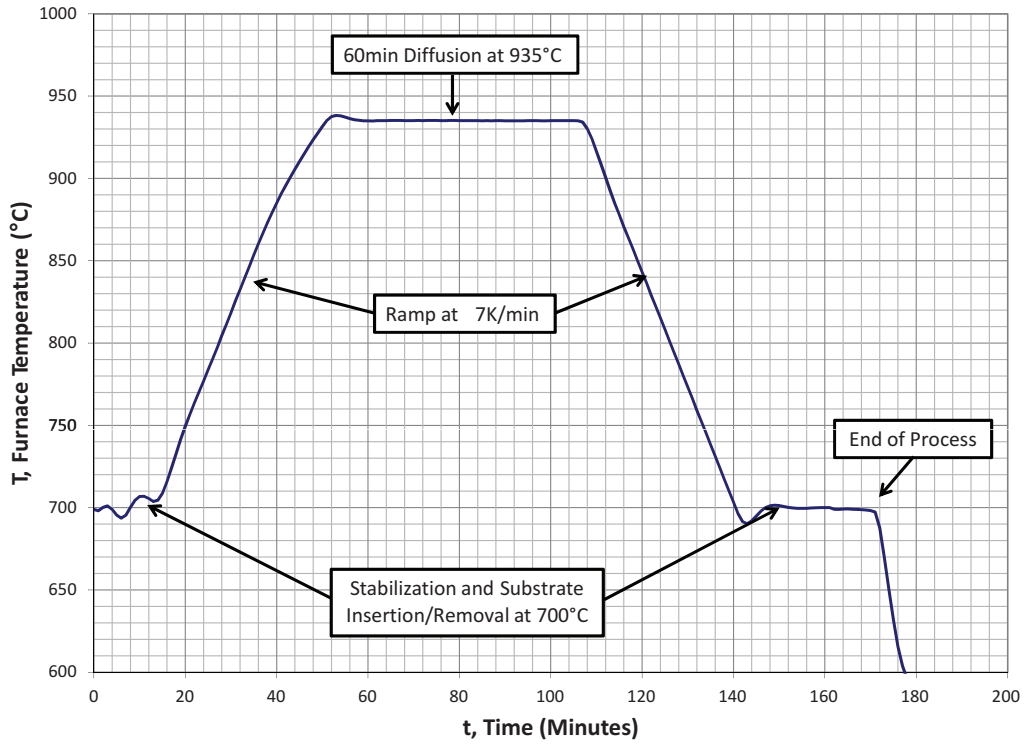

Figure 3.16. The furnace temperature profile for boron diffusion.

Four-point probe resistance testing was used before and after the doping procedure. This measurement allows four-wire resistances to be converted to

sheet resistance by multiplying by 4.53 [145]. Resistances of the undoped, cleaned wafers were measured as open, indicating a very low doping concentration. The resistance was measured again after the pre-deposition process, producing non-uniform sheet resistance values of approximately 1500Ω/sq. This sheet resistance was still very high compared to the expected result of approximately 50Ω/sq, indicating an absolute measurement system error or other sources of resistance (such as oxide growth during pre-deposition).

Thermal drive-in (annealing) was performed at 1000°C for four hours in a dry nitrogen environment, followed by two hours of wet oxide growth at 1000°C. These processes allowed the boron dopants to diffuse further into the silicon. Following the oxide growth, a BOE was used to remove the SiO_2 layer. Figure 3.17 shows photographs of a doped substrate before and after the BOE. A substantial amount of colour was introduced to the oxide layer by the boron atoms, indicating a loss of dopant material from the silicon during oxide growth and etching. A four-point probe measurement was taken after the BOE, indicating an average sheet resistivity of 66.2Ω/sq. Considering the potential for measurement error with the four-point probe, this result was deemed acceptable and a device fabrication microfabrication run was attempted.

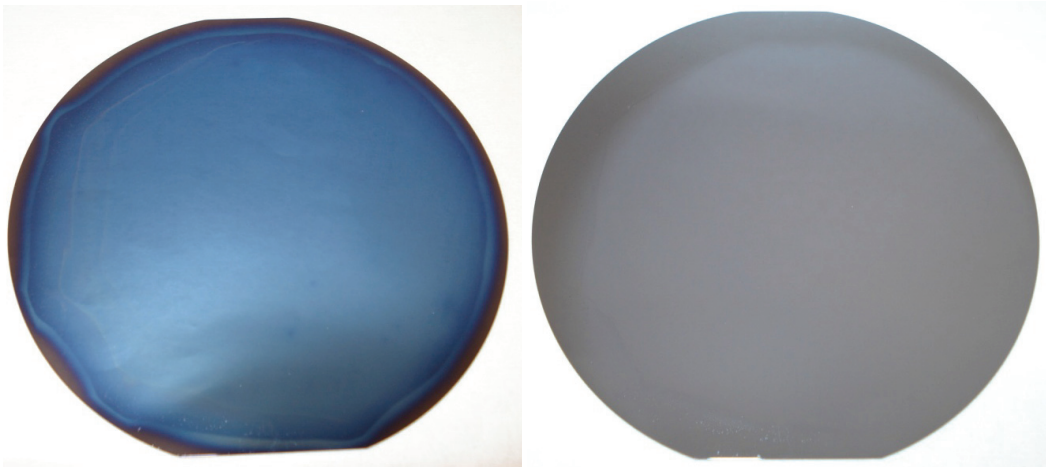

Figure 3.17. A substrate is shown after the diffusion doping and drive-in procedure. The left image shows the substrate before the BOE process, the right image is after the BOE.

3.7 - Through-Silicon Via Development

Through-silicon vias (TSVs), as introduced in Section 2.9.1, allow an electrical path to be made between the top and bottom of a silicon wafer or MEMS device. This technology provides advantages in terms of vertical integration and reduced footprint sizes, allowing packaged devices to be made smaller and less expensive, as well as offering improvements in device durability. Typical drawbacks to TSVs include the relatively low density achievable using typical microfabrication techniques, the complexity that they add to microfabrication process flows, and inadequate high frequency performance. The density issues have briefly been addressed in Section 3.4.4, having to do with the inability to etch holes through silicon with an aspect ratio higher than 20-30 [116, 119]. Another issue related to TSV aspect ratios is the difficulty with depositing an adequate amount of conductive material on the inside of small diameter TSV holes.

These challenges in TSV design are somewhat mitigated by a packaging constraint which placed a 100µm lower limit on FPCB conductor pitch and spacing. Since it was desired to connect the diced MEMS sensors to the FPCBs using wirebonding or flip chip techniques, both the device chips and FPCB layouts should have connection pads of equivalent size. Compared to the active device features on MEMS devices, these connection pads are relatively large. Since these large pad features are necessary for packaging, the additional space provides room for the creation of large TSVs which are not subject to common hole density constraints. Considering the 100µm limit for connection pad size, it was determined that minimum required hole diameters for the TSV would be around 75µm. This size reflects TSV hole aspect ratios greater than 6.7 for a 500µm wafer and greater than 4 for a 300µm wafer. A concept for TSV creation was developed that did not require core material deposition, requiring only the sputtered layer to provide conductivity. A schematic of this TSV concept is shown in Figure 3.18.

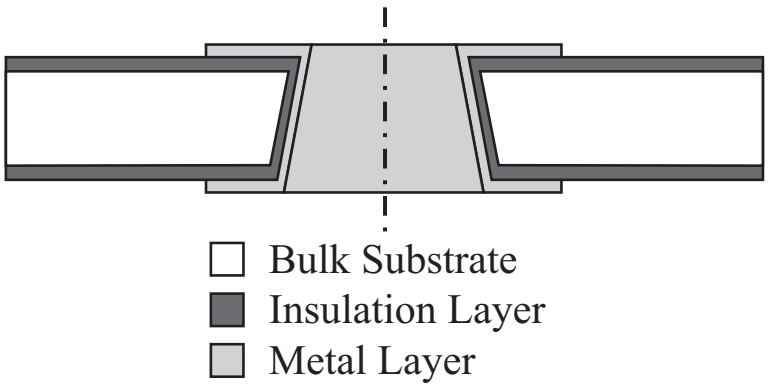

Figure 3.18. Schematic of the coreless TSV concept.

Precise control of the through-wafer etch and the aluminum sputter deposition are required for this coreless TSV concept to be executed. The typical conductor cross-sectional area on the MEMS devices is 20µm × 500nm and is composed of aluminum. To achieve an equivalent conductive area on a 75µm TSV hole, a thickness of only 43nm is required (assuming the hole profile and sputtered material are uniform). This equates to a necessary sidewall deposition ratio of less than 1:10, which was thought to be achievable using the NanoFab's equipment. To increase the amount of hole sidewall material deposited, a cryogenic etching process would be used. As described in Section 3.4.4, cryo-etching does not create scalloped hole sidewalls like the Bosch process. In addition, slightly undercut (angled) sidewalls can be produced by modifying the O_2 flow rate during cryo-etching, and the equipment allowed the etching to be performed without a carrier wafer. An image of a hole created using the cryo-etch process is shown in Figure 3.9.

3.7.1 - Through-Silicon Via Fabrication

A microfabrication protocol was devised to determine the viability of this TSV design. Figure 3.19 shows the basic process flow. A 1400nm layer of SiO_2 was grown on a cleaned, double sided polished, silicon substrate. Photolithography was then performed to expose the top-side hole features to be etched into the silicon. A BOE process was used to remove the oxide layer at the TSV hole locations. The SiO_2 was left on the bottom side of the substrate during this etch to

act as an etch stop. The remaining photoresist was removed, and then a cryo-etch was performed to create the through-holes. Following the etching, the patterned oxide layer was removed with BOE and an insulating thermal oxide layer (500nm) was grown. Sputtering of 500nm of aluminum was then performed on both sides of the wafer, followed by two additional photolithography steps to pattern the aluminum on both sides. Due to the through-holes, a carrier wafer was required for spin coating and patterning the aluminum. It is common for a carrier wafer to be bonded to a device incorporating through-holes, as microfabrication processes often utilize pressure differentials to retain wafers during spin coating processes. The bond to the carrier wafer was achieved using a thick layer of HPR504 or HPR506 photoresist, and removed with an ultrasonic acetone bath after processing.

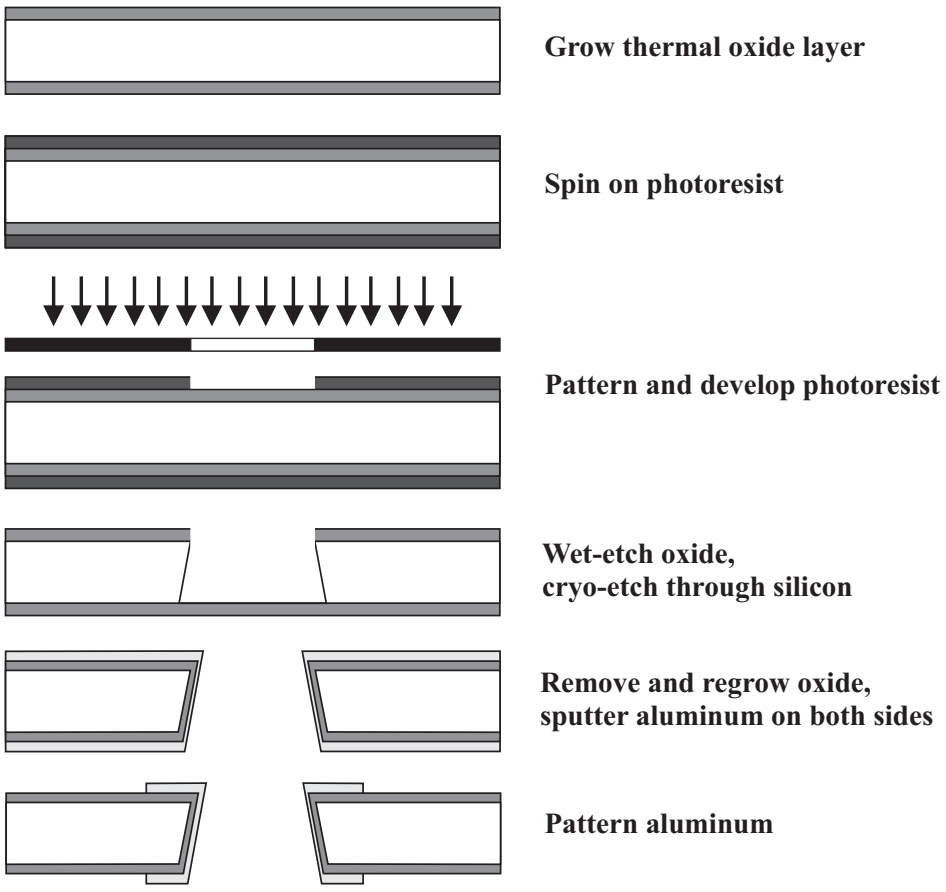

Figure 3.19. Microfabrication steps required to produce the coreless TSV test structures.

The streamlined process flow to produce coreless TSVs was performed on several wafers. Two photomasks were required to perform the fabrication. The via hole pattern layer consisted of square and circular holes with diameters or edge lengths of 100µm, 200µm, 500µm, 1mm, 2mm, and 3mm. The metallization layer consisted of square features large enough to cover the largest TSVs. The masks were designed to be symmetrical about the vertical axis in order to allow a single metallization layer photomask to be used on the front and backside of the wafer. Due to the relatively large minimum feature size, a mask was printed on a transparency film instead of a chrome-on-glass photomask. This technique avoided the costs and delays associated with having a chrome-on-glass photomask printed at the NanoFab. An image of a wafer produced with this process is shown in Figure 3.20.

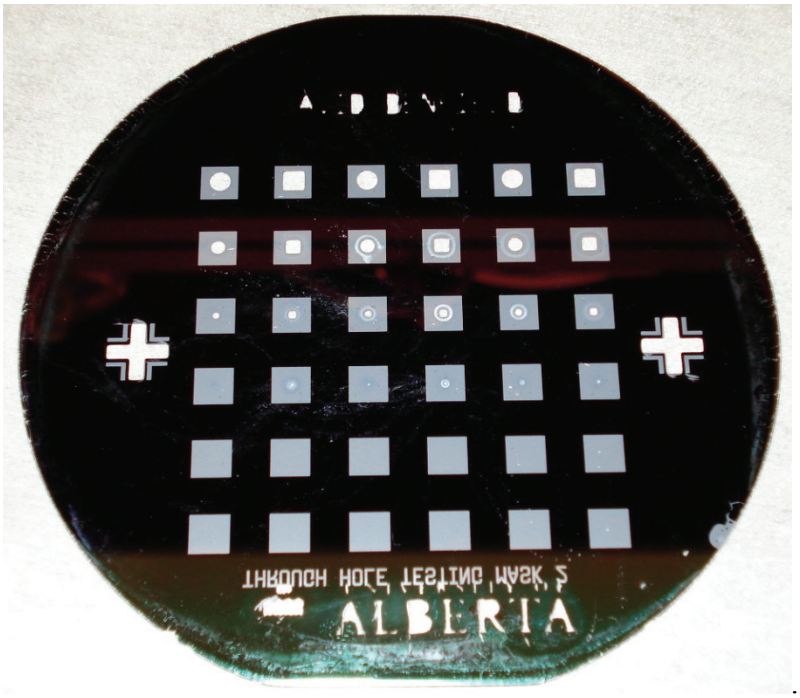

Figure 3.20. A photograph of a wafer processed using the coreless TSV microfabrication flow.

Several technical issues arose during the TSV fabrication process. Wafers processed using the transparency mask developed a rough surface under the masked portion after cryo-etching. This surface was likely due to an uneven SiO_2 layer created after photolithography and BOE etching, indicating that the transparency mask did not uniformly shield the photoresist from the UV light source. This issue was only problematic for the TSV layer, as the aluminum etch did not exhibit similar characteristics using an equivalent mask. The increase in the exposed silicon area created by this surface roughness may have altered the etch rates for this process, as discussed below. Figure 3.21 is an SEM micrograph of a 500μm diameter etched hole which shows the surface roughness, angled sidewalls, and rounded bottom produced with this cryogenic etching process.

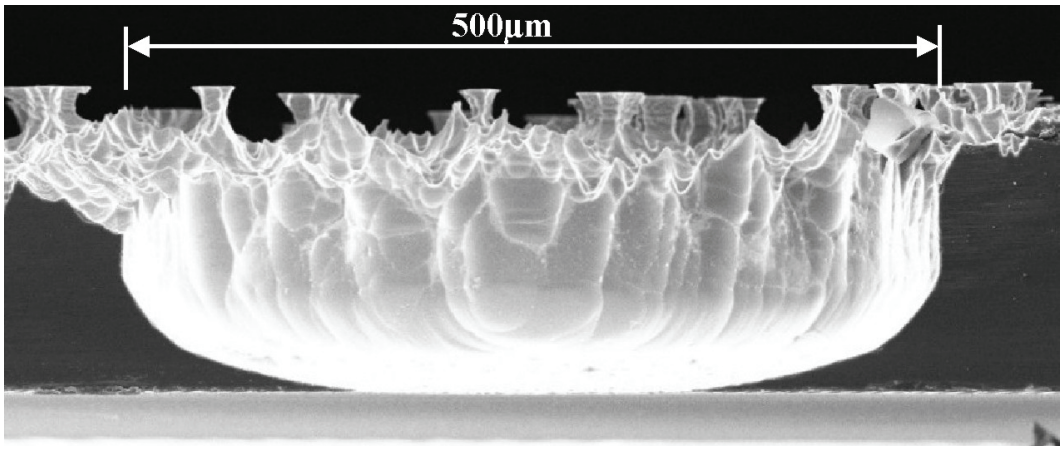

Figure 3.21. An SEM micrograph of a 500μm diameter hole etched with a cryogenic process. The partially closed, rounded bottom indicated that additional etching was required to create a more consistent sidewall profile.

Etch rates and selectivity were additional technical issues experienced during TSV fabrication. Etching was performed until the TSV holes were opened or the oxide mask was completely removed, and the effective etch rates were monitored. The successful through wafer etch shown in Figure 3.21 used an O_2 flow of 16sccm. Reducing this flow to 15sccm, which ostensibly would increase the amount of undercut [119], did not allow successful through wafer etching. In the reduced O_2 situation, the SiO_2 mask layer was completely removed, allowing the

entire wafer to be thinned, rather than etching deeper holes. It was later determined that this reduced Si:SiO_2 selectivity was indicative of cryo-etch equipment failure.

Additional attempts to etch through-holes using this process were not completely successful for several reasons. Technical issues with the liquid nitrogen supply for the cryogenic etch process led to prolonged equipment downtime. A wafer being broken during the unloading process of the cryo-etch also led to equipment unavailability, as the etch chamber had to be completely depressurized and opened to remove the wafer shards. Another issue was noted with the Oxford ICPRIE that allowed the via holes to expand in size. Inspection of these holes indicated that the etch was isotropic, despite using parameters which had previously produced anisotropic results. An image of an isotropically etched hole is shown in Figure 3.22. It is possible that this was caused by a lack of conductivity between the cooling chuck and the wafer, leading to excess temperatures and isotropic (chemically reactive) etching. The inconsistent results from this process required that the TSV testing be postponed until the cryo-etch equipment was recalibrated and re-commissioned. A chrome mask set was also produced during this time period to solve the issues with surface roughness.

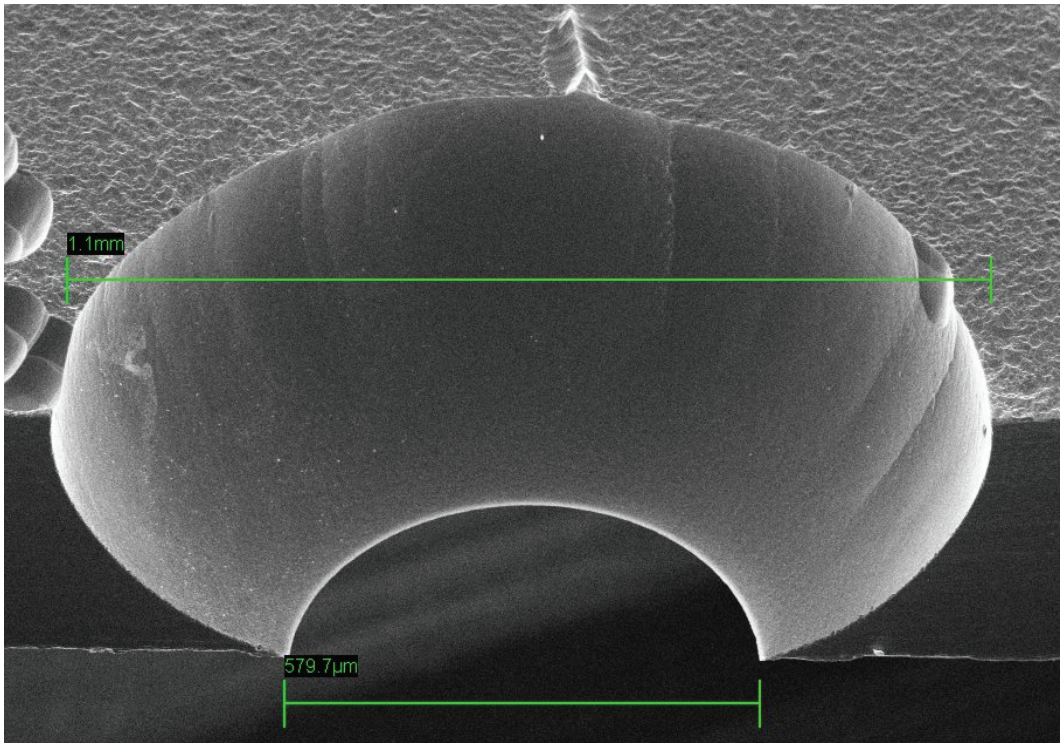

Figure 3.22. An SEM micrograph of a 500µm diameter hole etched with a cryogenic process. The isotropic profile was likely due to inadequate wafer cooling, allowing the hole diameter to expand from 500µm to 1.1mm.

3.7.2 - Through-Silicon Via Process Results

Four substrates were processed using the method described above. Of these four, two were originally 300µm thick and two were 500µm thick. Through-holes were not achieved on two of these four substrates: one of the 300µm substrates had a selectivity problem and was thinned to less than 200µm without etching through-holes, and a 500µm substrate was broken in the etch chamber. The surviving two wafers were diced to allow optical examination of the hole profiles. The 500µm wafer had etched isotropically, so further electrical characterization was not attempted. The remaining 300µm wafer was examined for TSV electrical conductivity. This determined that all but the smallest two TSV sizes (100µm and 200µm) in both the square and round profiles were conductive.

Two potential causes of the lack of conductivity for the 100µm and 200µm TSVs were inadequate sidewall coverage during sputtering or inadequate

etching depth. Due to concerns with sputtering mentioned in Section 3.4.6, it was possible that the sidewalls of the holes may not have been covered with metal completely due to their roughness or undercut angle. It was also possible that the sputtering could have closed over the hole openings, thus preventing further coating of the inner surfaces. Solutions to these problems included increasing the undercut angle during the cryo-etch to allow improved sputtering coverage, and by using collimated sputtering approaches to avoid hole closure. Inadequate etch depth issues could potentially be solved by increasing etch times. Scanning electron microscopy (SEM) was performed before and after a long aluminum etch to determine if the hole profiles were altered by the metallization.

Microscopy images taken with the SEM of the TSV holes revealed little change before and after the aluminum etch. Figure 3.23 shows three views of a 200µm hole after etching. This indicated that the lack of conductivity was caused by inadequate etch depth, and was not due to TSV holes being closed over during sputtering. For production devices, the etch rate for the TSV holes was to be carefully controlled to ensure that they were not under-etched. The 300µm and 500µm substrates were diced and measured using the SEM to estimate the achieved etching rates. The lateral hole growth was also measured to determine the level of anisotropy achieved with the cryo-etch. The etch rates are tabulated for both substrates in Table 3.2 and Table 3.3.

.

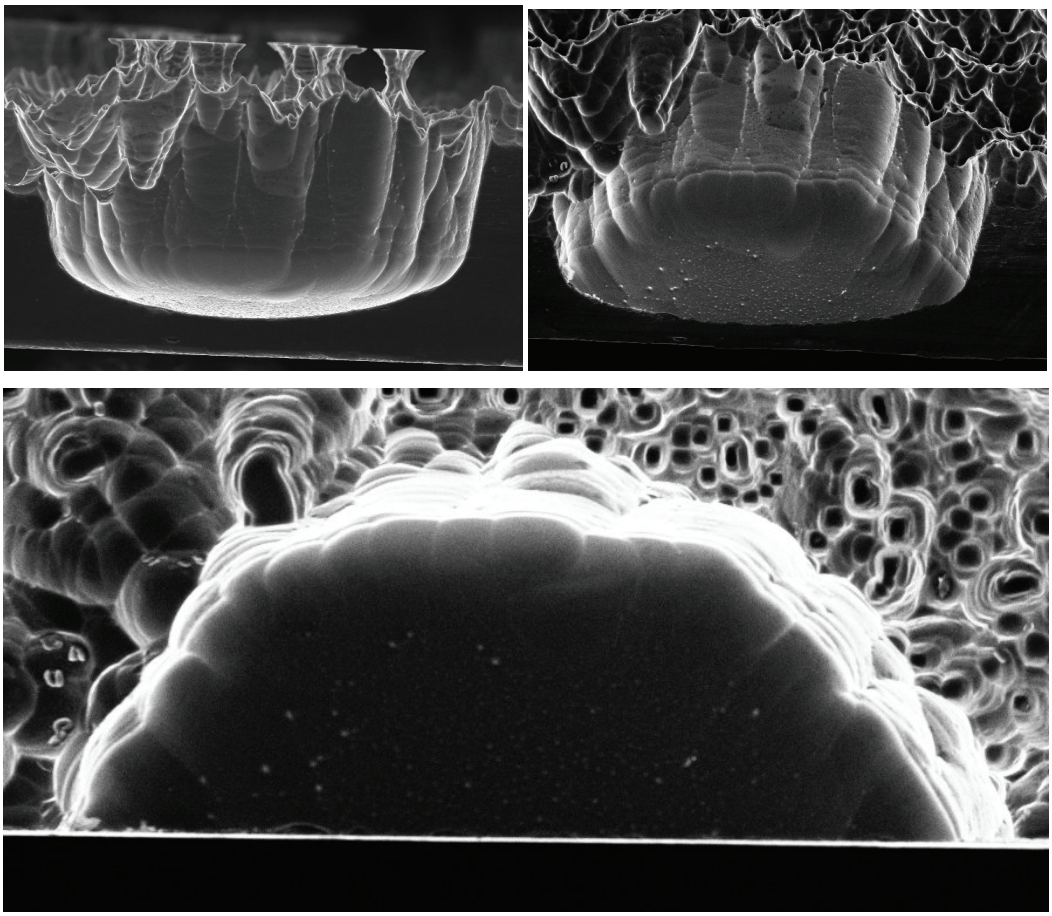

Figure 3.23. Three SEM micrographs showing a 200µm diameter hole etched into a silicon substrate.

Table 3.2. Apparent etch rates observed for the holes produced in the 300µm substrate during cryo-etch. This etch was performed with 16sccm of O_2 for 100min, and the oxide mask was intact after etching.

Mask Hole Width	**Actual Hole Width**	**Hole Depth**	**Final AR**	**Apparent Etch Rate**
1000µm	1390µm	300µm	0.21	3.0µm/min +
500µm	775µm	300µm	0.39	3.0µm/min
200µm	420µm	240µm	0.57	2.4µm/min
100µm	310µm	220µm	0.71	2.2µm/min

Table 3.3. Apparent etch rates observed for the holes produced in the 500μm substrate during cryo-etch. This etch was performed with 17sccm of O_2 for 200min, and the oxide mask was removed after etching, thinning the wafer to approximately 405μm.

Mask Hole Width	Actual Hole Width	Hole Depth	Final AR	Apparent Etch Rate
1000μm	1800μm	405μm	0.23	1.8μm/min +
500μm	1100μm	405μm	0.28	1.8μm/min
200μm	630μm	290μm	0.46	1.3μm/min
100μm	484μm	233μm	0.48	1.0μm/min

The etch rates in silicon are in the range of 1-3μm/min. This was substantially below the 4-5μm/min estimates provided in the system documentation, and was likely due to both ARDE concerns regarding the deep etch performed, and the high proportion of exposed silicon on the substrates used. Ongoing issues with the cryo-etch necessitated using a process flow which adapted the etch rate to the specific mask used and the condition of the etch equipment on any given day. The high variability of this process meant that the TSV holes should be produced as early in the microfabrication as possible, to account for the high risk of substrate destruction involved. Etch rates should also be confirmed with optical inspection to ensure that appropriate hole profiles are produced.

Through-silicon vias were produced using the procedure mentioned in Section 3.4 as part of the piezoresistive sensor microfabrication. The chrome photomasks produced for this microfabrication eliminated the surface roughness issues experienced when using the transparency masks. During the etching, the holes were optically inspected with a light microscope to determine if they had etched through and produced a tapered profile for the TSVs. These preliminary observations (and lack of other problems with the cryo-etch protocol) warranted the remainder of the fabrication to proceed. Following the remainder of the fabrication, a wafer was diced to allow TSV inspection with the SEM. An SEM micrograph of a 200μm TSV hole produced using this cryo-etch process on a 500μm thick substrate is shown in Figure 3.24. This imaging showed that the cryogenic etch produced some undesired results. The TSV hole surfaces were

rough, having surface pitting with an approximate diameter of 3µm. The holes also displayed rounding directly under the etch mask instead of a smooth profile. According to guidelines set out by de Boer *et al*., this rounding could imply inadequate O_2 flow or excessive charge coupled plasma power [119]. The undercut produced by this process had an average sidewall angle of 83º, excluding a widened region on the bottom of the wafer adjacent to the oxide layer.

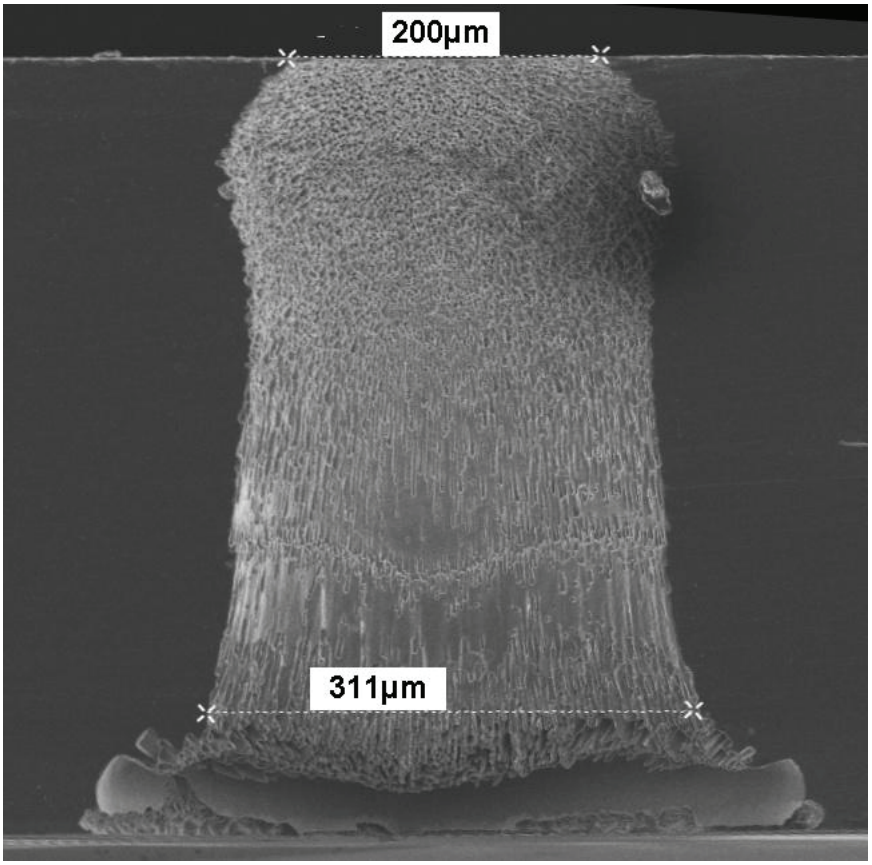

Figure 3.24. An SEM micrograph of a 200µm diameter circular TSV hole etched into a 500µm thick silicon substrate.

A four-wire resistance measurement was made on a sputtered TSV hole with a 2.5:1 aspect ratio. The via tested was similar in dimensions to the one shown in Figure 3.24, and was also made on a 500µm substrate. The measured resistance was approximately 20kΩ, indicating poor conduction due to limited and discontinuous aluminum sputtering on the hole sidewalls. Fortunately, the

conductivity of these TSVs may be improved by simply filling the holes with a conductive material, such as isotropic conductive epoxy. This technique has been successfully applied and was able to reduce the four-wire resistance of this TSV to approximately 1Ω. This technique and its application to packaging will be discussed further in Section 5.5.

3.8 - Conclusions

The development cycle for the sensor pads has been described. The phases of this cycle have included analytical analysis, FEA, microfabrication, and several types of characterization. The constraints placed on the sensor pads by the scoliosis surgery application have shaped their final design through an iterative process. The sensor pad developed consists of four, four-terminal piezoresistive sensors on a deformable single crystal silicon membrane, and is capable of detecting three-axis loads applied. This development cycle has included the study of piezoresistance, orthotropic material properties, numerical methods, and microfabrication techniques, and has achieved a prototype device that is ready for experimental characterization of its three-axis sensitivity.

Chapter 4: Analysis of Sensor Pad Sensitivity[1]

Parametric analysis of the sensor pads has been performed. This analysis involved varying the geometric and material properties of the sensor pads and evaluating the changes to their shear and normal sensitivities. Calibration techniques, both experimental and numerical, are discussed. Specific sensitivity trends resulting from varying these parameters are detailed, and different definitions of sensitivity are described. Of the parameters varied, increasing the mesa height was shown to cause the greatest increase in shear sensitivity, and decreasing the membrane thickness was shown to cause the greatest increase in normal sensitivity.

4.1 - Introduction

The six-axis sensor array proposed for use in scoliosis correction surgery achieves its axes of detection by operating a set of four, three-axis sensors in parallel. Each of the three-axis sensors, referred to as a sensor pad, is capable of detecting normal and shear forces applied at its surface. Appropriate characterization of the sensitivity in these three detection directions on each sensor pad is a necessary step in device calibration. In addition, it may be necessary to adjust the sensitivities of the sensor pads to compensate for performance variation created by microfabrication, packaging, or device deployment.

The sensor pads were required to be sensitive to three-axis loads in order to operate properly in scoliosis correction surgery, as well as in other tactile or interfacial applications. A schematic showing a sensor pad and the relevant axes of detection is shown in Figure 4.1. The ratio between the shear (X- and Y-axis) and normal (Z-axis) sensitivity of the sensor pads was another performance objective evaluated during characterization. Ensuring that the sensitivity on all three-axes was comparable was an important factor in the development of the sensor pads, so parameters were varied with the specific objective of achieving equivalent sensitivities in the shear and normal directions.

[1] Some of the material in this chapter has been previously published by Benfield *et al.* [41].

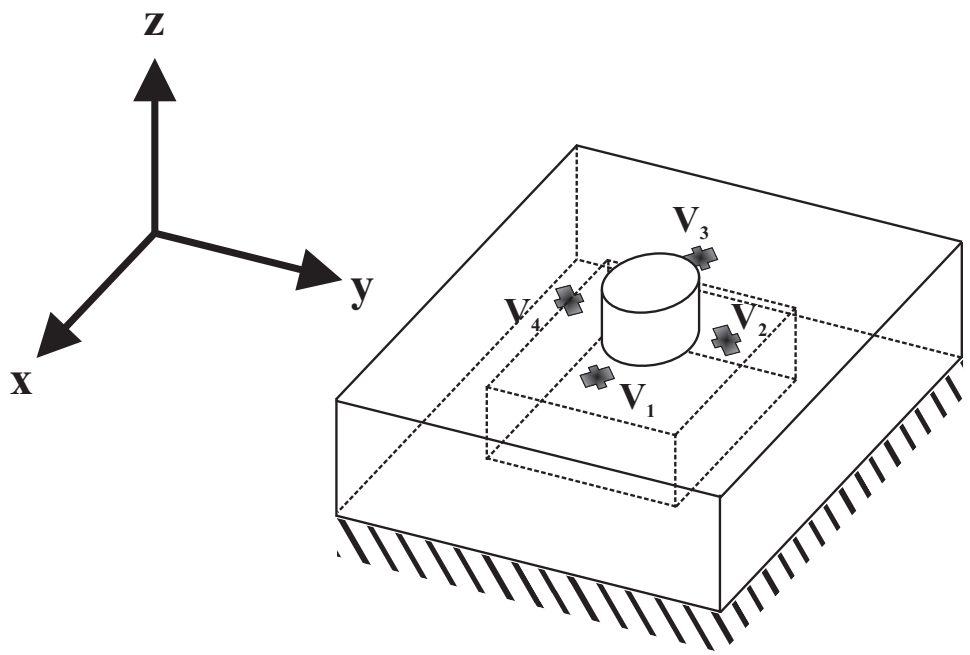

Figure 4.1. A schematic of a sensor pad with the coordinate system labelled. The X and Y directions represent shear loads which may be denoted with an "S", and the Z direction represents normal loading which may be denoted with an "N".

A process for characterizing the manufactured sensing pads for their shear and normal sensitivities has been developed and performed [41]. This characterization was achieved using numerical and experimental methods, and allowed individual parameters of the sensor pads to be analyzed separately for their effects on sensitivity. The experimental characterization method for the sensor pads did not require a complete packaging solution, which allowed performance verification at an earlier stage in the development cycle. Experimental characterization was complimented by numerical techniques, which allowed parametric variation with higher precision. These characterization methods have allowed for accurate determination of shear and normal sensitivity trends. The main sensor pad parameters varied were the size and location of the force application site, mesa height, membrane thickness, piezoresistive doping levels, and position of the piezoresistors on the membrane.

4.2 - Preliminary Evaluation of Shear Sensitivity

Several devices have been noted in the literature which are capable of detecting applied shear and normal loading, as discussed in Section 2.8. These devices are used for the measurement of interfacial forces, tactile detection, force feedback, and surgical applications. The overall designs of these devices vary greatly, with some devices achieving higher sensitivities in the normal direction [42, 49, 97, 98, 132], and others achieving higher sensitivities in the shear directions [43-45, 129, 130]. The objective for this parametric analysis was to achieve approximately equal sensitivities in all three directions, while still maintaining a durable sensor design utilizing a piezoresistor on membrane detection scheme.

4.2.1 - Numerical Analysis

Numerical analysis of the sensor pad design was initially performed as part of the FEA design phase for the complete device, as described in Section 3.3. Upon production of prototypes, further FEA simulation was performed to establish sensitivity baselines in the shear and normal directions that could directly be compared to experimental results. The FEA models were built using parameters, elements, and boundary conditions similar to those shown in Figure 3.4. These models consisted of a single-crystal silicon substrate with a thinned section used to define a square membrane. The base of this substrate was fully mechanically constrained. Four, four-terminal piezoresistive sensors were placed near the middle of the membrane edges to allow detection of stresses induced during membrane deflection. A mesa was optionally placed near the middle of the membrane surface to allow loads to be applied with a vertical offset. Figure 4.2 shows an image of a sensor pad modelled with FEA.

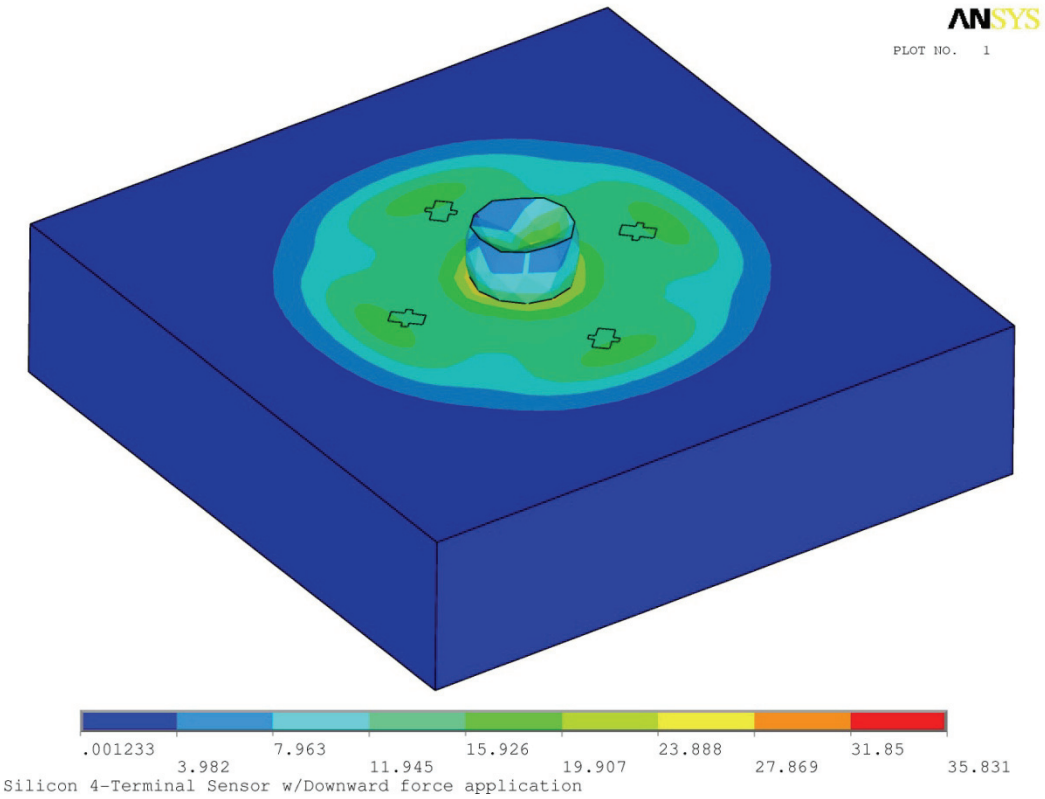

Figure 4.2. The sensor pad modelled with FEA. A downward normal load is applied to a mesa, and the von Mises stress distribution is shown.

The four piezoresistors on the membrane provided the necessary outputs to resolve the three-axis loads. Essentially, the applied normal and shear forces create a stress-strain distribution within the membrane that is unique to the magnitude and direction of these forces. The piezoresistors detect this stress-strain distribution at four distinct locations, which were specifically chosen to coincide with the largest stresses induced in the membrane, as discussed in Section 2.6.1. Each of the piezoresistors is a four-terminal gauge designed to produce voltage outputs that are both highly localized and temperature compensating. By examining the four voltage outputs from the piezoresistors during load application, it has been shown to be possible to use these outputs to recreate the original loading applied.

The piezoresistive elements used in the multiphysics simulations performed allowed the input voltage and ground conditions to be applied as

constraints alongside the structural loads. This enabled the FEA models to produce differential voltage outputs (collected from appropriate terminals on the four-terminal gauges) that could be directly compared with those produced during experimental characterization. The FEA allowed normal and shear sensitivities to be examined as various parameters of the membrane sensor pad design were altered. The varied parameters included geometric parameters, such as membrane thickness, membrane edge length, mesa height, and load application point location, as well as material property parameters, such as piezoresistive coefficients and bulk electrical resistivity. Stress levels could also be monitored during the FEA, thereby determining the overall strength of the simulated devices. This numerical characterization process was useful as it allowed changes to design parameters to be examined for their effect on device sensitivity more quickly than in a manufacturing run, and it also allowed specific issues with sensitivity experienced during experimental characterization (e.g. load misalignment) to be examined very precisely.

Initial characterization using FEA was performed on a simulated sensor pad. This sensor pad was defined as a 2000µm × 2000µm × 500µm block of (1 0 0) single crystal silicon with a square prism removed from the bottom surface to create a 1000µm × 1000µm × 65µm membrane centrally located and aligned to the top surface. The four-terminal gauges were defined to be 100µm × 50µm rectangular piezoresistive regions with 20µm × 20µm output terminals. The four-terminal gauges were located on the top surface of the membrane, and each was oriented to be central to a membrane edge. For maximum sensitivity, the four-terminal gauges were oriented at 45º to the membrane edges with their long axes aligned to the [1 0 0] direction. To position the sensors entirely on the membrane and not on the bulk silicon block, the four-terminal gauges were each spaced 100µm toward the membrane center. This model is defined schematically in Figure 3.3, and is similar to devices shown in Figure 4.1 and Figure 4.2. A mesa was not implemented in this initial characterization model.

The loads and boundary conditions applied to the initial characterization model consisted of constant electrical voltage inputs, full mechanical constraints

on the base, and variable force loads applied to the membrane or mesa. Displacement constraints were first placed on the lower surface of the bulk silicon block. A variable force load was then applied to the top surface of membrane, defined to be distributed over a 40µm × 40µm region in its centre. Nodes were selected at the ends of the long axes of the piezoresistors to apply three volts of input electrical potential. Similarly, nodes were selected at the ends of the two output terminals that allowed differential output voltages to be collected from each four-terminal gauge. Figure 4.3 shows a chart comparing the voltage outputs from the four piezoresistors used in this model as the normal force applied to the centre of the membrane was varied.

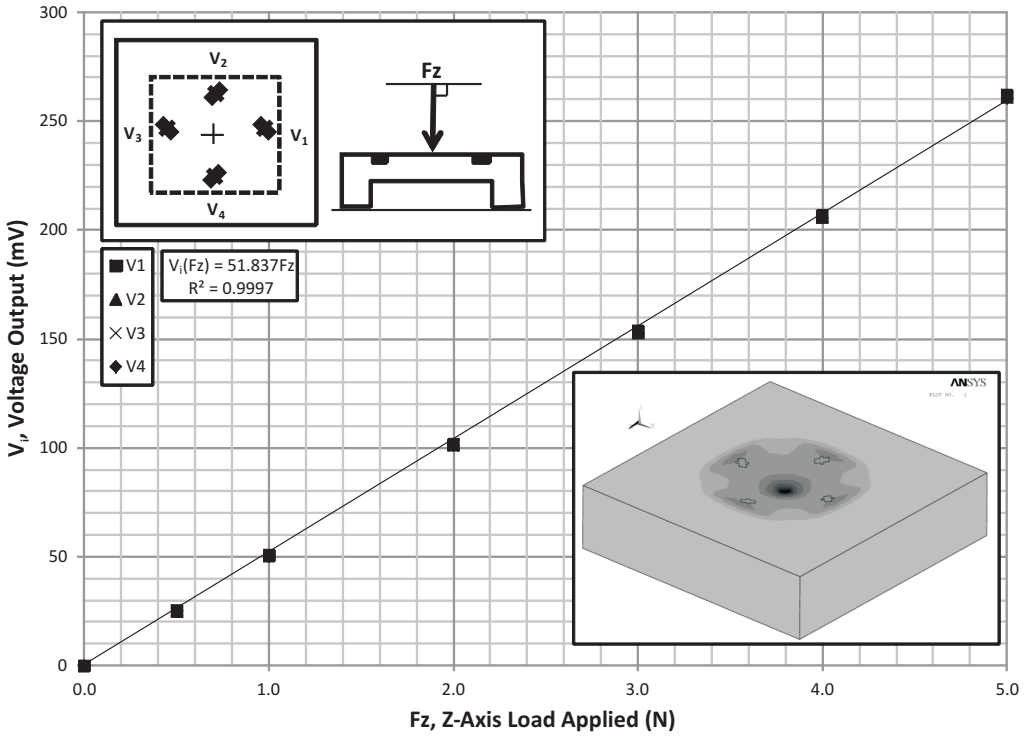

Figure 4.3. Simulated sensor pad response to a centralized downward load. Responses from gauges V_1-V_4 are coincident on this graph.

The output response for all four piezoresistors was shown to be highly linear and nearly identical for the normal loading scenario. The sensitivity calculated from this sensor response was found to be 51.8mV/N, which was a classified as a high

value due to the relatively low 65µm membrane thickness. The four piezoresistors, schematically defined in Figure 4.1, had their outputs numbered V_1-V_4 and were plotted on the same chart. This method of plotting the piezoresistor outputs allowed trends between the four resistors to be identified as the loading conditions were altered. Figure 4.4 shows the output voltages for four piezoresistors defined in an FEA model as above, except that the loads have been applied at an angle of 20º from vertical with the shear component pointing toward the V_2 piezoresistor.

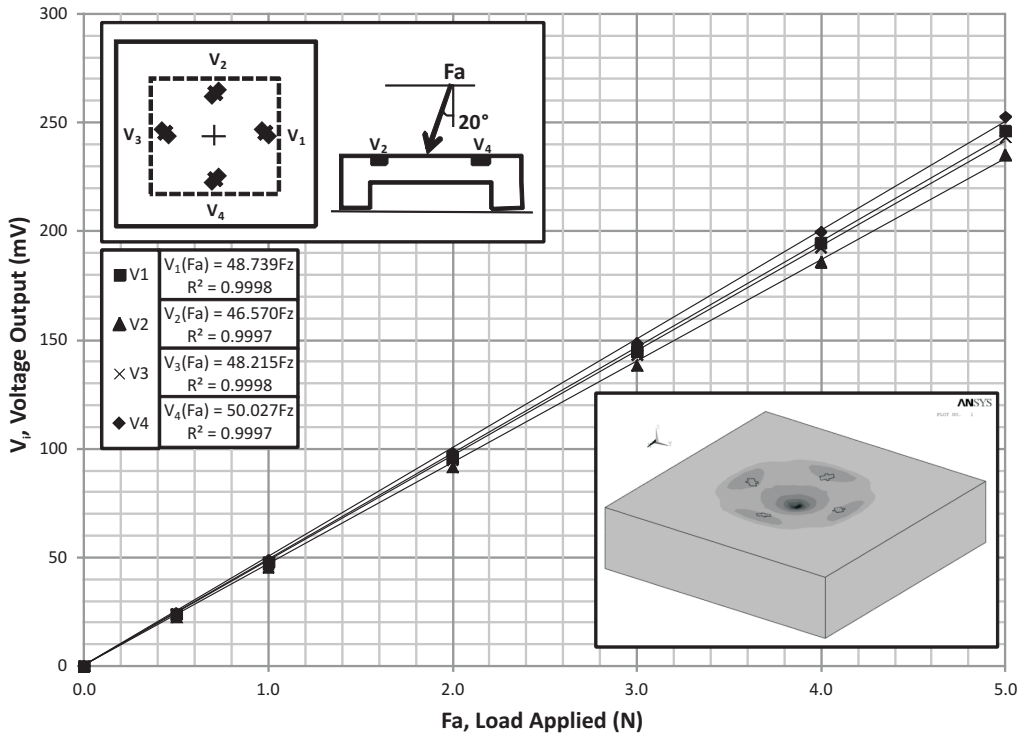

Figure 4.4. Simulated sensor pad response to a centralized load angled at 20º from vertical. The shear force component was directed toward the V_2 piezoresistor. Responses from gauges V_1 and V_3 are coincident on this graph.

The output responses in Figure 4.4 are shown to be highly linear. Outputs from the V_1 and V_3 piezoresistors were nearly coincident, with slightly lowered sensitivities (48.7mV/N and 48.2mV/N, respectively) when compared to the normal loading scenario defined above in Figure 4.3. The output sensitivity from

the V_2 piezoresistor was 46.6mV/N, lower than the V_1 and V_3 values. The V_4 piezoresistor had a higher sensitivity at 50.0mV/N. This differentiated response set indicates that the shear component of loading is technically detectable in the simulated voltage outputs. The difference between the responses of the V_1 and V_3 piezoresistors and the V_2 and V_4 piezoresistors may be used to define the load components in the X and Y directions, respectively. Normal loading, which represents a larger portion of the load applied in the 20º angled scenario shown in Figure 4.4, may then be defined based on the average of all four voltage responses.

4.2.2 - Shear Sensitivity Ratio

In a simplified form, the relationship between the shear and normal responses produced during load application may be defined as a ratio between shear and normal load responses. These shear sensitivity ratio parameters, defined as R_X and R_Y in Equation (4.1), indicate the proportion that a voltage difference between two opposing piezoresistors represents in terms of the average voltage output of all four piezoresistors. The orientation of the four piezoresistors on the membrane was used to define these equations in terms of their effective X- and Y-axis components.

$$R_X = \frac{4(V_3 - V_1)}{V_1 + V_2 + V_3 + V_4}, R_Y = \frac{4(V_4 - V_2)}{V_1 + V_2 + V_3 + V_4} \tag{4.1}$$

The shear sensitivity ratios calculated for the load outputs were then compared to the physical components of the applied load inputs. Average values for R_X and R_Y calculated for the numerical 20º load application scenario above are -1.1% and 7.1%, respectively. When computed using the tangent of the load application angles, the actual ratio between shear to normal forces applied is 0.0% and 36.4% for the X- and Y-axis, respectively. The fact that this Y-axis shear to normal force ratio is substantially higher than the calculated R_Y parameter reflects the fact that this device is more sensitive in the normal than the shear directions. The calculated R_X value of -1.1% is indicative of the numerical error in this experiment, as a shear force was not applied in the X direction.

Numerical analysis was also used to evaluate the detected shear sensitivity ratios as model parameters were varied. The goal of this analysis was primarily to determine how to increase the shear sensitivity ratios so they would be approximately equivalent to the actual applied shear to normal force ratio; i.e., to achieve equivalent sensitivity in the normal and shear directions. Increasing the shear sensitivity ratios would allow larger outputs corresponding with applied shear loads to be produced with less influence from numerical or experimental sources of error. Equivalent sensitivities in the normal and shear directions were also important for effective data collection when the outputs from four three-axis devices are combined in the scoliosis sensor application.

4.2.3 - Load Application Angle

The FEA results depicted in Figure 4.4 show numerically calculated outputs from the four piezoresistive four-terminal gauges as varying loads are applied to the membrane surface at a 20º angle. Since the angle of load application effectively controls the ratio of shear to normal forces applied, varying this angle creates calibration data points in the shear and normal directions with constant total force application. Figure 4.5 shows simulated output responses for the four piezoresistors as the load application angle was varied between 0º and 60º. The shear sensitivity ratio in the Y direction, R_Y, has also been plotted on Figure 4.5. Average R_X, or shear sensitivity ratio for the X direction, was less than 1% and has been omitted from the figure.

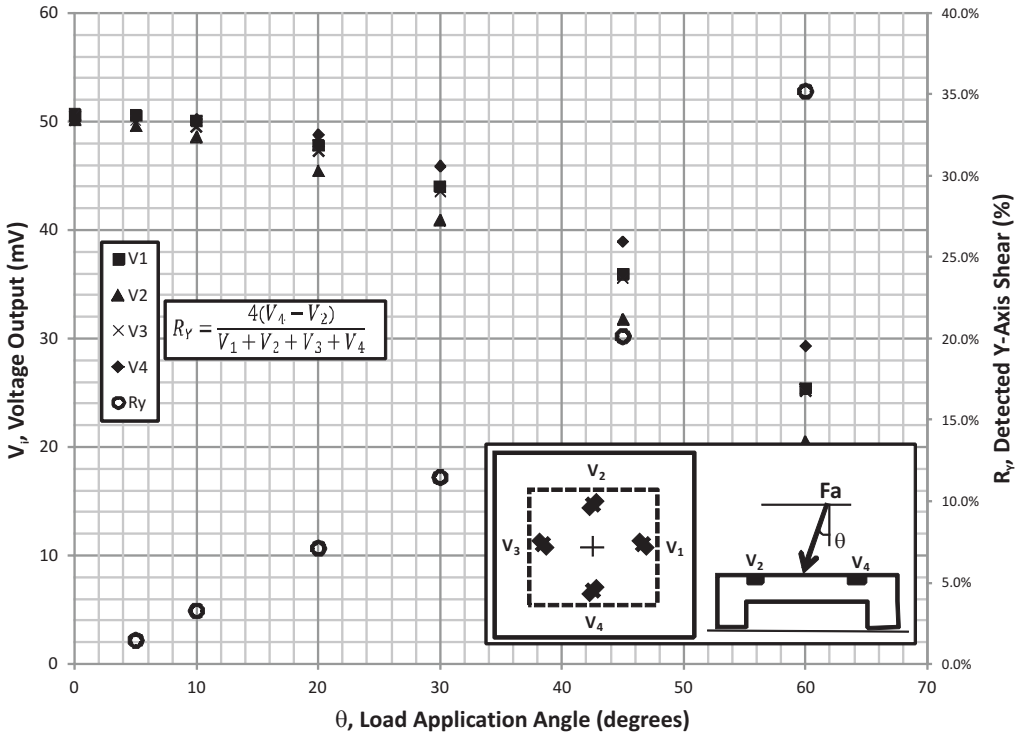

Figure 4.5. Simulated sensor pad response and calculated Y direction shear sensitivity ratio as load angle is altered. Responses from gauges V_1 and V_3 are coincident on this graph.

The 45º angle load was significant for this experiment as it represented equivalent shear and normal load application. This angle produced a R_Y value of approximately 20%. When the other R_Y data points were divided by the tangent of the load angle, it was found that an average value of 19.2% was obtained with a standard deviation of 1.4%. This consistency in the normalized shear sensitivity ratio indicates that this numerical model has shear and normal sensitivities that are stable over a range of load application angles. The value of 19.2% for the shear sensitivity ratio over a range of angles and loads confirms a normal to shear sensitivity of approximately 5:1 for the device modelled with a 65µm thick membrane.

4.2.4 - Load Application Area Position and Size

The positioning and size of the applied load on the membrane surface was also examined for its effect on the shear and normal sensitivity of the sensor pads. These alignment parameters were important to evaluate as they were found to be significant sources of experimental error. Output results for a numerical model were first evaluated as the force application region (40μm × 40μm) was moved toward the V_2 piezoresistor. These results have been plotted in Figure 4.6. This analysis showed that the output from the V_2 piezoresistor increased as the load application region was moved toward it on the membrane surface. Similarly, the outputs from the other three piezoresistors tended to decrease as the load application region was moved away from the centre. The results from this FEA also showed that once misalignment increased to 200μm and 250μm, the output from the V_2 piezoresistor began to decrease again. Factors contributing to this decrease in output include the decrease in overall membrane deflection, as well as localized stress interference effects due the load application region encroaching on the piezoresistor.

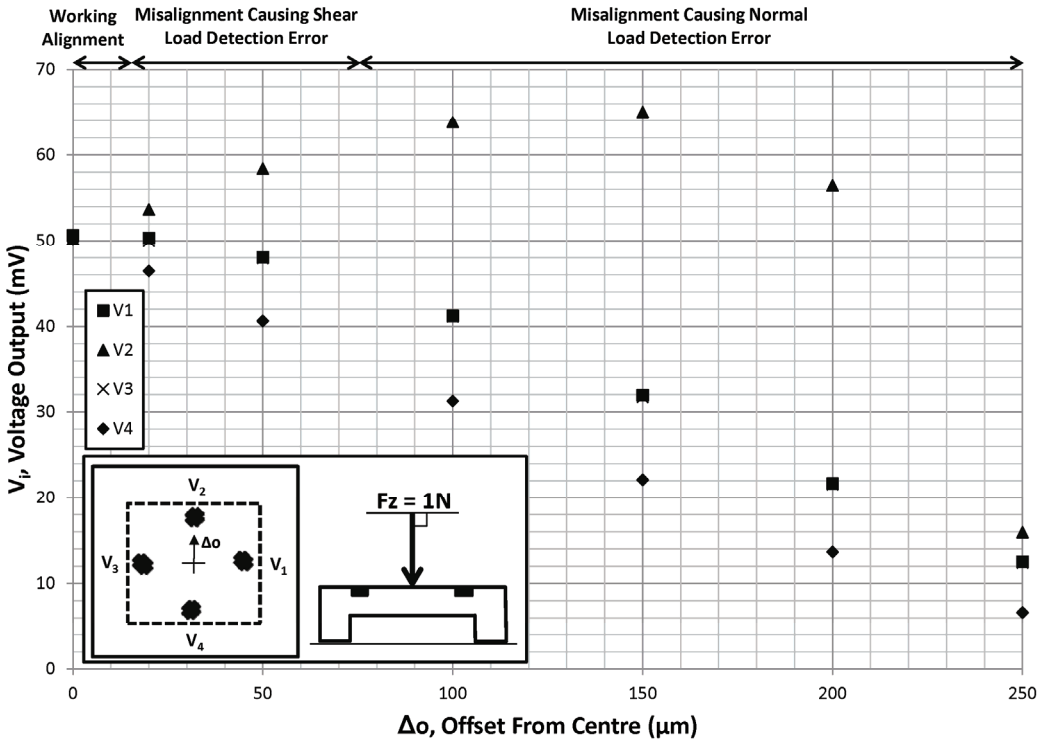

Figure 4.6. Simulated sensor pad response due to moving the load application region closer to the V_2 gauge. Responses from gauges V_1 and V_3 are coincident on this graph.

The data collected as the load application region was moved toward the V_2 piezoresistor indicated (through linear interpolation) that a shear load could be inaccurately detected after approximately 15µm of misalignment. This manifested as a detected shear sensitivity ratio greater than 10% without any actual shear loading applied. As this misalignment was increased beyond 75µm, greater than 10% distortions in detected normal load were observed. Approximately five times greater misalignment was required to achieve the same amount of error in the detected normal load as in the detected shear load. This error ratio is again illustrative of the sensitivity differential between the normal and shear directions for the device examined. It should also be noted that due to symmetry of the four piezoresistors on the square membrane, similar results were achieved if the load was moved toward any of the other piezoresistors.

Another simulation was performed to further evaluate load application region alignment for the simulated device. This was a similar analysis, except that the force application region was moved closer to the corner between the V_1 and V_2 piezoresistors. The results of this analysis have been plotted in Figure 4.7. This analysis showed that the outputs from the V_1 and V_2 piezoresistors increased as the load application region was moved up to 100µm away from the membrane centre, and then decreased as it was moved further away. As before, these results were due to a combination of local stresses near the load application region and induced stresses due to membrane deflection. The V_3 and V_4 piezoresistor outputs were found to decrease linearly as the load application region was moved away from the membrane centre. For this analysis, 30µm of misalignment caused a falsely detected shear sensitivity ratio of 10% and 125µm of misalignment was required to cause a 10% discrepancy in detected normal load.

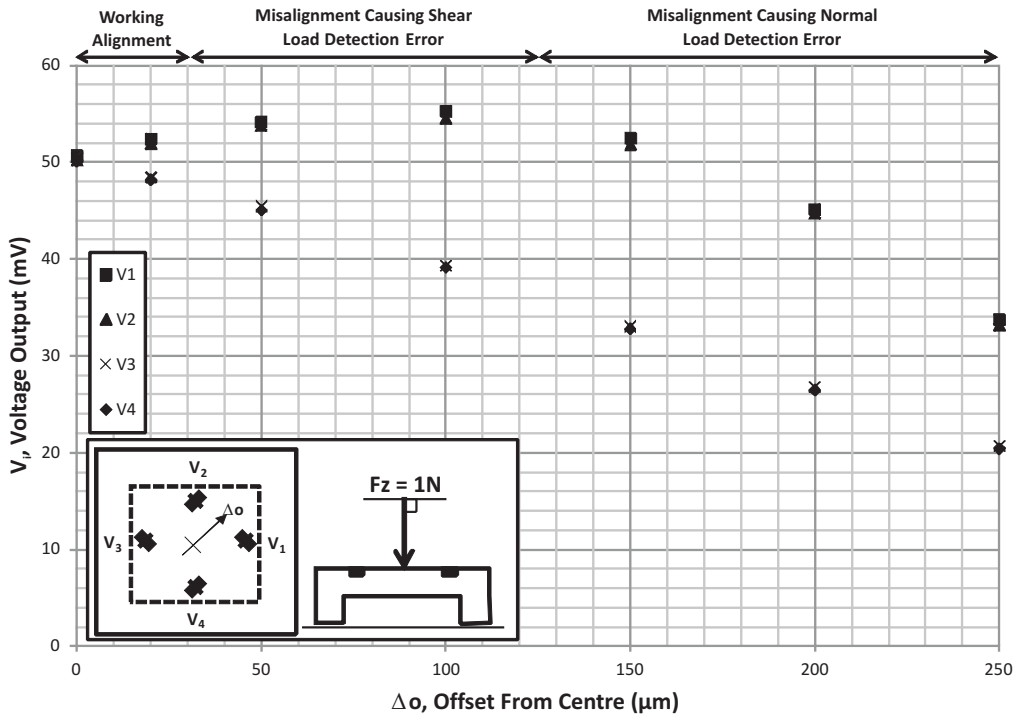

Figure 4.7. Simulated sensor pad response due to moving the load application region toward the corner between the V_1 and V_2 gauges.

The size of the load application region was also examined in terms of its effect on the voltage outputs from the piezoresistors. This parameter was representative of changes to the load application tool that could occur experimentally (such as blunting). Figure 4.8 shows the outputs from the four piezoresistors as the load application region was varied in size. This region was square shaped with edge lengths that varied from 40µm to 500µm. The applied load was 5N applied at 20º, with the (smaller) shear component pointing toward the V_2 piezoresistor. The result of changing the load application region's size was shown to be less significant than its location in terms of creating errors in the detected shear and normal load. Changes that were created in the piezoresistor responses are illustrative of the difference between applying point or distributed loads to a membrane surface. Provided the load application tool chosen is consistent, load application region size should not negatively impact shear or normal force detection.

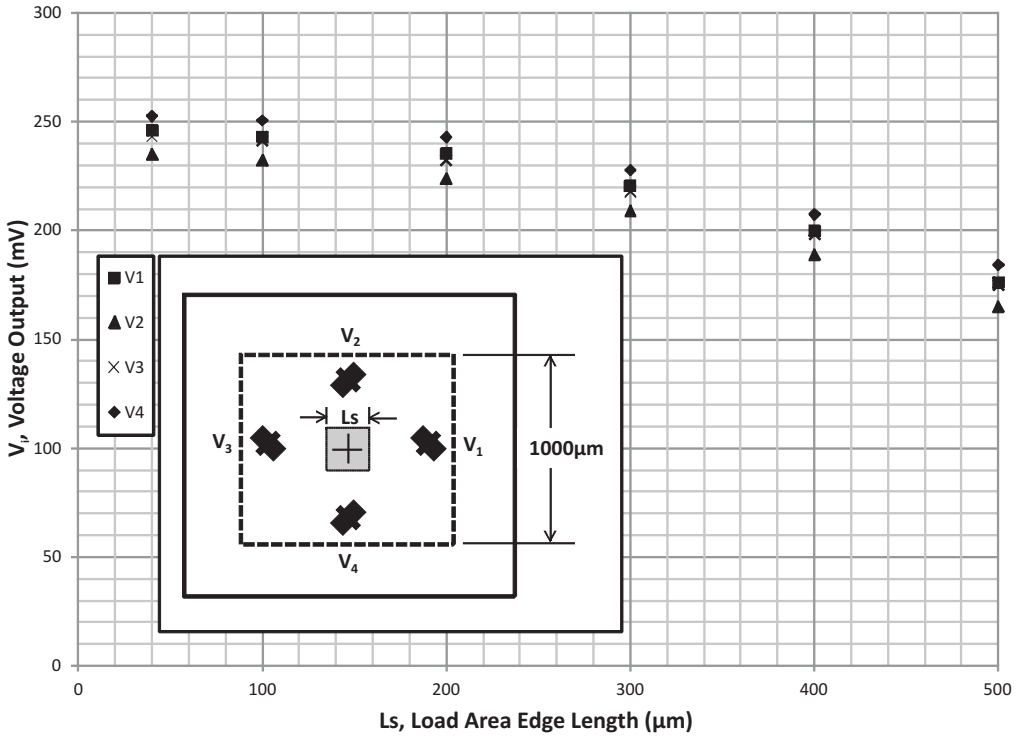

Figure 4.8. Simulated sensor pad response as the load is distributed over a larger area. A 5N load was applied at an angle of 20º, pointing toward the V_2 piezoresistor. Responses from gauges V_1 and V_3 are coincident on this graph.

The above investigations indicated that lower sensitivity in the shear direction, as compared to the normal direction, might cause shear load detection problems for the sensor design. It was also shown that these detection problems would be amplified if the load application region was not centered on the membrane surface. In order to resolve the sensitivity and the alignment problems, the results of adding a mesa to the membrane surface were examined. The mesa was found to enhance the shear sensitivity by imparting a moment load to the membrane surface during shear force application. As this mesa would also raise the load application area above the surface of the membrane, it would also act to centre the applied loads. As a result, the loads may be applied to the top of a mesa with less precision than they would require if they were applied directly to the membrane surface.

4.2.5 - Mesa Implementation

The FEA model of the sensor pad was modified to have a cylindrical mesa with a 300μm diameter bonded to the centre of the membrane. A cylinder was used to avoid stress risers on the surface of the membrane created at the corners of the mesa. The mesa was specified to be constructed of an isotropic material that was softer than the single crystal silicon substrate (E = 50GPa, ν = 0.3), which was representative of epoxy or photoresist. Figure 4.2 shows an image of the FEA model with the mesa attached. Figure 4.9 shows simulated sensor pad outputs and the calculated shear sensitivity ratio as mesa height was varied. This experiment was performed with a 1N load applied at a 20º angle, with the shear component pointed toward the V_2 piezoresistor.

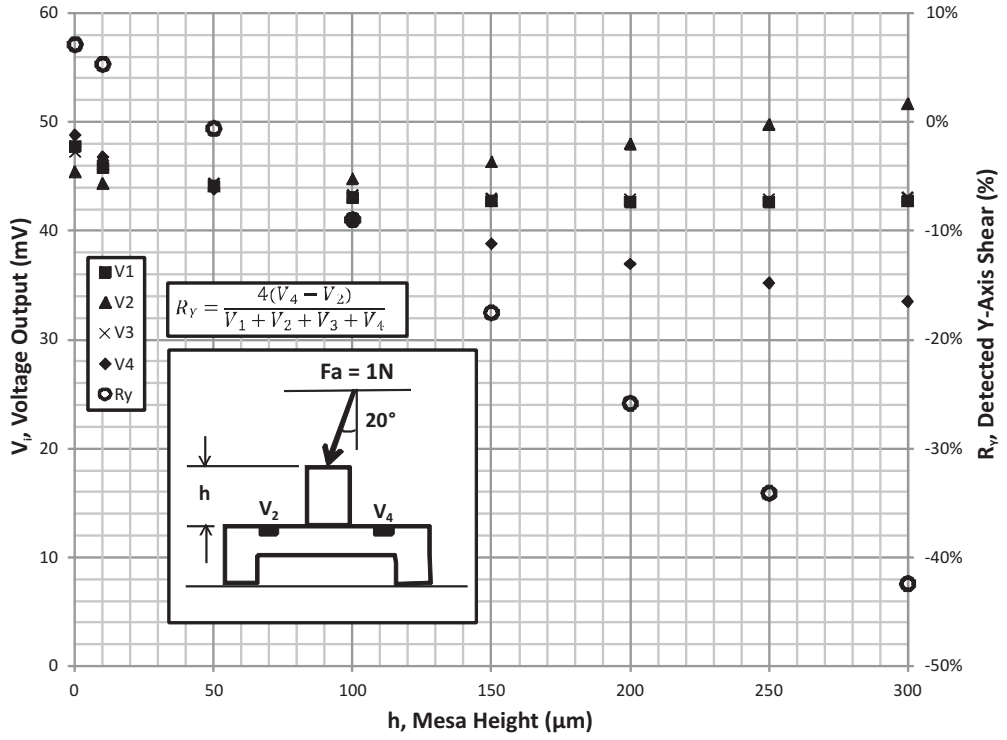

Figure 4.9. Simulated sensor pad response as mesa height was varied. A load of 1N at a 20º angle was applied to the top of a 300µm diameter mesa. Responses from gauges V_1 and V_3 are coincident on this graph.

This simulation showed that relatively constant results for detected normal loads were achieved as the mesa height was varied. This indicates that the normal sensitivity was not substantially affected by the addition of the mesa. Conversely, the shear sensitivity ratio (R_Y) decreased linearly as the mesa height was increased, to a minimum calculated value of -42.4% with a mesa height of 300µm. This value is significant for several reasons. First, the absolute value of the detected shear sensitivity ratio is actually higher than the ratio between shear and normal forces applied, indicating that the mesa has increased the shear sensitivity beyond the normal sensitivity of this device. Second, the sign of R_Y is negative, indicating that a minimum mesa height is required to have a beneficial net effect on shear sensitivity.

This simulation also showed that a mesa height of 50µm achieved a shear sensitivity ratio of nearly zero. Mesas shorter than 50µm had positive shear

sensitivity ratios, while mesas taller than 50µm had negative shear sensitivity ratios. This is due to the fact that shear loading applied to a mesa induces deflection in the membrane surface from both the applied shear and the bending moment created by the height of the mesa. With a mesa height of 50µm, these two influences on membrane deflection distribution cancel each other out. In order to achieve increased shear sensitivity with a mesa, this simulation indicates that a mesa height of at least 100µm is required. This is illustrated in Figure 4.9, as the absolute value of the detected shear sensitivity ratio is approximately equivalent for mesas of 0µm and 100µm in height. In order to achieve equivalent sensitivity in the normal and shear directions, a detected shear ratio of 36.4% is required. This can be achieved for the simulated device with a mesa height of approximately 260µm.

4.2.6 - Membrane Thickness

Silicon membrane thickness was also examined for its effect on shear and normal sensitivities for the numerical model. This parameter was relatively simple to control during microfabrication, and was explicitly relevant to sensitivity as a function of the membrane equations mentioned in Section 2.6. The FEA model was used to evaluate simulated sensor response and detected shear sensitivity ratio as the membrane thickness was varied. A load of 1N was applied to a mesa with a height of 200µm and a diameter of 300µm. Two simulations were performed using load angles of 20º and 45º. In both cases, the shear load components were pointing toward the V_4 piezoresistors. Figure 4.10 shows the result of the 20º simulation, and Figure 4.11 shows the result of the 45º simulation.

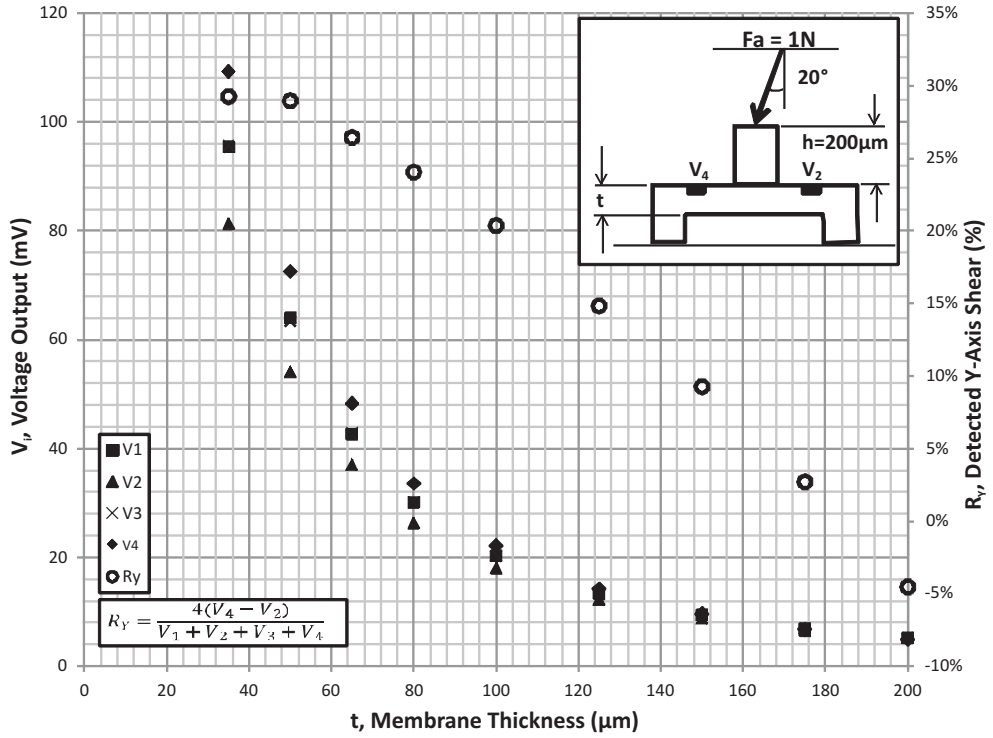

Figure 4.10. Simulated sensor pad response as membrane thickness was varied. A load of 1N at a 20º angle was applied to a 200µm × Ø300µm mesa. Responses from gauges V_1 and V_3 are coincident on this graph.

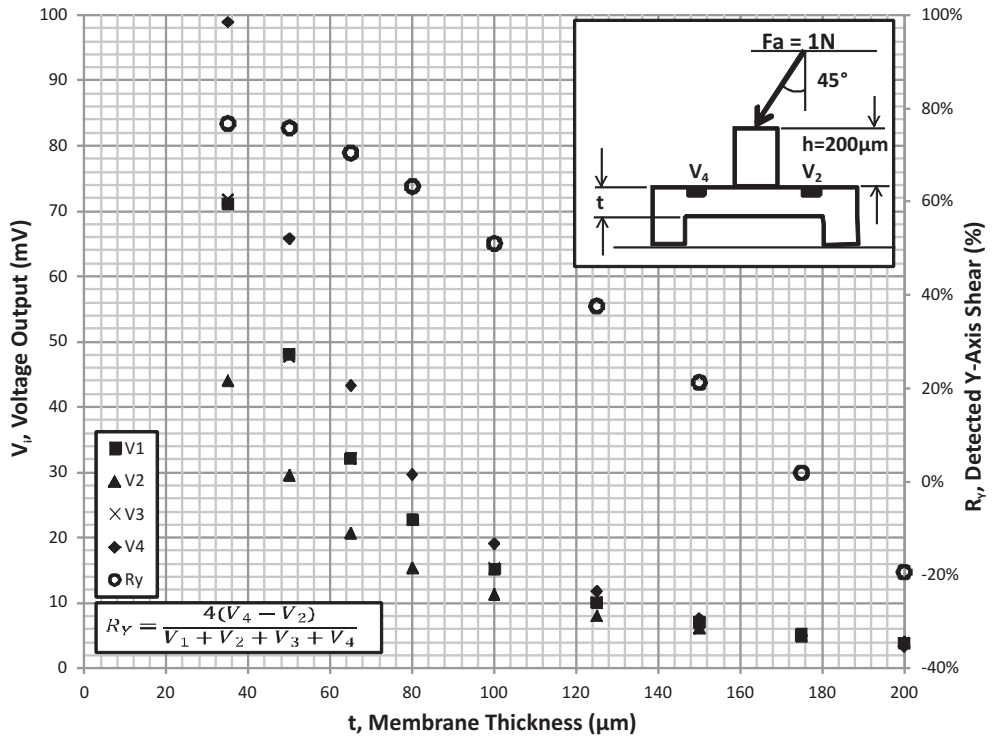

Figure 4.11. Simulated sensor pad response as membrane thickness was varied. A load of 1N at a 45º angle was applied to a 200µm × Ø300µm mesa. Responses from gauges V_1 and V_3 are coincident on this graph.

Both of the numerical simulations indicated that an increase in membrane thickness reduced the detected shear sensitivity ratio as well as the overall normal sensitivity. For the membranes examined that were less than 125µm thick, the shear sensitivity results from the 20º analysis were approximately 36% of those produced with 45º analysis. This result corresponds to the ratio between the two experiments for the shear force divided by normal force applied (tan(20°) / tan(45°) = 0.36). For membrane thicknesses greater than 125µm, this ratio was not maintained, indicating that the detected shear was low enough to be affected by small numerical errors in the FEA results. This analysis has shown that the thickness of the membrane should be reduced in order to increase both the shear and normal sensitivity of the sensor pad.

The manufacturing scheme presented in Section 3.4 allows for modification of the sensing pad sensitivity by changing the membrane thickness,

mesa height, and doping concentration. Using the numerical simulation presented above, it was determined that square membranes with 1000μm edge lengths and baseline (low doped) piezoresistive parameters would require a mesa height of 200μm and a membrane thickness of less than 150μm to achieve a detected shear sensitivity ratio of more than 10% at a 20° load application angle. Alternatively, a detected shear sensitivity ratio of 10% at a 20° load application angle is achieved using a mesa height of approximately 110μm when evaluating a membrane thickness of 65μm. This 10% value for R_Y was determined to represent an improvement over a device with no mesa attached (R_Y = 7.1% for 20º load application without a mesa, as shown in Figure 4.9). Additionally, an absolute value of R_Y which is greater than 10% represents an amount of shear sensitivity that is detectable experimentally even considering alignment and other sources of error.

4.3 - Experimental Characterization

Analytical design and numerical simulation have been used extensively in the development of the MEMS sensor pads. This involved parametric variation in order to characterize the shear and normal sensitivities of these three-axis devices. Specific concessions had to be made to accommodate the sensor pads within the six-axis wireless devices for use in surgery, but at this phase of the development cycle the three-axis sensor pads were evaluated independently. Once the sensor pads were manufactured, it was necessary to characterize these prototypes to confirm the results determined using analytical and numerical methods. In the interest of saving time and avoiding any discrepancies of sensitivity that could be created by the device packaging, a characterization regime was developed that did not require the sensor pads to be packaged.

The sensor pads were manufactured and processed to point where diced sensors had mesas attached to their top surfaces. Characterization was performed on a microscope probing station which was modified to accept an electronic balance. Figure 4.12 shows a photograph of the modified probing station. The probing station consisted of a stereomicroscope and ferromagnetic platform

suspended above an X-Y translation stage. Three-axis linear adjustment probes with magnetic bases were placed on the platform during characterization. These probes allowed accurate positioning of their tips, which were used to apply electrical and force loads to the sensor pads during testing. The stage was large enough to hold the electronic balance, which enabled measurements to be taken of normal forces applied by the probes.

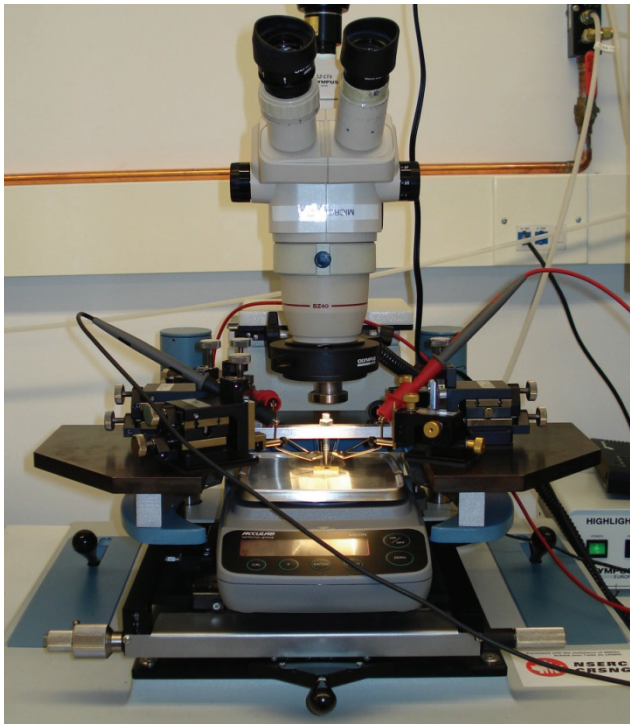

Figure 4.12. A photograph of the microscope probing station with the electronic balance installed.

Characterization data was collected using the following procedure: The sensor pad to be calibrated was placed on the balance and aligned using the microscope. Electrical connections were made using the three-axis probes, which had very fine points, allowing the electrical contact pads on the three-axis sensors to be connected to the required voltage source or detection system. The balance was zeroed at this point to compensate for sensor weight and forces applied by the electrical probes. An additional probe (or probes) was then used to apply a downward force to the centre of the membrane. Electrical output from the

devices and the force registered by the balance were then recorded to produce a calibration curve.

4.3.1 - Normal Load Application

The probe tips used for applying the electrical connections (Quater Research & Development XYZ 500TIS with standard tips) had extremely fine points. These tips were capable of damaging the aluminum contact pads and traces on the sensor pads, so care needed to be taken when aligning the electrical connections. In addition, the standard tips were not capable of producing enough force to flex the membranes and produce an output voltage. To solve this issue, a length of 1.5875mm (1/16") diameter stainless steel welding rod was bent and sharpened to function as a force application tool. A photograph of this tool is shown in Figure 4.13. Upon replacement of the standard tip with the modified application tool, it became possible to apply normal loading to the sensing pad adequately.

Figure 4.13. Force application probe constructed of 1.5875mm diameter stainless steel rod.

The response of a single-piezoresistor sensor pad to normal loading applied with this cantilever force application probe is shown in Figure 4.14. An excitation voltage of 5V was applied and the response to normal loading was examined.

Compared to the idealized FEA simulation result shown in Figure 4.3, the sensitivity is lower and an offset voltage has been produced. The offset voltage could have been caused by electrical contact misalignment created during microfabrication. The reduction in sensitivity was likely due to the increased doping concentration and thicker membrane used in the manufactured device. A 95% confidence interval is also shown on Figure 4.14 for this data. This confidence interval indicates that the variation in device sensitivity, which largely may be attributed to experimental factors such as load application misalignment and hysteresis, was larger than the difference induced by a 20º change in load application angle calculated using FEA (shown in Figure 4.4). This variation artifact was significant as it necessitated a more accurate method of load application or devices with higher shear sensitivity for this characterization method to be effective.

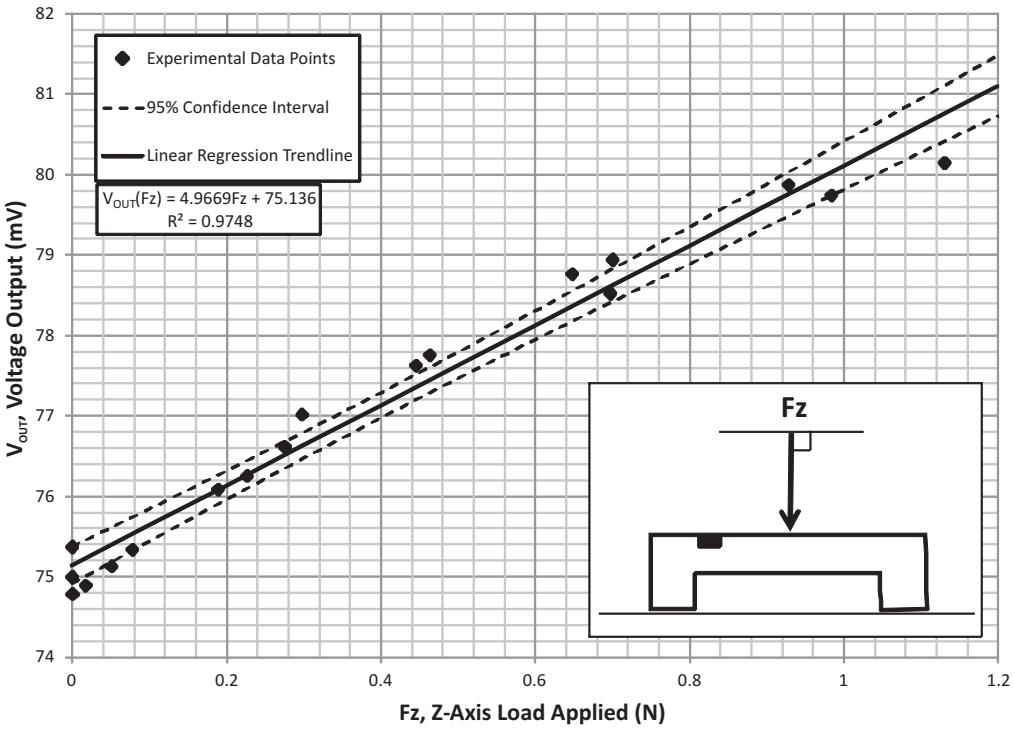

Figure 4.14. Experimental sensor response to a centralized downward point load applied with the cantilever force application tool.

4.3.2 - Angled Load Application

The characterization procedure described above was technically only valid for normal loads applied to the sensor pad. In order to characterize the shear sensitivities, the MEMS devices were held at a known angle between the balance and the probe while the above process was repeated. This was accomplished using wedges. The wedges were fabricated with known angles of 20º and 45º, and were made of an insulating acrylic material. These angles were chosen to correspond with the combined sensitivity simulations from Section 4.2. Vertical loads produced by the force application probes and detected by the balance were thus transformed into combined normal and shear loads, according to the wedge angle. This is illustrated schematically in Figure 4.15. Combined shear and normal sensitivity could then be compared to normal sensitivity for a sensor pad, and the shear sensitivity could be extracted.

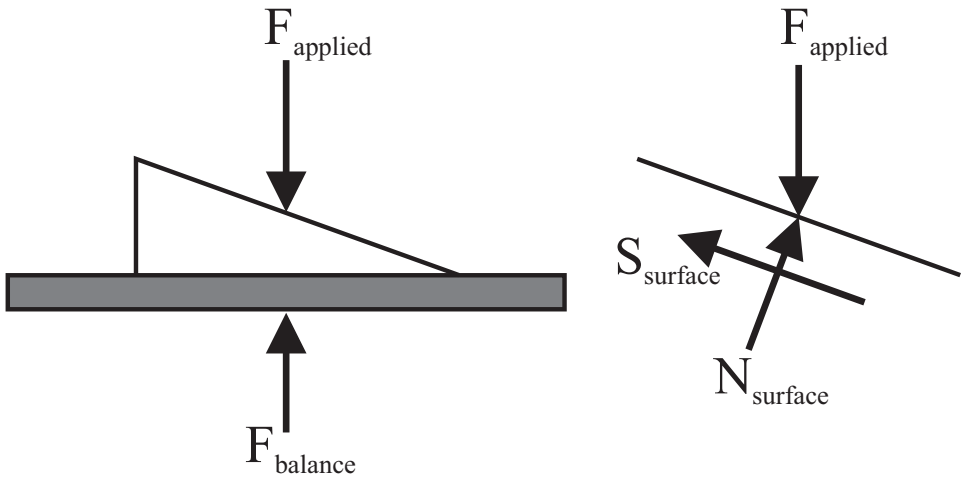

Figure 4.15. Schematic illustration of the load applied to a wedge with a probe. This demonstrates the creation of shear and normal loads at the membrane surface.

The cantilever force application tool shown in Figure 4.13 was not able to apply loads consistently during experiments utilizing the wedges. Single crystal silicon membrane surfaces (when testing devices without mesas attached) were found to provide very little friction with which the probes could apply shear forces. This

made it difficult to apply shear loads consistent with the angle at which the wedge held the sensor. In addition, the 1.5875mm welding rod probe was prone to flexing as load was applied through it, creating different load vectors at its tip during normal and combined sensor pad characterization experiments. These factors created excessive variation in sensor pad outputs during angled load application, making it impossible to accurately characterize sensor pad shear sensitivity with the cantilever force application tool.

A set of measurements was taken on the probing station to quantify the stiffness of the load application tool for the flat and angled scenarios. This was performed to further examine the issues with the angled force application experiments. A sensor pad was not used for this measurement set, instead, the probe tip shown in Figure 4.13 was aligned to directly contact the electronic balance. A fixed amount of vertical displacement was applied by turning the appropriate adjustment knob on the probe, and the reaction load was measured using the balance. For the flat loading scenario, 0.0785g-f/° (of the probe's vertical adjustment knob) was observed. With the probe tip contacting the 20º wedge, 0.2197g-f/° was observed. The results for both experiments were linear; a plot for the angled case has been shown in Figure 4.16.

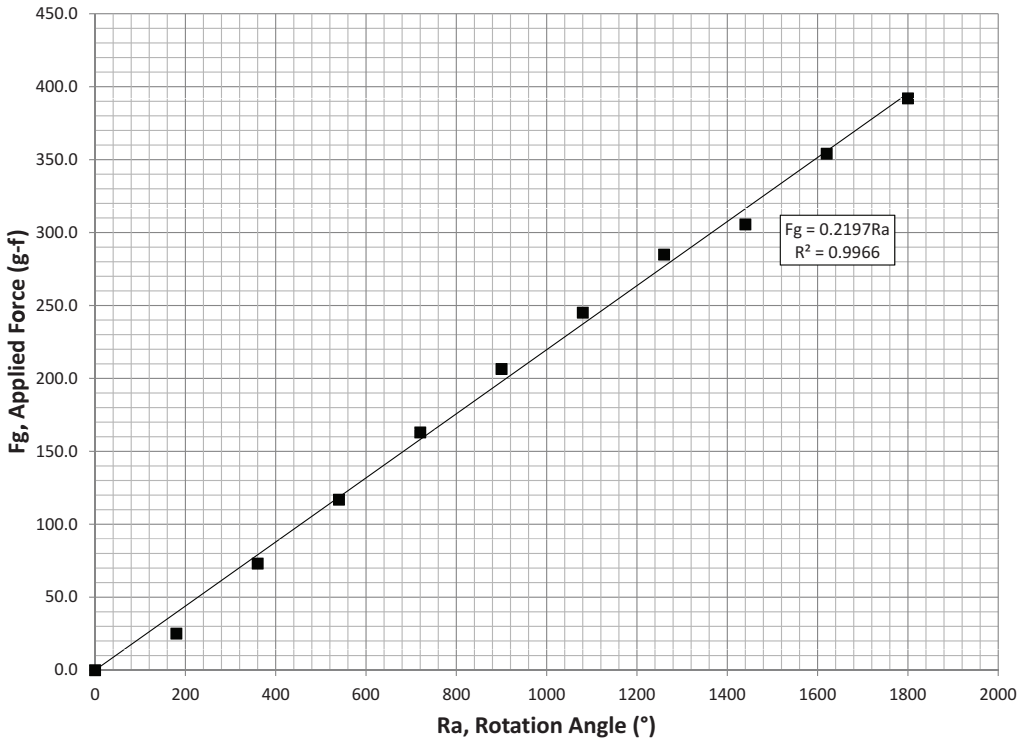

Figure 4.16. Angled load application with the cantilever force application tool. A 20º wedge was used.

The probe is applying nearly three times (0.2197g-f/° / 0.0785g-f/° = 2.80) the load per vertical displacement with the 20º wedge as compared to the flat experiment. Considering the force application tool is effectively a cantilever beam subject to an end-load and undergoing small displacements, it is assumed that it acts like a linear spring [146]. This implies that there is nearly three times the vertical displacement in the angled experiment. The explanation for this additional displacement is as follows: as the force application tool is lowered at the probe body, the tip slides upward on the wedge surface, creating additional bending in the tool and adding to the load detected by the balance. Bending of the tool in the non-vertical direction may also be a contributing factor to the additional detected load.

In order to compensate for the lack of stiffness in the cantilever load application tool, an enhanced load application device was built. This new load application tool was stiffened by bridging two individual probes with a solid beam

and applied loads using a 6.35mm pin threaded into the midpoint of this beam. This application tool was rigid enough to apply shear forces at its tip to properly characterize the sensors for the shear and combined loading cases. The bridged nature of this new tool prevented sliding on the wedges during angled characterization, and allowed loads to be applied more consistently. This bridged load application tool is shown in Figure 4.17.

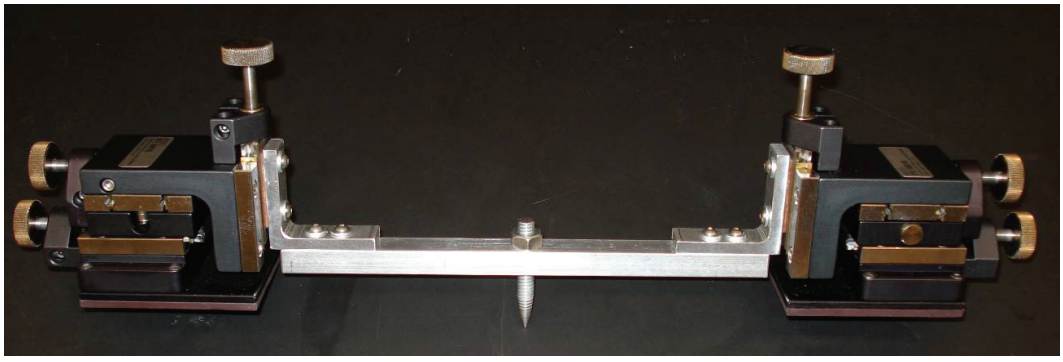

Figure 4.17. The bridged force applicator attached to two probes.

The bridged load application tool was examined for its stiffness. This was performed in the same manner as with the cantilever tool, except that the displacements were applied by turning both of the vertical adjustment knobs simultaneously. Displacements were applied to flat, 20º, and 45º scenarios and the balance was used to detect the induced load. Data from this experiment is shown in Table 4.1. The sensitivities achieved for load application at 0º, 20º, and 45º were 1.415g-f/°, 1.379g-f/°, and 0.774g-f/°, respectively. Multiplying the 0º stiffness by the cosine of the wedge angles obtains 1.330g-f/° and 1.000g-f/° for the 20º and 45º load application angles, respectively. Comparing the calculated and measured results for detected stiffness achieves 3.7% error for the 20º angle and 22.6% error for the 45º angle. This indicates that a substantial improvement in stiffness has been made.

Table 4.1. Load application data with the bridged force application tool.

Rotation Angle (°)	Applied Force (g-f)		
	0°	20°	45°
0	0	0	0
90	97.1	95.5	73.5
180	241.4	239.5	156.5
270	386.0	366.1	180.4
360	520.8	513.0	290.8

4.3.3 - Nonlinear Effects

Eliminating the movement between the probes, sensor pad, wedge, and balance surface was also necessary for successful experimental characterization. Movement created noise in the sensor output, and also altered the device sensitivity. This sensitivity change occurred when the device slid laterally on the wedge, affecting the preload from the electrical and force application probes. Securely adhering the sensor to the wedge and the wedge to the balance was extremely important in minimizing movement. During characterization experiments in which a mesa was adhered to the sensor membrane, an additional interface was created between the membrane surface and the mesa. It was necessary to ensure consistent adhesion was achieved at this interface to further eliminate relative movement. Relative movement during characterization was more of an issue during application of shear loads, so alternative force application methods, such as those described in the literature [44, 132], may be considered in cases of higher shear load application.

Schottky barrier effects were noted during the characterization of sensing pads. These effects, which are discussed further in Section 2.5, presented as very high resistances on the four-terminal gauges, as well as non-linear current-voltage relationships. To minimize these effects, approximately 10V of potential was applied across each metal-piezoresistor junction. By monitoring the current flow across the junction during voltage application, the switch to more ohmic contact behavior could be observed. Non-linear effects were still observed for the four-terminal gauges on the sensing pads, as illustrated in Figure 4.18. In contrast, nonlinear effects were less pronounced on a full Wheatstone bridge that was

manufactured during the same production run. The output from the Wheatstone bridge device is shown in Figure 4.19.

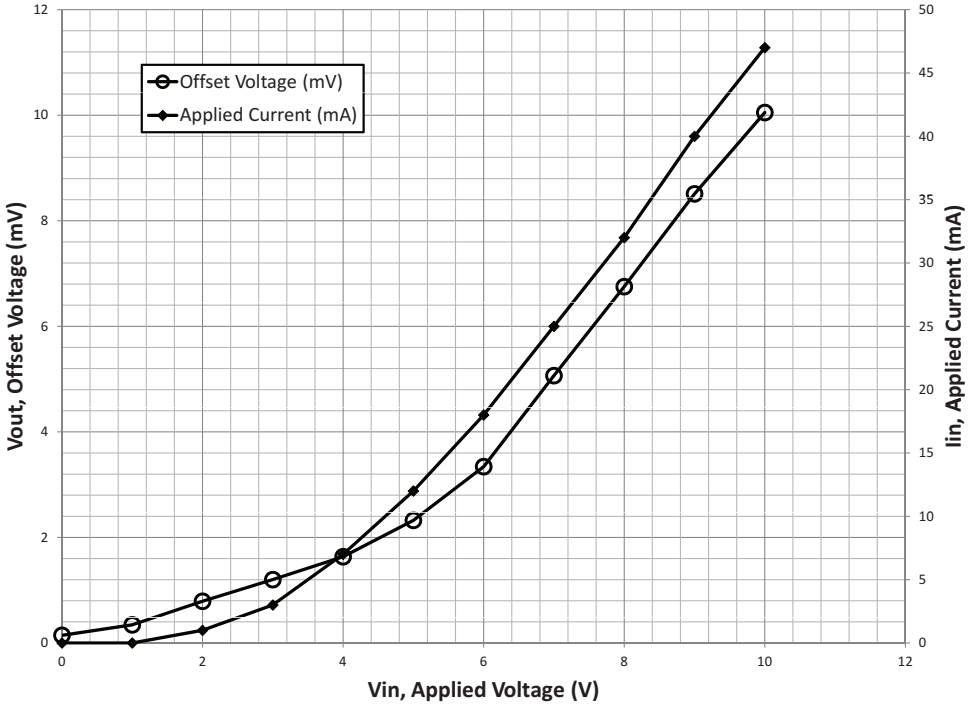

Figure 4.18. Four-terminal gauge offset voltage and current requirements plotted against input voltage.

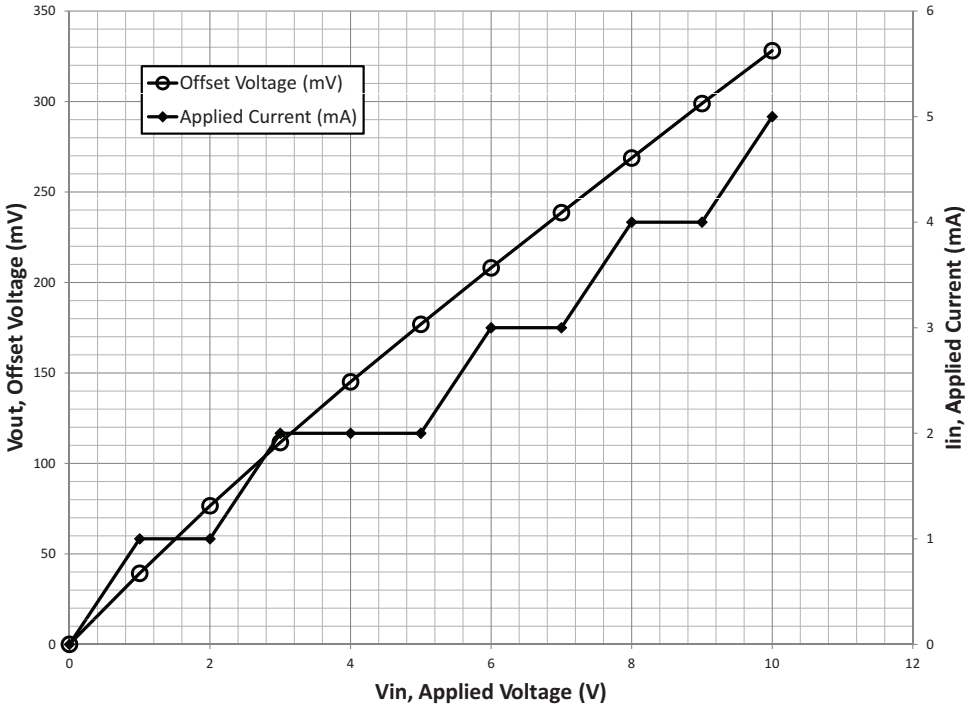

Figure 4.19. Wheatstone bridge offset voltage and current requirements plotted against input voltage.

The four-terminal gauge examined was shown to draw more current than the full Wheatstone bridge. This was likely due to the fact that its sole piezoresistor was two-squares long, while each of the four resistors in the Wheatstone bridge was 10-squares long. In addition, the four-terminal gauge was shown to have a lower offset voltage than the full Wheatstone bridge. This is indicative of an out of balance (i.e. non-symmetrical) bridge circuit, illustrating the reduced manufacturing tolerances required to produce a functional four-terminal gauge. This offset voltage had to be considered when evaluating sensor pad sensitivity. It should also be noted that the offset voltage to input voltage response, including the nonlinearity, was slightly different for each sensor tested. However, the majority of devices achieved relatively linear input voltage to offset voltage responses once at least three volts of input voltage was applied.

The nonlinear effects detected during experimental characterization also included current directionality artifacts. Piezoresistor offset voltages and I-V curves were different when the devices were connected to the DC power supply

with the terminals reversed. Fortunately, current direction was not found to have a significant influence on sensor pad sensitivity during loading; the variance in device sensitivity when the current direction was changed was approximately equivalent to the variance observed between multiple characterizations of the same device. This equivalence allowed offset voltages and polarity differences to be removed by normalizing the output voltages in post processing.

4.3.4 - Sensor Pad Rotation

Once ohmic behavior was achieved by applying an adequate input voltage, the manufactured devices could be examined for their responses to normal and angled loading. Due to the limited area on the ferromagnetic platform, only four electrical probes could be used at one time. This necessitated that the V_1-V_4 piezoresistors have their responses measured sequentially during characterization. Devices were built to accomplish this in two different ways: The electrical probes could be repositioned to touch separate sets of electrical contact pads, located around the perimeter of the membrane, which would electrically activate the four piezoresistors sequentially during loading. Alternatively, the sensor pads could be rotated on the wedges to recreate the four necessary orientations. Both of these methods required that the load be reapplied after the probes were repositioned. However, the latter (sensor rotation) method was preferable for this phase of characterization. Sensor rotation required that the Schottky barriers be broken for only one device, thus reducing the risk of "burning-out" the contacts during application of high-voltages. This method also only required that one piezoresistor be built on each membrane, allowing more space for larger electrical contact pads and traces. The larger pads were simpler to align with the electrical probe tips and the larger traces were less prone to damage from stray probe tips: If a trace was damaged during characterization, the device was rendered un-usable.

A sensor pad utilizing a single four-terminal gauge was examined for its response to normal loading using an excitation of 5V. In this experiment, the bridged load application tool was used and care was taken to ensure the sensor pad was well constrained. The results of this loading are shown in Figure 4.20.

These results have been displayed with the offset voltage removed. The sensitivity of this device was higher than values obtained with FEA which were presented in Figure 4.3. This could be the result of membrane thickness, doping concentration, or several other factors. More importantly, when compared to data collected using the cantilever force application tool (shown in Figure 4.14), the 95% confidence interval was substantially smaller and was nearly coincident with the trend line on the chart. In addition, the coefficient of determination (R^2) value for the linear trend line was much closer to unity, 0.9999 for the bridged tool and 0.9748 for the cantilever tool.

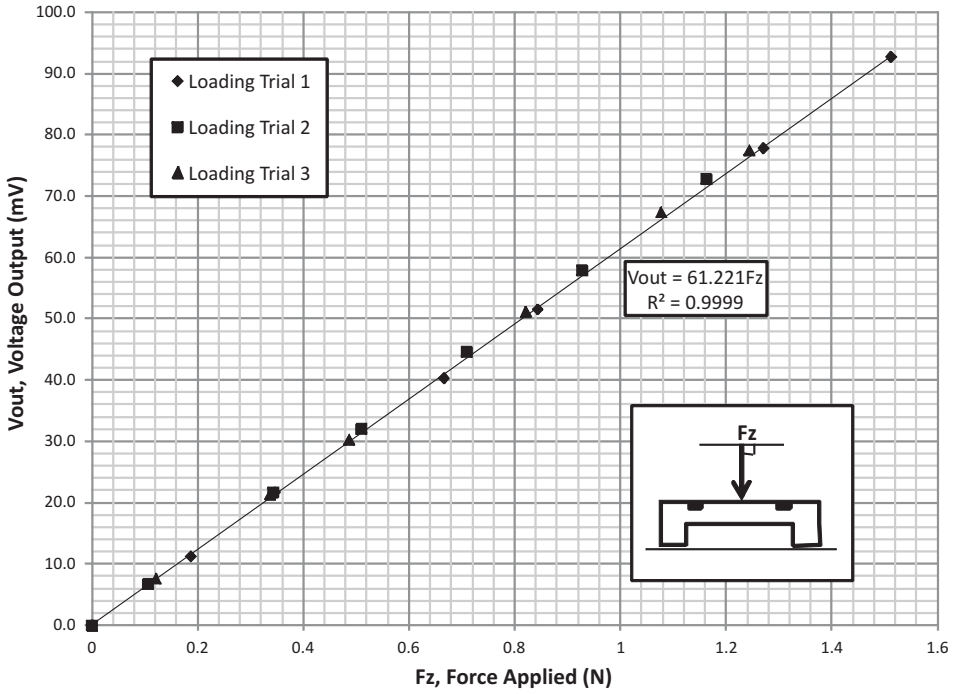

Figure 4.20. Experimental sensor response to a centralized downward point load applied with the cantilever force application tool.

4.3.5 - Mesa Affixation

The use of a mesa on the membrane surface was also considered during sensor pad characterization. In order to minimize processing prior to testing, semi-spherical / cylindrical mesas were created using adhesive. This was done by placing a small amount of viscous adhesive (the best results were achieved using

epoxy) on the membrane surface using a 25 gauge needle and a syringe. Prior to hardening, the adhesive could be reshaped to slightly adjust its position and height. Two epoxy mesas are shown in Figure 4.21 with heights of 625µm and 375µm. Clearly the epoxy mesas are not perfectly centred or cylindrical, however, they did provide adequate height to increase the shear sensitivity of the sensor pads. It was necessary to allow the adhesive mesas to fully cure before testing to prevent them from deforming or breaking off during load application with the bridged load application tool.

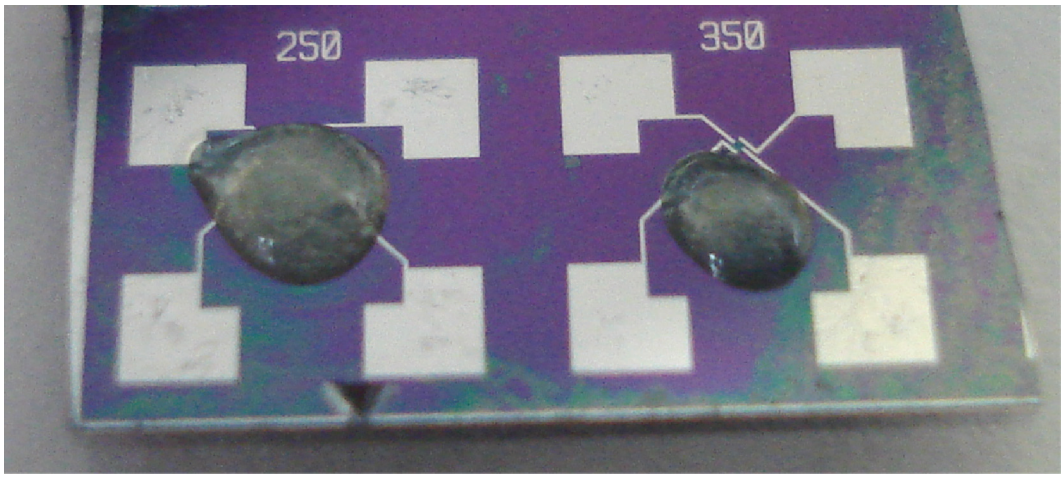

Figure 4.21. Epoxy mesas used for characterization of the sensor pads. The height of the left mesa is 625µm, and the height of the right mesa is 375µm. Note: these sensor pads are 2X scale, with 2000µm membrane edge lengths.

4.4 - Sensitivity Results

Substantial differences existed between numerically calculated and experimentally measured sensor pad responses. Moreover, the sensitivities observed using both methods varied significantly depending on geometric, electrical, material, and characterization parameters. To further validate sensitivity trends obtained using FEA, comparisons had to be made between numerical and experimental data taking parametric variation into account. Accurate measurements were taken of the experimentally tested sensor pads and the FEA models were then altered to achieve parametric consistency with the

manufactured devices. Sensitivity was also defined more rigorously to aide in the comparison.

To build FEA models using the actual dimensions of the manufactured devices, accurate parametric characterization of the sensor pads had to be performed. Overall final thickness of the silicon substrate was measured with an anvil micrometer. This was a necessary measurement to take as initial substrate thicknesses varied (usually by 1-2μm), and the multiple thermal oxide growth and etching steps during microfabrication thinned the silicon substrates. Cross sectional profiles of the membrane cavity were measured using optical and contact profilometry. Curvature of the backside of the membrane was studied in previous work [1, 2] and was shown to have less effect on sensitivity than the mean thickness. Optical microscope measurements were also taken to ensure the topside features, specifically the piezoresistor shapes, corresponded to the dimensions defined by the photomasks. Characterization structures, such as Greek crosses, Kelvin crosses, cross bridges, and multiresistors, as explained in Section 3.4, were used in combination with four-point probe measurements and doping simulation to define appropriate piezoresistive coefficients.

A prototype sensor pad was measured and characterized for its response to normal loading. This sensor pad was a 2X scale version of the model device shown in Figure 3.4, and had a 2000μm × 2000μm × 90μm square membrane. The FEA model specified that the membrane be built in a 4000μm × 4000μm × 500μm (1 0 0) silicon substrate. The piezoresistive four-terminal gauges were 200μm × 100μm and were spaced 700μm from the centre of the membrane, aligned with the midpoints of the membrane edges. The boron doping concentration was determined to be 5×10^{19}atoms/cm^3, and corresponding resistivity and piezoresistive coefficient values were applied ($\rho_0 = 2.5\times10^{-3}\Omega$-cm, $\pi_{44} = 41.4\times10^{-11}$/Pa). A 5V source voltage was applied to each piezoresistor and a variable normal load was applied to the centre of the membrane. Figure 4.22 shows the experimental response of this device compared to FEA simulation of a numerical model with similar dimensions.

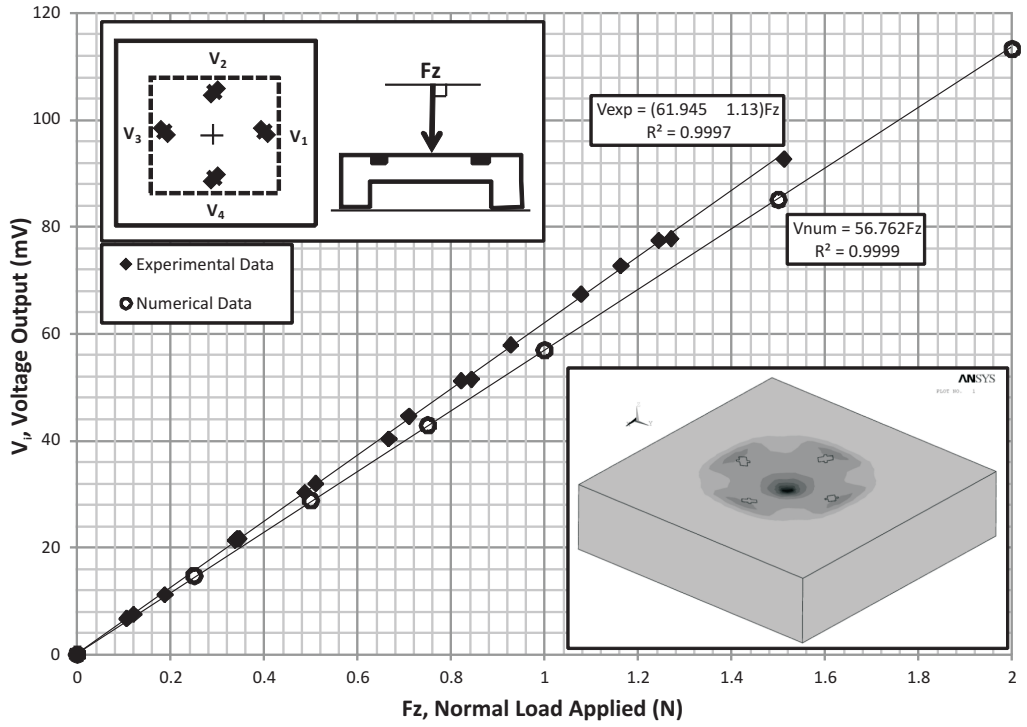

Figure 4.22. Experimental and numerical sensor pad responses to a variable normal (downward) load.

The numerical and experimental responses for this device are both similar and linear, as illustrated by the R^2 values nearing unity for both linear regression trend lines. A small amount of nonlinearity was predicted by membrane deflection theory (which is further discussed in Section 2.6) for the strain responses of the piezoresistive regions [85]. This nonlinearity has been further discussed in the analysis of a similar device noted in literature [44]. The voltage outputs from each of the four piezoresistors (V_1-V_4) produced trend lines that were nearly coincident for both experimental devices and numerical simulations. It should also be noted that an offset voltage was removed during post-processing of the experimental output signal. The experimentally tested device was slightly more sensitive than the simulated device, which is likely due to slight variation in membrane geometry or load misalignment. The influence of these factors is discussed in detail in Section 4.2. Other possible explanations for the difference in sensitivities include inaccuracy in the simulated piezoresistive coefficients and

resistivity due to experimental boron doping variation, diode effects at the metal-piezoresistor interfaces creating leakage current, conductor trace damage or inefficiency, or signal loss due to imperfect contact between the electrical probe tips and the contact pads on the experimental devices.

Further experimentation was performed to produce data sets for angled loading at 20º and 45º. Input loads were applied with the shear load components pointing toward the V_2 gauges on the sensing pads examined. Experimental data is shown for angled loading applied at 20º for a sensing pad in Figure 4.23. This sensing pad had a membrane that was 90μm in thickness and was similar to the device used for the normal loading scenario described above. Output voltages from the angled loading experiments and simulations produced trend lines that were reasonably linear and similar to the comparison shown in Figure 4.22. The angled load application was shown to produce differing output trends from each of the four piezoresistors on the sensing pad. To allow the differences between the four piezoresistor responses to be more clearly visualized, the numerical simulation results were not plotted on Figure 4.23.

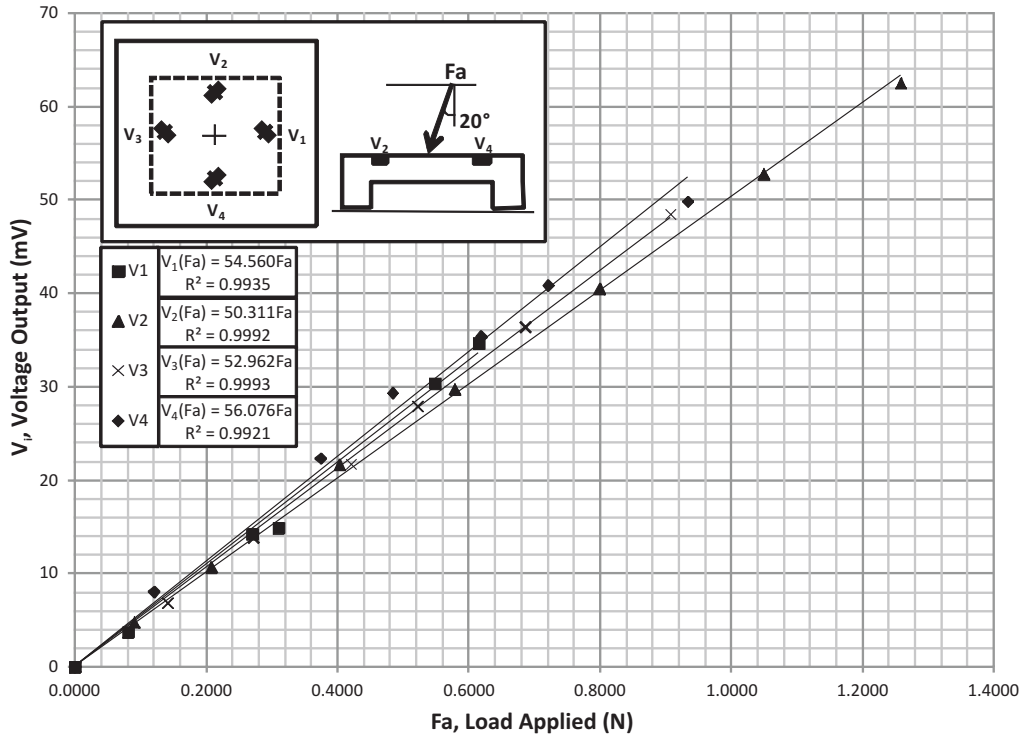

Figure 4.23. Experimental sensor pad responses to a variable angled load applied at 20º.

4.4.1 - Calculation of Sensitivity

The sensitivity of experimentally tested sensing pads was directly compared to the numerical simulation results. Using a similar methodology to the shear sensitivity ratio defined in Section 4.2.2 by Equation (4.1), the differences in the responses between the V_1 and V_3 piezoresistors and the V_2 and V_4 piezoresistors were used to define the sensitivity of the sensing pads in the normal, X-shear, and Y-shear directions. These sensitivities are defined in Equation (4.2) as N_S, X_S, and Y_S, respectively. In these equations, $F_{N\text{-}APP}$, $F_{X\text{-}APP}$, and $F_{Y\text{-}APP}$ represent the forces applied in the specific direction of detection, V_{IN} represents the source voltage applied to each piezoresistor, and V_1-V_4 are the individual piezoresistor outputs.

$$N_S = \frac{V_1 + V_2 + V_3 + V_4}{4 \cdot V_{IN} \cdot F_{N-APP}}, X_S = \frac{V_3 - V_1}{V_{IN} \cdot F_{X-APP}}, Y_S = \frac{V_4 - V_2}{V_{IN} \cdot F_{Y-APP}} \quad (4.2)$$

4.4.2 - Angled Load Application

The above equations were used to convert the voltage output data from Figure 4.23 into directional sensitivity information. A sensing pad with a single piezoresistor was examined to obtain the experimental data, so the sensor rotation method was used during data collection. This method caused each voltage output data point to be produced at a separate load value, necessitating that an average value obtained from the trend line be used for the other voltages in Equation (4.2). This produced twice as many sensitivity data points for N_S as compared to X_S or Y_S. Figure 4.24 shows the results of this conversion, and depicts both numerical simulation and experimental results for the three sensitivities. The error bars depict a 95% confidence interval for the voltages, converted to sensitivity.

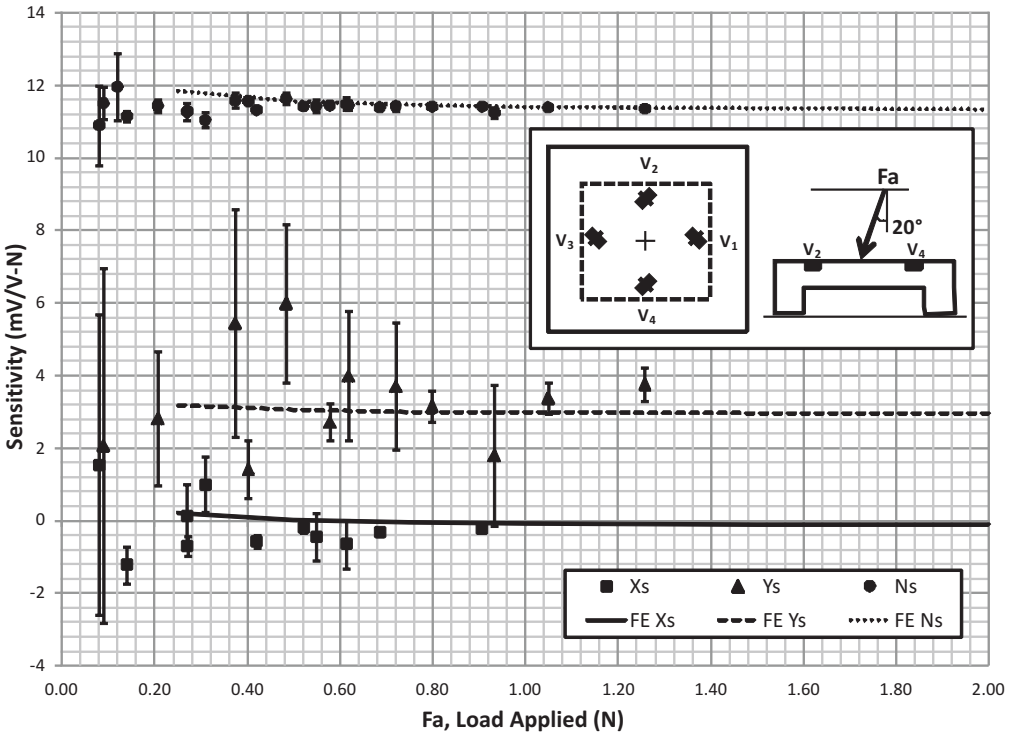

Figure 4.24. Simulated and experimental sensor pad sensitivity responses to a variable angled load applied at 20º.

The average sensitivities calculated from the numerical simulation results are N_S = 11.5mV/V-N, Y_S = 3.0mV/V-N, and X_S = 0.0mV/V-N. The sensitivities

calculated from the experimental results were largely supportive of the numerical averages, although experimental error, particularly for the shear sensitivity values at lower force levels, obscured the correlation. Since there was zero X direction loading applied in this example, non-zero X_S values were also indicative of experimental error.

4.4.3 - Angled Load Application to a Mesa

To reduce the experimental error and to improve the ability of these sensing pads to detect shear loads, mesas were added to the membrane surfaces. These mesas would increase the relative voltage difference between the V_2 and V_4 piezoresistors during shear load application, decreasing the experimental error relative to the V_4-V_2 and V_3-V_1 values. This would also serve to increase the ratio between the Y_S and N_S sensitivities. A cylindrical mesa with a 600μm diameter and 400μm height was added to a sensor pad similar to those used in the preceding experiments. Experimental and numerical results were determined for this sensing pad. Experimentally determined voltage output responses are shown in Figure 4.25. As in Figure 4.23, the numerical results were not shown to improve the clarity of this graph.

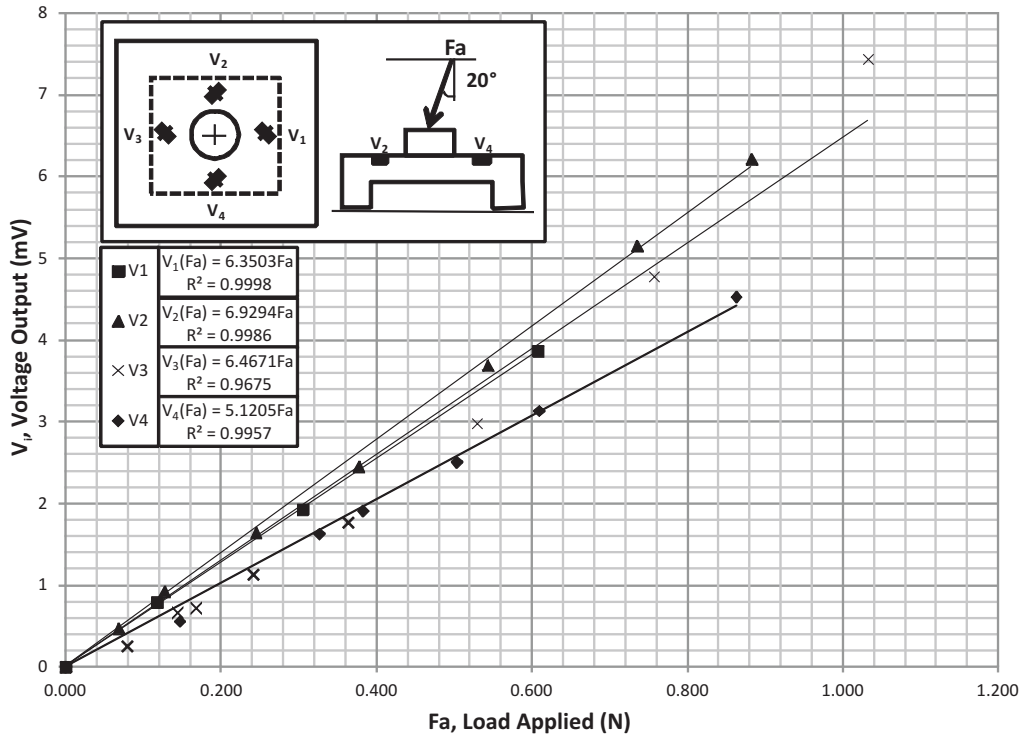

Figure 4.25. Experimental sensor pad responses to a variable angled load applied at 20º. A mesa with 400µm height and diameter of 600µm was attached to the membrane surface.

The difference between the slopes of the trend lines from each of the four piezoresistors is more defined with the mesa attached, despite the overall reduction in voltage output from the sensor pad tested. This data was once again used to calculate experimental sensitivity values, which was then compared to numerical simulation data from a parametrically corresponding device. The results of this comparison are shown in Figure 4.26. Although relatively large 95% confidence intervals still appear for shear sensitivity values at low force levels, Figure 4.26 clearly shows improved correlation between experimental and numerical sensitivities when compared to the experiment without a mesa shown in Figure 4.24.

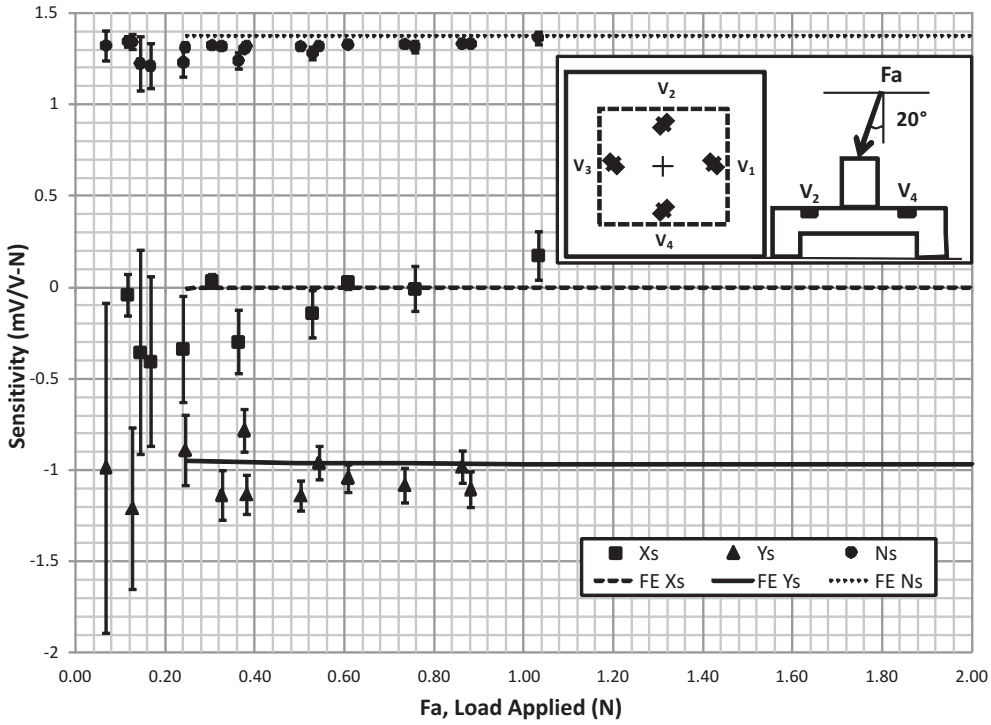

Figure 4.26. Simulated and experimental sensor pad sensitivity responses to a variable angled load applied at 20°. A mesa with 400μm height was attached to the membrane surface.

The average sensitivity values of N_S = 1.4mV/V-N, Y_S = -1.0mV/V-N, and X_S = 0.0mV/V-N indicate a higher absolute ratio between the Y_S and N_S sensitivities for the device with the mesa attached. This ratio is approximately Y_S/N_S = -0.8 for the device with the mesa and Y_S/N_S = 0.26 for the device without the mesa. This increased sensitivity ratio indicated more accurate experimental detection of shear loading was possible. A reduction in overall sensitivity was also noted for the sensing pad with the mesa, and was attributed to the thicker, 130μm, membrane and a higher surface concentration of boron in the piezoresistive regions ($>10^{21}$atoms/cm^3).

4.4.4 - Parametric Effects on Sensitivity

The comparisons made between experimental and numerical results indicated that the FEA used in Section 4.2 to evaluate trends in device sensitivity were

acceptable. It was also noted that the absolute values of sensitivity (N_S, X_S, and Y_S) were more significant indicators of performance in the sensor pads than the shear sensitivity ratio defined in Equation (4.1). For these reasons, the numerical simulations from Section 4.2 were re-evaluated to present the effects of parametric variation in terms of shear and normal sensitivities. It is worth noting that, unlike the above three experimental to numerical comparisons, the following numerical sensitivity analyses were calculated using membranes with 1000μm edge lengths.

The location of the load application region was evaluated first for its effect on shear and normal sensitivity. Figure 4.27 shows sensitivity results as the 40μm × 40μm load application region is moved from the centre of the membrane toward the V_2 piezoresistor, and Figure 4.28 shows the sensitivity results as the load is moved toward the corner between the V_1 and V_2 piezoresistors. Alignment regions for shear and normal loading are defined in these two figures, which correspond to those defined by the shear sensitivity ratio (discussed in Section 4.2). A false Y_S that is greater than 10% of the N_S value is achieved with 15μm of misalignment in Figure 4.27, and with 30μm of misalignment in Figure 4.28. A value for N_S that differs from its centered load value by more than 10% is achieved with 75μm of misalignment in Figure 4.27 and with 125μm of misalignment in Figure 4.28.

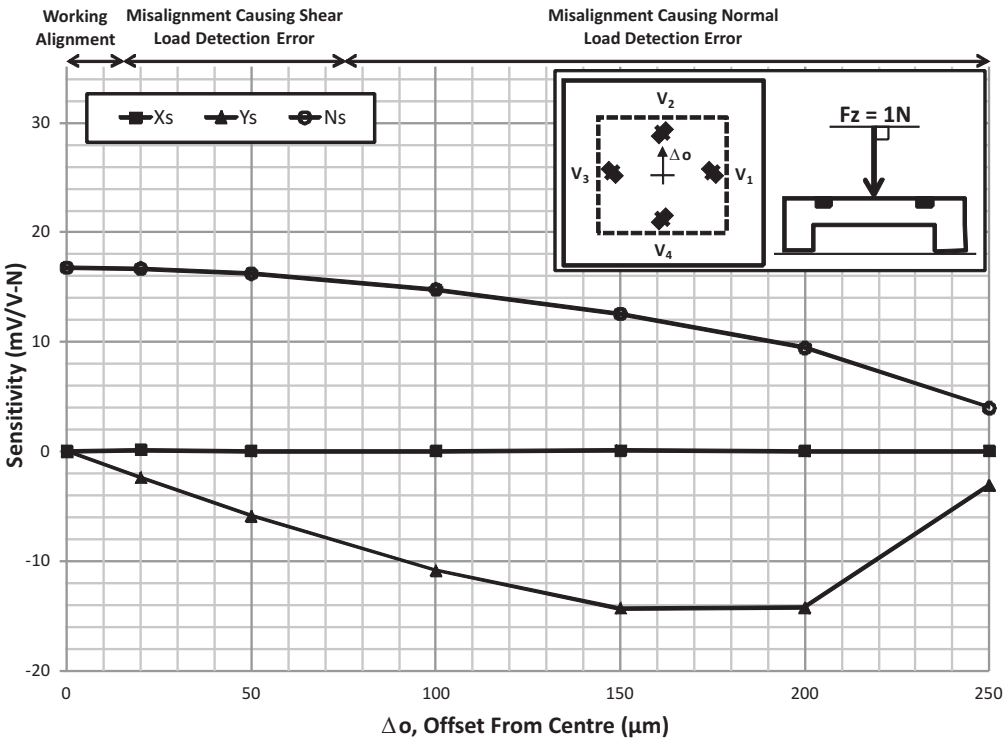

Figure 4.27. Simulated sensor pad sensitivity responses due to moving the load application region closer to the V_2 gauge.

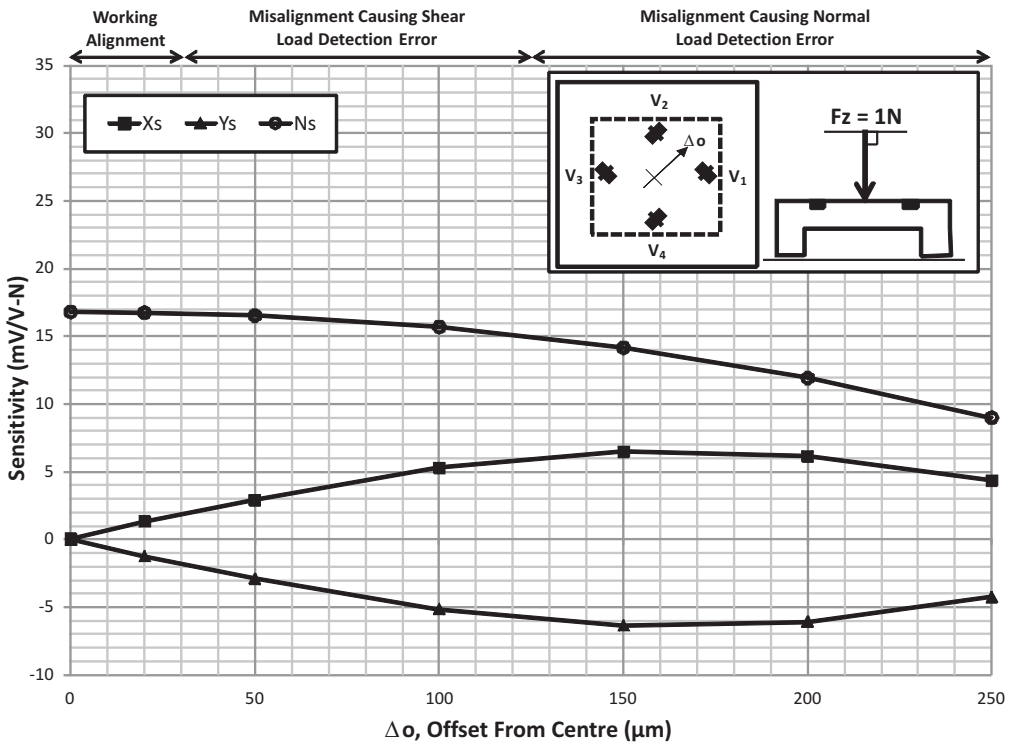

Figure 4.28. Simulated sensor pad sensitivity responses due to moving the load application region closer to the corner between the V_1 and V_2 gauges.

A shear load was not applied in the above two sensitivity studies, implying that the shear sensitivity variation observed is only due to alignment effects. To examine the sensitivity variation with a shear load applied, the numerical study presented in Figure 4.27 was repeated with the load applied at a 20° angle (toward the V_2 piezoresistor). The shear and normal sensitivity results of this study for an angled load are shown in Figure 4.29. When the results shown in Figure 4.27 and Figure 4.29 are compared, similar results for the N_S and X_S sensitivity values are found. However, increased (absolute) sensitivity for the Y_S shear sensitivity value is detected during angled load application as the amount of misalignment increases. This is due to increased output from the V_2 piezoresistor in response to increased stresses created by the local loading effects.

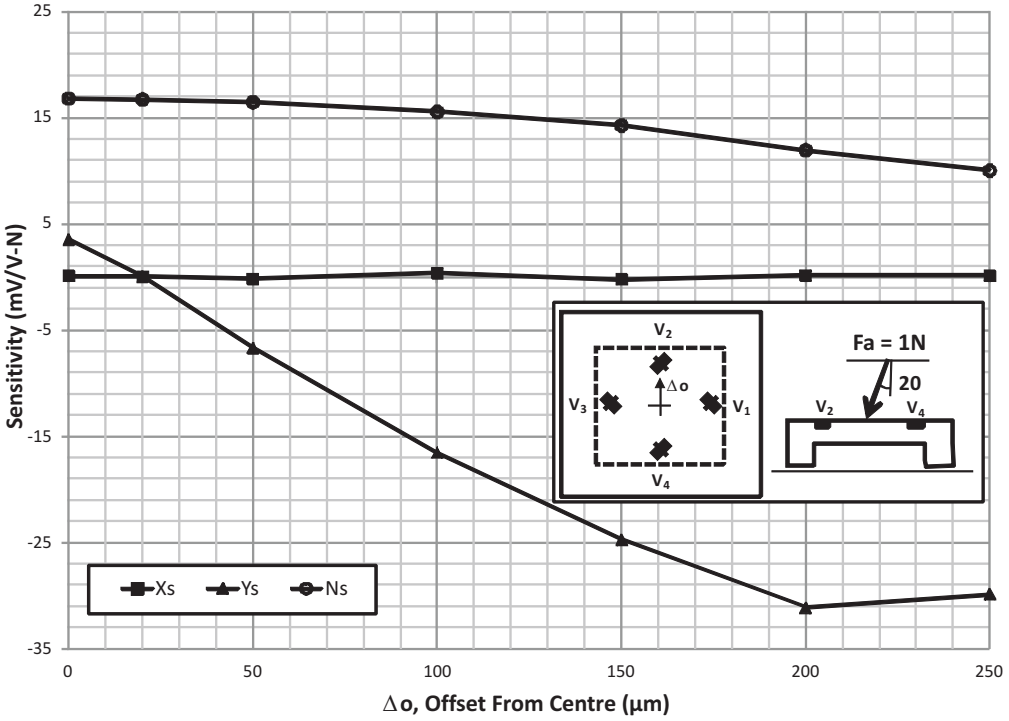

Figure 4.29. Simulated sensor pad sensitivity responses due to moving an angled load application region closer to the V_2 gauge.

The size of the centered load application region was the next parameter varied to examine the effect on normal and shear sensitivity. An angled load of 5N was applied at 20º (toward the V_2 piezoresistor) and was distributed over a square application area with varying edge lengths. The shear and normal sensitivity results are plotted in Figure 4.30. This simulation determined that the N_S value was reduced as the load application area increased in size. This result is consistent with analytical membrane theory [85]. The X_S and Y_S values were found to remain constant as the load application area increased in size.

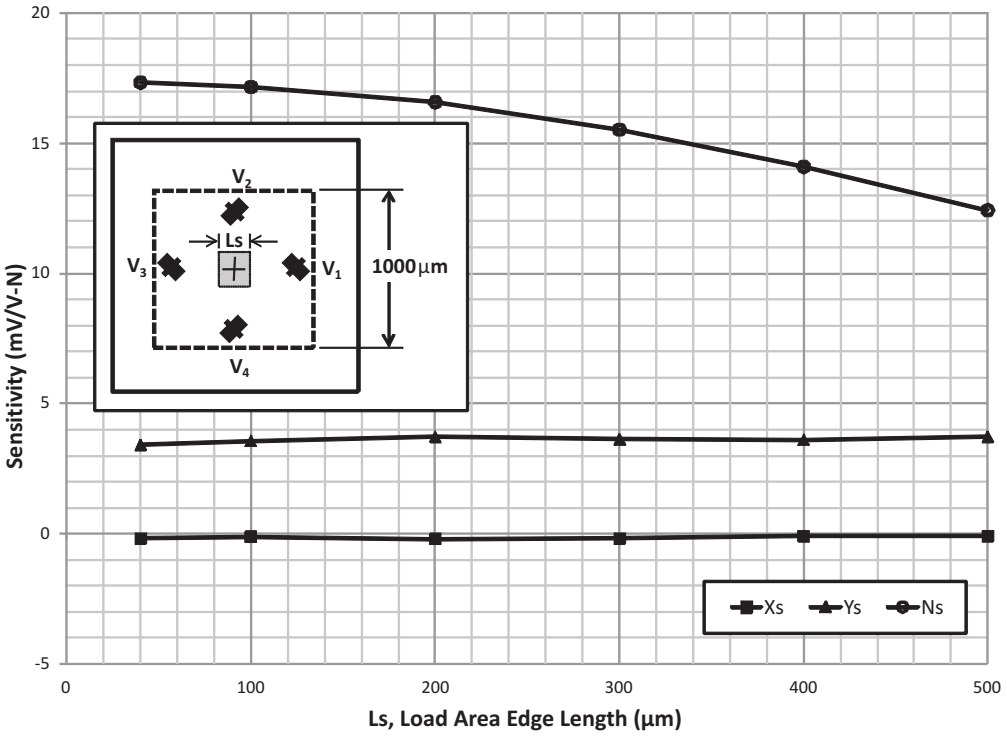

Figure 4.30. Simulated sensor pad sensitivity responses due to increasing the size of the centered load application region.

The location of the four piezoresistors on the membrane surface was also evaluated for its effect on normal and shear sensitivity. This numerical analysis calculated sensitivities as the piezoresistors were moved inward from the membrane edges. The loads applied in this analysis were again 1N, angled at 20º toward the V_2 piezoresistor and were distributed over a square area with 40µm edge lengths. The results from this analysis are shown in Figure 4.31. This figure illustrates that the normal sensitivity decreases as piezoresistors are moved away from the membrane edges, which is consistent with results from membrane deflection theory. In addition, the shear sensitivity increases as the resistors are moved away from the membrane edges, which is again the result of increased stresses due to local loading effects.

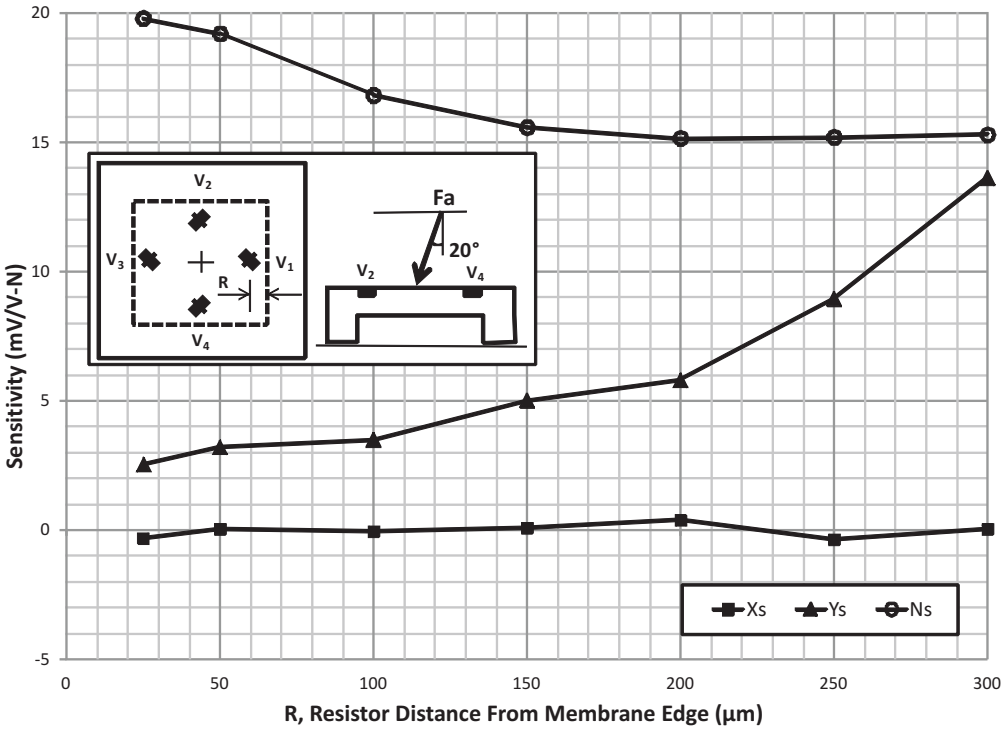

Figure 4.31. Simulated sensor pad sensitivity responses due to moving the piezoresistors away from the membrane edges.

Finally, mesa height and membrane thickness were evaluated for their effects on shear and normal sensitivities. A force application of 1N was applied at 20º to a membrane with 1000µm edge lengths for both of these simulations. Mesa diameter was 300µm for both simulations. For the mesa height simulation shown in Figure 4.32, a 65µm membrane thickness was used and the sensitivities were evaluated as mesa height was varied. The results of this simulation were very similar to the shear sensitivity ratio results shown in Section 4.2, with many of the same conclusions applying. The primary conclusion was that a mesa height above 100µm will yield a net increase in shear sensitivity. For the membrane thickness simulation shown in Figure 4.33, a mesa height of 200µm was used while the membrane thickness was varied. This simulation showed that both shear and normal sensitivity decreased as the membrane thickness increased. In addition, the Y_S/N_S ratio was shown to increase as the membrane thickness

decreased; this indicated, as discussed in Section 4.2, that the relative shear sensitivity will be higher with a thinner membrane.

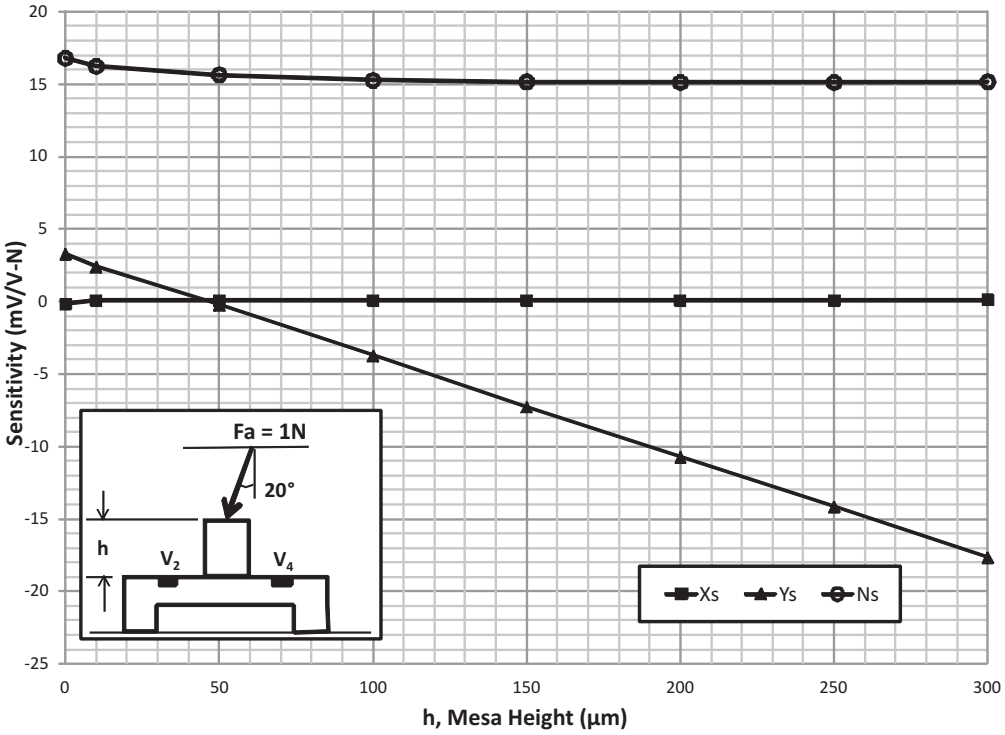

Figure 4.32. Simulated sensor pad sensitivity responses as the mesa height is varied.

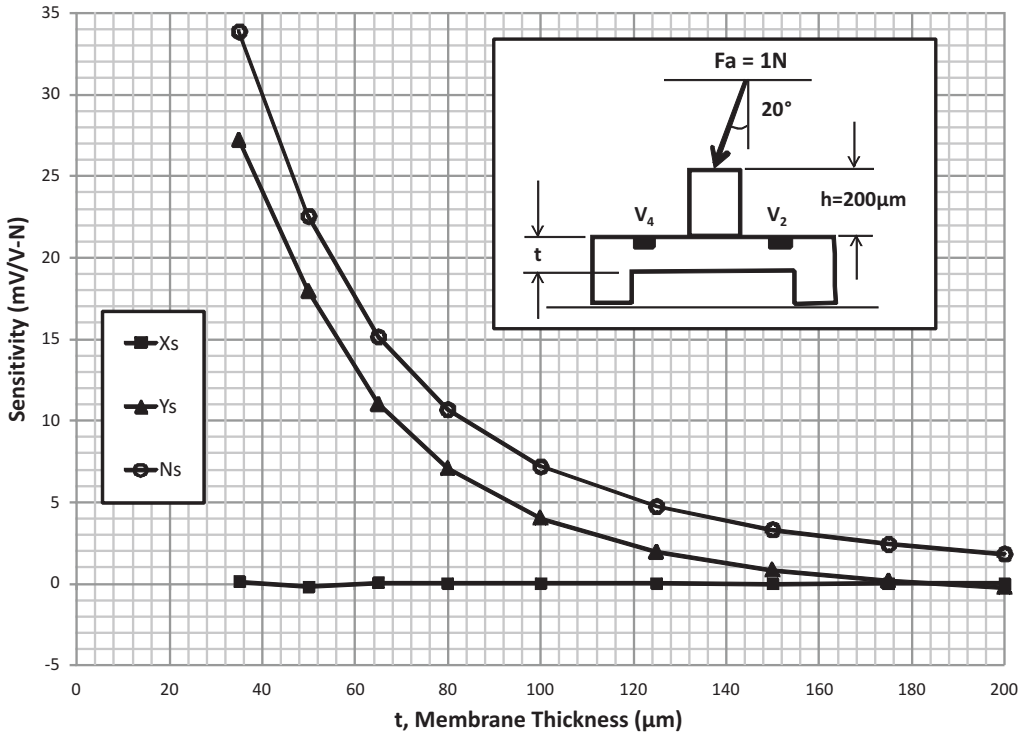

Figure 4.33. Simulated sensor pad sensitivity responses as the membrane thickness is varied.

The results of the preceding analyses are summarized in Table 4.2. Combined normal and shear loads were applied to the sensor pads, with zero loading applied in one of the two shear directions. This has allowed the sensitivity detected in the zero load direction to be indicative of detection error. Generally speaking, parametric changes that increase the overall stresses or deflection of the membrane will increase the normal sensitivity, and changes which increase the directional or localized stresses will increase the shear sensitivity. Error is increased in cases where localized stresses are induced asymmetrically.

Table 4.2. Effects of varying specific sensor pad parameters on the normal sensitivity, shear sensitivity, and detection error.

Parameter Varied	Variation Direction	Normal Sensitivity	Shear Sensitivity	Detection Error
Load Misalignment	Increase	Decrease	Increase	Increase
Load Application Area Size	Increase	Decrease	No Change	No Change
Piezoresistor Distance from Membrane Edge	Increase	Decrease	Increase	Small Increase
Mesa Height	Increase	No Change	Increase	No Change
Membrane Thickness	Increase	Decrease	Decrease	No Change
Dopant Concentration	Increase	Decrease	Decrease	No Change

4.5 - Individual Sensor Matrices

Multiple sources of shear and normal sensitivity variation have been detected during the simulation and characterization of the sensing pads. This variation required that the individual sensor pads be calibrated prior to their implementation in the scoliosis sensor array. Values for the shear and normal sensitivities may be obtained using the experimental method described in Section 4.3. Essentially, this method involved applying known loads to the sensing pads in the normal and shear directions and monitoring the response from each of the four piezoresistors. To compensate for sensitivity variation, curves (Figure 4.24 and Figure 4.26) were produced, allowing sensitivity to be calculated at several force application levels to obtain average N_S, X_S, and Y_S values. Equation (4.2) may then be rearranged to produce the relationships shown in Equation (4.3), which allow applied forces to be solved given the output voltages from the four piezoresistors.

$$F_{N-APP} = k_1\left(\frac{V_1 + V_2 + V_3 + V_4}{4}\right), k_1 = \frac{1}{V_{IN} \cdot N_S}$$
$$F_{X-APP} = k_2(V_3 - V_1), k_2 = \frac{1}{V_{IN} \cdot X_S} \quad (4.3)$$
$$F_{Y-APP} = k_3(V_4 - V_2), k_3 = \frac{1}{V_{IN} \cdot Y_S}$$

These equations may then be combined to produce a calibration matrix [$\boldsymbol{k}$], as shown in Equation (4.4), which allows the three forces to be solved for simultaneously.

$$\{\boldsymbol{F}\} = [\boldsymbol{k}]\{\boldsymbol{V}\}$$

$$\begin{Bmatrix} F_{N-APP} \\ F_{X-APP} \\ F_{Y-APP} \end{Bmatrix} = \begin{bmatrix} k_1/4 & k_1/4 & k_1/4 & k_1/4 \\ -k_2 & 0 & k_2 & 0 \\ 0 & -k_3 & 0 & k_3 \end{bmatrix} \begin{Bmatrix} V_1 \\ V_2 \\ V_3 \\ V_4 \end{Bmatrix} \tag{4.4}$$

These calibration equations were presented in a slightly different form in previous work [1, 2]. Since multiple values for the $\{\boldsymbol{F}\}$ and $\{\boldsymbol{V}\}$ vectors are available during calibration, an over-determined linear system is formed and a least squares or equivalent alternative method [147, 148] may be used to solve for the terms in [$\boldsymbol{k}$]. The least squares method represents a general calibration method; compensation is provided for changes in voltage outputs due to a mesa addition, axis rotation or reversal, or a single resistor with anomalous sensitivity. This implies that [$\boldsymbol{k}$] determined using the least squares method will have 12 coefficients, and will still be arranged in the 3×4 matrix format shown in Equation (4.4). In order to solve for these 12 coefficients, at least 12 independent equations must be utilized. These equations are created from the $\{\boldsymbol{F}\}$ and $\{\boldsymbol{V}\}$ vectors and must include forces applied in all three load directions. Typically, the solution set to these equations is obtained using a Moore-Penrose pseudoinverse method [148, 149].

The least squares method also allows determination of cross-sensitivity terms. The relationships shown in Equation (4.3) are further modified to produce three functions as defined in Equation (4.5).

$$g_1(\boldsymbol{V}) = \left(\frac{V_1 + V_2 + V_3 + V_4}{4}\right), g_2(\boldsymbol{V}) = (V_3 - V_1), g_3(\boldsymbol{V}) = (V_4 - V_2) \tag{4.5}$$

These functions may then be substituted into Equation (4.4) to produce the relationship shown in Equation (4.6).

$$\{\boldsymbol{F}\} = [\boldsymbol{B}]\{\boldsymbol{g}(\boldsymbol{V})\}$$

$$\begin{Bmatrix} F_{N-APP} \\ F_{X-APP} \\ F_{Y-APP} \end{Bmatrix} = \begin{bmatrix} b_{11} & b_{12} & b_{13} \\ b_{21} & b_{22} & b_{23} \\ b_{31} & b_{32} & b_{33} \end{bmatrix} \begin{Bmatrix} g_1(\boldsymbol{V}) \\ g_2(\boldsymbol{V}) \\ g_3(\boldsymbol{V}) \end{Bmatrix} \tag{4.6}$$

The Moore-Penrose pseudoinverse method may then be applied to produce the terms in the [$\boldsymbol{B}$] matrix. Provided that the response from the sensor being examined is adequately decoupled by Equation (4.5), the diagonal terms in the [$\boldsymbol{B}$] matrix (b_{11}, b_{22}, and b_{33}) should be approximately equivalent to the k_1, k_2, and k_3 terms defined in Equation (4.3) and the remaining off-diagonal terms should be null. Moreover, the least squares method allows higher order (or other nonlinear) terms to be added to the calibration equations, as exemplified by Equation (4.7).

$$\{\boldsymbol{F}\} = [\boldsymbol{C}]\{\boldsymbol{f}(\boldsymbol{V})\} + [\boldsymbol{D}]\{\boldsymbol{h}(\boldsymbol{V})\} + \cdots \tag{4.7}$$

The least squares method was tested using numerical data points created using a FEA model similar to the model used to produce the sensitivity values shown in Figure 4.24. These data points were required to include $\{\boldsymbol{F}\}$ and $\{\boldsymbol{V}\}$ values from loads applied in the F_N, F_X, and F_Y directions. This least squares analysis produced:

$$[\boldsymbol{B}] = \begin{bmatrix} 0.0177 & -0.0007 & -0.0004 \\ -0.0005 & 0.0824 & -0.0035 \\ -0.0004 & 0.0011 & 0.0890 \end{bmatrix} \tag{4.8}$$

Inverting the [$\boldsymbol{B}$] matrix and dividing the terms by the applied voltage (5V) produced the sensitivity matrix [$\boldsymbol{E}$] shown in Equation (4.9):

$$[\boldsymbol{E}] = \frac{[\boldsymbol{B}]^{-1}}{V_{IN}} = \begin{bmatrix} 11.2929 & 0.0911 & 0.0568 \\ 0.0698 & 2.4271 & 0.0959 \\ 0.0500 & -0.0301 & 2.2456 \end{bmatrix}, \tag{4.9}$$

$$\{\boldsymbol{g}(\boldsymbol{V})\} = V_{IN} \cdot [\boldsymbol{E}]\{\boldsymbol{F}\}$$

Comparing the diagonal terms in [$\boldsymbol{E}$] with the average normal and Y-axis shear sensitivity values shown on Figure 4.24 (N_S =11.48mV/V-N and Y_S =3.01mV/V-N) produced differences of 1.71%, 23.9%, and 33.9% between e_{11} and N_S, e_{22} and X_S, and e_{33} and Y_S, respectively. (This comparison assumed that $X_S = Y_S$.) These results indicated that the least squares analysis detected a significant amount of cross-sensitivity in the X- and Y-axis directions for this sensor configuration. However, due to the shallow 20° angle of X- and Y-axis load application, this discrepancy in sensitivity was more likely due to the input data set being biased toward normal load application, thus illustrating the importance of thorough device calibration. Calibration methods for the sensor array are discussed further in Section 6.3.

4.6 - Conclusions

The manufactured sensor pads have been characterized using experimental and numerical methods. This characterization allowed sensitivity trends to be determined as specific geometric and material parameters were varied. Sensor pad parameters varied included the size and location of the force application site, mesa height, membrane thickness, piezoresistive doping levels, and position of the piezoresistors on the membrane. Increasing the mesa height was shown to cause the greatest increase in shear sensitivity, and decreasing the membrane thickness was shown to cause the greatest increase in normal sensitivity. Adding asymmetry or load misalignment was shown to be the largest cause of experimental error. In addition, a substantial decrease in both shear and normal sensitivities was caused by an increase in impurity doping concentration due to the related decrease in piezoresistive coefficients.

Chapter 5: Deployment and Packaging[2]

Specific details regarding the deployment of the MEMS sensor array on the scoliosis pedicle screws are provided. Through-silicon vias were utilized as part of a packaging solution to structurally and electrically connect the sensor array to an FPCB with a minimized footprint. Several technologies were studied during the development of this packaging solution, including circuit board design, wire bonding, and flip-chip. In addition, the use of several types of adhesives has been explored. Adhesives were used for structural adhesion, electrical conductivity, and sealing in this application. The performance and biocompatibility of these solutions has been examined. Ohmic electrical connections with resistances below 1Ω were made between the MEMS sensor array and FPCB using TSVs filled with isotropic conductive adhesive and various flip-chip techniques.

5.1 - Introduction

Deployment of the MEMS sensor array on the pedicle screws used in scoliosis correction surgery presented several unique challenges. The MEMS sensing components, wireless module, and power module must be structurally attached to the pedicle screw, electrically connected, and then sealed using biocompatible materials. This packaging solution is a retrofit of the existing surgical instrumentation, and as such must have an extremely low profile. In addition, it must be possible for the surgeons to collect 3D force and moment information using this sensor array without radically altering the surgical procedure.

An overview of the packaging solution developed to deploy the sensor array onto the pedicle screws is as follows: The TSV solution described in Section 3.7 has been used to reduce the footprint size of the MEMS sensor pads, and also allows them to be flush-mounted onto an FPCB. The FPCB was then wrapped around the head of the pedicle screw, providing connectivity and space for the power and wireless modules to be mounted on the outside surfaces of the screw head. The sensor pads were positioned within the U-shaped notch of the pedicle

[2] Some of the material in this chapter has been submitted for publication as a paper in the *Journal of Micromechanics and Microengineering.*

screw in a manner that allows the membranes to be appropriately deformed by the rod during load application. Adhesives were then used to form a protective layer over the instrumented screw head in sensitive areas where damage or contamination could occur. An image of a sensor array deployed on a screw head mockup is shown in Figure 5.1.

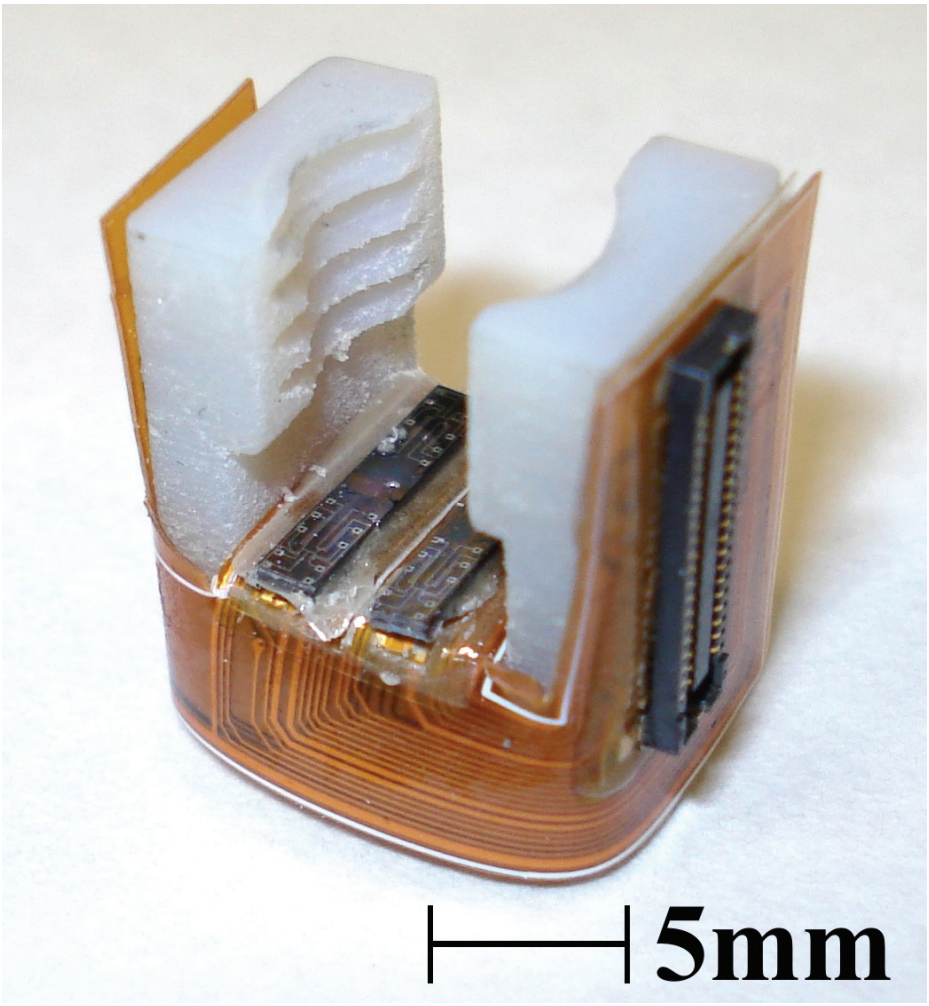

Figure 5.1. A scoliosis pedicle screw mockup with the sensor strips and FPCB attached. The component on the right of the image is the connector for attaching the wireless module.

Successful implementation and development of this packaging solution required research in several areas. The layout and material selection for the FPCBs was examined, including methods to apply and bond the FPCB to the pedicle screw.

Mounting the MEMS sensor pads and supporting components onto the FPCBs utilized techniques in wire bonding, flip-chip, soldering, and adhesive selection. Sealing and providing mechanical protection for the deployed sensor array has also required research into adhesive selection, as well as determining the biocompatibility of materials and the sterilizability of the construct. Additionally, it is important to ensure that the packaging of the devices does not negatively affect the sensitivity of the MEMS sensing components. All phases of the development of this packaging process have considered that devices produced should be durable enough to survive temporary implantation into a patient during the correction phase of a spinal fusion surgery.

5.2 - Circuit Board Design

Flexible printed circuit boards, as introduced in Section 2.9.2, are useful for the deployment of low-volume MEMS devices. The scoliosis surgery application specifically required the use of FPCBs to allow the components to be wrapped around the head of the pedicle screw. A double layer FPCB composed of a biocompatible Kapton polyimide core with gold-plated copper traces was designed and printed. Wireless and power modules were designed to be attached to the FPCB using standard surface-mounted connectors. The MEMS sensor array, consisting of two sensor pads placed together on a single piece of single crystal silicon and referred to as a strip, was also provided with mounting locations on the FPCB. Two strips were required on each FPCB, and each pair used the pinout configuration shown in Figure 5.2. The FPCB served to connect each of the 40 connections to the appropriate terminal(s) on the power and wireless modules.

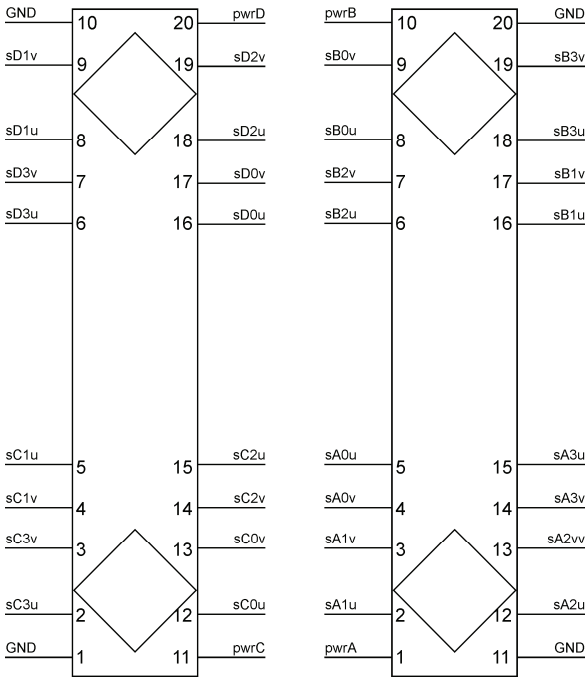

Figure 5.2. The pinout configuration used to determine connectivity on the FPCB.

The sensing regime used for this device required that the sensing strips be accurately aligned with the notch in the head of the spinal screw. This ensured that contact occurred between the strips and the rod at appropriate points, aligning applied loads with the sensing pad membranes. Alignment was achieved by shaping the FPCBs to be precisely folded around the spinal screw, which also achieved connectivity between the sensor strips in the notch and the power and wireless components positioned on the outside of the screws. Several variations of the FPCB design allowed the strips to be mounted using wire-bonding (discussed in Section 5.3) or flip-chip (discussed in Section 5.4) techniques. In addition, several methods of folding the FPCB around the screw head were devised, and separate FPCB patterns were produced. An image of an FPCB layout created using CAD software (Altium Design Explorer DXP) is shown in Figure 5.3. A photograph of the corresponding manufactured FPCB is shown in Figure 5.4. The FPCBs were manufactured by Dynamic & Proto Circuits Inc.

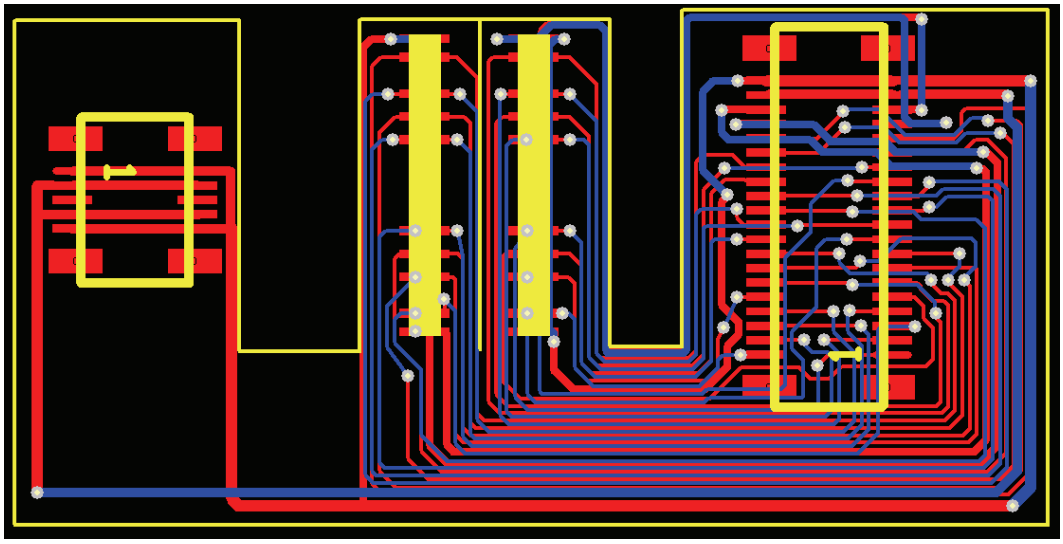

Figure 5.3. An image of the FPCB layout used for the pedicle screw FPCB.

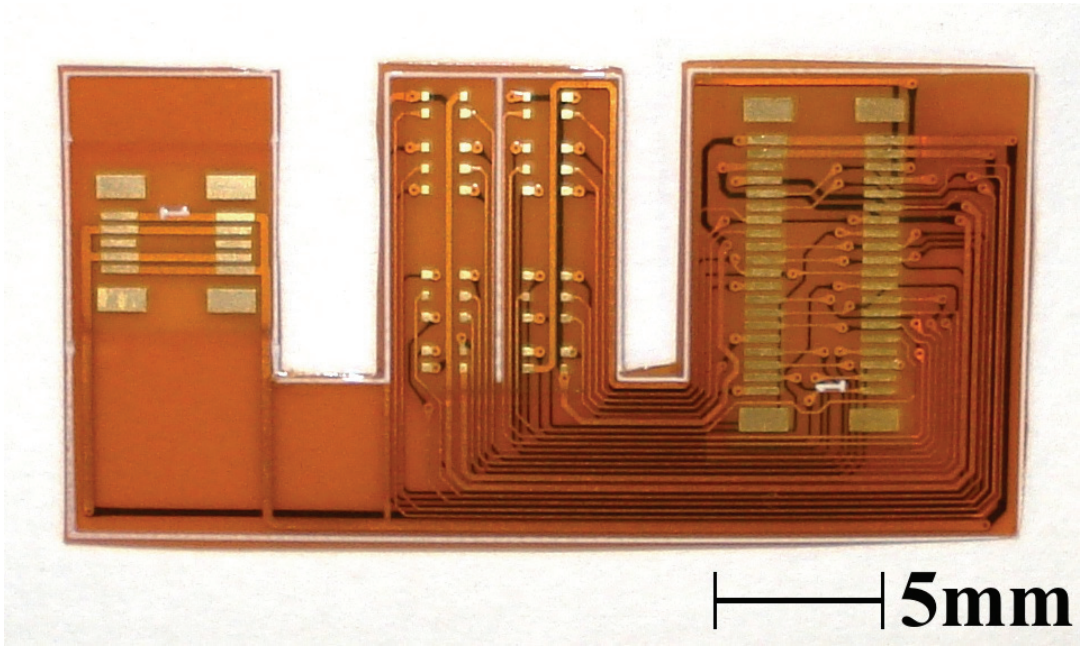

Figure 5.4. A photograph of the printed FPCB with reliefs removed to facilitate placement on the head of the pedicle screw.

Prior to designing the FPCB layout shown in Figure 5.3, several preliminary PCB and FPCB designs were produced. This was done for the purpose of experimentation with bonding and layout techniques. It was determined that appropriate mounting methodology using wire bonding or flip-chip should be

developed for the sensing pads and strips before experimenting with the complete package layout. A close-up image of a PCB designed to connect to a single-piezoresistor sensor pad using flip-chip is shown in Figure 5.5, and an image of a single-layer FPCB designed to connect to a scoliosis sensor strip using wire bonding is shown in Figure 5.6. These designs allowed various wire bonding, flip-chip, and adhesive packaging techniques to be tested.

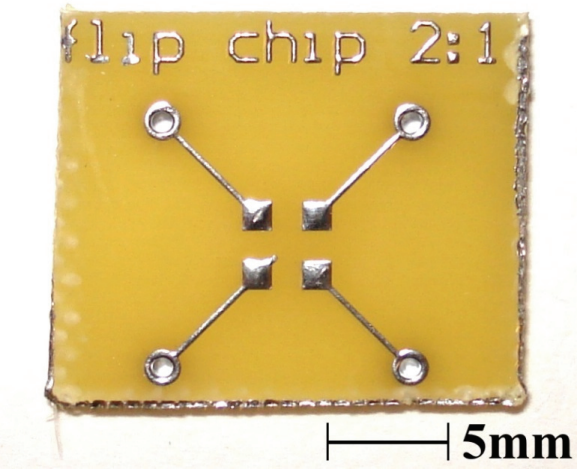

Figure 5.5. A PCB used to determine appropriate flip-chip bonding techniques for the single-piezoresistor sensor pads.

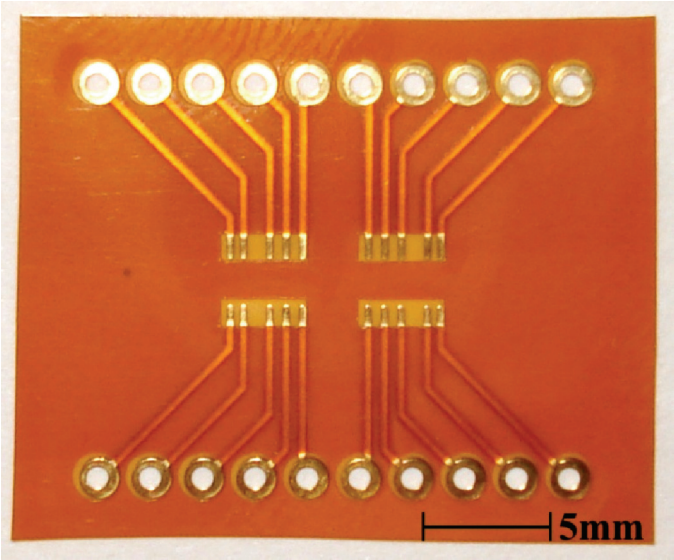

Figure 5.6. An FPCB used to determine wire bonding techniques for the scoliosis sensor strips.

The mechanical properties of the FPCBs were also evaluated. Due to the small radius, multi-directional bends required to fold the FPCB around the pedicle screw, there was a risk of tearing. This risk was more pronounced with the two-layer FPCB material tested. Figure 5.7 shows an image of a two-layer FPCB that was torn at a fold point. This tear occurred as the FPCB was folded and twisted simultaneously to allow the sensor strips to lie flat within the screw notch. An alternative FPCB layout which used a different folding pattern experienced tearing at the same location, as illustrated in Figure 5.8. Reducing the amount of FPCB folding while fitting the sensor array in the screw notch was required to successfully deploy the sensor array on the pedicle screw. This was accomplished by building up adhesive material within the screw notch, and is discussed further in Section 5.5.2.

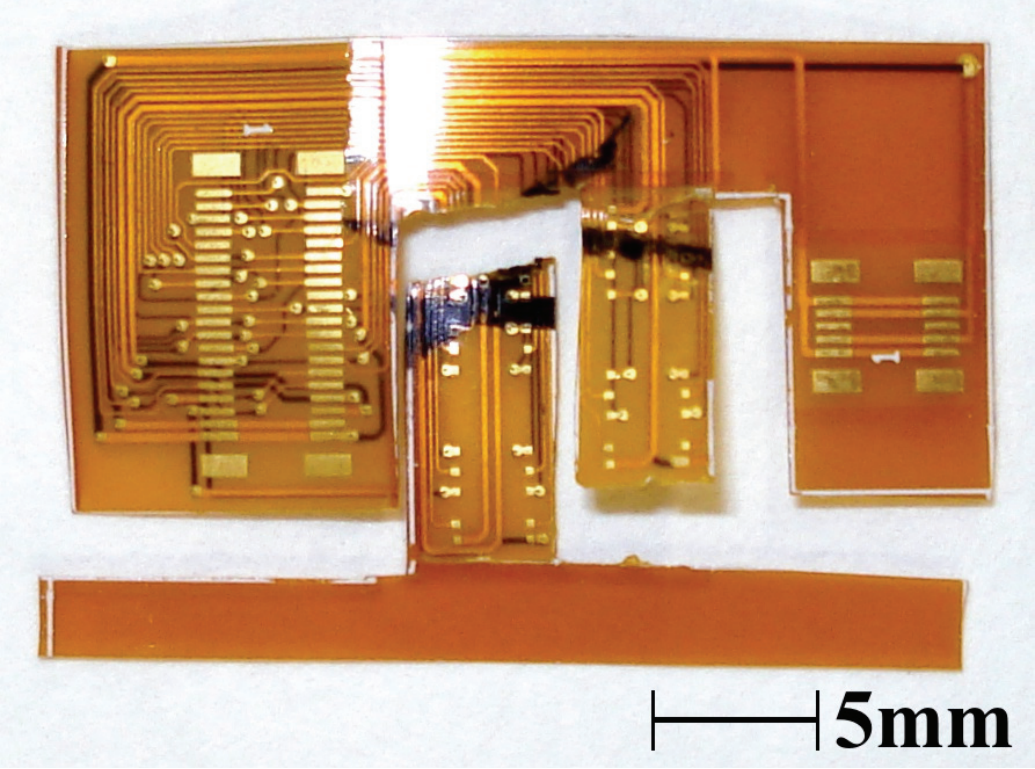

Figure 5.7. A close-up photograph of a two-layer FPCB showing failure at a fold point near the pedicle screw notch.

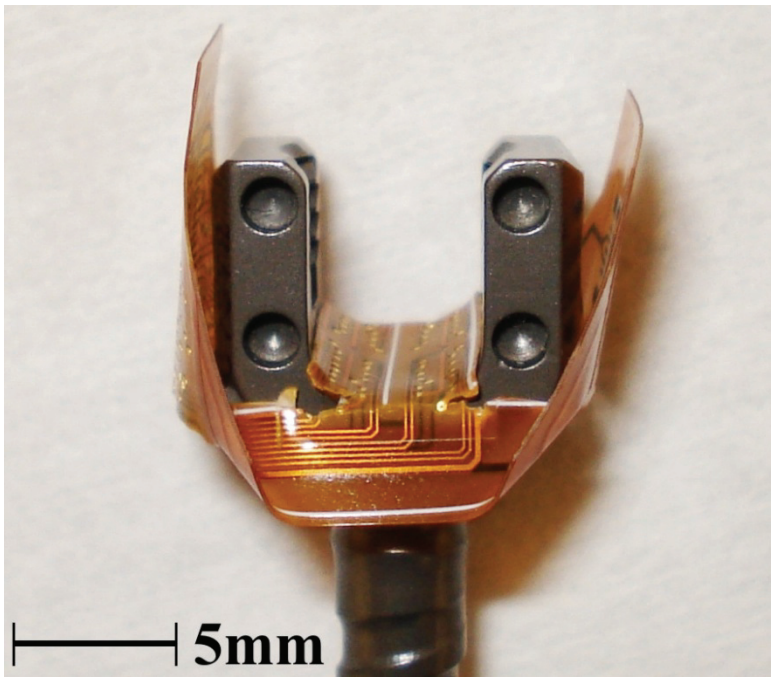

Figure 5.8. A close-up photograph of a screw head with an FPCB folded around it. Tearing is observed at the same location as shown in Figure 5.7.

5.3 - Wire Bonding

Wire bonding, as introduced in Section 2.9.3, is a packaging technique that creates electrical connections using fine-pitched wires. To differentiate wire bonding from soldering or other electrical interconnection methods, it is specified that a wire bond use heat, force, and ultrasonic energy to locally weld the fine wires to contact pads. The wire bond technology used for packaging the sensor pads and scoliosis sensing array was ball-bonding using 25.4µm (1mil) gold wire. This method was chosen as the ball-bonding head allowed the user to place the second (stitch) bond away from the first (ball) bond in any direction. This reduced the need to reposition the sensor pad and PCB/FPCB during the wire bonding process, and added some flexibility in terms of device and circuit board layouts. The ball bonds were also found to be more reliable than the wedge or stitch bonds when connecting a variety of materials. Coined bumps (single ball bonds which have been compressed to a uniform height) were also used in this packaging solution for flip-chip applications.

A wire bonder (West·Bond 747677E) that was capable of being set up for either ball-stitch or wedge-wedge bonding was used for the wire bonding performed, and is shown in Figure 5.9. This wire bonder allowed several bonding parameters to be varied, which allowed the bonds to be adjusted for differing materials. Ultrasonic energy applied could be adjusted through the ultrasonic power and time settings, bonding force could be altered, and the chip temperature could be specified. Parameters affecting the ball forming power, wire tail length, and wire loop height could also be adjusted, having a secondary effect on the bond and wire tail qualities. Furthermore, capillary tip (tool) shape, wire diameter, and wire material also affected the size and shape of the ball and stitch bonds produced. Of these parameters, ultrasonic energy was the most significant to bond adhesion and could be adjusted individually for the ball and stitch bonds used in the ball-bonding process.

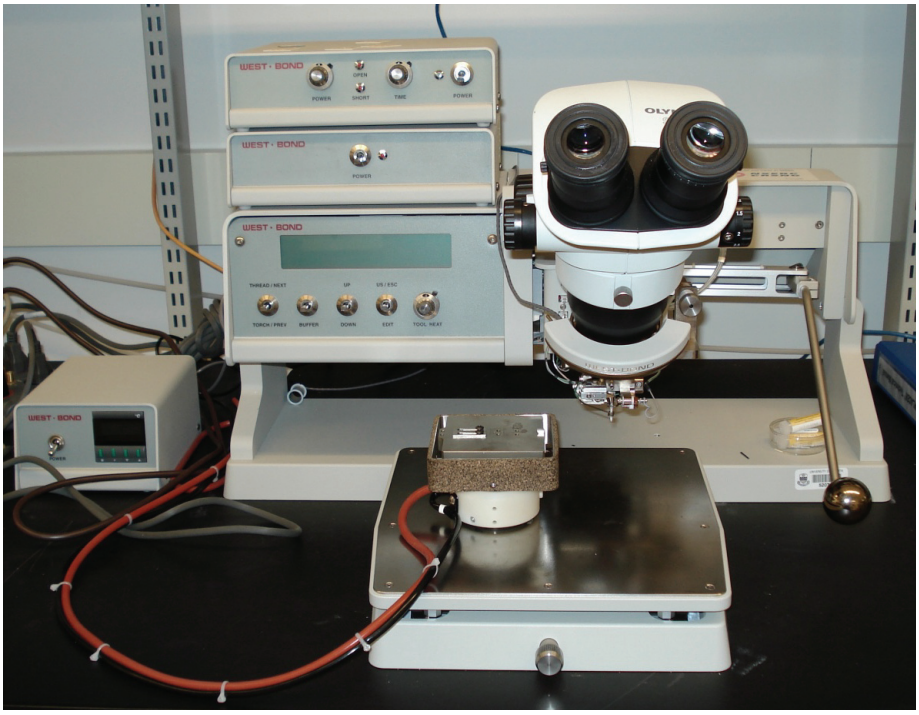

Figure 5.9. The West·Bond 747677E wire bonder.

Appropriate ultrasonic energy for wire bonding depended upon the pad material, capillary tool choice, and ultrasonic power and time settings. The wire bonder

allowed the power to be varied between 0-2W and the time to be varied between 0-999ms. Inadequate energy created weak or non-sticking bonds due to a poor weld between the pad and the wire. This was often characterized by a reduced contact area between the pad and the wire. In addition, ball bonds with inadequate energy were often prone to failure at the wire tail coming out of the ball; the wire tail may not have been heated appropriately during bonding, causing damage due to a lack of wire material ductility. Figure 5.10 shows several SEM images of a ball-stitch bond on an aluminum pad created with inadequate ultrasonic energy.

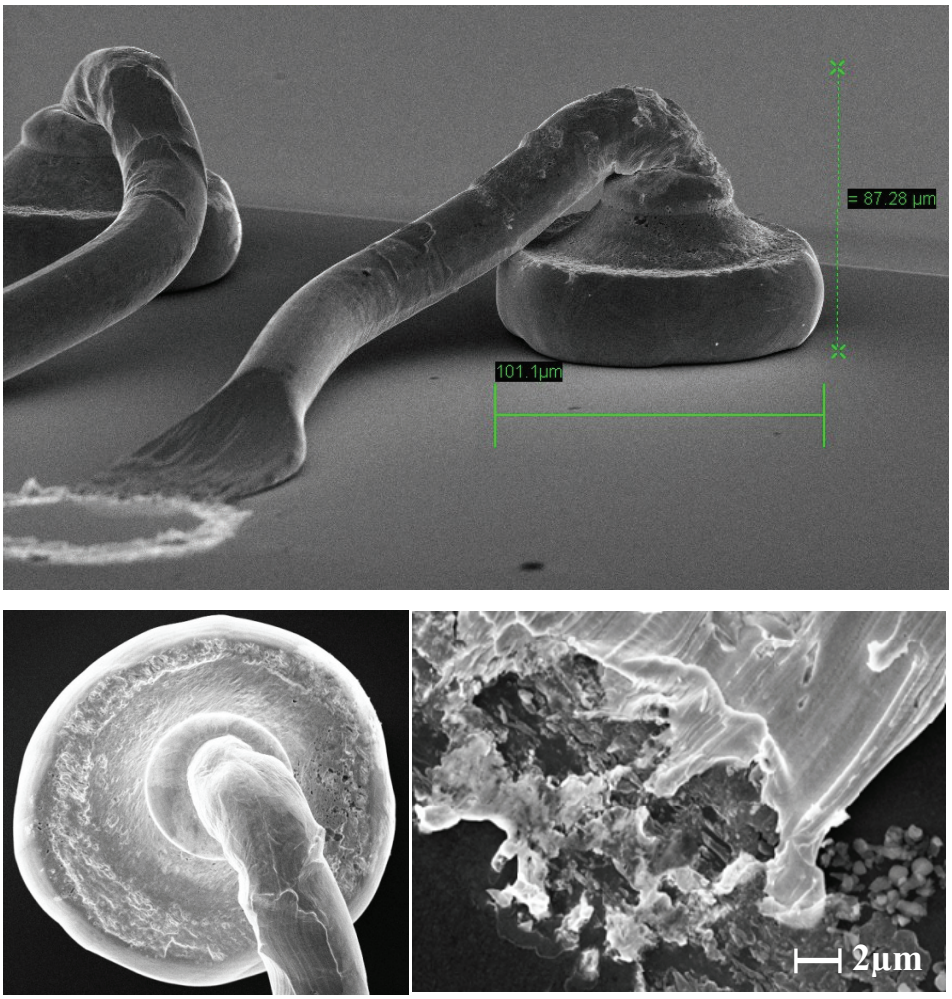

Figure 5.10. A gold wire to aluminum pad ball-stitch bond created with inadequate ultrasonic energy. The lack of energy was created by reducing the ultrasonic time to 10ms. Ultrasonic power was set to 600mW.

Conversely, excessive ultrasonic energy also created poor bonds when connecting the sensor pads. The additional energy created contact areas that were asymmetrical and puddle-like, with substantial amounts of wire material flowing away from the force application zone of the capillary tool and the wire tail. Excessive amounts of ultrasonic energy also had the potential to damage the contact pads, particularly during creation of stitch bonds. This not only created a weak second bond, but also often made additional bonding attempts impossible. Excessive ultrasonic energy applied by extending the bonding time introduced another risk during wire bonding: the user could break the bond by moving the bond head during energy application. Figure 5.11 shows several SEM images of a ball-stitch bond on an aluminum pad created with excessive ultrasonic energy.

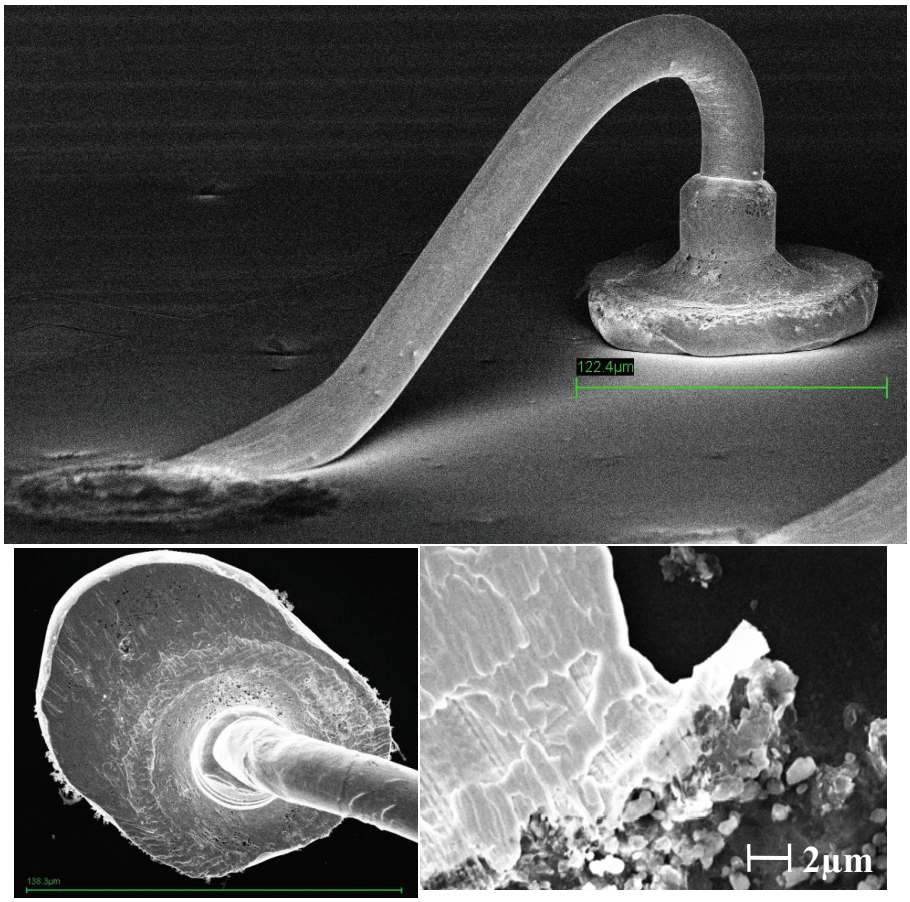

Figure 5.11. A gold wire to aluminum pad ball-stitch bond created with excessive ultrasonic energy. Increasing the ultrasonic power to 1200mW created the excess energy. Ultrasonic time was set to 30ms.

The wire bonder settings could also be adjusted to produce a single ball bond, referred to as a stud bump (or bump). Stud bumps produced in this manner would not terminate in a stitch bond on an adjacent connection pad, and as such were more useful for vertical packaging solutions such as flip-chip. Stud bumps could also be used to reinforce the stitch bonds when bonding to pad materials that achieved better bond fixation from the ball bond process. Figure 5.12 shows an SEM image of a gold stud bump attached to an aluminum pad. Bump size was largely controlled by the wire diameter (25.4µm, in this case), although some variation in gold volume could be achieved by adjusting the ball forming power and wire tail length settings. The height of the bump was a more critical parameter to control, since bumps were typically used for vertical packaging applications. To control the height, a ball-bonding tool without a capillary tube was installed and used to flatten, or coin, the bumps. This coining tip used ultrasonic energy to flatten the tails on the bumps, making them all the same height. An SEM image of a coined bump is shown in Figure 5.13.

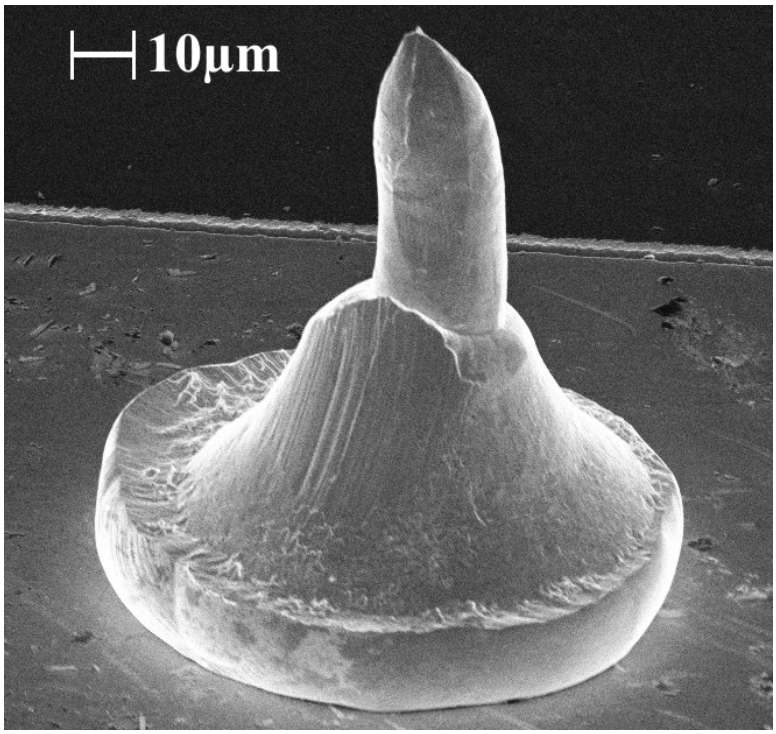

Figure 5.12. A stud bump (single ball bond) created using the wire bonder. The wire material was gold and the pad material was aluminum.

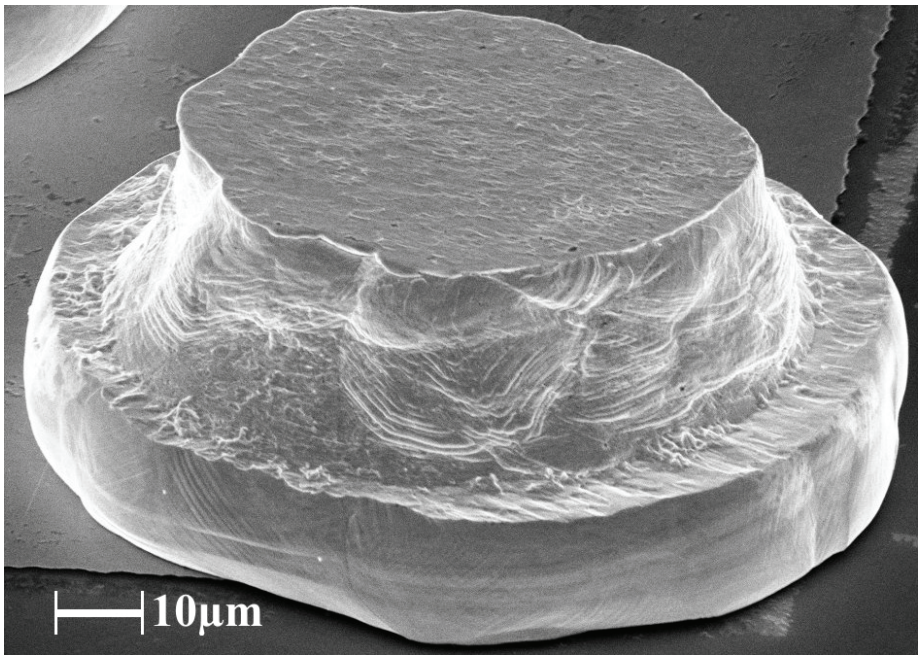

Figure 5.13. A coined bump (flattened stud bump) created using the wire bonder. The wire material was gold and the pad material was aluminum.

Special consideration of wire bonder settings needed to be made to ball-bond onto FPCBs. The polyimide core of the FPCBs was soft, and did not allow efficient transfer of ultrasonic energy from the tool through to the pad. To compensate for this damping effect, higher ultrasonic power settings needed to be used when bonding to FPCBs. Stitch bonds were less successful on FPCBs, so ball bonds were used when possible. Heating the FPCB was also shown to improve bonding performance, although temperatures had to be kept lower than 170ºC to avoid damaging the polyimide FPCB material. An SEM image of a gold bump on an FPCB is shown in Figure 5.14.

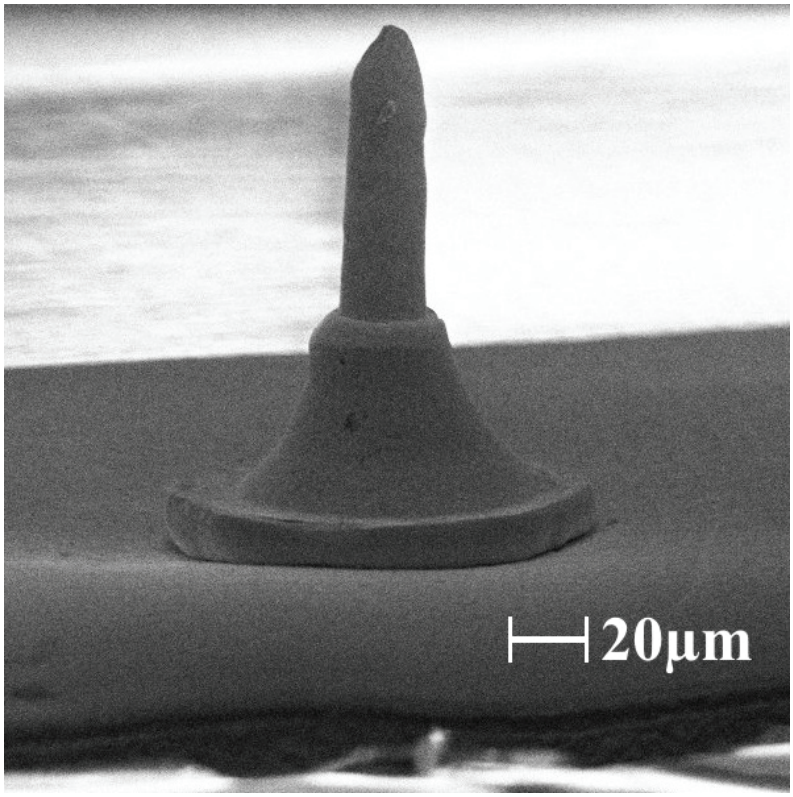

Figure 5.14. A gold stud bump produced on an FPCB. Significant deflection of the gold/copper pad is observed below the bond site.

Resolving problems with wire bonding, in general, required trial and error until appropriate machine parameters for the materials being bonded were determined. These problems typically manifested as non-conductive or non-sticking bonds and were amplified by the following factors: contamination of the pads, inappropriate pad material, non-planarity between the capillary tool tip and the pad face, inadequate clamping of the substrate leading to poor ultrasonic energy transfer, or an excessively small capillary tip diameter leading to inadequate stitch bond size. In addition, using new wire, new capillary tools, and ensuring that all surfaces being bonded were clean increased the chance of producing successful bonds. An image of a sensor pad wire bonded to a PCB is shown in Figure 5.15, and an image of a scoliosis sensor strip bonded to an FPCB is shown in Figure 5.16. In both processes, 1400mW of ultrasonic power was applied for 100ms to achieve the ball bond to the PCB/FPCB and 800mW of ultrasonic power was applied for 30ms to achieve the stitch bond to the aluminum pads on the MEMS devices. For

both cases, a conventional ball-bonding tool (Gaiser P/N 1513-15-625GM) was used and substrate heating was not applied. The four-wire resistance was measured between the pads on the sensor strip and FPCB using a microscope probing station (as described in Section 4.3) and high-resolution meter (Keithley Instruments Model 2400 SourceMeter). Average and standard deviation resistance values for wire bonds produced on the test device shown in Figure 5.16 are 0.1015Ω and 9.77mΩ, respectively. The resistances of these wire bond connections were ohmic; the current-voltage response of a typical wire bond is shown in Figure 5.17.

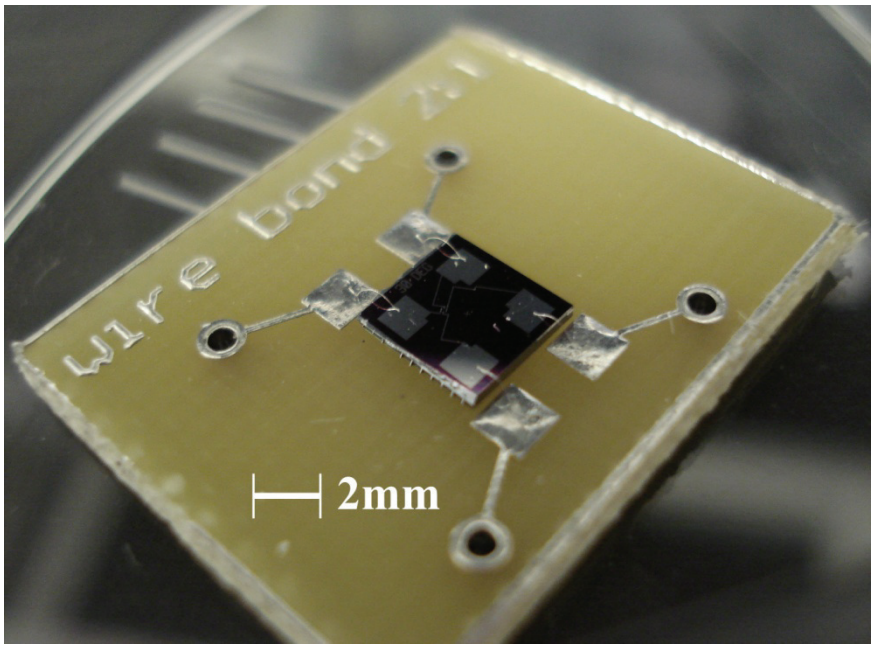

Figure 5.15. Gold wire bonds created between solder-covered copper pads on a PCB and aluminum pads on a sensor pad chip.

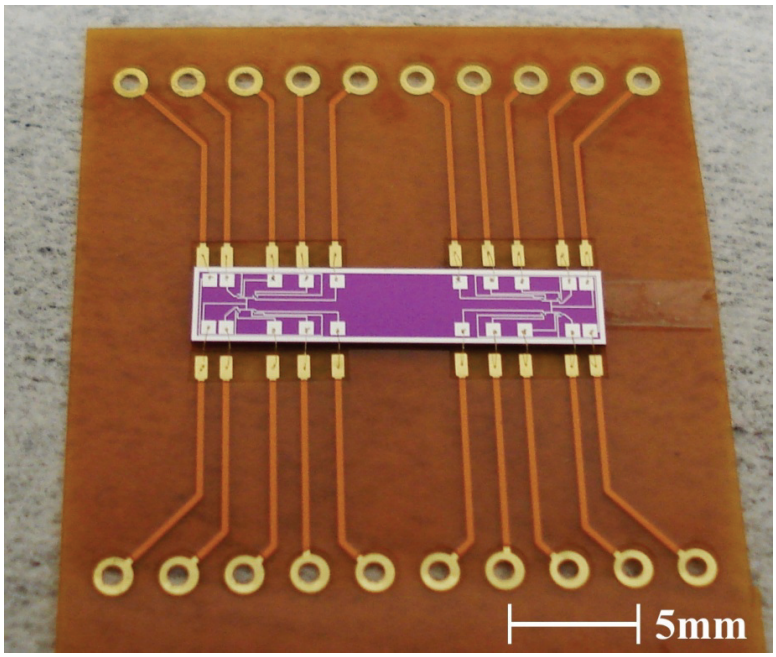

Figure 5.16. Gold wire bonds created between gold-plated copper pads on an FPCB and aluminum pads on a scoliosis sensor strip.

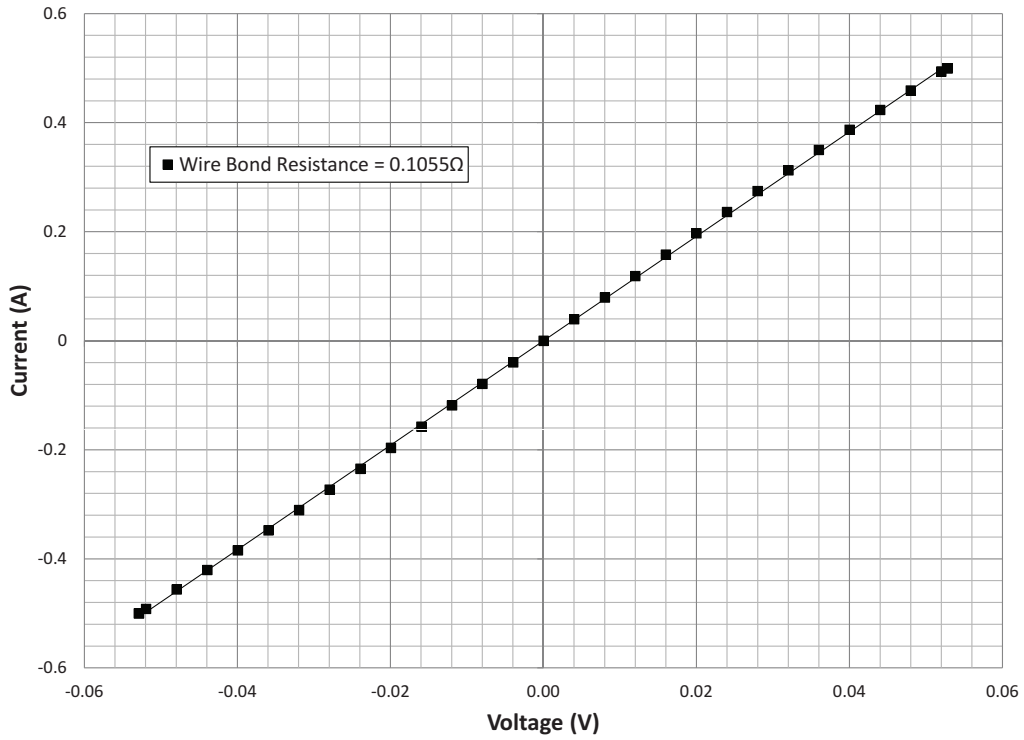

Figure 5.17. The current-voltage response of a typical wire-bond connection produced between a sensor strip and FPCB.

The wire-bonding process offered several advantages in terms of packaging the scoliosis sensor array: The setup for bonding was simple and it was easy to mount a substrate onto an FPCB for bonding, the electrical connection was completely visible so a lack of conductivity could be easily evaluated and remedied, and the mechanical adhesion of the substrate to the FPCB could be changed without affecting the electrical connections. This allowed the electrical and mechanical bond properties to be controlled independently. Disadvantages to the wire-bond process for this application included fragility, as the fine wires utilized using this process were exposed and prone to breaking or detaching from either the substrate or FPCB. In addition, wire-bonding required more space on the FPCB when compared to flip-chip packaging methods. Protecting and sealing the exposed wire bonds using adhesive was also more difficult than sealing flip-chipped devices, and is discussed further in Section 5.5.2.

5.4 - Flip-Chip

Flip-chip packaging, as introduced in Section 2.9.4, is a technique primarily used for vertical device integration. A flip-chip system is fundamentally an alignment system which utilizes an optical square, prism, and multiple light sources to align the top of one chip (or package, PCB, FPCB, integrated circuit, etc.) with the bottom of another. After alignment is achieved, any of several methods may be used to bond the two chips together and electrically connect the contact pads. Flip-chip techniques typically use pressure, heat, ultrasonic energy, or a combination of these to create the electrical and mechanical bonds. These bonds are most often created with solder, although coined stud bumps, conductive adhesives (isotropic or anisotropic), and other materials and methods may also be used. Flip-chip techniques are particularly useful for creating electrical connections in low-volume packages and in devices which require their sensing elements to be positioned on the exterior of the package. When compared to wire bonding for the scoliosis surgery application, a flip-chip solution incorporating TSVs reduces the FPCB footprint by 33% at the sensor strip bond sites. The flip-

chip method also increases device durability by removing exposed fine wires from the package.

A variety of flip-chip techniques were evaluated for their effectiveness in creating packages for the scoliosis sensor array. These techniques were attempted using a flip-chip system (Finetech Fineplacer Pico) equipped with ultrasonic, bonding force, substrate heating plate, and chip contact heating modules. An image of this system is shown in Figure 5.18. Experiments attempting to bond the sensor chips to the FPCBs (or PCBs) typically used the thermal and force modules in combination to perform thermocompression bonding. Alternatively, experiments using the thermal, force, and ultrasonic modules in combination performed what is referred to as thermosonic bonding. Preliminary experiments determined that a temperature ceiling of approximately 260°C should be maintained for PCB materials and a ceiling of 170ºC should be maintained for FPCB materials. Exceeding these temperature limits was found to cause scorching or melting of the PCB/FPCB. Images of a PCB and an FPCB that were exposed to excessive temperatures are shown in Figure 5.19 and Figure 5.20, respectively.

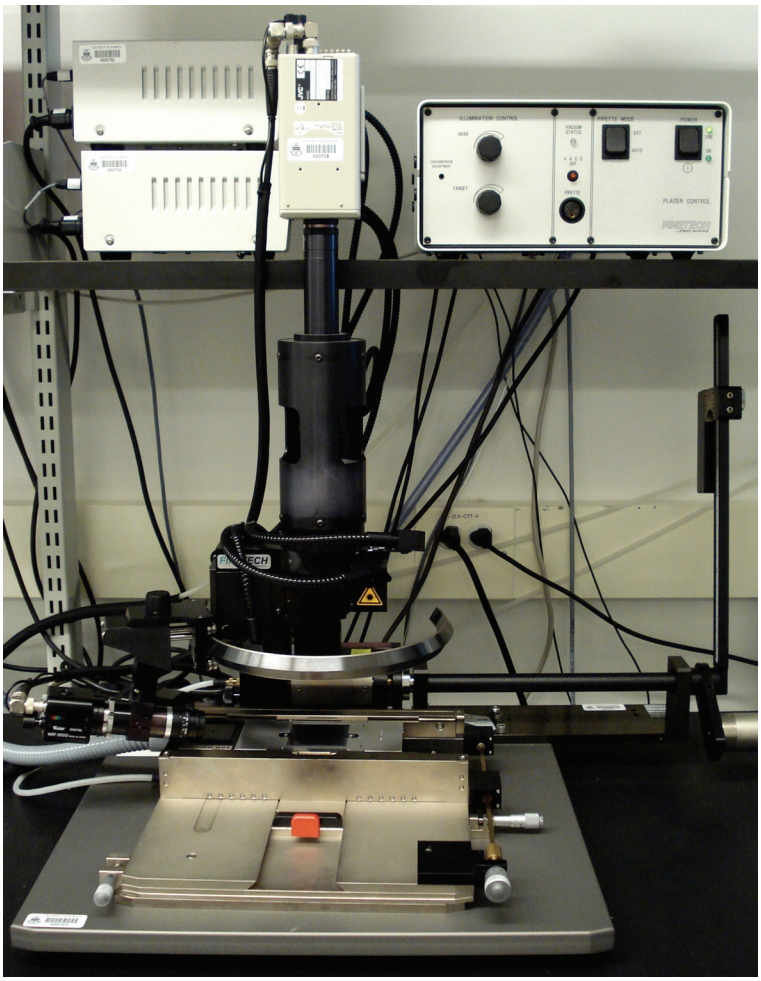

Figure 5.18. The Finetech Fineplacer Pico flip-chip system.

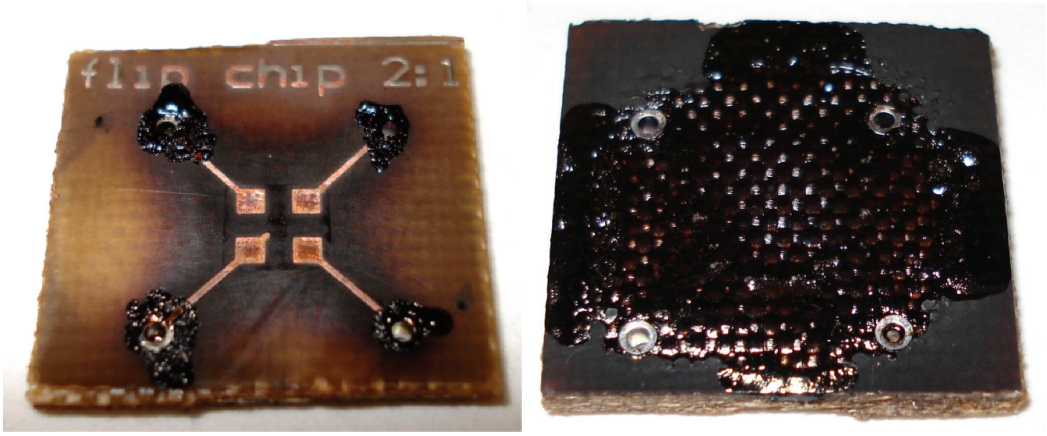

Figure 5.19. A PCB exposed to excessive temperature (285ºC) while attempting a thermal flip-chip bond.

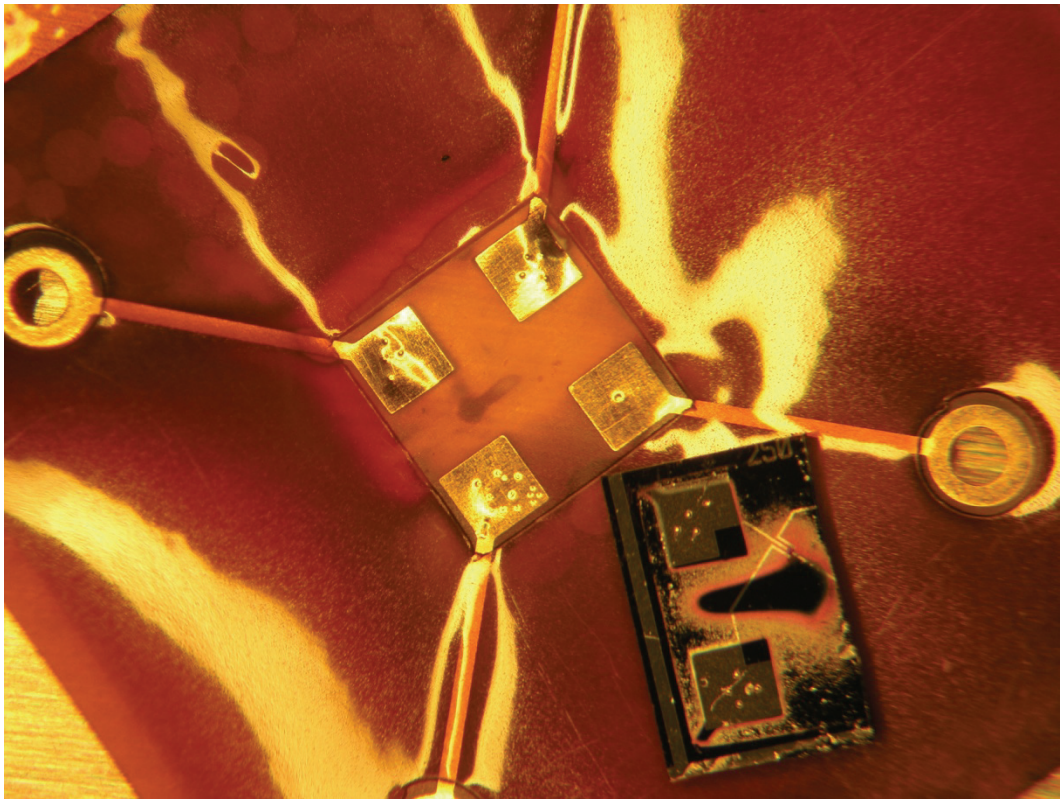

Figure 5.20. An FPCB exposed to excessive temperature (260ºC) while attempting a thermal flip-chip bond.

Despite the dramatic failure modes which occurred when attempting thermal flip-chip bonding using excessive temperatures, unsuccessful flip-chip bonds normally produced only non-conductive electrical connections. This failure mode was observed at some point for all types of flip-chip bonds attempted. Another common result of an inadequate bond was the mechanical disconnection of the chip from the FPCB. This was typical for bonds that attempted to use coined stud-bumps without an adhesive underfill. Such techniques typically used thermosonic or thermocompression bond settings to bond several coined bumps (previously bonded to a chip with a wire bonder) to an FPCB. The energy produced with the flip-chip system was inadequate to weld the coined bumps to the FPCB, however, this method would often produce a conductive electrical connection until the chip was moved and mechanically separated from the FPCB.

Flip-chip bonding methods utilizing solder produced more success. The solder, particularly 63/37 tin-lead solder which has a melting point of 183ºC, was able to reflow during flip-chip bonding without exceeding the temperature limits for the PCB and FPCB materials. This allowed thermosonic and thermocompression techniques to be used effectively, and also produced strong mechanical connections. Care needed to be taken when applying the solder, as excessive solder would create short circuits between adjacent contact pads. This issue with solder reflow was found to be partially mitigated by applying coined bumps on the chip contact pads prior to flip-chip bonding, as the vertical gap created by the coins prevented short circuiting. Solder could be applied by either tinning the contact pads on the PCB or by affixing an appropriately sized solder ball between the chip and the circuit board using flux. The manual process used to apply the solder was a considerable disadvantage due to the excess time consumed during application. Another disadvantage to solder methods was the material itself, as lead-based solder (with the lower melting point) is not a biocompatible material.

To accommodate the drawbacks to flip-chip methods using solder, a hybrid solution using stud bumps was explored for bonding the scoliosis sensor to an FPCB. First, coined gold stud bumps were placed on the sensor chip that is to be mounted on the FPCB using a wire bonder. Their small size (<100μm in diameter) allowed several to be placed on each pad. Biocompatible, non-conductive adhesive was then applied between the pads to be bonded. The flip-chip system was used to align the chip and FPCB pads; pressure and heat created by the system (thermocompression bonding) was used to remove the adhesive from between the stud bumps and the FPCB pads and to cure the adhesive. Ultrasonic power may also be applied (thermosonic bonding) to further remove adhesive from between the coined stud bumps and FPCB pads. A conductive path was created from the chip to FPCB through the stud bumps, and the adhesive served as an underfill material and achieved the mechanical bond. A schematic of this process is shown in Figure 5.21. Top-view microphotographs of the chip and FPCB are shown in Figure 5.22, and a cross-sectional view of a bond is shown in

Figure 5.23. This hybrid flip-chip bonding technique offered advantages over solder methods in terms of biocompatibility and speed of production. In addition, this method eliminated short circuiting issues due to solder reflow. To increase the compensation for a lack of planarity between the sensor pad chip and FPCB, multiple coined stud bumps could also be stacked on top of each other, as shown in Figure 5.24.

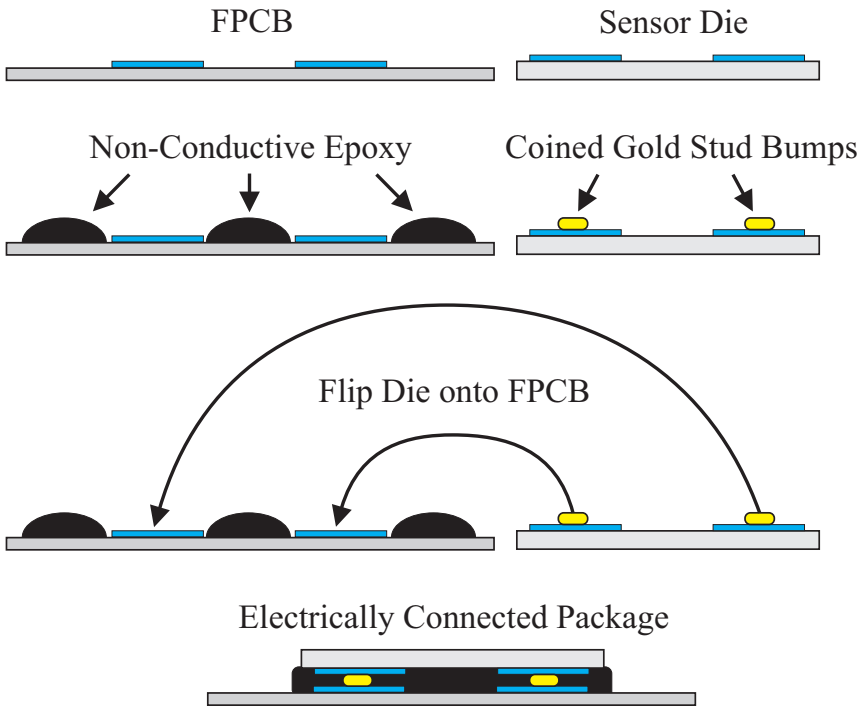

Figure 5.21. The flip-chip bonding process using coined stud bumps and an underfill adhesive. A sensor pad (die) is bonded to an FPCB.

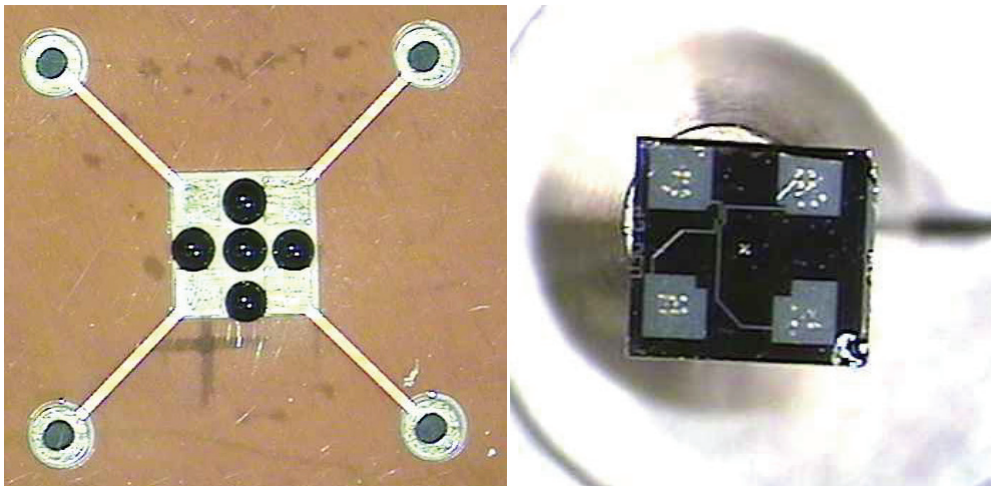

Figure 5.22. Microphotographs of the FPCB and sensor pad chip being flip-chip bonded using coined stud bumps and underfill adhesive. Left: FPCB with non-conductive adhesive between the contact pads. Right: sensor pad chip with several gold coined stud bumps affixed to each pad using the wire bonder.

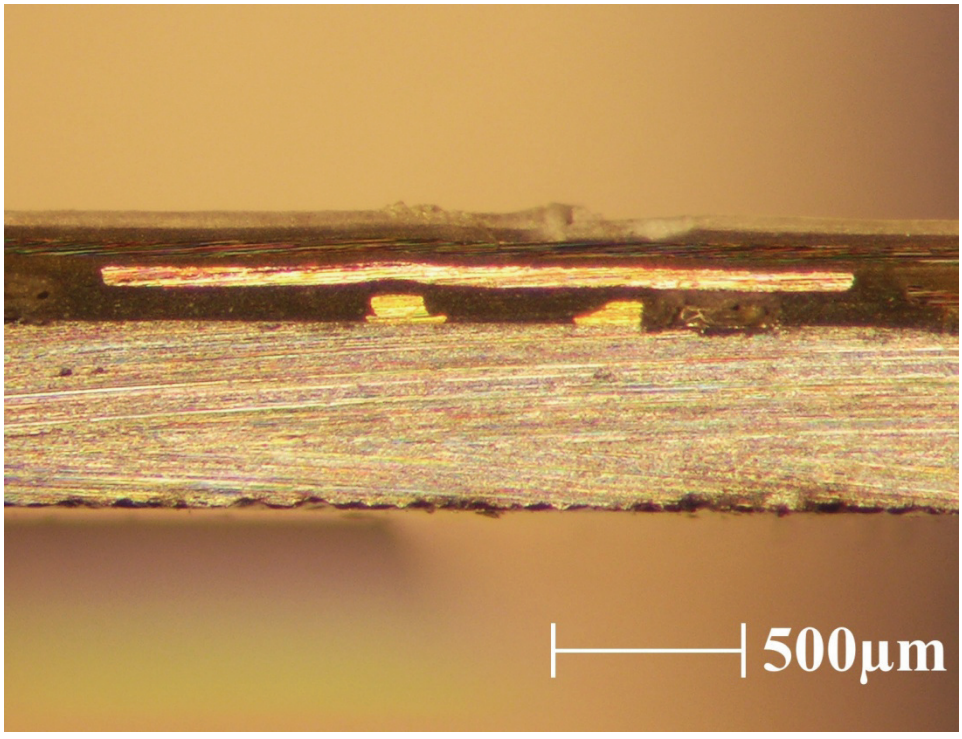

Figure 5.23. A cross-sectional view of a flip-chip bond between an FPCB and a sensor chip created using coined gold stud bumps and an underfill adhesive. The gaps between the stud bumps and the FPCB contact pad were caused by a lack of planarity during the flip-chip process.

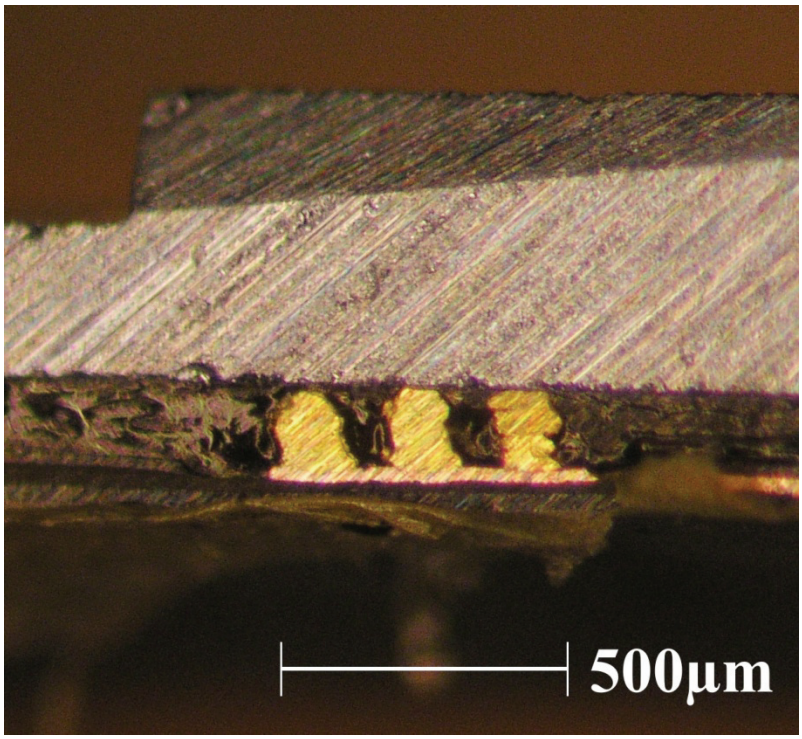

Figure 5.24. A cross-sectional view of a flip-chip bond between a sensor chip and FPCB created using stacked coined stud bumps and an underfill adhesive.

Anisotropic conductive adhesive (ACA) and anisotropic conductive film (ACF) were also examined for flip-chip attachment of the scoliosis devices to the FPCBs. These materials allow the creation of a layer that is conductive in the vertical direction but insulating in the two perpendicular directions. This is typically accomplished by suspending conductive particles in a liquid or solid adhesive medium. A vertical conductive path can be produced by compressing the ACA or ACF to bring conductive particles together, and then applying heat to cure the adhesive. The use of an ACF is shown schematically in Figure 5.25 for a flip-chip application. The use of ACA or ACF enabled electrical and mechanical connections to be produced in a single step, reducing packaging time by removing the requirement to produce coined gold stud bumps or to apply solder balls to the chips.

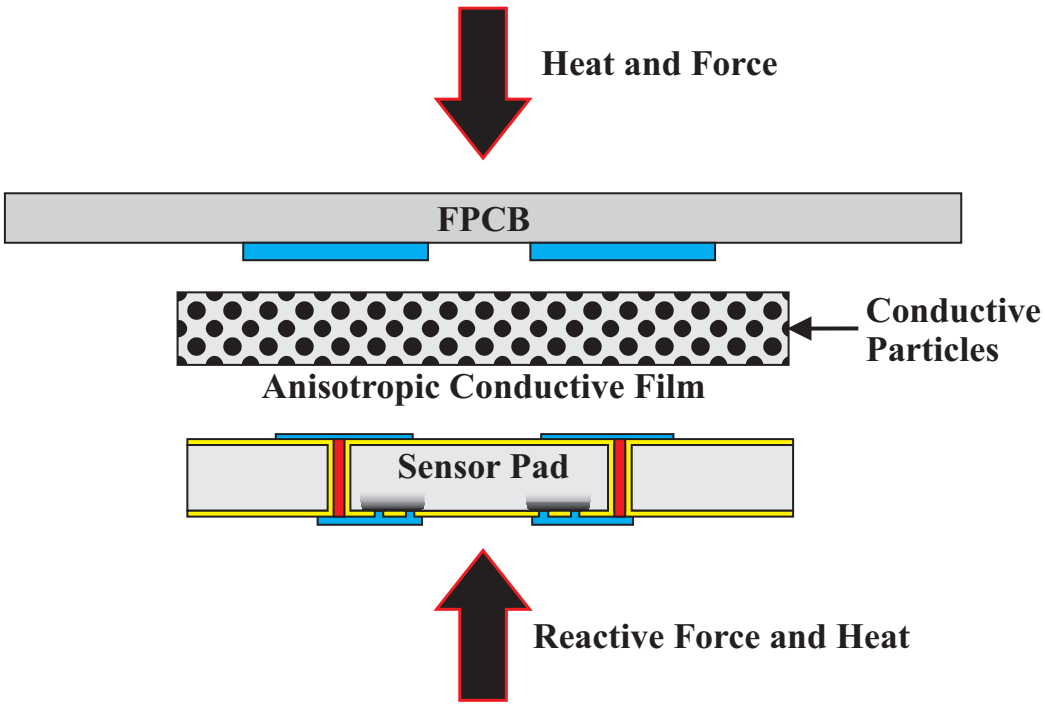

Figure 5.25. A schematic of an ACF being used in a flip-chip application.

Both ACA and ACF were evaluated during the flip-chip packaging process. The ACA (Henkel AG & Co. Hysol CE3126 epoxy) was dispensed with an adhesive dispenser (Nordson EFD Ultimus II) in a thin layer directly on the contact pads to be bonded. Epoxy application beyond the edges of the contact pads was acceptable, as the anisotropic conductivity of the material prevented shorting between adjacent pads. Excessively thick layers of epoxy, however, were found to produce non-conductive connections. The ACF (Creative Materials Inc. 121-24) was trimmed to fit over all of the pads on the chip that required bonding and electrical interconnection. The ACA and ACF were then cured using thermocompression flip-chip bond settings, which were selected according to the manufacturer's instructions.

5.4.1 - Flip-Chip Bond Resistance

Flip-chip bonds created with ACA, ACF, and coined gold stud bumps were examined for their electrical properties. As the flip-chip bonds were physically constrained between the MEMS sensor strip and FPCB being connected, it was

not possible to measure the resistance of these bonds in an isolated way. As such, four-wire resistance was measured between the top of the TSV on the sensor chip and the end of the FPCB trace. The resistance of the FPCB trace was measured separately and subtracted from the initial measurement, producing a resistance measurement of the TSV and the flip-chip bond in connected in series. Table 5.1 displays resistances for TSVs and flip-chip bonds produced with coined gold stud bumps, ACA, and ACF (at least seven bonds of each type were evaluated). The TSVs used for these measurements were 100µm in diameter, produced in 300µm thick substrates, and were filled with an isotropic conductive adhesive (more details on TSV filling are presented in Section 5.5.1).

Table 5.1. Four-wire resistance measurements of flip-chip bond types. Bond resistances were measured in series with TSVs as described in the main text.

Flip-Chip Bond	**Stud Bumps**	**ACA**	**ACF**
Mean Resistance (Ω)	0.4206	10.5986	1.2603
Standard Deviation (Ω)	0.2553	12.0491	1.8412

The flip-chip method utilizing coined gold stud bumps produced the lowest resistance in combination with a TSV. This was likely due to the compensation the raised bumps provided for any lack of planarity between the sensor chip and FPCB. Achieving planar surfaces was important during flip-chip packaging as it allowed the applied force to be distributed evenly over all of the electrical contact pads being bonded. A lack of pressure on any individual pair of electrical contact pads typically resulted in a non-conductive bond. The gaps shown in Figure 5.23 between the coined stud bumps and the FPCB contact pad are illustrative of a lack of planarity; a raised feature elsewhere in the bond plane did not allow the stud bumps to create an electrical connection with the FPCB.

The ACA method produced flip-chip bonds with the highest resistance in combination with a TSV. This was likely due to the thin layers of adhesive required being unable to compensate for any lack of planarity in the bond surface. The thicker ACF achieved substantially better results for this application. The current-voltage responses of the flip-chip bonds and TSVs were ohmic, as

illustrated for the coined gold stud bumps and ACF in Figure 5.26. As with the results presented in Table 5.1, this current-voltage response was produced for flip-chip bonds attached to conductive adhesive-filled TSVs with a diameter of 100µm in a 300µm thick substrate.

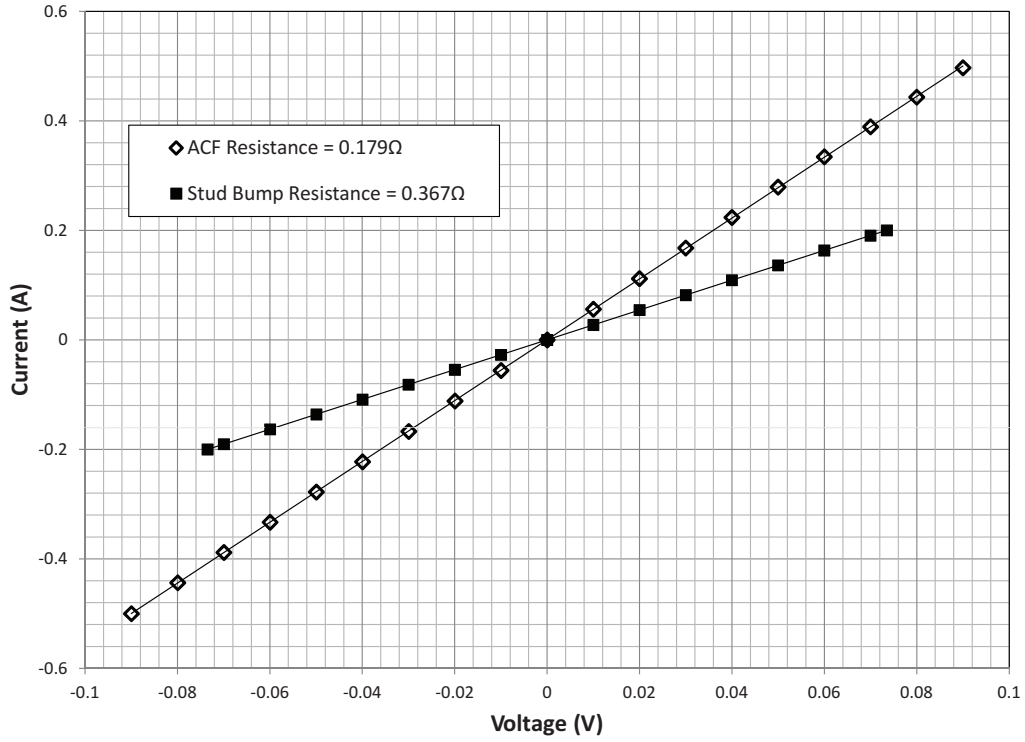

Figure 5.26. Current-voltage responses of coined gold stud bumps and ACF flip-chip bonds in combination with TSVs.

The high frequency responses of the flip-chip bond and TSV combinations were also evaluated. This was performed by connecting an AC function generator (Agilent 33220A) and oscilloscope (Tektronix TDS2024) to the probe station, as shown in the circuit diagram in Figure 5.27. Since the finely tipped probes had their own impedance properties, insertion losses and phase angle changes were measured at different frequencies with the samples attached and with the probe tips directly connected to each other. Insertion loss measurements are shown in Figure 5.28 and phase angle change measurements are shown in Figure 5.29. When compared to direct probe connection measurements, TSVs and flip-chip

bonds created with ACF produced similar sets of results. This supports the ohmic performance detected during DC characterization. When the direct probe connection measurements were compared to TSV and flip-chip bonds created with coined gold stud bumps, a substantial change in insertion loss and phase angle change was detected, beginning at a frequency of approximately 1kHz. This may have been due to capacitive effects between the adjacent stud bumps used to create the electrical path. A more advanced experimental setup would be required to rigorously characterize the high frequency responses of the flip-chip packaging solutions. However, for the low frequency data collection used for the scoliosis surgery application, either of the flip-chip bonding methods presented is appropriate.

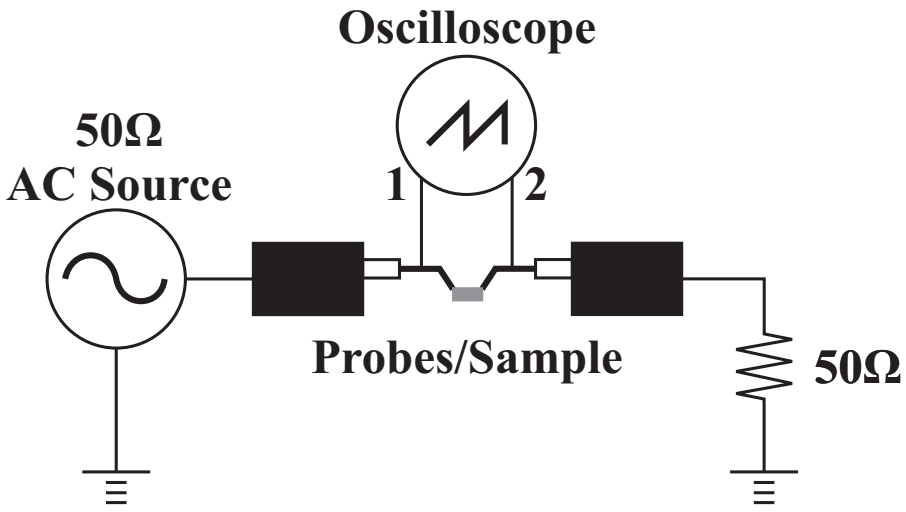

Figure 5.27. The circuit diagram showing the configuration used to determine high frequency flip-chip bond and TSV performance.

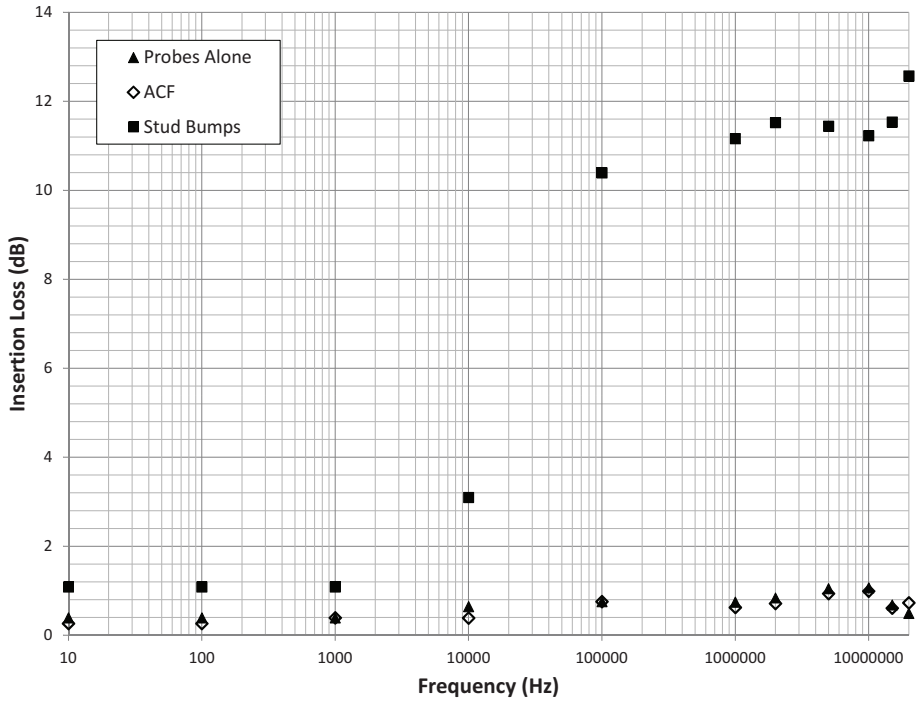

Figure 5.28. Insertion loss plotted against frequency for flip-chip bonds and TSVs created with ACF and coined gold stud bumps.

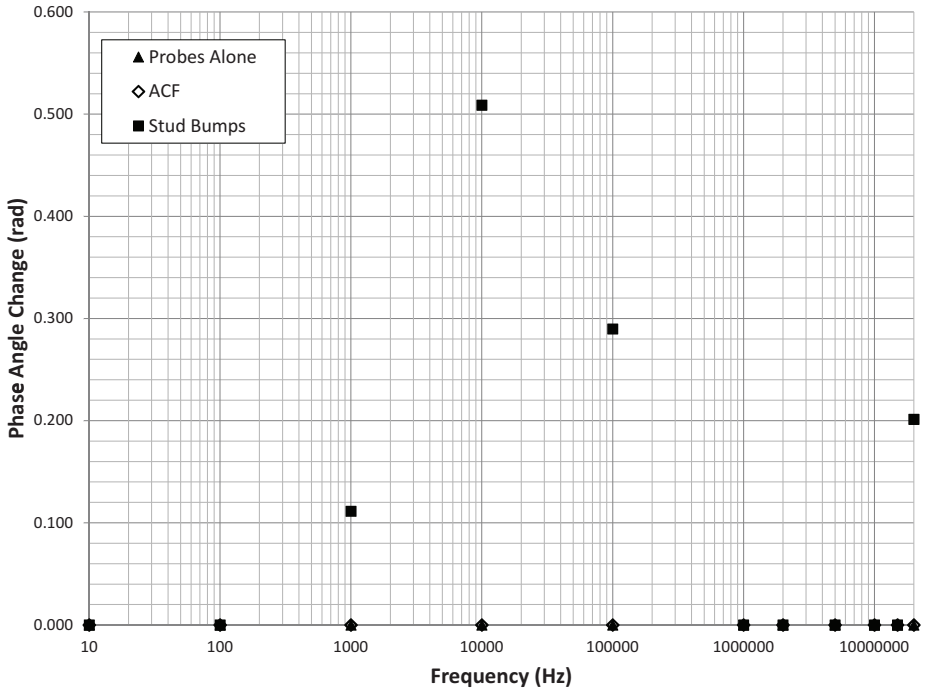

Figure 5.29. Phase angle change plotted against frequency for flip-chip bonds and TSVs created with ACF and coined gold stud bumps.

5.5 - Adhesives in Packaging

Several adhesives were examined for use on the sensor array during packaging. The three main types of adhesives tested were isotropic conductive adhesives for use in TSV filling, biocompatible sealing and structural adhesives, and anisotropic conductive adhesives for use in flip-chip processes, which were described in Section 5.4. The majority of adhesives tested were dispensed using the adhesive dispenser system with a variety of syringe tip sizes. An image of the adhesive dispenser is shown in Figure 5.30. For all types of adhesives used, it was important to consider the durability, strength, biocompatibility, sterilizability, and when applicable, the electrical conductivity. In addition, the viscosity, particle size, and curing schedule for the adhesives were important for successful application.

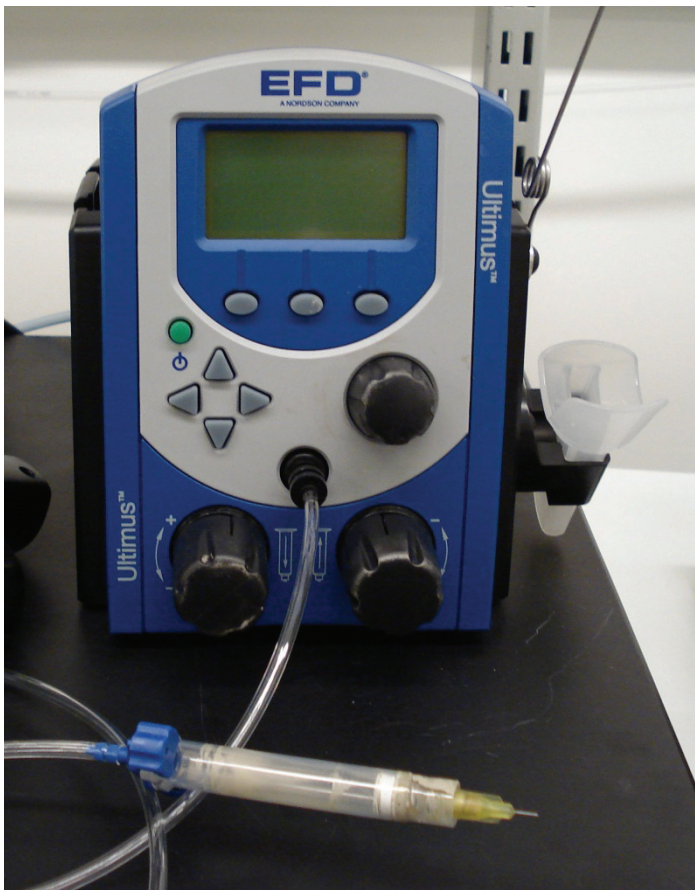

Figure 5.30. The Nordson EFD Ultimus II adhesive dispenser system.

5.5.1 - Through-Silicon Via Filling Adhesives

Isotropic conductive adhesives were used during production of TSVs to compensate for an issue encountered with microfabrication. As explained in Section 3.7.2, the sputtered aluminum used during TSVs fabrication did not provide an adequate conductive path from the top to the bottom of the wafer. To compensate for this manufacturing flaw, the TSV holes were filled with an isotropic conductive adhesive during packaging. The isotropic conductive adhesives tested were similar to the ACAs discussed in Section 5.4, except that the cured layers produced were isotropically conductive and did not require compression during curing. A large variety of isotropic conductive adhesives are available commercially, and typically use suspended silver particles ranging from 1-50μm in diameter to achieve conductivity.

The use of conductive adhesives for filling TSVs has been previously documented in literature as a viable TSV manufacturing process [108]. Several types of conductive adhesives were tested for this purpose, and were dispensed into the TSV holes using the EFD dispenser and very fine (50μm and 100μm) syringe tips. Figure 5.31 shows a photograph of a TSV hole being filled with an isotropic conductive adhesive. This method allowed accurate placement of adhesive within via holes which were as small as 100μm in diameter. Adhesive selection was very important during this process, as the adhesive selected had to have an adequately low viscosity and sufficiently small conductive particle size to flow through the syringe tip and into the TSV hole.

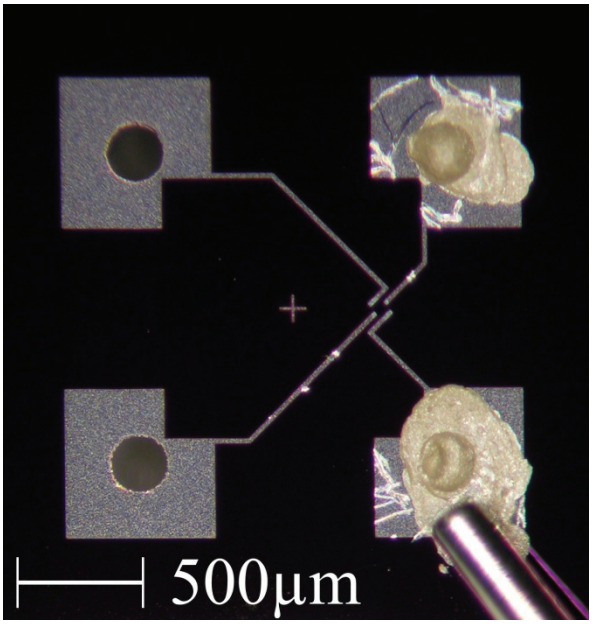

Figure 5.31. A 200µm TSV hole being filled with a 100µm (32 gauge) ID syringe tip.

The isotropic conductive adhesives examined for TSV hole filling included conductive ink (Techspray Trace Tech), two-part conductive epoxy (Epoxy Technology Epo-Tek H20E and Transcene Silver Bond Type 60), and one-part conductive epoxy (Ablestik Ablebond 84-1LMISR4). To ensure that the vias were filled completely, the chips were flipped to allow filling from both sides. Following filling, the adhesives were cured according to manufacturer instructions. Conductive vias were produced using all four of these products, however, the epoxies did not flow through the 50µm syringe tips, and thereby limited their abilities to fill the highest aspect ratio holes tested. To achieve more consistent comparison results for the various sizes of TSVs produced, the conductive ink product was used for all sizes examined.

The resistance of the TSVs were examined after filling the via holes with the conductive adhesives. This measurement captured the four-wire resistance of the TSVs using the same protocols observed for the flip-chip bonds described in Section 5.4. This measurement was performed using the probe station described in Section 4.3; a photograph of this experimental setup is shown in Figure 5.32. Due to the difficulty attaching probes to opposite sides of a sensor chip, two

adjacent TSVs were shorted together on one side of the substrate using the conductive adhesive, as shown in Figure 5.33. Four-wire resistance measurements could then be taken between adjacent TSVs on the top and bottom of the substrate, the difference between these measurements was then used to determine the average resistance for the linked TSVs. Resistances were collected for 100, 200, and 400µm diameter TSVs produced on 300 and 500µm thick substrates. At least 12 of each TSV size were examined. Resistance results for the six aspect ratio TSVs examined are shown in Table 5.2.

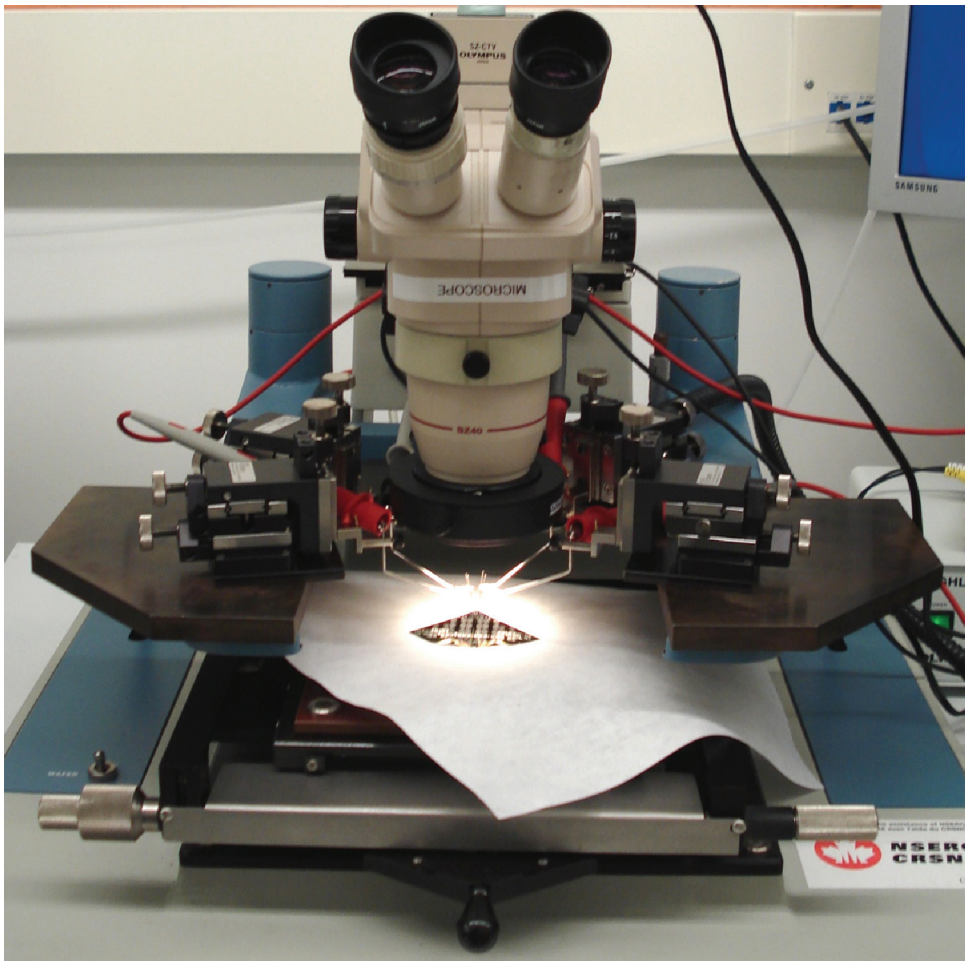

Figure 5.32. The experimental setup for making a four-point probe measurement of a TSV.

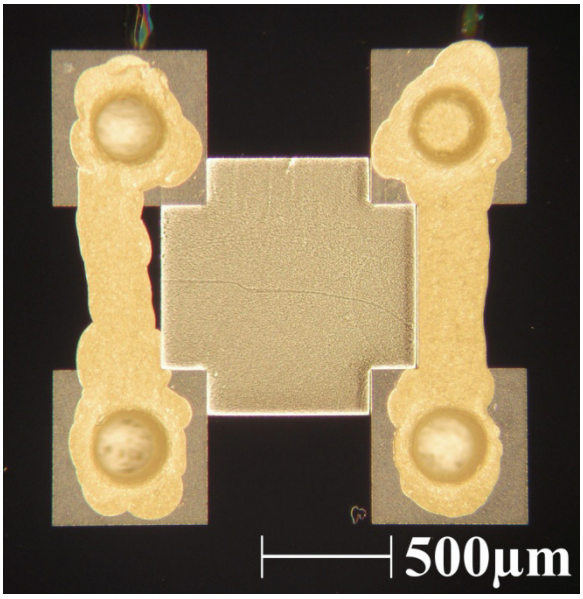

Figure 5.33. A photomicrograph of adjacent TSVs being shorted together on a sensor chip.

Table 5.2. Four-wire resistance measurements for TSVs filled with conductive adhesive.

TSV Depth (µm)	300	300	300	500	500	500
TSV Diameter (µm)	100	200	400	100	200	400
Mean Resistance (Ω)	0.4117	1.2525	0.1566	2.4399	0.5191	0.2088
Standard Deviation (Ω)	0.3909	0.7134	0.0875	2.1697	0.5457	0.2365

The measured resistances of the TSVs had high degrees of variation. This manifested as large standard deviation values and a poor correlation between mean resistance and aspect ratio. This variation was largely caused by incomplete filling of the TSVs leading to a broken conductive path. Figure 5.34 shows an image of an incompletely filled TSV. The main cause of incomplete TSV filling was the surface tension of the conductive adhesive creating bubble-like surfaces within the via holes that prevented further adhesive penetration. This issue could be mitigated by filling the TSV holes with adhesive from both sides and by using the syringe tip to break the surface tension bubbles prior to curing the adhesive. The hole sidewall surface roughness created during the cryo-etch process also may have added to the difficulty in filling the TSV holes completely.

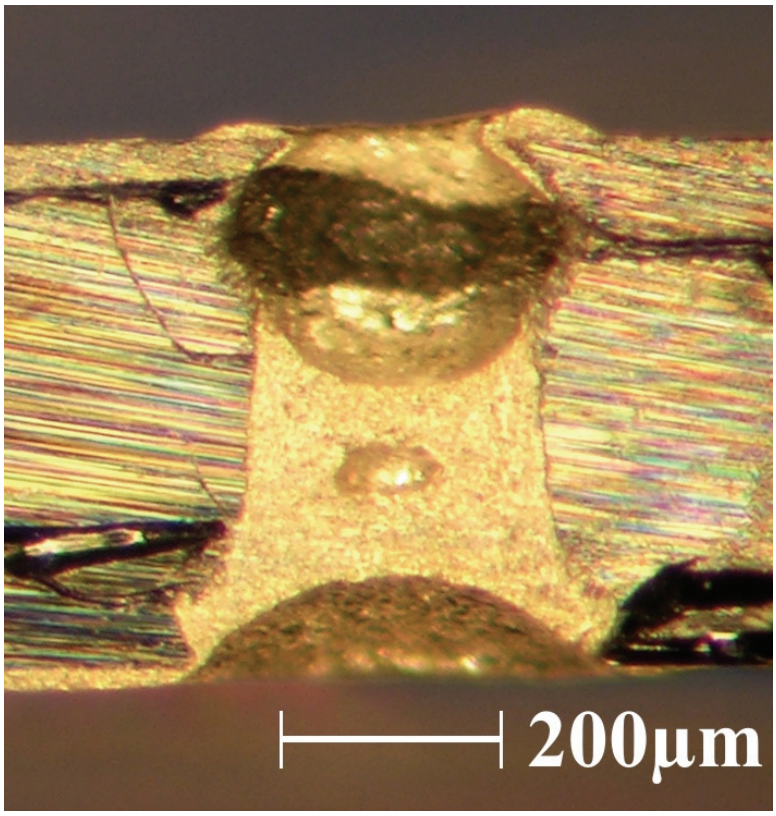

Figure 5.34. A photomicrograph of an incompletely filled TSV.

When filled completely, the current-voltage response of the TSV was ohmic. This response is shown in Figure 5.35 for a pair of linked TSVs with an average resistance of 0.167Ω. The TSVs were produced using a 100µm diameter hole in a 300µm thick substrate. High frequency results, collected using the same procedure as described in Section 5.4.1, were obtained for a pair of TSVs. The insertion loss is plotted in Figure 5.36. As noted for the flip-chip bonds created with the ACF, very little change in performance was observed for the TSVs relative to the probes alone. This provides additional evidence of ohmic TSV performance. Phase angle change results were also collected, but have not been plotted due to their extremely small magnitudes throughout the frequency range examined.

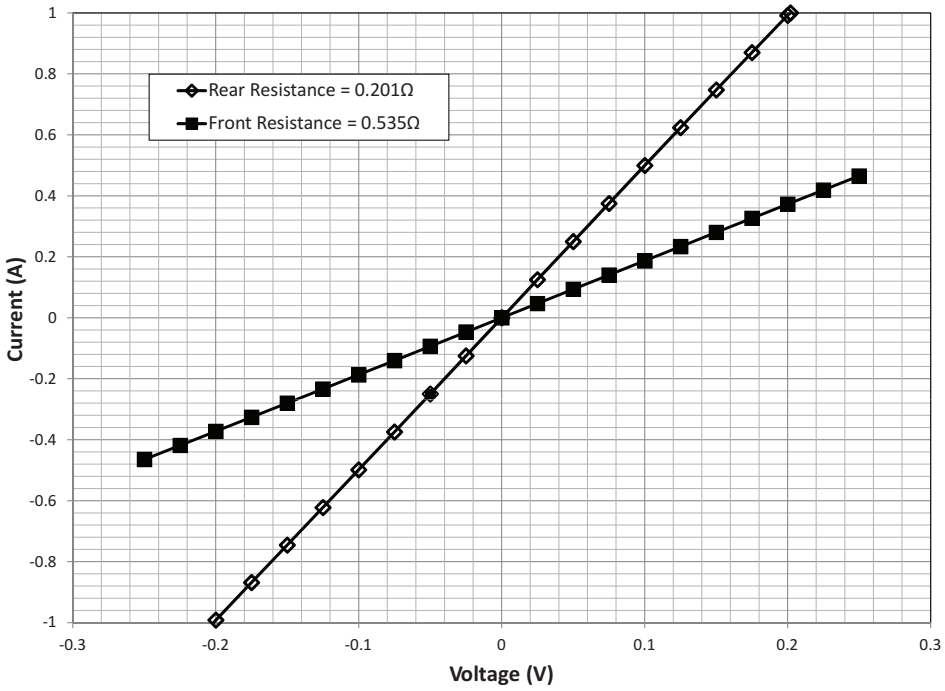

Figure 5.35. Current-voltage responses of two linked TSVs as measured on the front and rear of the substrate. The diameter and depth of the TSVs were 100µm and 300µm, respectively, and the average resistance was 0.167Ω.

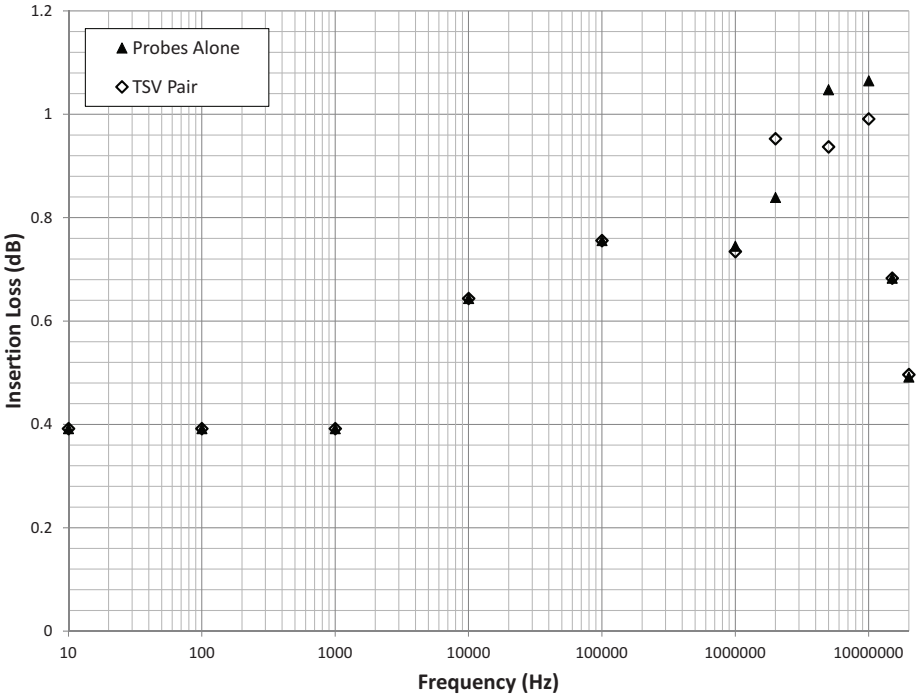

Figure 5.36. Insertion loss plotted against frequency for a linked pair of filled TSVs.

5.5.2 - Sealants and Structural Adhesives

Preparation of the sensor array for use during surgery produced a set of requirements that were necessary for successful application. The sensor array needed to be sterilized prior to surgical use, and also needed to be durable enough to survive the surgical procedure. The sensor array had to function in the same way as a non-instrumented spinal screw during surgery, which ensured that surgical protocols did not have to be significantly modified. To achieve these requirements, adhesives were tested for their ability to form biocompatible protective layers over the sensor array, and also to securely anchor the array components to the FPCBs and pedicle screws.

A sterilization procedure is one of several methods designed to eradicate any microorganisms that may be present on a device or surface. Methods of sterilization include autoclaving (high-pressure steam), dry heat, irradiation (gamma radiation or electron beam processing), gas (ethylene oxide, low-pressure steam and formaldehyde, or gas plasma), and chemical processing [99]. Autoclaving and gas sterilization (using ethylene oxide) are commonly used processes in the sterilization of surgical equipment. The autoclaving process was determined to be unsuitable for the scoliosis sensor array, as the moisture and elevated temperature used was found to be harmful to the electronic components. Ethylene oxide sterilization, which is a process specifically suited to temperature sensitive products, was eventually selected as the sterilization protocol for the scoliosis sensor array. Sealant and structural adhesives were thus selected based around the parameters of the ethylene oxide sterilization protocol.

The scoliosis surgical protocol, as described in Section 1.2.3, includes mechanically installing the pedicle screws into the vertebrae of the spine and placing a rod into notches in the pedicle screw heads. The nature of this procedure implied that the sensor array needed to be adequately protected from mechanical damage during installation. This requirement was applied in addition to the requirements created by the ethylene oxide sterilization procedure. This made sealant and structural adhesives which cured to form a mechanically hard layer superior for the scoliosis application. The most important zone in terms of

adhesive protection was the detection surfaces of the sensor pads: The mesas and membranes needed to be free to deflect and detect loading, but the metal traces on the top surfaces had to be covered to prevent short circuiting or physical damage.

Various adhesives were evaluated to determine their abilities to seal and protect the scoliosis sensor array. These included epoxy (specifically Henkel Loctite 3128), cyanoacrylates, and bone cement. These adhesives have been used in previous devices [9, 11-13] which have survived ethylene oxide sterilization procedures, so a focus was placed on the mechanical and durability concerns. Figure 5.37 shows a wire-bonded sensor strip on an FPCB with epoxy and cyanoacrylate adhesives used to protect the wire-bonds and sensor surface. The epoxy bonded acceptably well to the silicon sensor strip, although it was not able to bond to the polyimide cover on the FPCB effectively. The epoxy had an appropriate viscosity to fill around and cover the raised wire-bonds. The epoxy was required to be cured at an elevated temperature (80°C), and was found to foam if adequate heat was not applied to the adhesive. This foaming, as illustrated in Figure 5.37, made this adhesive layer too thick and soft for the scoliosis sensor application. The cyanoacrylate was found to bond acceptably well to the silicon sensor strip and the polyimide FPCB, however it was not viscous enough while being dispensed to cover the raised wire-bonds. The cyanoacrylate was also found to cure quickly and remained clear to allow damage to the traces to remain visible. The bone cement was found to particulate when stressed, and as such was not appropriate for application at an interfacial loading location.

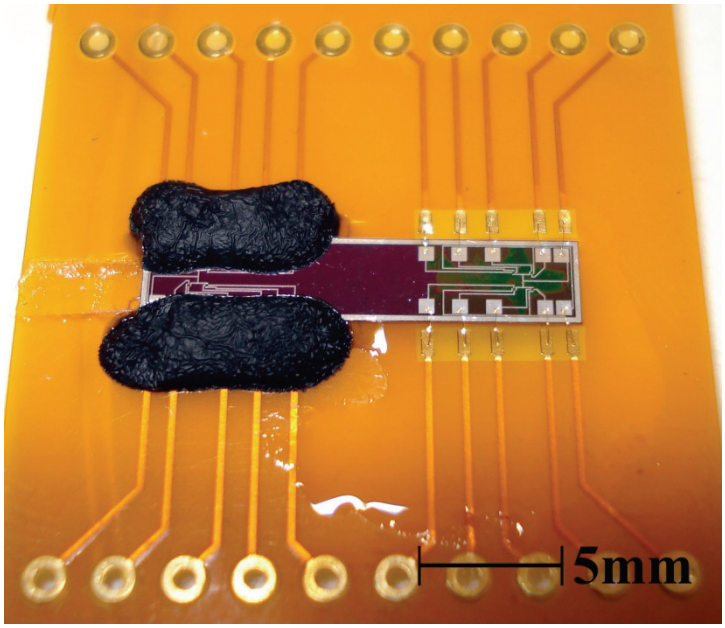

Figure 5.37. A sensor strip on an FPCB with wire bonds protected using epoxy (left) and cyanoacrylate (right). The epoxy foamed during curing, illustrating a potential problem which has been described in further detail in the text.

Since the final deployment solution did not utilize wire-bonding, the cyanoacrylate was found to be adequate for a coating application. The low viscosity of this adhesive was adequate to protect the electrical traces, yet did not produce a layer that would negatively affect membrane deflection. An additional advantage of this cyanoacrylate adhesive was that it could be thinned with acetone if the viscosity was not appropriate at the time of delivery. An image of an FPCB with sensors attached which was coated in a protective layer of adhesive is shown in Figure 5.38.

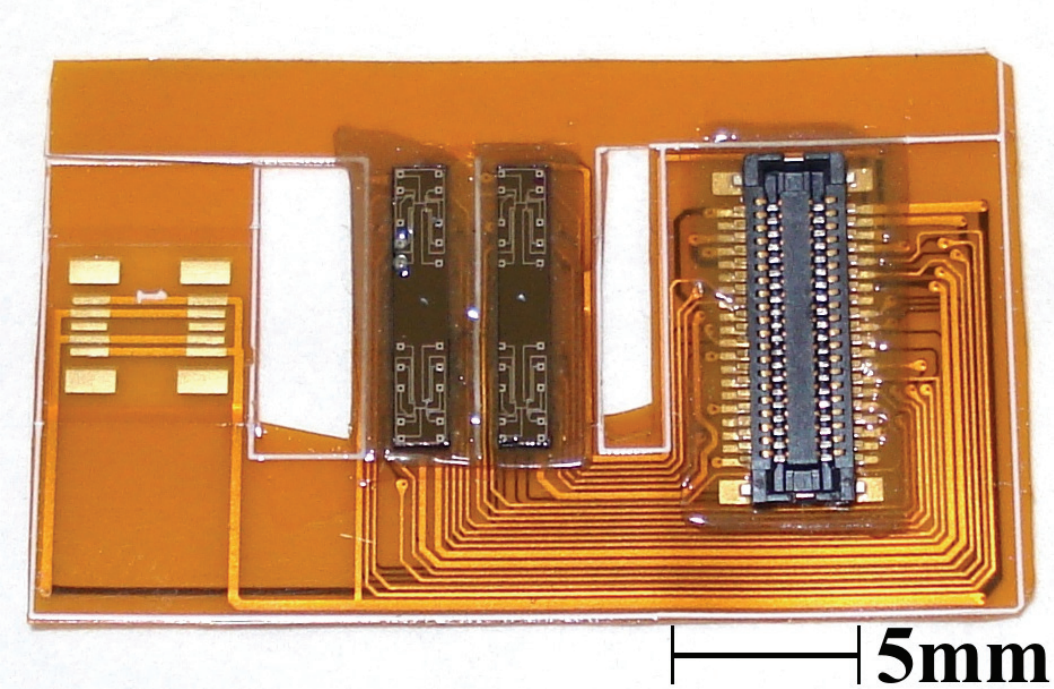

Figure 5.38. An image of the FPCB and sensor strips with a cyanoacrylate coating layer applied.

An additional use for the sealant and structural adhesives was to reduce the curvature of the screw notch to prevent FPCB tearing, as introduced in Section 5.2. This was a solution to a material property issue with the FPCB, and could also be remedied with a stronger FPCB material or a different layout. The adhesive solution involved building up material within the screw notch below the FPCB. Figure 5.39 shows an image of a screw notch within which bone cement has been used to reduce the curvature. Alternatively, a screw head with less curvature has also been constructed for characterization purposes, as shown in Figure 5.1.

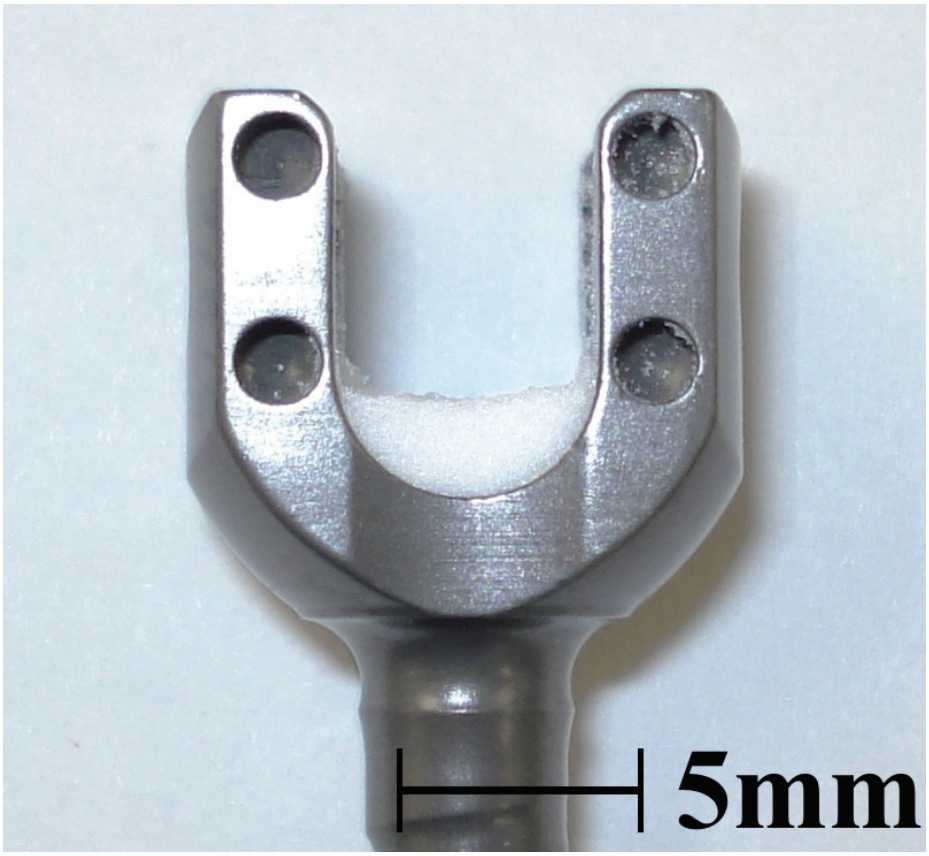

Figure 5.39. A screw head notch which has had its curvature reduced by application of bone cement.

5.6 - Conclusions

Details on the packaging and deployment of the MEMS sensor array on the pedicle screws have been provided. In order to create a packaged device durable enough to survive ethylene oxide sterilization and the scoliosis correction surgery procedure, a solution which attaches the sensor pads, wireless module, and power module to an FPCB which has been wrapped around the head of the pedicle screw has been used. This solution used TSVs filled with isotropic conductive adhesive and flip-chip techniques to attach the sensing components to the FPCB. These methods produced ohmic electrical connections with low (<1Ω) resistances. A cyanoacrylate coating was then used to protect and seal the sensor strips and FPCBs.

Chapter 6: Calibration[3]

The packaged device is now calibrated. A custom loading frame was designed and built to calibrate the scoliosis sensor array. This frame uses a set of five manual perpendicular actuators to apply loads to the sensor array. These loads are measured and collected using a commercial six-axis load cell and data acquisition system, which allow them to be directly compared with the voltage outputs from the scoliosis sensor array. Calibration equations are then produced that facilitate conversion between the voltage outputs from the scoliosis sensor array and the applied loads. Parameters for the wireless and power modules are also presented. Finally, recommendations for improving the durability of the device for use during surgery are given.

6.1 - Introduction

Unique calibration issues and challenges exist for six-axis load cells. These challenges include cross-sensitivity between channels, difficulty in precisely applying unidirectional calibration loads, and managing differing sensitivities between channels. In addition, the compact layout of the proposed scoliosis sensor array introduces challenges due to the sensor not having linear and independent outputs for each of the six axes of detection. The magnitude of the loads applied during the calibration procedure must be similar to those expected during surgical usage when determining sensitivity and resolution, and loads higher than those expected in surgery should be applied to determine safe usage limits and failure modes. These requirements necessitate a robust calibration apparatus and protocol.

A calibration procedure has been developed for the pedicle screw instrumented with the six-axis sensor array. This procedure utilized a custom load application frame capable of simulating the 3D forces and moments applied by a surgeon during scoliosis correction. The load application frame was instrumented with a commercial six-axis load cell, allowing outputs from the

[3] Some of the material in this chapter has been submitted for publication as a paper in the *Journal of Micromechanics and Microengineering.*

commercial load cell to be directly compared to the outputs from the MEMS sensor array being calibrated. The sensor array produced 16 differential voltage outputs in response to the six-axis input loads. A data acquisition system (DAQ) was used to collect the outputs from the sensor array and commercial load cell. After the application of appropriate calibration loads, linear and nonlinear calibration equations were produced which then allowed the 16 voltage outputs from the sensor array to be converted back into six-axis load information. Following this initial calibration, concerns regarding the durability of the sensor array were addressed.

6.2 - Calibration Frame Design

The calibration of the six-axis scoliosis sensor array required that the outputs from the array be compared to known 3D force and moment load inputs. This was accomplished by comparing the output from the sensor array with the output from a commercial six-axis load cell (AMTI MC3A-6-250). Equivalent and simultaneous loads were applied to the sensor array and load cell by rigidly connecting them together and placing them between movable and fixed stages. The commercial load cell was attached to the movable lower stage and the sensor array was attached to the fixed upper stage. Sensing elements on both the sensor array and the load cell were positioned to be close to each other, allowing conformity in the loads applied to each sensor. Manipulating a five-axis actuator stack that was attached to the lower stage allowed controllable, 3D loads to be created between the movable and fixed stages which could then be detected by the load cell and the sensor array simultaneously, thus enabling calibration. This calibration concept is shown schematically in Figure 6.1.

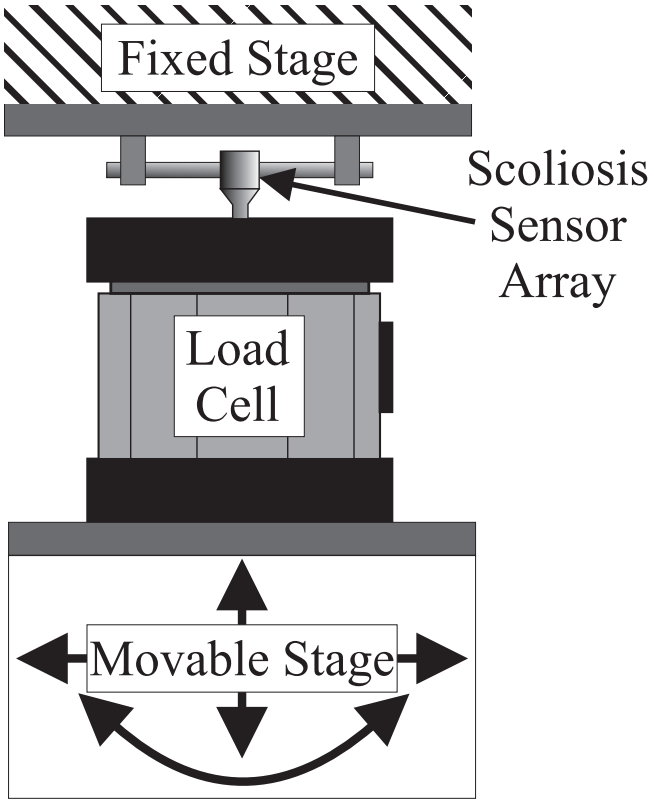

Figure 6.1. A conceptual schematic of the apparatus used to calibrate the scoliosis sensor array. The movable stage consisted of a five-axis actuator stack which was able to induce uniaxial or multiaxial forces and moments in both the commercial load cell and the scoliosis sensor array.

6.2.1 - Six-Axis Load Application

The five-axis actuator stack enabled 3D force and moment loads to be applied to the sensor array and load cell. This actuator stack consisted of a set of custom built, translation/rotation actuators able to apply orthogonal X, Y, and Z-axis displacements and orthogonal Y and Z-axis rotations. A third rotational degree of freedom was not required as it could be produced using a combination of the other two rotational directions [150]. The Z-axis rotation center was placed concentrically with the vertical centerline of the load cell and the Y-axis rotation center was placed about a point approximately 84mm above the surface of the lower stage. This point is above the top surface of the commercial load cell

(which is 76.2mm tall), minimizing discrepancy between the recorded moments of the scoliosis sensor array and commercial load cell.

Previous research into the range of loads applied during scoliosis correction surgery indicated that 1kN forces and 4N-m moments were expected, as mentioned in Section 1.2.4. These loads necessitated that the stages, frame, and actuator stack be strong and rigid to avoid unnecessary deflection or failure. In addition, the base of the actuator stack needed to be rigidly connected to the upper stage, to avoid misalignment and to provide structural support. This was accomplished by constructing a supportive frame from slotted aluminum beams (80/20 Inc. 15 Series). The actuator stack consisted of five individual linear and rotational actuation elements that could be operated independently. These actuators were connected in series and were designed to be very stiff; movement was restricted in directions other than on their operational axes, as well as on their operational axes when they were not being actuated. This was accomplished using precision bearing elements and screw drives with features to minimize backlash. Each actuator was manual in operation. The commercial load cell was bolted to the top of the actuator stack with provisions made for installation of a spinal screw and rod to simulate the surgical use of the instrumentation. Figure 6.2 shows a photograph of the six-axis load application device (SALAD).

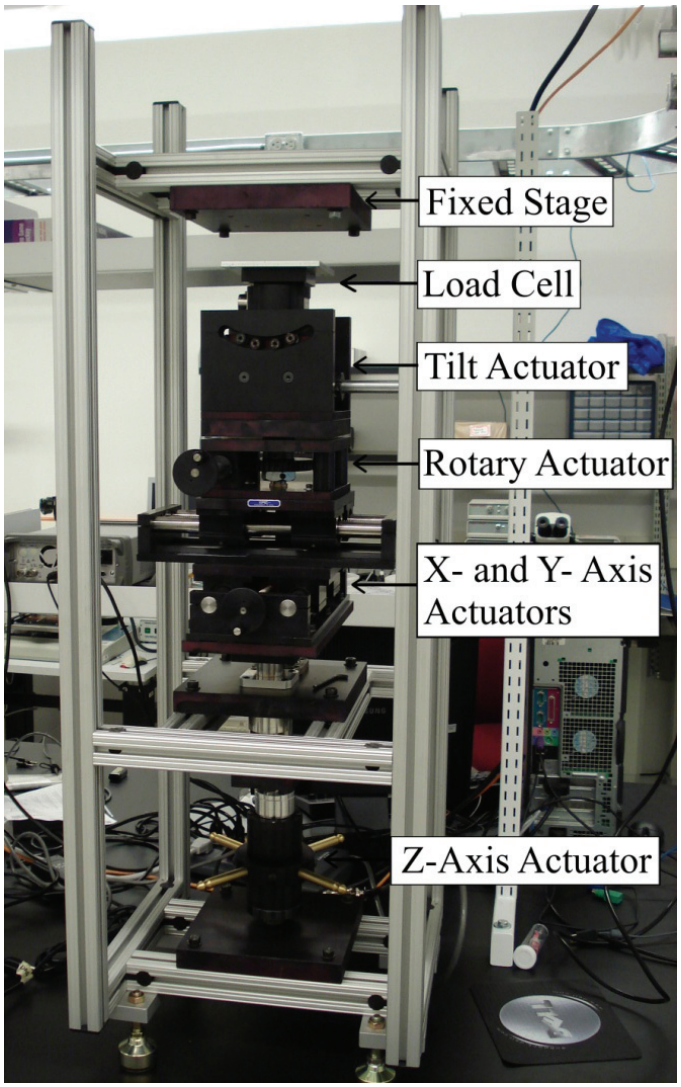

Figure 6.2. A photograph of the assembled calibration frame and load cell, known as the six-axis load application device (SALAD).

During assembly, the slotted beams were measured for length and cut quality. This determined that the beams were cut squarely, and their lengths were within 300μm of the design specification. Aligning the frame elements carefully during assembly ensured that frame flexibility was kept to a minimum. This also assisted with load application and kept the applied forces and moments aligned with the detection axes of the six-axis load cell. Specific steps were also taken to reduce backlash and bearing play in the actuators during assembly of the SALAD. A linear bearing was replaced with a high-precision brass bushing in the Z-axis

linear actuator to reduce lateral free play. In addition, a ball joint in the Z-axis linear actuator was replaced with a custom flange mount for a cartridge bearing to reduce vertical free play. The Z-axis rotary actuator had its keyway tapped for a setscrew to reduce free space and eliminate a tendency to wobble. By making these modifications during assembly of the SALAD, the precision with which forces and moments could be applied was increased.

Customized adapters were developed to allow the scoliosis sensor array to be mounted to the commercial load cell and upper stage. These adapters consisted of an L-bracket and P-clip system which was used to affix a length of rod to the upper stage, and a threaded shaft and mounting plate which was used to attach the sensor array to the commercial load cell. To reduce the packaging concerns regarding FPCB tearing introduced in Section 5.2, and also to simplify attachment of the threaded rod to the sensor array, a mockup of the pedicle screw head was used for calibration purposes. This mockup used a flat-bottomed notch to reduce FPCB tearing on installation, and a separate cradle to allow shear force transmission and alignment to the sensor strips. This adapter configuration is shown in Figure 6.3. In order to achieve accurate calibration, the offset height of the rod centerline was noted as being 18.3mm above the surface of the load cell, which corresponded to a height of 50.2mm above the geometric centre of detection (COD) for the commercial load cell. The COD concept for the sensor array and commercial load cell is explained further in Sections 6.2.2 and 6.2.3.

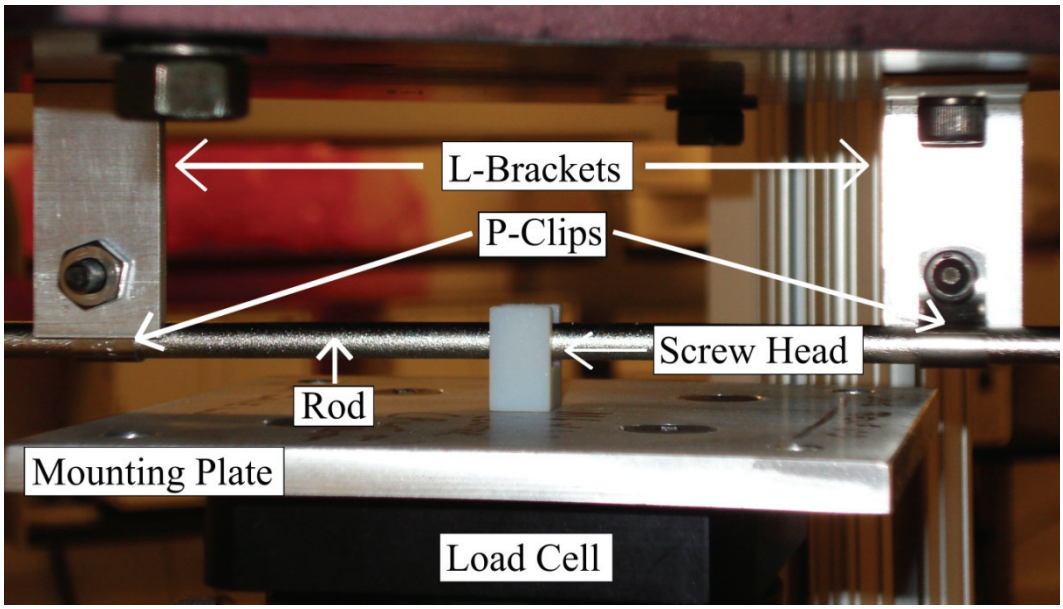

Figure 6.3. The L-bracket and P-clip system used to affix the rod to the upper stage. Also shown is a simulated scoliosis screw head affixed to a mounting plate bolted to the commercial load cell.

The SALAD allowed variable forces and moments to be applied to the sensor array independently or in combination during calibration. This was accomplished by adjusting the actuators in the stack until the desired response was output from the commercial load cell. The SALAD was used to evaluate the sensor array for its response to applied loads within the force and moment ranges of the commercial load cell. Loads were applied individually (according to the detection axes of the commercial load cell), which provided necessary data for calibration. Loads could also be applied in a superimposed state, which allowed the validity of the calibration equations to be determined.

In comparison to commercially available six-axis actuation and load detection systems, the SALAD was substantially less expensive. In addition, the modular nature of the actuator stack allowed individual actuation components to be removed if they were not required. Removing unnecessary actuators could be advantageous during calibration of a sensor with fewer directions of detection, as it would add stiffness to the actuator stack and frame assembly. For example, a

load cell that was capable of detecting 3-axis forces could be calibrated using only the linear actuators.

With the addition of an appropriate displacement detection system, the SALAD could be used to evaluate multi-axis material or structural properties. This displacement detection system would need to be able to detect the 3D rotation and translation of the movable stage and load cell. This type of system could be used to determine the stiffness or strength of tissues, materials, devices, or constructs. The multi-axis force application capability of the SALAD could specifically be useful for quantifying the anisotropic properties of medical devices and biomaterials. The high load capacity of the actuator stack and load frame could also be beneficial for determining failure modes and load capacities of biomedical products and tissues.

6.2.2 - Commercial Load Cell and Data Acquisition System

During operation of the SALAD, it was necessary to collect and capture the force and moment outputs produced by the commercial load cell. The commercial load cell detected the induced loading through the use of multiple thin foil strain gauges, which were attached to deformable elements within the load cell. The output signals from the strain gauges consisted of a set of six differential voltages, each corresponding to a force or moment in the X, Y, or Z direction. The output voltages were each sent through a separate signal conditioning and amplification circuit board (Dataforth 8B38-05) which provided a gain of 250. Input voltage of 10.0V was supplied to the load cell's strain gauges using a power supply (IDEC PS5R-A05) attached to this same board. Input and output signals were transmitted to the commercial load cell via a shielded cable connection.

The six amplified and conditioned output signals were sent to a DAQ (National Instruments USB-6225) that allowed display and storage on a computer. This DAQ used a 16-bit analog to digital (A/D) converter and was capable of collecting data at up to 250kS/s. The DAQ had 40 differential input channels, which was more than the commercial load cell required, allowing the output from the scoliosis sensor array to be collected simultaneously with the load cell's

output. The sensor array added 16 additional differential channels to the six from the commercial load cell. This allowed an aggregate data acquisition rate of up to 5.6kHz on each of the 22 total channels. This maximum data rate was extremely high for the quasi-static load application, and allowed filtering to be performed on the acquired data.

The DAQ allowed the voltage range of each channel to be adjusted individually to correspond with the outputs from the load cell and scoliosis sensor array. The amplification circuit produced a maximum voltage output of ±5V for each channel of the commercial load cell. The force ranges of the load cell were 1100N in the Z-axis direction and 560N in the X-axis and Y-axis directions. The moment range of the load cell was 14N-m in the Z-axis direction and 28N-m in the X-axis and Y-axis directions. The 16-bit DAQ produced a resolution of 153μV for this 10V voltage range, which corresponded to a resolution of 91.4mN for the Z-axis force direction and 23.7mN in the X-axis and Y-axis force directions. Resolution for moments was 0.640N-mm for the Z-axis direction and 0.429N-mm in the X-axis and Y-axis directions. These resolution values were based on load cell sensitivity values provided by the manufacturer, as shown in Table 6.1. Linearity and hysteresis values for the commercial load cell were specified as ±0.2% full-scale output, and accuracy of the DAQ was 1.62mV for this voltage range. These factors limited the accuracy of the data collected from the commercial load cell.

Table 6.1. Commercial load cell sensitivities in the detection directions.

Load Direction	Unamplified Load Cell Sensitivity
Fx	2.5778μV/V-N
Fy	2.5667μV/V-N
Fz	0.6678μV/V-N
Mx	142.2927μV/V-N-m
My	143.5605μV/V-N-m
Mz	95.3862μV/V-N-m

Amplified load cell outputs were examined for noise using an oscilloscope in Fast Fourier Transform (FFT) mode. This determined that the noise was centered on

60Hz and 2.2MHz frequencies. In order to reduce the noise, adjacent unused inputs on the DAQ were shorted out and differential output wire pairs were twisted together. To reduce signal drift, a 30-minute warm-up was performed prior to data collection. Cross-sensitivity (or crosstalk) between channels on the load cell was another concern that was examined. This phenomenon was found to be minor as the manufacturer provided a compensation equation to remove crosstalk effects from the signal during post-processing.

The DAQ was used to examine the output from the six-axis load cell as the individual actuators were operated. The fixed and moveable stages were bolted together for this trial, which amplified a cross-sensitivity effect induced by deflections and small misalignments in the frame and actuator stack. Figure 6.4 depicts the output from the six load cell channels as the Y direction linear actuator was operated on the actuator stack. Noise was particularly evident on the F_Z channel, and is a result of the commercial load cell having an increased range and reduced sensitivity in the Z-axis force direction. Cross-sensitivity due to misalignment and deflection was observed as a resultant moment application in the X-axis direction (M_X). This cross-sensitivity was due to the difference between the COD of the commercial load cell and the application location of the forces and moments. Further explanation of the COD concept is discussed in Section 6.2.3.

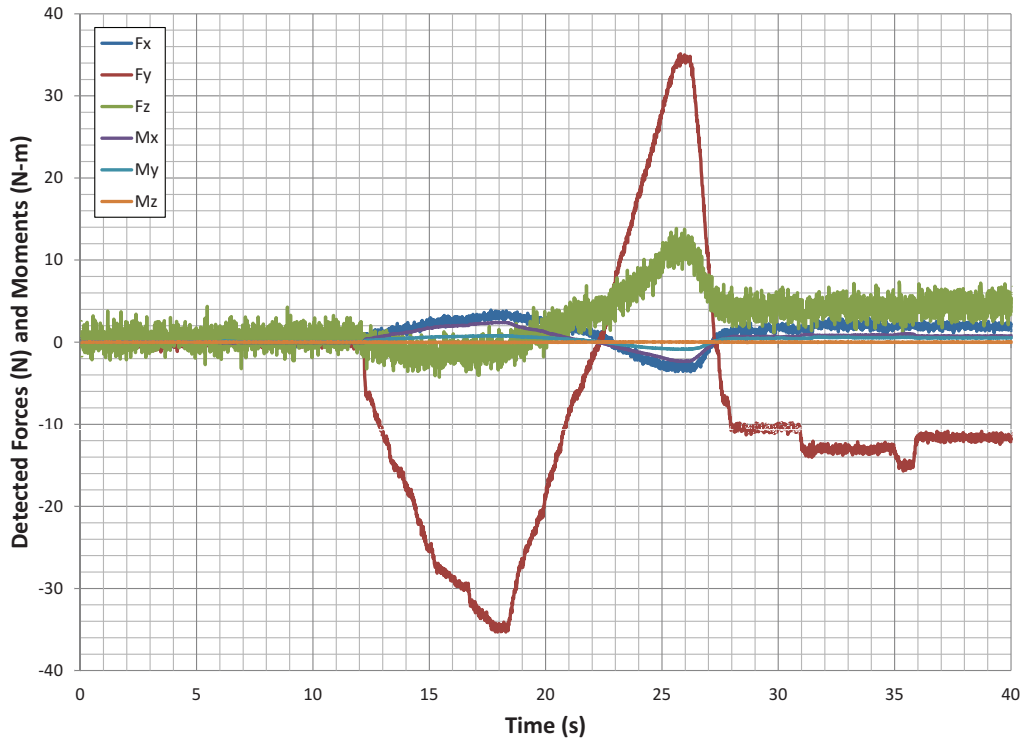

Figure 6.4. Data output from the SALAD's load cell while operating the Y-axis linear actuator. The response from the F_Y channel represents the expected output data, the F_Z response illustrates signal noise, and the M_X response illustrates uncompensated cross-sensitivity between channels.

6.2.3 - Calibration Protocol

The first step in calibrating the sensor array using the SALAD was to ensure that the output being produced by the commercial six-axis load cell was accurate. Force loads were applied using masses affixed to the load cell. This method relied on gravity and enabled comparison of outputs from the load cell with that of a calibrated balance. Moment loads were applied by adding a cantilever beam of known length between the load cell and the masses. This process determined that the force and moment outputs from the commercial load cell, as calculated using the provided equations, were accurate.

The scoliosis sensor array was mounted to the SALAD and a 3V input voltage was applied. An image of the mounted sensor array is shown in Figure 6.5. A wired connection was used to attach the scoliosis sensor array to the same

DAQ as the load cell, and a maximum voltage range for these unamplified output channels was set to ±1V. The mechanical actuators were then used to apply single- and multi-axis loads. The applied loads were monitored using the output voltages from the commercial load cell; linearly independent load combinations could be produced by operating the five actuators appropriately. As discussed in Section 4.5, linearly independent load application in the six application directions was necessary for the calibration of the scoliosis sensor array. Calibration equations were then produced to correlate the six outputs from the commercial load cell with the 16 voltage outputs from the sensor array. Finally, multi-axis loads were applied to more rigorously evaluate and validate the calibration.

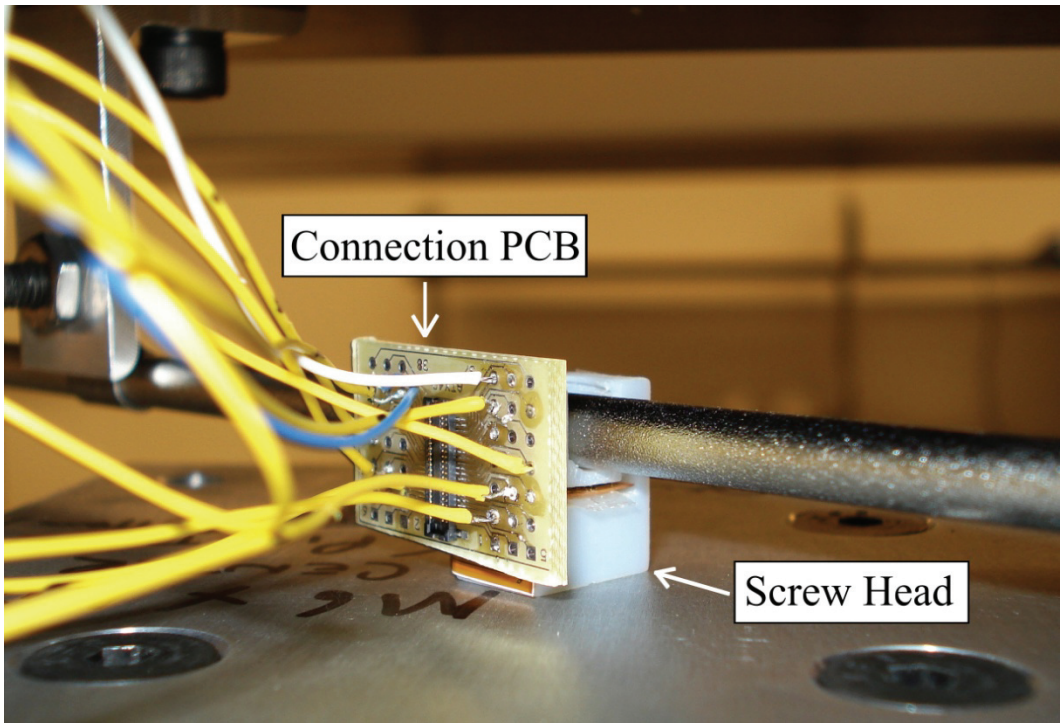

Figure 6.5. The scoliosis sensor array and wired connection PCB mounted on the SALAD.

One correction which had to be made during calibration arose from the small amount of vertical separation between the commercial load cell and the sensor array. These sensors are each capable of detecting force and moment loads, implying that there must be points defining CODs for both devices. The

significance of the COD is that force vectors applied that do not pass through this point will also apply a moment to the sensor. The distance between the CODs of the commercial load cell and scoliosis sensor array changes the moments detected at each sensor. This difference is illustrated in Figure 6.6 for a rigid connection with supportive information in Equation (6.1). Effectively, this relationship implies that positive Y-axis forces detected by the load cell will impart a negative X-axis moment at the sensor array. Conversely, positive X-axis forces detected by the load cell will impart a positive Y-axis moment at the sensor array. These corrections are incorporated into the input load vector for the sensor array, $\{\boldsymbol{S}\}$, as compared to the detected load vector of the load cell, $\{\boldsymbol{L}\}$, in Equation (6.2). Figure 6.6 also shows that the rotational radius of the X-axis moment actuation (tilt) table is not precisely aligned with the COD of either the load cell or sensor array. This produced a small amount of reactive force application during large rotations of the tilt table. However, due to a small deflection assumption that was made during calibration, forces induced by the tilt table that differed between the load cell and sensor array were not considered.

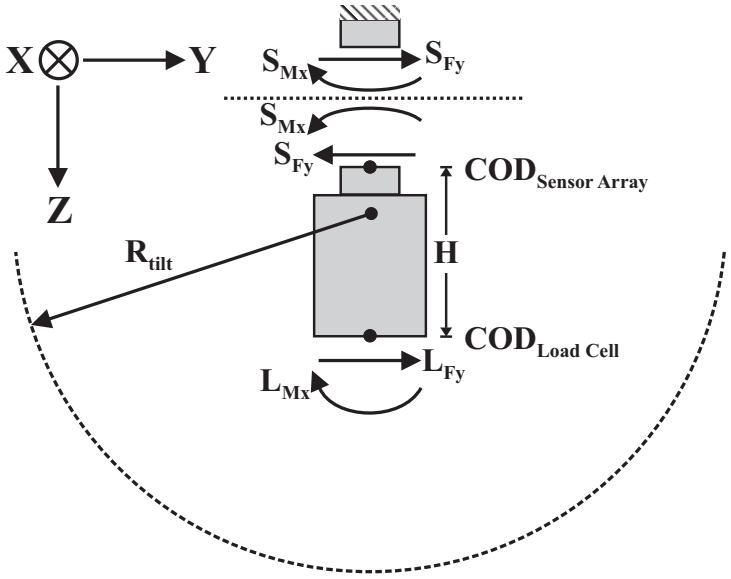

Figure 6.6. An explanatory figure is shown to explain the discrepancy between the detected moments at the center of detection (COD) of the commercial load cell and the scoliosis sensor array. Supportive equations are shown in Equation (6.1); H = 50.2mm and R_{tilt} = 95.3mm for the SALAD.

$$\begin{gathered}\Sigma F_Y = 0 = L_{Fy} - S_{Fy}; L_{Fy} = S_{Fy} \\ \Sigma M_{X(COD_{Load\ Cell})} = 0 = L_{Mx} - S_{Mx} - S_{Fy} \cdot H \\ S_{Mx} = L_{Mx} - L_{Fy} \cdot H\end{gathered} \tag{6.1}$$

$$\{\boldsymbol{S}\} = \{\boldsymbol{L}\} + \{\Delta\} = \begin{Bmatrix} S_{Fx} \\ S_{Fy} \\ S_{Fz} \\ S_{Mx} \\ S_{My} \\ S_{Mz} \end{Bmatrix} = \begin{Bmatrix} L_{Fx} \\ L_{Fy} \\ L_{Fz} \\ L_{Mx} \\ L_{My} \\ L_{Mz} \end{Bmatrix} + \begin{Bmatrix} 0 \\ 0 \\ 0 \\ -L_{Fy} \cdot H \\ L_{Fx} \cdot H \\ 0 \end{Bmatrix} \tag{6.2}$$

Symmetry was used in the calibration procedure to allow the use of a quarter model sensor array. This was done due to a lack of reliability in the prototype packaging during calibration. Wire breakage, connector failure, various FPCB problems, and disconnection in the TSV, wire-bond, and flip chip connections caused signal loss throughout the calibration procedure. By reducing the 16 differential channels to four by using quarter-model symmetry, the power and data channels were lowered from 37 to 10, making the use of the prototype sensor array more manageable. The local coordinate systems for each sensor pad defined by quarter-model symmetry are illustrated in Figure 6.7. The output forces detected at each sensor pad in response to forces and moments applied to the sensor array COD are listed in Table 6.2.

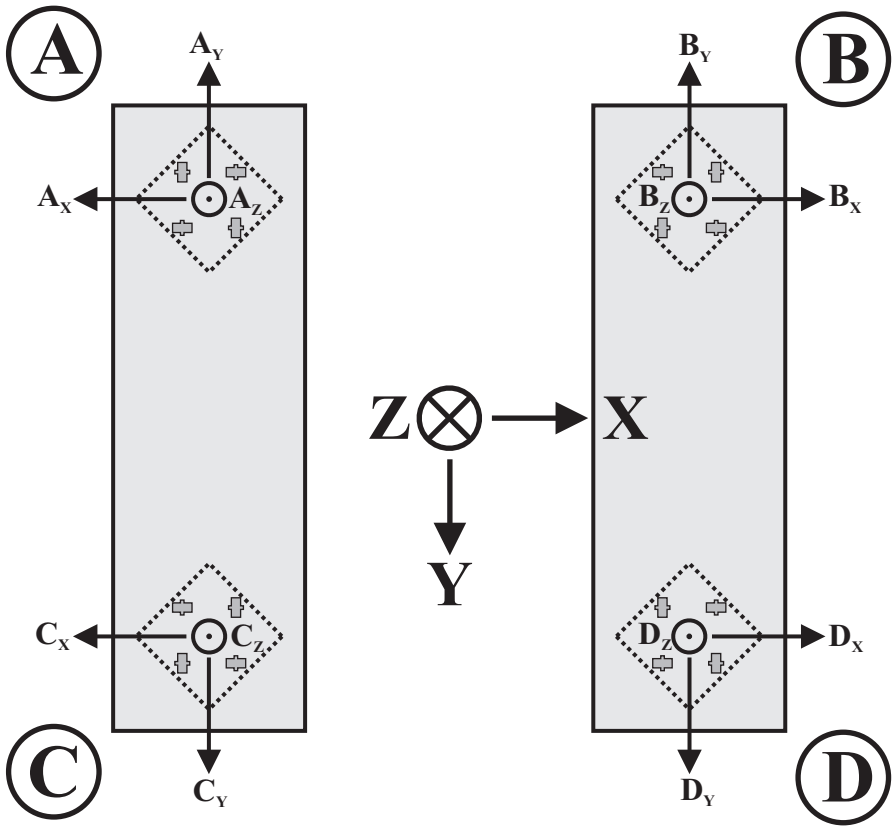

Figure 6.7. Local coordinate systems used for each sensor pad as defined by quarter-model symmetry. A coordinate system defined by the sensor array COD is also shown.

Table 6.2. Local outputs from each sensor pad in response to loads applied at the COD of the sensor array.

Global Load	Sensor Pad A	Sensor Pad B	Sensor Pad C	Sensor Pad D
+Fx	-Fx	+Fx	-Fx	+Fx
+Fy	-Fy	-Fy	+Fy	+Fy
+Fz	-Fz	-Fz	-Fz	-Fz
+Mx	+Fz	+Fz	-Fz	-Fz
+My	-Fz	+Fz	-Fz	+Fz
+Mz	-Fx, +Fy	+Fx, -Fy	+Fx, -Fy	-Fx, +Fy

6.3 - Sensor Outputs and Calibration Equations

The SALAD allows known force and moment data output from the load cell and the raw output voltages from the sensor array to be collected for comparison using the same DAQ system. Using the calibration protocol discussed in Section 6.2.3, a substantial amount of calibration information was produced. It was desirable that the input load vector $\{\boldsymbol{S}\}$ contain only one non-zero term for calibration of the sensor array, however, this was not necessary provided an adequate number of independent calibration data points including each of the six loading directions were used. A 16 term output voltage vector $\{\boldsymbol{Vn}\}$ was produced by the scoliosis sensor array in response to the applied loads. Assuming a linear correlation for simplicity, a 6×16 term calibration matrix $[\boldsymbol{G}]$ can be populated using a Moore-Penrose pseudoinverse method (or alternative, as discussed in Section 4.5) for the sensor array. The relationship between $\{\boldsymbol{S}\}$, $[\boldsymbol{G}]$, and $\{\boldsymbol{Vn}\}$, is shown in Equation (6.3).

$$\{\boldsymbol{S}\} = [\boldsymbol{G}]_{6\times16}\{\boldsymbol{Vn}\} \tag{6.3}$$

Once the 96 terms in $[\boldsymbol{G}]$ were determined, a $\{\boldsymbol{Vn}\}$ vector could be used to recreate the terms in $\{\boldsymbol{S}\}$ for various loading scenarios. This recreated load data could then be compared with the output from the commercial load cell. As was presented in Section 4.5, this calibration equation can be modified for nonlinearity by introducing additional functions of $\{\boldsymbol{Vn}\}$ to the calibration equation, as shown in Equation (6.4).

$$\{\boldsymbol{S}\} = [\boldsymbol{P}]\{\boldsymbol{f_1}(\boldsymbol{Vn})\} + [\boldsymbol{Q}]\{\boldsymbol{f_2}(\boldsymbol{Vn})\} + \cdots \tag{6.4}$$

The scoliosis sensor array consists of four similar sensor pads able to detect shear and normal loads on their surfaces. This represents symmetry in the sense that four sets of four voltages are each detecting three-axis force loads relative to their surfaces. As a result of this symmetry, the voltage combinations for each pad presented in Equations (4.5) and (4.6) become an obvious choice for a function of $\{\boldsymbol{Vn}\}$. Briefly referring to the 16 terms in $\{\boldsymbol{Vn}\}$ by the four sensor pads A,B,C, and D having voltage outputs 1,2,3, and 4 from each, a function in the form of Equation (6.5) may be used.

$$\{\boldsymbol{S}\} = [\boldsymbol{P}]\{\boldsymbol{f_1(Vn)}\} = [\boldsymbol{P}]_{6\times12}\begin{Bmatrix} (V_{A1}+V_{A2}+V_{A3}+V_{A4})/4) \\ (V_{A3}-V_{A1}) \\ (V_{A4}-V_{A2}) \\ (V_{B1}+V_{B2}+V_{B3}+V_{B4})/4) \\ \vdots \\ (V_{D4}-V_{D2}) \end{Bmatrix}_{12\times1} \quad (6.5)$$

The [***P***] matrix in Equation (6.5) has 72 terms, which is a reduction from the 96 terms in the [***G***] matrix presented in Equation (6.3). Following sufficient data collection, both [***G***] and [***P***] matrices were populated using a quarter model sensor array mounted in the SALAD. Samples of the four voltage outputs from the quarter-model sensor array are shown for a Z-axis force application using the SALAD in Figure 6.8, and the corresponding force and moment outputs from the commercial load cell are shown in Figure 6.9.

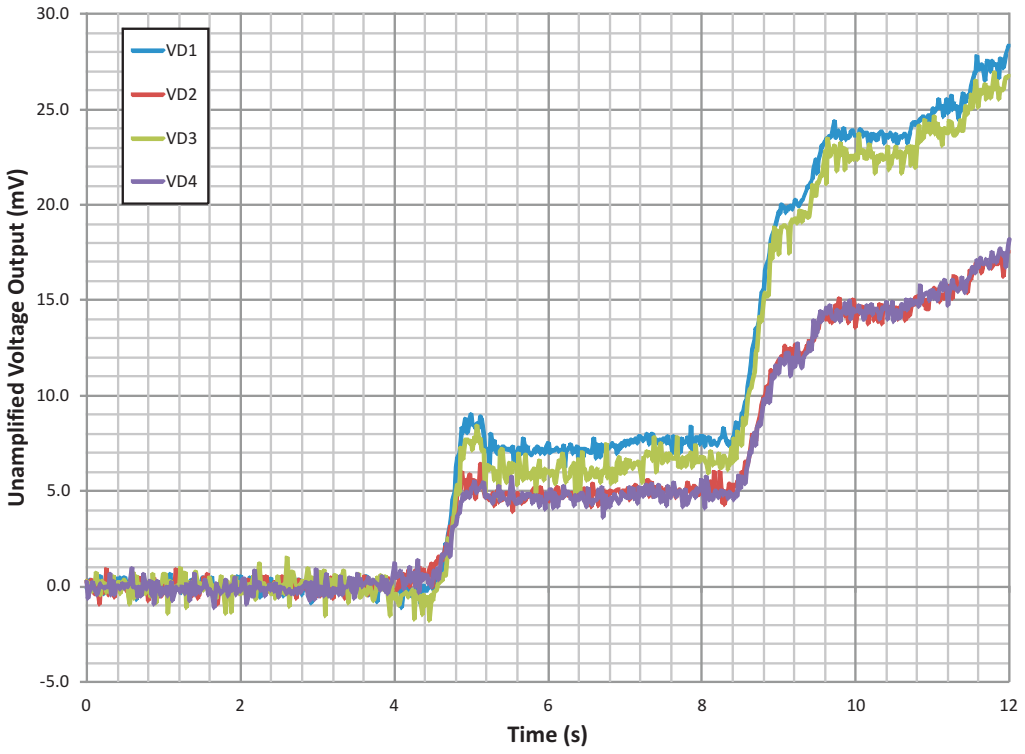

Figure 6.8. Voltage output from a quarter model sensor array experiencing Z-axis force application on the SALAD.

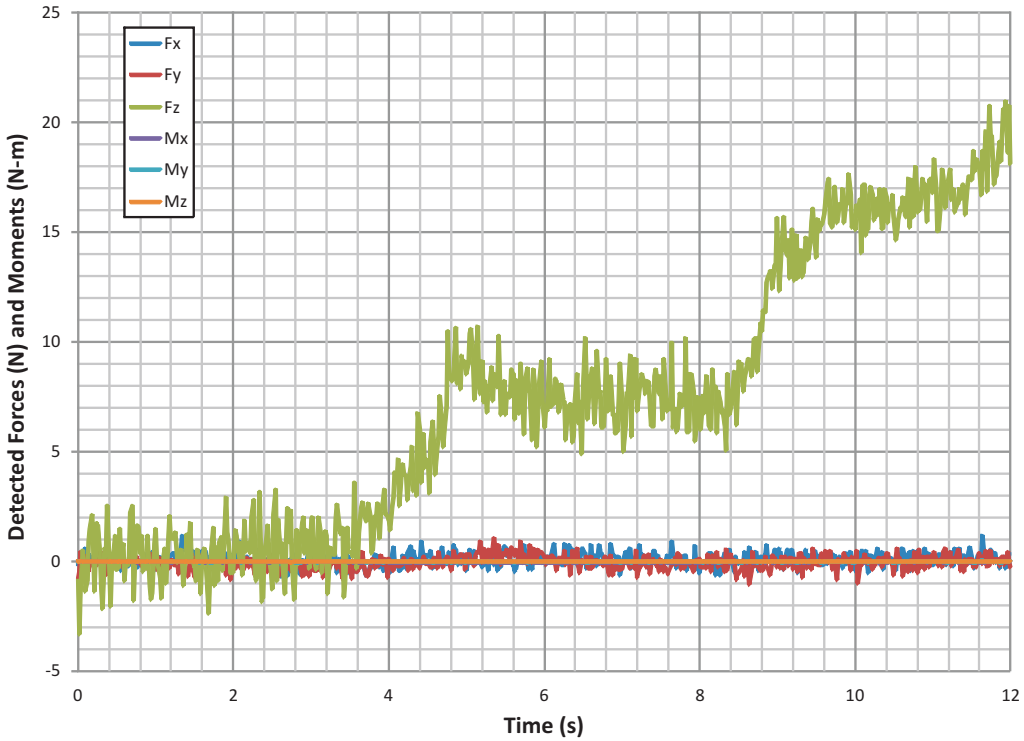

Figure 6.9. Force and moment output from the commercial load cell corresponding to the Z-axis force load application voltage outputs shown in Figure 6.8.

An independent set of voltage outputs were collected for the quarter model sensor array using the SALAD. The [***G***] and [***P***] matrices and calibration equations were then used to convert the voltage outputs back to force and moment values. Force and moment values collected with the commercial load cell are compared to corresponding values calculated with the [***G***] matrix in Figure 6.10. This relationship is relatively linear within a range of approximately 45N. Noise from the commercial load cell and DAQ was a significant source of error with the low force and moment ranges tested. This calibration represents an unamplified Z-axis force sensitivity of 439μV/V-N for the scoliosis sensor array.

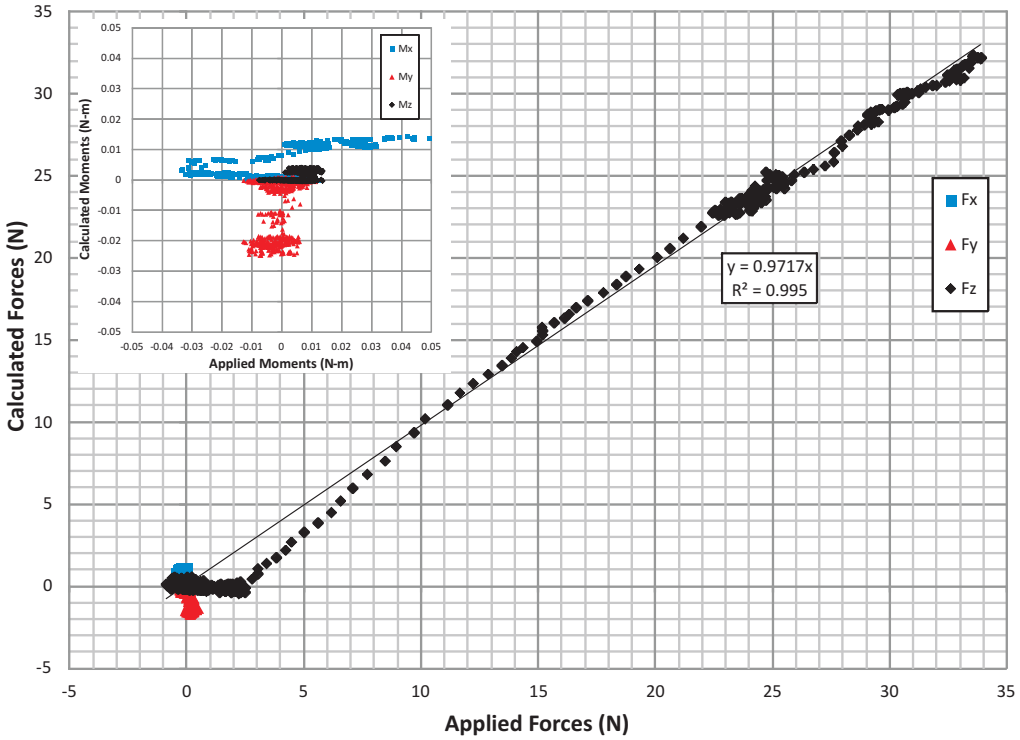

Figure 6.10. Applied versus detected loads as calculated using the [***G***] matrix calibration term.

The linear calibration terms calculated enabled the output voltage data from the scoliosis sensor array to be converted to superimposed force and moment loads. However, limitations in the packaging of the sensor array did not allow large loads to be applied, particularly in directions that required shear force transmission through the sensor pads. This issue caused a bias toward Z-axis force detection, and was largely due to the sensor strips having to be flat-mounted in the mockup screw notch to avoid FPCB tearing. The reduction of the individual sensor pads' abilities to transmit and detect shear loads during calibration reduced the signal to noise ratio of the sensor array's outputs in the X-axis and Y-axis force directions, as well as in the Z-axis moment direction. The ranges of detectable forces and moments were also substantially reduced by these packaging limitations. These issues may require an alternative packaging solution or remanufacture of the sensor pads according to the parametric study presented in Section 4 to improve the shear load detection performance.

6.4 - Wireless and Power Module Integration

Initial calibration of the scoliosis sensor array was carried out using a wired connection to onboard data ports integrated on the device packaging. This allowed the device to be directly connected to the DAQ and powered by an external supply. The advantage of using a wired connection for preliminary calibration was primarily consistency: the power supply was consistent and not subject to depletion and the data transmission rate was not limited by wireless throughput or multiplexing. However, since the final device design required that it be operated in a wireless manner, it was necessary to verify the performance of the sensor array with the power and wireless modules attached.

The wireless and power modules were developed by collaborators and were specifically designed for the 16 voltage outputs produced by the scoliosis sensor array [12, 151, 152]. Both systems were modular in that they could be connected to the wireless and power supply connectors attached to the FPCBs on the device packaging. The wireless and power modules were mounted on independent PCBs that attached to the outer surfaces of the pedicle screws.

The wireless module allowed transmission of voltage output data from the scoliosis sensor array to a personal computer with a receiver module attached. The 16 differential voltages were multiplexed using four, two-channel 4:1 multiplexers (Maxim Integrated Products MAX4782) prior to being passed to a transmitter. The wireless module used a custom protocol which transmitted at 403MHz and was able to transmit 10-bit data at a rate of 10Hz. The power consumption of the wireless module was 0.75μA at 3.0V during sleep mode and 5.62mA at 3.0V during data transmission [151].

The data transmitted by the wireless module was sent at a sufficient rate for the relatively low frequency input loads applied by the surgeons during scoliosis correction surgery, and did not differ substantially from data collected using the wired connection. The wireless module quantized the voltage data with 10-bit resolution, which was a reduction compared to the 16-bit resolution of the DAQ used for wired calibration. The range of voltage outputs produced by the

scoliosis sensor array was found to vary between ±250mV for the load ranges experimentally applied; with these voltage limits the resolution of the wireless module was 488μV. In comparison, the resolution of the DAQ was 31μV when set to an input range of ±1V (with an absolute accuracy of 360μV). As both of these resolution values were below the noise threshold of the scoliosis sensor array, the decreased resolution of the wireless module was not problematic for the operation of the sensor array.

A power module for the scoliosis sensor array was also produced, based on the power consumption of the sensor and wireless module. A current-voltage diagram for a quarter model sensor array is shown in Figure 6.11. The sensing components of the array drew 61mA at 3.0V, which corresponds to 183mW. Due to the multiplexer arrangement, the full model sensor will draw the same amount of current. The power module was a custom design which consisted of a lithium-ion battery. The battery was capable of delivering 110mAh at 3.7V. This system was larger than was optimal for surgery, but could achieve 115 minutes of run time in data collection mode and 172 hours of standby time. These runtime estimates are based on the power consumption of the sensor array and wireless module given above and 95% voltage conversion efficiency.

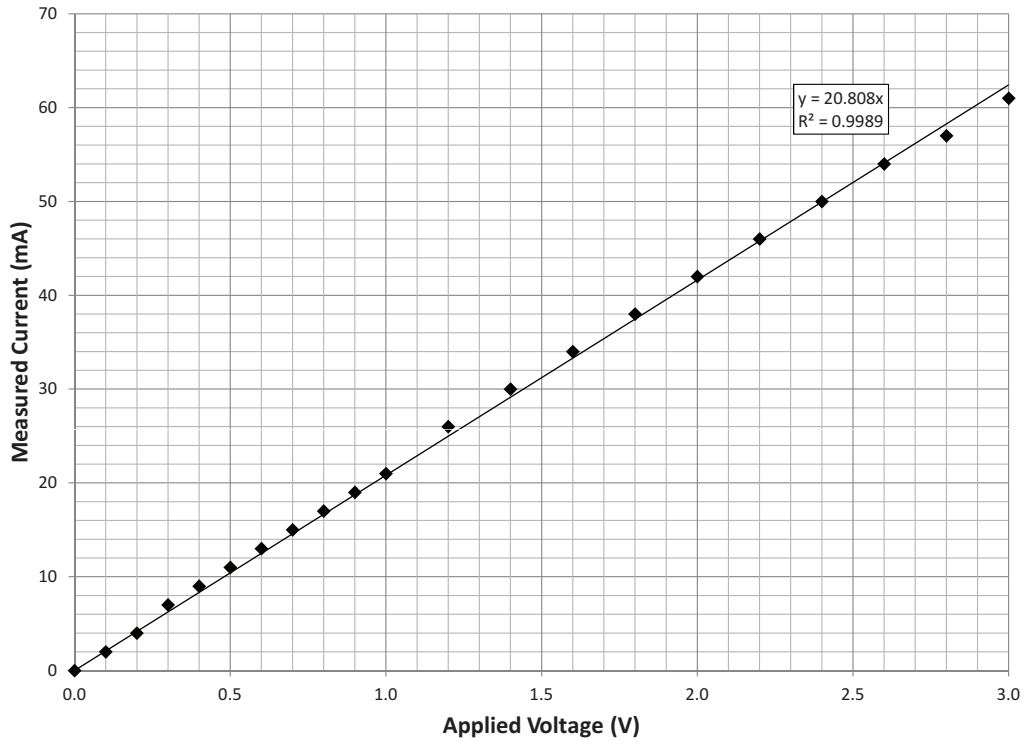

Figure 6.11. The current-voltage response for the quarter model scoliosis sensor array.

6.5 - Durability Testing

The calibration protocol described in this chapter uncovered several concerns relevant to the usage of the scoliosis sensor array during surgery. The first of these concerns noted during calibration was variability in the preload applied to the sensor array by the break-off bolt as the rod was secured. This preload was the primary method of securing the rod to the sensor array and enabled tensile force loads to be detected, so achieving some normality of this parameter was necessary. A known amount of preload could be applied to the sensor array in the SALAD by controlling the Z-axis linear actuator and monitoring the force output prior to securing the break-off bolt, however, this was not possible during surgery. A method to ensure consistent loading by the break-off bolts that can be used in a surgical situation is desirable.

The overall durability of the scoliosis sensor array is also a major concern. The wireless and power modules were not completely encapsulated at this phase

of development, and were too large to be incorporated within or flush against the screw body. This represented a potential risk during surgical usage, as these extended features on the packaged sensor array represent a durability concern. Surgeons should be consulted on the ergonomics of the sensor array during the next phase of development to determine if the packaged device is adequate for operating room usage. However, initial testing has shown that with some additional care being taken when handling the packaged sensor array, the modular features may be acceptable for load detection during surgery.

The packaging materials were the largest concern for the durability of the scoliosis sensor array. As introduced in Section 6.2.3, issues such as tearing of the FPCBs and electrical disconnections were problematic even after coating the sensor strips with a protective layer of adhesive. Individual packaging techniques used were relatively reliable, however, attempting to perform several steps sequentially led to a high rate of prototype device failure. An improvement of the materials and techniques for FPCB creation and implementation, TSV production, and flip-chip electrical connection could improve both the yield and durability of the prototype sensor arrays. A scoliosis screw with the sensor array, power module and wireless module integrated within the screw body itself would ultimately be a superior solution.

6.6 - Conclusions

A quarter model scoliosis sensor array was packaged and mounted to a custom built calibration frame (SALAD). Calibration loads were applied, and linear equations were produced relating voltage outputs from the sensor array to the loads applied. The sensitivity of the scoliosis sensor array was 439μV/V-N in the Z-axis force direction, and was tested to a range of approximately 45N. Parameters for a wireless and power module were specified, and the system defined was capable of transmitting data in the operating room for up to 115 minutes. Improvements to the packaging of the sensor array have also been recommended which will allow the system to be used for a surgical trial.

Chapter 7: Conclusions

A synopsis of the research performed in the preceding chapters is presented. Brief details on the design, manufacturing scheme, packaging, and calibration of the six-axis scoliosis sensor array are given. An outline of the work remaining to prepare the sensor array for an operating room trial is also presented. This remaining work will include tasks to confirm the packaged devices' durability and usability by the orthopaedic surgeons performing the scoliosis correction. Future work also includes analysis of the data collected using the scoliosis sensor array as well as the implementation of the load detection components into other devices and applications.

7.1 - Accomplished Objectives

An investigation of a six-axis sensor able to be retrofit onto existing surgical instrumentation has been performed. Specifically focused on six-axis detection in a scoliosis surgery application, a wireless MEMS sensor array has been designed, simulated, manufactured, packaged, and calibrated. The main contributions of this research have included the novel implementation of TSVs into a piezoresistive microfabrication flow, the parametric characterization of sensor pads in terms of shear and normal sensitivities, the development and characterization of packaging techniques for MEMS devices and FPCBs, and the development and validation of a custom six-axis calibration apparatus and protocol.

This thesis has been divided into seven chapters. Chapter one outlines and describes the motivation for this research, chapter two presents the relevant literature, chapter three focuses on production of the piezoresistive sensing components, chapter four details a sensitivity analysis of the piezoresistive sensing components, chapter five describes packaging and deployment techniques, and chapter six gives a description of device calibration. Further details on the objectives accomplished and described in chapters three through six are provided below.

The third chapter described the development cycle for the MEMS sensor pads. This cycle included analytical analysis, FEA, microfabrication, and verification of the fabrication parameters. Evaluation of the requirements of the scoliosis surgery application led to the development of a piezoresistive sensing solution. The sensor pads developed consisted of four, four-terminal piezoresistive gauges on deformable single-crystal silicon membranes, which allowed the detection of 3D loads applied to their surfaces. Development of the MEMS sensor pads included the study of piezoresistivity and silicon dopants, numerical methods, TSVs, and a variety of microfabrication techniques.

Chapter four provided details on the experimental and numerical characterization of the manufactured sensor pads. Methodology was defined that allowed trends in sensitivity to be determined as specific geometric and material parameters of the sensor pads were varied. These parameters included the size and location of the force application site, mesa height, membrane thickness, piezoresistive doping levels, and the position of the piezoresistors on the membrane surface. As the sensor pads were capable of detecting 3D applied loads, both normal and shear sensitivities were examined. It was determined that decreasing the membrane thickness caused the greatest increase in normal sensitivity and increasing the mesa height caused the greatest increase in shear sensitivity. In addition, asymmetrical load application (misalignment) was found to have significant effects on sensor pad sensitivity and was a major source of experimental error.

The focus of chapter five was packaging and deployment of the MEMS sensor pads on the pedicle screws. This allowed four sensor pads, a wireless module, a power module, and interconnection circuitry (FPCBs) to be installed on a pedicle screw, thus forming the scoliosis sensor array. Research was conducted with the goal of making the scoliosis sensor array durable enough to be used safely during a surgical procedure. This included producing and examining TSVs, which used tapered through-holes filled with isotropic conductive adhesive. In addition, various wire bonding and flip-chip techniques were evaluated for their mechanical and electrical properties in this application.

Adhesives were also examined for their ability to improve the durability of the scoliosis sensor array.

Chapter six described the method used to calibrate the scoliosis sensor array. A custom calibration frame (the SALAD) was commissioned that allowed the voltage output from the scoliosis sensor array to be compared to the output from a commercial six-axis load cell. In addition, a flexible automated technique for producing calibration equations was presented. A quarter model scoliosis sensor array was used to test the calibration equipment and methodology. Despite durability issues encountered during calibration, the sensitivity of the scoliosis sensor array was determined to be 439μV/V-N in the Z-axis force direction and was tested to a range of approximately 45N. Chapter six also described the DAQ components, wireless module, and power module used for the SALAD and scoliosis sensor array. These parameters determined that surgical data could be transmitted for over 115 minutes at 10Hz with 10-bit quantization.

7.2 - Future Work

A six-axis sensor array has been designed, manufactured, packaged, and calibrated. Efforts were made throughout the development cycle to create a device appropriate for use in scoliosis surgery. However, considering the lack of durability and range that the sensor array displayed during calibration, the device is clearly not ready for a surgical trial.

The next phase in the development of this sensor array will be to improve the packaging and deployment solution to resolve the lack of durability and load range. Provided this can be done successfully, the sensor array must then be thoroughly examined for factors such as sterilizability, battery life, ergonomics, and potential for interference with surgical protocols. Another concern that may need to be examined in this future phase has to do with the temporary installation of the sensor. If the scoliosis sensor array needs to be removed after the procedure is finished, it inherently adds time and patient risk. Therefore, an obvious upgrade to the current sensor array would be an energy harvesting or

remotely rechargeable power module. This would allow the scoliosis sensor array to be left in the patient for monitoring spinal loads post-operatively.

Provided demands of the orthopaedic surgeons can be satisfied and there is adoption of this technology during scoliosis correction and other spinal fusion surgeries, there is potential for substantial gain in terms of knowledge of the spine's mechanical behavior. Initially, this mechanical behavior will be able to make scoliosis surgery safer and more effective. On a longer time scale, studying the mechanical behavior will allow biological properties to be measured and evaluated. Scoliosis curves have inherent strength. Adjusting these curves by a known amount while collecting the 3D forces and moments applied has potential to capture specific strength and stiffness information on the deformity. This information could be used in pre-surgical planning, or in biomedical models to simulate the spine's behavior.

Validation of this load detection concept during scoliosis correction surgery also could lead to its application in other biomedical applications. Implants, surgical tools, dental braces, and prosthetics are potential medical applications which could benefit from the six-axis load detection provided by this sensor array. The small size of this sensor array will allow the implementation of sensing components with a minimum effect on the size or usage of the existing medical hardware.

Another application of this sensor array technology is for a general-use load cell. The proposed six-axis sensing array is approximately an order of magnitude smaller than the smallest (non-custom) six-axis load cell currently available (ATI Nano17). The proposed scoliosis sensor array is also packaged with a wireless system, which is relatively uncommon in commercial six-axis load cells. Reducing the size and relative cost of a six-axis sensor represents a substantial improvement to the load cell field, and could lead to the discovery of new applications where 3D force and moment sensing can be implemented.

Bibliography

[1] D. Benfield, "A High Load MEMS Sensor for Use in Scoliosis Correction Surgery," *M.Sc. Thesis in Mechanical Engineering.* University of Alberta, 2005.

[2] D. Benfield, E. Lou, and W. Moussa, "Development of a MEMS-based sensor array to characterise in situ loads during scoliosis correction surgery," *Computer Methods in Biomechanics and Biomedical Engineering,* vol. 11, pp. 335-350, Aug 2008.

[3] A.D.A.M. Inc.,"Scoliosis," in *A.D.A.M. Medical Encyclopedia*, 2009.

[4] N. H. Miller, "Cause and natural history of adolescent idiopathic scoliosis," *Orthopedic Clinics of North America,* vol. 30, pp. 343-352, Jul 1999.

[5] F. Graichen, R. Arnold, A. Rohlmann, and G. Bergmann, "Implantable 9-channel telemetry system for in vivo load measurements with orthopedic implants," *IEEE Transactions on Biomedical Engineering,* vol. 54, pp. 253-261, 2007.

[6] J. M. Hicks, A. Singla, F. H. Shen, and V. Arlet, "Complications of Pedicle Screw Fixation in Scoliosis Surgery A Systematic Review," *Spine,* vol. 35, pp. E465-E470, May 2010.

[7] J. P. Kostuik, E. Munting, and A. Valdevit, "Biomechanical Analysis of Screw Load Sharing in Pedicle Fixation of the Lumbar Spine," *Journal of Spinal Disorders,* vol. 7, pp. 394-401, Oct 1994.

[8] E. H. Ledet, M. P. Tymeson, D. J. DiRisio, B. Cohen, and R. L. Uhl, "Direct real-time measurement of in vivo forces in the lumbar spine," *Spine Journal: Official Journal of the North American Spine Society,* vol. 5, pp. 85-94, 2005.

[9] K. Duke, "The Design of Instrumentation for Force Measurement During Scoliosis Surgery," *M.Sc. Thesis in Mechanical Engineering.* University of Alberta, 2000.

[10] H. K. Dunn, A. U. Daniels, and G. G. Mcbride, "Intra-Operative Force Measurements during Correction of Scoliosis," *Spine,* vol. 7, pp. 448-455, 1982.

[11] E. Lou, D. L. Hill, J. V. Raso, M. J. Moreau, and J. K. Mahood, "Instrumented rod rotator system for spinal surgery," *Medical & Biological Engineering & Computing,* vol. 40, pp. 376-379, Jul 2002.

[12] E. Lou, V. J. Raso, B. Martin, D. Schile, M. Epper, J. K. Mahood, M. Moreau, and D. L. Hill, "Wireless surgical tools for mechanical measurements during scoliosis surgery," *2005 27th Annual International Conference of the IEEE Engineering in Medicine and Biology Society,* vol. 1-7, pp. 7131-7134, 2005.

[13] V. J. Raso, E. Lou, S. Dowler, D. Hill, M. J. Moreau, and J. K. Mahood, "Intra-Operative Load Measurement," *International Research Society of Spinal Deformities*, pp. 266-269, 2004.

[14] A. Rohlmann, U. Gabel, F. Graichen, A. Bender, and G. Bergmann, "An instrumented implant for vertebral body replacement that measures loads in the anterior spinal column," *Medical Engineering & Physics,* vol. 29, pp. 580-585, Jun 2007.

[15] J. Dubousset and Y. Cotrel, "Application Technique of Cotrel-Dubousset Instrumentation for Scoliosis Deformities," *Clinical Orthopaedics and Related Research,* pp. 103-110, Mar 1991.

[16] D. J. Hedequist, "Surgical treatment of congenital scoliosis," *Orthopedic Clinics of North America,* vol. 38, pp. 497-509, Oct 2007.

[17] B. S. Lonner, "Emerging minimally invasive technologies for the management of scoliosis," *Orthopedic Clinics of North America,* vol. 38, pp. 431-440, Jul 2007.

[18] A. B. Schultz and C. Hirsch, "Mechanical Analysis of Harrington Rod Correction of Idiopathic Scoliosis," *Journal of Bone and Joint Surgery-American Volume,* vol. 55, pp. 983-992, 1973.

[19] A. Rohlmann, F. Graichen, U. Weber, and G. Bergmann, "Monitoring in vivo implant loads with a telemeterized internal spinal fixation device," *Spine,* vol. 25, pp. 2981-2986, 2000.

[20] K. Pehrsson, S. Larsson, A. Oden, and A. Nachemson, "Long-Term Follow-up of Patients with Untreated Scoliosis - a Study of Mortality, Causes of Death, and Symptoms," *Spine,* vol. 17, pp. 1091-1096, Sep 1992.

[21] K. Pehrsson, A. Nachemson, J. Olofson, K. Strom, and S. Larsson, "Respiratory-Failure in Scoliosis and Other Thoracic Deformities - a Survey of Patients with Home Oxygen or Ventilator Therapy in Sweden," *Spine,* vol. 17, pp. 714-718, Jun 1992.

[22] P. R. Harrington, "Treatment of Scoliosis - Correction and Internal Fixation by Spine Instrumentation," *Journal of Bone and Joint Surgery,* vol. 44, pp. 591-634, 1962.

[23] C. Hirsch and T. Waugh, "Introduction of Force Measurements Guiding Instrumental Correction of Scoliosis," *Acta Orthopaedica Scandinavica,* vol. 39, pp. 136-144, 1968.

[24] A. F. Dwyer, "Anterior Instrumentation for Scoliosis," *Israel Journal of Medical Sciences,* vol. 9, pp. 805-812, 1973.

[25] K. Zielke and B. Pellin, "42 Scoliosis Operations Using Harringtons Equipment-Report on Experiences - Comment," *Zeitschrift Fur Orthopadie Und Ihre Grenzgebiete,* vol. 113, pp. 1103-1105, 1975.

[26] K. Zielke, "Surgical Management of Scoliosis in Adults," *Zeitschrift Fur Orthopadie Und Ihre Grenzgebiete,* vol. 114, pp. 598-604, 1976.

[27] W. A. Herndon, R. D. Ellis, J. E. Hall, and M. B. Millis, "Correction with a Transverse Loading System in the Operative Management of Scoliosis," *Clinical Orthopaedics and Related Research,* pp. 168-171, 1982.

[28] Y. Cotrel, J. Dubousset, and M. Guillaumat, "New Universal Instrumentation in Spinal Surgery," *Clinical Orthopaedics and Related Research,* pp. 10-23, Feb 1988.

[29] U. R. Liljenqvist, H. F. H. Halm, and T. M. Link, "Pedicle screw instrumentation of the thoracic spine in idiopathic scoliosis," *Spine,* vol. 22, pp. 2239-2245, Oct 1997.

[30] S. I. Suk, C. K. Lee, W. J. Kim, Y. J. Chung, and Y. B. Park, "Segmental Pedicle Screw Fixation in the Treatment of Thoracic Idiopathic Scoliosis," *Spine,* vol. 20, pp. 1399-1405, Jun 1995.

[31] S. I. Suk, C. K. Lee, H. J. Min, K. H. Cho, and J. H. Oh, "Comparison of Cotrel-Dubousset Pedicle Screws and Hooks in the Treatment of Idiopathic Scoliosis," *International Orthopaedics,* vol. 18, pp. 341-346, Dec 1994.

[32] U. Liljenqvist, L. Hackenberg, T. Link, and H. Halm, "Pullout strength of pedicle screws versus pedicle and laminar hooks in the thoracic spine," *Acta Orthop Belg,* vol. 67, pp. 157-163, Apr 2001.

[33] G. Elfstrom and A. Nachemson, "Telemetry Recordings of Forces in Harrington Distraction Rod - Method for Increasing Safety in Operative Treatment of Scoliosis Patients," *Clinical Orthopaedics and Related Research,* pp. 158-172, 1973.

[34] F. Graichen, G. Bergmann, and A. Rohlmann, "Telemetry System for in-Vivo Measurement of the Loading of an Internal Spinal Fixation Device," *Biomedizinische Technik,* vol. 39, pp. 251-258, Oct 1994.

[35] G. G. McBride, H. K. Dunn, and A. U. Daniels, "Force measurements during operative correction of spinal deformities," *Biomedical Sciences Instrumentation,* vol. 15, pp. 19-24, 1979.

[36] A. Nachemson and G. Elfstrom, "Intravital Wireless Telemetry of Axial Forces in Harrington Distraction Rods in Patients with Idiopathic Scoliosis," *Journal of Bone and Joint Surgery,* vol. 53, pp. 445-465, 1971.

[37] A. Rohlmann, G. Bergmann, and F. Graichen, "A Spinal Fixation Device for In-Vivo Load Measurement," *Journal of Biomechanics,* vol. 27, pp. 961-967, Jul 1994.

[38] A. Rohlmann, L. H. Riley, G. Bergmann, and F. Graichen, "In vitro load measurement using an instrumented spinal fixation device," *Medical Engineering & Physics,* vol. 18, pp. 485-488, Sep 1996.

[39] V. K. Goel and L. G. Gilbertson, "Applications of the Finite-Element Method to Thoracolumbar Spinal Research - Past, Present, and Future," *Spine,* vol. 20, pp. 1719-1727, Aug 1995.

[40] Y. Majdouline, C. E. Aubin, A. Sangole, and H. Labelle, "Computer simulation for the optimization of instrumentation strategies in adolescent idiopathic scoliosis," *Medical & Biological Engineering & Computing,* vol. 47, pp. 1143-1154, Nov 2009.

[41] D. Benfield, E. Lou, and W. A. Moussa, "Parametric evaluation of shear sensitivity in piezoresistive interfacial force sensors," *Journal of Micromechanics and Microengineering,* vol. 21, Apr 2011.

[42] M. S. Bartsch, W. Federle, R. J. Full, and T. W. Kenny, "A multiaxis force sensor for the study of insect biomechanics," *Journal of Microelectromechanical Systems,* vol. 16, pp. 709-718, Jun 2007.

[43] L. Beccai, S. Roccella, A. Arena, F. Valvo, P. Valdastri, A. Menciassi, M. C. Carrozza, and P. Dario, "Design and fabrication of a hybrid silicon three-axial force sensor for biomechanical applications," *Sensors and Actuators A-Physical,* vol. 120, pp. 370-382, May 2005.

[44] A. Tibrewala, A. Phataralaoha, and S. Buttgenbach, "Development, fabrication and characterization of a 3D tactile sensor," *Journal of Micromechanics and Microengineering,* vol. 19, Dec 2009.

[45] P. Valdastri, S. Roccella, L. Beccai, E. Cattin, A. Menciassi, M. C. Carrozza, and P. Dario, "Characterization of a novel hybrid silicon three-axial force sensor," *Sensors and Actuators A-Physical,* vol. 123-124, pp. 249-257, Sep 2005.

[46] L. Wang and D. J. Beebe, "A silicon-based shear force sensor: development and characterization," *Sensors and Actuators A-Physical,* vol. 84, pp. 33-44, Aug 2000.

[47] J. Dargahi, M. Parameswaran, and S. Payandeh, "A micromachined piezoelectric tactile sensor for an endoscopic grasper - Theory, fabrication and experiments," *Journal of Microelectromechanical Systems,* vol. 9, pp. 329-335, Sep 2000.

[48] M. C. Hsieh, Y. K. Fang, M. S. Ju, G. S. Chen, J. J. Ho, C. H. Yang, P. M. Wu, G. S. Wu, and T. Y. F. Chen, "A contact-type piezoresistive micro-shear stress sensor for above-knee prosthesis application," *Journal of Microelectromechanical Systems,* vol. 10, pp. 121-127, Mar 2001.

[49] E. S. Hwang, J. H. Seo, and Y. J. Kim, "A polymer-based flexible tactile sensor for both normal and shear load detections and its application for robotics," *Journal of Microelectromechanical Systems,* vol. 16, pp. 556-563, Jun 2007.

[50] J. W. Gardner, V. K. Varadan, and O. O. Awadelkarim, *Microsensors, MEMS, and smart devices*. Chichester ; New York: J. Wiley, 2001.

[51] S. D. Senturia, *Microsystem design*. Boston: Kluwer Academic Publishers, 2001.

[52] J. C. Irvin, "Resistivity of Bulk Silicon and of Diffused Layers in Silicon," *Bell System Technical Journal,* vol. 41, pp. 387-410, 1962.

[53] K. E. Petersen, "Silicon as a Mechanical Material," *Proceedings of the Ieee,* vol. 70, pp. 420-457, 1982.

[54] C. S. Smith, "Piezoresistance Effect in Germanium and Silicon," *Physical Review,* vol. 94, pp. 42-49, 1954.

[55] C. Herring, "Transport Properties of a Many-Valley Semiconductor," *Bell System Technical Journal,* vol. 34, pp. 237-290, 1955.

[56] W. P. Mason and R. N. Thurston, "Use of Piezoresistive Materials in the Measurement of Displacement, Force, and Torque," *Journal of the Acoustical Society of America,* vol. 29, pp. 1096-1101, 1957.

[57] W. G. Pfann and R. N. Thurston, "Semiconducting Stress Transducers Utilizing Transverse and Shear Piezoresistance Effects," *Journal of Applied Physics,* vol. 32, pp. 2008-2019, 1961.

[58] M. G. Buehler, S. D. Grant, and W. R. Thurber, "Bridge and Van-Der-Pauw Sheet Resistors for Characterizing Line-Width of Conducting Layers," *Journal of the Electrochemical Society,* vol. 125, pp. 650-654, 1978.

[59] M. G. Buehler and W. R. Thurber, "Experimental-Study of Various Cross Sheet Resistor Test Structures," *Journal of the Electrochemical Society,* vol. 125, pp. 645-650, 1978.

[60] W. R. Thurber, R. L. Mattis, and Y. M. Liu, "Resistivity-Dopant Density Relationship for Silicon," *Journal of the Electrochemical Society,* vol. 125, pp. C136-C136, 1978.

[61] W. R. Thurber, R. L. Mattis, Y. M. Liu, and J. J. Filliben, "Resistivity-Dopant Density Relationship for Phosphorus-Doped Silicon," *Journal of the Electrochemical Society,* vol. 127, pp. 1807-1812, 1980.

[62] W. R. Thurber, R. L. Mattis, Y. M. Liu, and J. J. Filliben, "Resistivity-Dopant Density Relationship for Boron-Doped Silicon," *Journal of the Electrochemical Society,* vol. 127, pp. 2291-2294, 1980.

[63] Y. Kanda, "Optimum Design Considerations for Silicon Pressure Sensors Using a 4-Terminal Gauge," *Sensors and Actuators,* vol. 4, pp. 199-206, 1983.

[64] S. J. Proctor, L. W. Linholm, and J. A. Mazer, "Direct Measurements of Interfacial Contact Resistance, End Contact Resistance, and Interfacial Contact Layer Uniformity," *Ieee Transactions on Electron Devices,* vol. 30, pp. 1535-1542, 1983.

[65] M. H. Bao and Y. Wang, "Analysis and Design of a 4-Terminal Silicon Pressure Sensor at the Center of a Diaphragm," *Sensors and Actuators,* vol. 12, pp. 49-56, Jul 1987.

[66] M. H. Bao, W. J. Qi, and Y. Wang, "Geometric Design Rules of 4-Terminal Gauge for Pressure Sensors," *Sensors and Actuators,* vol. 18, pp. 149-156, Jun 1989.

[67] K. Seeger, *Semiconductor physics : an introduction*, 9th ed. Berlin ; New York: Springer, 2004.

[68] M.-H. Bao, *Micro mechanical transducers : pressure sensors, accelerometers, and gyroscopes*. Amsterdam New York: Elsevier, 2000.

[69] D. R. Lovett, *Tensor properties and crystals*. Bristol, England ; Philadelphia: Adam Hilger, 1989.

[70] B. E. Sernelius, "Temperature-Dependent Resistivity of Heavily Doped Silicon and Germanium," *Physical Review B,* vol. 41, pp. 3060-3068, Feb 1990.

[71] Y. Kanda, "Piezoresistance Effect of Silicon," *Sensors and Actuators A-Physical,* vol. 28, pp. 83-91, Jul 1991.

[72] O. N. Tufte and E. L. Stelzer, "Piezoresistive Properties of Silicon Diffused Layers," *Journal of Applied Physics,* vol. 34, pp. 313-318, 1963.

[73] O. N. Tufte and E. L. Stelzer, "Piezoresistive Properties of Heavily Doped N-Type Silicon," *Physical Review A-General Physics,* vol. 133, pp. 1705-1716, 1964.

[74] Y. Kanda, "A Graphical Representation of the Piezoresistance Coefficients in Silicon," *Ieee Transactions on Electron Devices,* vol. 29, pp. 64-70, 1982.

[75] F. Bordoni and A. Damico, "Noise in Sensors," *Sensors and Actuators A-Physical,* vol. 21, pp. 17-24, Feb 1990.

[76] J. A. Harley and T. W. Kenny, "1/F noise considerations for the design and process optimization of piezoresistive cantilevers," *Journal of Microelectromechanical Systems,* vol. 9, pp. 226-235, Jun 2000.

[77] A. C. Diebold, *Handbook of silicon semiconductor metrology*. New York: Marcel Dekker, 2001.

[78] R. C. Jaeger, *Introduction to microelectronic fabrication*. Reading, Mass.: Addison-Wesley Pub. Co., 1987.

[79] P. B. Joshi and P. Ramakrishnan, *Materials for electrical and electronic contacts : processing, properties, and applications*. Enfield, NH, USA: Science Publishers, 2004.

[80] B. Pellegrini, "Properties of Silicon-Metal Contacts Versus Metal Work-Function, Silicon Impurity Concentration and Bias Voltage," *Journal of Physics D-Applied Physics,* vol. 9, pp. 55-68, 1976.

[81] R. R. Spencer, B. M. Fleischer, P. W. Barth, and J. B. Angell, "A Theoretical-Study of Transducer Noise in Piezoresistive and Capacitive Silicon Pressure Sensors," *Ieee Transactions on Electron Devices,* vol. 35, pp. 1289-1298, Aug 1988.

[82] L. K. J. Vandamme and S. Oosterhoff, "Annealing of Ion-Implanted Resistors Reduces the 1/F Noise," *Journal of Applied Physics,* vol. 59, pp. 3169-3174, May 1986.

[83] Motorola,"Motorola Master Semiconductor Guide," 7th ed., 1994.

[84] A. V. Gridchin and V. A. Gridchin, "The four-terminal piezotransducer: theory and comparison with piezoresistive bridge," *Sensors and Actuators A-Physical,* vol. 58, pp. 219-223, Mar 1997.

[85] S. Timoshenko and S. Woinowsky-Krieger, *Theory of plates and shells*, 2nd ed. New York: McGraw-Hill, 1959.

[86] Y. Matsuoka, Y. Yamamoto, M. Tanabe, S. Shimada, K. Yamada, A. Yasukawa, and H. Matsuzaka, "Low-Pressure Measurement Limits for Silicon Piezoresistive Circular Diaphragm Sensors," *Journal of Micromechanics and Microengineering,* vol. 5, pp. 32-35, Mar 1995.

[87] C. Pramanik, H. Saha, and U. Gangopadhyay, "Design optimization of a high performance silicon MEMS piezoresistive pressure sensor for biomedical applications," *Journal of Micromechanics and Microengineering,* vol. 16, pp. 2060-2066, Oct 2006.

[88] A. P. Boresi and R. J. Schmidt, *Advanced mechanics of materials*, 6th ed. New York: John Wiley & Sons, 2003.

[89] J. O. Smith and C. K. Liu, "Stresses due to tangential and normal loads on an elastic solid with application to some contact stress problems," *Journal of Applied Mechanics,* vol. 71, pp. 157-166, 1963.

[90] C. C. Chang, C. T. Lieu, and M. K. Hsich, "Study of the fabrication of a silicon pressure sensor," *International Journal of Electronics,* vol. 82, pp. 295-302, Mar 1997.

[91] H. E. Elgamel, "Closed-form expressions for the relationships between stress, diaphragm deflection, and resistance change with pressure in silicon piezoresistive pressure sensors," *Sensors and Actuators A-Physical,* vol. 50, pp. 17-22, 1995.

[92] L. W. Lin and W. J. Yun, "Design, optimization and fabrication of surface micromachined pressure sensors," *Mechatronics,* vol. 8, pp. 505-519, Aug 1998.

[93] Y. Matsuoka, Y. Yamamoto, K. Yamada, S. Shimada, M. Tanabe, A. Yasukawa, and H. Matsuzaka, "Characteristic Analysis of a Pressure Sensor Using the Silicon Piezoresistance Effect for High-Pressure Measurements," *Journal of Micromechanics and Microengineering,* vol. 5, pp. 25-31, Mar 1995.

[94] O. N. Tufte, D. Long, and P. W. Chapman, "Silicon Diffused-Element Piezoresistive Diaphragms," *Journal of Applied Physics,* vol. 33, pp. 3322-3327, 1962.

[95] M. G. El-Hak, *The MEMS handbook*. Boca Raton, FL: CRC Press, 2002.

[96] Z. Y. Chi and K. Shida, "A new multifunctional tactile sensor for three-dimensional force measurement," *Sensors and Actuators A-Physical,* vol. 111, pp. 172-179, Mar 2004.

[97] B. J. Kane, M. R. Kutkosky, and G. T. A. Kovacs, "A traction stress sensor array for use in high-resolution robotic tactile imaging," *Journal of Microelectromechanical Systems,* vol. 9, pp. 425-433, 2000.

[98] T. Mei, W. J. Li, Y. Ge, Y. Chen, L. Ni, and M. H. Chan, "An integrated MEMS three-dimensional tactile sensor with large force range," *Sensors and Actuators A-Physical,* vol. 80, pp. 155-162, Mar 2000.

[99] S. P. Denyer and R. M. Baird, "Guide to microbiological control in pharmaceuticals and medical devices," 2nd ed. London: CRC Press, 2007.

[100] S. L. Burkett, X. Qiao, D. Temple, B. Stoner, and G. McGuire, "Advanced processing techniques for through-wafer interconnects," *Journal of Vacuum Science & Technology B,* vol. 22, pp. 248-256, Jan-Feb 2004.

[101] Y. H. Cao, W. G. Ning, and L. Luo, "Wafer-Level Package With Simultaneous TSV Connection and Cavity Hermetic Sealing by Solder Bonding for MEMS Device," *Ieee Transactions on Electronics Packaging Manufacturing,* vol. 32, pp. 125-132, Jul 2009.

[102] E. M. Chow, V. Chandrasekaran, A. Partridge, T. Nishida, M. Sheplak, C. F. Quate, and T. W. Kenny, "Process compatible polysilicon-based electrical through-wafer interconnects in silicon substrates," *Journal of Microelectromechanical Systems,* vol. 11, pp. 631-640, Dec 2002.

[103] P. Dixit, J. Salonen, H. Pohjonen, and P. Monnoyer, "The application of dry photoresists in fabricating cost-effective tapered through-silicon vias and redistribution lines in a single step," *Journal of Micromechanics and Microengineering,* vol. 21, Feb 2011.

[104] A. C. Fischer, M. Grange, N. Roxhed, R. Weerasekera, D. Pamunuwa, G. Stemme, and F. Niklaus, "Wire-bonded through-silicon vias with low capacitive substrate coupling," *Journal of Micromechanics and Microengineering,* vol. 21, Aug 2011.

[105] F. Ji, E. Leppadvuori, I. Luusua, K. Hentfinen, S. Eranen, H. Hietanen, and M. Juntunen, "Fabrication of silicon based through-wafer interconnects for advanced chip scale packaging," *Sensors and Actuators A-Physical,* vol. 142, pp. 405-412, Mar 2008.

[106] Y. H. Joung and M. G. Allen, "A micromachined chip-to-board interconnect system using electroplating bonding technology," *Ieee Transactions on Advanced Packaging,* vol. 31, pp. 357-366, May 2008.

[107] J. Jozwiak, R. G. Southwick, V. N. Johnson, W. B. Knowlton, and A. J. Moll, "Integrating through-wafer interconnects with active devices and circuits," *Ieee Transactions on Advanced Packaging,* vol. 31, pp. 4-13, Feb 2008.

[108] S. W. R. Lee, R. Hon, S. X. D. Zhang, and C. K. Wong, "3D stacked flip chip packaging with through silicon vias and copper plating or conductive adhesive filling," *55th Electronic Components & Technology Conference, Vols 1 and 2, 2005 Proceedings,* pp. 795-801, 2005.

[109] M. Motoyoshi, "Through-Silicon Via (TSV)," *Proceedings of the Ieee,* vol. 97, pp. 43-48, Jan 2009.

[110] S. J. Ok, C. H. Kim, and D. F. Baldwin, "High density, high aspect ratio through-wafer electrical interconnect vias for MEMS packaging," *Ieee Transactions on Advanced Packaging,* vol. 26, pp. 302-309, Aug 2003.

[111] J. Tian, S. Sosin, J. Lannacci, R. Gaddi, and M. Bartek, "RF-MEMS wafer-level packaging using through-wafer interconnect," *Sensors and Actuators a-Physical,* vol. 142, pp. 442-451, Mar 2008.

[112] Z. Y. Wang, L. W. Wang, N. T. Nguyen, W. A. H. Wien, H. Schellevis, P. M. Sarro, and J. N. Burghartz, "Silicon micromachining of high aspect ratio, high-density through-wafer electrical interconnects for 3-D multichip packaging," *Ieee Transactions on Advanced Packaging,* vol. 29, pp. 615-622, Aug 2006.

[113] J. H. Wu and J. A. del Alamo, "Fabrication and Characterization of Through-Substrate Interconnects," *Ieee Transactions on Electron Devices,* vol. 57, pp. 1261-1268, Jun 2010.

[114] J. H. Wu, J. Scholvin, and J. A. del Alamo, "A through-wafer interconnect in silicon for RFICs," *Ieee Transactions on Electron Devices,* vol. 51, pp. 1765-1771, Nov 2004.

[115] S. L. Lai, D. Johnson, and R. Westerman, "Aspect ratio dependent etching lag reduction in deep silicon etch processes," *Journal of Vacuum Science & Technology A,* vol. 24, pp. 1283-1288, Jul-Aug 2006.

[116] J. Yeom, Y. Wu, J. C. Selby, and M. A. Shannon, "Maximum achievable aspect ratio in deep reactive ion etching of silicon due to aspect ratio dependent transport and the microloading effect," *Journal of Vacuum Science & Technology B,* vol. 23, pp. 2319-2329, Nov-Dec 2005.

[117] S. Aachboun, P. Ranson, C. Hilbert, and M. Boufnichel, "Cryogenic etching of deep narrow trenches in silicon," *Journal of Vacuum Science & Technology A-Vacuum Surfaces and Films,* vol. 18, pp. 1848-1852, Jul-Aug 2000.

[118] J. W. Coburn and H. F. Winters, "Conductance Considerations in the Reactive Ion Etching of High Aspect Ratio Features," *Applied Physics Letters,* vol. 55, pp. 2730-2732, Dec 1989.

[119] M. J. de Boer, J. G. E. Gardeniers, H. V. Jansen, E. Smulders, M. J. Gilde, G. Roelofs, J. N. Sasserath, and M. Elwenspoek, "Guidelines for etching silicon MEMS structures using fluorine high-density plasmas at cryogenic temperatures," *Journal of Microelectromechanical Systems,* vol. 11, pp. 385-401, Aug 2002.

[120] P. J. Gilgunn, J. F. Alfaro, and G. K. Fedder, "Model for aspect ratio dependent etch modulated processing," *Journal of Vacuum Science & Technology A,* vol. 28, pp. 334-346, Mar 2010.

[121] S. K. Dew, "Theoretical and Practical Aspects of Collimated Sputtering," *Journal of Applied Physics,* vol. 76, pp. 4857-4862, Oct 1994.

[122] S. K. Dew, D. Liu, M. J. Brett, and T. Smy, "Spatial and Angular Nonuniformities from Collimated Sputtering," *Journal of Vacuum Science & Technology B,* vol. 11, pp. 1281-1286, Jul-Aug 1993.

[123] S. M. Rossnagel, D. Mikalsen, H. Kinoshita, and J. J. Cuomo, "Collimated Magnetron Sputter Deposition," *Journal of Vacuum Science & Technology A-Vacuum Surfaces and Films,* vol. 9, pp. 261-265, Mar-Apr 1991.

[124] All Flex Flexible Circuits, "Flexible Circuit and Heater Design Guide.", 2011.

[125] N. Jackson and J. Muthuswamy, "Flexible Chip-Scale Package and Interconnect for Implantable MEMS Movable Microelectrodes for the Brain," *Journal of Microelectromechanical Systems,* vol. 18, pp. 396-404, Apr 2009.

[126] B. Majeed, I. Paul, K. M. Razeeb, J. Barton, and S. C. O'Mathuna, "Effect of gold stud bump topology on reliability of flip chip on flex interconnects," *Ieee Transactions on Advanced Packaging,* vol. 30, pp. 605-615, Nov 2007.

[127] H. Maruo, Y. Seki, and Y. Unami, "Development of ultrasonic flip chip bonding for flexible printed circuit," *Proceedings of the Sixth Ieee Cpmt Conference on High Density Microsystem Design and Packaging and Component Failure Analysis (Hdp'04),* pp. 307-310, 2004.

[128] D. Benfield, W. Moussa, and E. Lou, "A high-load stress sensor for scoliosis surgery application," *2004 International Conference on Mems, Nano and Smart Systems, Proceedings,* pp. 659-662, 2004.

[129] Z. Chu, P. M. Sarro, and S. Middelhoek, "Silicon three-axial tactile sensor," *Sensors and Actuators A-Physical,* vol. 54, pp. 505-510, Jun 1996.

[130] W. L. Jin and C. D. Mote, "A six-component silicon micro force sensor," *Sensors and Actuators A-Physical,* vol. 65, pp. 109-115, Mar 1998.

[131] W. L. Jin and C. D. Mote, "Development and calibration of a sub-millimeter three-component force sensor," *Sensors and Actuators A-Physical,* vol. 65, pp. 89-94, Feb 1998.

[132] L. Wang and D. J. Beebe, "Characterization of a silicon-based shear-force sensor on human subjects," *Ieee Transactions on Biomedical Engineering,* vol. 49, pp. 1340-1347, Nov 2002.

[133] J. Dargahi, "A piezoelectric tactile sensor with three sensing elements for robotic, endoscopic and prosthetic applications," *Sensors and Actuators A-Physical,* vol. 80, pp. 23-30, Mar 2000.

[134] J. J. Wortman and R. A. Evans, "Youngs Modulus Shear Modulus and Poissons Ratio in Silicon and Germanium," *Journal of Applied Physics,* vol. 36, pp. 153-156, 1965.

[135] G. S. May and S. M. Sze, *Fundamentals of semiconductor fabrication*, New York Chichester: Wiley, 2004.

[136] Heidelberg Instruments Mikrotechnik GmbH, "DWL-2000," 2008.

[137] K. J. Kuhn, "Moore's crystal ball: Device physics and technology past the 15 nm generation," *Microelectronic Engineering,* vol. 88, pp. 1044-1049, Jul 2011.

[138] M. W. Pruessner, W. S. Rabinovich, T. H. Stievater, D. Park, and J. W. Baldwin, "Cryogenic etch process development for profile control of high aspect-ratio submicron silicon trenches," *Journal of Vacuum Science & Technology B,* vol. 25, pp. 21-28, Jan-Feb 2007.

[139] Techneglas Technical Products,"BoronPlus High Purity Planar Dopant," 2000.

[140] T. Aoyama, H. Tashiro, and K. Suzuki, "Diffusion of boron, phosphorus, arsenic, and antimony in thermally grown silicon dioxide," *Journal of the Electrochemical Society,* vol. 146, pp. 1879-1883, May 1999.

[141] J. S. Christensen, H. H. Radamson, A. Y. Kuznetsov, and B. G. Svensson, "Phosphorus and boron diffusion in silicon under equilibrium conditions," *Applied Physics Letters,* vol. 82, pp. 2254-2256, Apr 2003.

[142] G. L. Vick and K. M. Whittle, "Solid Solubility and Diffusion Coefficients of Boron in Silicon," *Journal of the Electrochemical Society,* vol. 116, pp. 1142-1144, 1969.

[143] S. W. Jones, "Diffusion in Silicon," IC Knowledge LLC, 2000.

[144] K. R. Williams and R. S. Muller, "Etch rates for micromachining processing," *Journal of Microelectromechanical Systems,* vol. 5, pp. 256-269, Dec 1996.

[145] L. J. van der Pauw, "A method of measuring specific resistivity and Hall effect of discs of arbitrary shape," *Phillips Research Reports,* vol. 13, pp. 1-9, 1958.

[146] R. C. Juvinall and K. M. Marshek, *Fundamentals of machine component design*, 3rd ed. New York: John Wiley, 1999.

[147] K. Kim, Y. Sun, R. M. Voyles, and B. J. Nelson, "Calibration of multi-axis MEMS force sensors using the shape-from-motion method," *Ieee Sensors Journal,* vol. 7, pp. 344-351, Mar-Apr 2007.

[148] C. M. Oddo, P. Valdastri, L. Beccai, S. Roccella, M. C. Carrozza, and P. Dario, "Investigation on calibration methods for multi-axis, linear and redundant force sensors," *Measurement Science & Technology,* vol. 18, pp. 623-631, Mar 2007.

[149] A. Umeda, M. Onoe, K. Sakata, T. Fukushia, K. Kanari, H. Iioka, and T. Kobayashi, "Calibration of three-axis accelerometers using a three-dimensional vibration generator and three laser interferometers," *Sensors and Actuators A-Physical,* vol. 114, pp. 93-101, Aug 2004.

[150] E. W. Weisstein, "Euler Angles," in *MathWorld--A Wolfram Web Resource*, 2011.

[151] D. Zbinden, "Wireless Implantable Load Monitoring System for Scoliosis Surgery," *M.Sc. Thesis in Electrical Engineering.* University of Alberta, 2010.

[152] D. Zbinden, E. Lou, and N. Durdle, "Wireless Implantable Sensor Platform," *2010 IEEE Instrumentation Measurement Technology Conference Proceedings,* pp. 1607-1612, 2010.